UNIVERSITY OF SOUTHAMPTON

FACULTY OF ENGINEERING AND THE ENVIRONMENT

Civil, Maritime and Environmental Engineering

Volume I of I

Catalytic Carbon-Carbon Coupling and Reduction using Crystalline Porous Solids for Sustainability and Environmental Applications

by

Elpiniki Georgiou

Thesis for the degree of Doctor of Philosophy

December 2017

UNIVERSITY OF SOUTHAMPTON

ABSTRACT

FACULTY OF ENGINEERING AND THE ENVIRONMENT

Civil, Maritime and Environmental Engineering and Science

Thesis for the degree of Doctor of Philosophy

Catalytic Carbon-Carbon Coupling and Reduction using Crystalline Porous Solids for Sustainability and Environmental Applications

Elpiniki Georgiou

Three-dimensional porous solid structures, which accrue from the coordination of imidazole-based ion with metal ions and topologically mimic well-known zeolitic materials, afford the potential platform to achieve photocatalytic reactions and organic transformations in environmentally friendly conditions, using transition metals with partially or fully filled 3d orbitals. Cobalt and copper-based zeotypes and metal-organic frameworks (MOFs) have been evaluated for a Cross-Dehydrogenative Coupling (CDC) reaction under the irradiation of visible light and the presence of molecular oxygen. The highest conversion was obtained for the cobalt-based zeolitic imidazole framework ZIF-9, while the cobalt isomorphously substituted aluminophosphate (CoAlPO-5) did not appear promising. Interesting photocatalytic activities were demonstrated for the copper-based AlPO-5 and MOF.

Aiming to correlate the structural properties to the catalytic performance of the materials, detailed physicochemical and spectroscopic characterization was performed with pXRD, SEM/EDX, BET and ICP. Further investigation of the nature of the active sites was conducted with Electron Paramagnetic Resonance and Diffuse Reflectance UV-VIS. Oxidation states of the transition metals in the scaffolds were identified utilizing XPS, while the occurrence, reversibility and stability between oxidation states were measured in the application of potential with Cyclic Voltammetry to reflect electrochemical behaviour.

ZIF-9 and the rest of the synthesized materials were additionally assessed for catalytic reduction applications with borohydrides. Employed for the conversion

of 4-nitrophenol to 4-aminophenol, ZIF-9 outperformed the AlPOs and MOFs and structural & surface characterization was applied to the spent material to probe the changes it undergoes during the reaction. Kinetic studies showed that ZIF-9 performs efficiently as a heterogeneous catalyst, but with the material having been reported for a series of non-catalytic applications in the literature, it was further challenged under dye decolouration reactions. Due to the nature of its structural units, ZIF-9 was applied in aqueous and non-aqueous dye-solutions and achieved decolourisation of Oil-Red-O dye and dyed wastewater.

Overall, ZIF-9, comprising properties from different classes of crystalline porous materials, has superior photocatalytic and catalytic properties for a range of chemical reactions. For this reason, the material has been characterised further for its photocatalytic properties with time-resolved absorption spectroscopy to gain insight into the lifetime of its excited states. Successful modification of its basic structure with graphene suggests an additional role of ZIF-9 in materials' science and engineering.

Table of Contents

List of Tables

List of Tables

List of Figures

List of Figures

List of Figures

List of Figures

List of Figures

List of Schemes

List of Abbreviations

1,10-phen	1,10-phenanthroline
2-pymo	2-pyrimidinolate
4,4′-bipy	4,4′-bipyridine
4-AP	4-aminophenol
4-NP	4-nitrophenol
AFI	AlPO-5 framework code
AlPO	Aluminophosphate
BDC	1,4-benzodicarboxylic acid
BEA	Framework designation of zeolite Beta
BET	Brunauer, Emmett and Teller
BETA	Zeolite Beta
bpba	Bis-pyridyl-bis-amide
bpTC	Biphenyl-3,3',5,5'-tetracarboxylic acid
bpy	2,2'-bipyridine
BTC	1,3,5-benzenetricarboxylic acid
CDC	Cross-Dehydrogenative Coupling
CHA	AlPO-34 framework code
CoMOF-74	Cobalt-based metal-organic framework with empirical formula Co_2(dhBDC)
dhBDC	2,5-dihydroxy-terephthalic acid
dmpz	2,5-dimethylpyrazine
DR UV-VIS	Diffuse Reflectance Ultraviolet-Visible Spectroscopy
dtbbpy	4,4'-di-t-butyl-2,2'-bipyridine

EDX	Energy Dispersive X-ray
EPR	Electron Paramagnetic Resonance
ETS-10	Engelhard Titanium Silicalite 10
FTIR	Fourier Transform Infra-red Spectroscopy
HKUST-1	Hong-Kong University of Science and Technology copper-based metal-organic framework with empirical formula $Cu_3(BTC)_2(H_2O)_3$
HOMO	Highest Occupied Molecular Orbital
ICP-OES	Inductively Coupled Plasma-Optical Emission Spectroscopy
L	Ligand 5-[bis(4-carboxybenzyl)-amino]isophthalate
LUMO	Lowest Unoccupied Molecular Orbital
MFI	Zeolite framework topology
MIL-101	Chromium-based metal-organic framework with empirical formula $Cr_3(O)OH(BDC)_3(H_2O)_2$
MOF	Metal-organic framework
MOF-5	Zinc-based metal-organic framework with empirical formula $Zn_4O(BDC)_3$
MOR	Modernite
NMR	Nuclear magnetic Resonance
NP	Nanoparticles
PhIm	Benzimidazole
PhTHIQ	Phenyl tetrahydroisoquinoline
PXRD	Powder X-ray Diffraction
SAPO	Silicoaluminophosphate
SBA	Zeolite SBA
SDA	Structure Directing Agent

SEM	Scanning Electron Microscopy
tBHP	tert-Butyl Hydroperoxide
TCCP	Tetra(4-carboxyphenyl)porphyrin
TS-1	Titanium Silicalite 1 (MFI structure)
USY	Ultrastable zeolite Y
UV-VIS	Ultraviolet-Visible Spectroscopy
XPS	X-ray Photoelectron Spectroscopy
Y	Zeolite Y
ZIF	Zeolite-imidazole framework
ZIF-9	Cobalt-based zeolite-imidazole framework with empirical formula $Co(PhIm)_2$
ZSM-5	Zeolite Socony Mobil-5 of MFI framework type

Declaration Of Authorship

I, Elpiniki Georgiou,

declare that this thesis and the work presented in it are my own and has been generated by me as the result of my own original research.

Catalytic Carbon-Carbon Coupling and Reduction using Crystalline Porous Solids for Sustainability and Environmental Applications

I confirm that:

1. This work was done wholly or mainly while in candidature for a research degree at this University;
2. Where any part of this thesis has previously been submitted for a degree or any other qualification at this University or any other institution, this has been clearly stated;
3. Where I have consulted the published work of others, this is always clearly attributed;
4. Where I have quoted from the work of others, the source is always given. With the exception of such quotations, this thesis is entirely my own work;
5. I have acknowledged all main sources of help;
6. Where the thesis is based on work done by myself jointly with others, I have made clear exactly what was done by others and what I have contributed myself;
7. None of this work has been published before submission and parts of it have been discussed as oral presentations (2016: 18th International Zeolite Conference, Brazil and 2017: 5th International Conference in Engineering, Science and Waste Management, Singapore).

Signed: .....

Date: ..... 11 December 2017.....

Acknowledgements

My PhD journey has been literally a very long one and as such, it got sometimes tiring or disheartening and other times joyful or encouraging. The common denominator of every aspect of this experience was how much I learned and how much I grew from this. For this reason, it has been a great opportunity I was given, for which I would like to thank my supervisory team in Southampton, Dr Robert Raja and Dr James Blake. Not only was I given the chance to complete my PhD studies in UK and Singapore, abroad from Greece, but I was also financially supported and funded by EPSRC, SMMI and A*STAR.

I was very lucky to be exposed to new scientific techniques and carry out my research in different working and scientific environments. Not always easy to adjust fast or smoothly, it has been a great opportunity to meet and work with people from different countries and of different backgrounds. All the members of Prof. Raja's group have been interesting to learn from. Many thanks go to Danni Sun for guiding me through my first steps into the lab and Stephanie Newland for her interest in my difficulties; further thanks to Arran Gill for his help with the XPS analysis and settling in Singapore, Will Mothersole for his explicit suggestions, Chris Hinde for keeping my expectations low in the most optimistic way and Matthew Potter for making me realize how much I appreciate calm people and noise-free working ambience.

I especially acknowledge Dr Raja and Dr Ramon Rios Torres for their guidance in the project of photocatalysis and the – MChem then, PhD currently – student Cameron Ross, with whom I am very grateful to have worked, as he is a very diligent and willing student. I believe that this project motivated both of us to learn more and work harder, trying new materials and focusing more on the details. I wish him success with his own PhD and every luck with his attachment to A*STAR.

Following strictly the order of appearance and not importance, I would like to thank Dr Tan Wui Siew, my supervisor in IMRE/A*STAR for my attachment during the last two years. I very much appreciate her courage to accept me in her group despite the lack of any overlap between our scientific fields in the vision of accomplishing something new. Her willingness to help me led to my close collaboration with Dr Chen Chao, whose ideas, advice and contribution have been valuable and significant for the progress of my PhD during the last months.

Acknowledgements

It would be a great ignorance from my side to not mention the closest people in my life, without whom this journey would never have a bright side. I especially thank and feel proud and lucky having my parents by my side, Panagiotis Georgiou and Rena Psalti. Disregarding the distance between Greece and UK or the time difference between Greece and Singapore, they have engaged themselves in the new forms of technology to show their great support. I thank them for being great listeners and advisors, always encouraging, inspiring and hopeful and for something more tangible… like the smaller or bigger packages and the old-school letters that they sent to me to remind me their physical presence. Last but not least, I thank Miloš Petrović, an outstanding advice-giver and remarkably good researcher, for his problem-solving skills and helpful scientific discussions.

Ending soon this journey, I acknowledge that I changed as a person and, in spite of the many difficulties that appeared, it has been an exciting, challenging and important experience for my personal and professional evolution. I really look forward to closing successfully this cycle of studies and to confidently opening a new chapter in my life.

Chapter 1: Introduction

1.1 Concepts and Advantages of Catalysis and Sustainable Processes

1.1.1 The mechanism of heterogeneous catalysis and its role in modern society

The word catalysis describes a chemical phenomenon, where the presence of a substance in a chemical system is the key to facilitate and accelerate the chemical reaction taking place. This substance, called catalyst, is usually a liquid or a solid, which interacts with the chemical reactants and intermediates suggesting a new, faster reactive path of, usually, lower energy requirements. The catalyst does not interfere with the feasibility of the reaction, which is principled only by the laws of thermodynamics.

The thermodynamics of a chemical transformation is reflected in the Gibbs free energy change ΔG (Equation 1.1), which involves the change in enthalpy and the change in entropy. While enthalpy change ΔH is linked with the reaction being exothermic or endothermic, entropy change ΔS is linked with the higher or lower possibility of the reaction to happen. In detail, a negative change of enthalpy means that heat has been released to the environment as the products are found at a lower energy level. According to the second law of thermodynamics, the entropy never decreases and that also applies to catalysed reactions. The negative change of the entropy due to the formation of a new substance with a lower entropy means that the system of reactants and products involves another system (catalyst), which is reorganised to compensate for the loss of entropy.

$$\Delta G = \Delta H - T \cdot \Delta S \qquad \text{Equation 1.1}$$

It is important to highlight that the catalysts do not change any of these thermodynamic properties involved in the Equation 1.1. What the catalysts change is the activation energy E_a, a magnitude connected to the mechanism and the kinetics of the reaction, as reflected in a classic energy diagram (Figure 1.1). The reduction of the activation energy can occur via different mechanisms, which in turn can be more or less efficient, effective or selective, leaving space for a number of materials to be able to catalyse a reaction. For instance, among the

different pathways that a catalyst can lead the reaction through, some of the most typical mechanisms are bringing and holding the reactants together at an effective angle, interacting with functional groups to favour specific products due to shape confinement or transferring the required electron charge easier within the reaction mixture.[1]

Except for the catalytic mechanism, there are different parameters that affect the rate of a reaction, with a concentration of reactants, pressure and temperature being the most significant ones. It is common to demonstrate the reaction rate r as the product of a rate constant k and the concentrations of the reactants raised to a power. If the reaction is totally or partially connected with the gas phase, the concentrations are connected with the partial pressures. The power is a magnitude calculated from the coefficients of the reaction for elementary reactions or estimated experimentally and reveals the reaction's order. Finally, the parameter of temperature appears in the constant rate *k*, described by the Arrhenius equation (Equation 1.4). Equations Equation 1.2, Equation 1.3 and Equation 1.4 summarize algebraically the aforementioned concepts and are used to determine the set of conditions that influence the kinetics of a reaction.

Reaction: $$A + B \xrightarrow{cat.} C + D$$

Rate of reaction: $$r = k \cdot [A]^x \cdot [B]^y$$ Equation 1.2

$[A], [B]$: $concentrations\ of\ reactants$

$x + y$: $power\ of\ reaction$

Ideal gas law: $$P_i = C_i \cdot R \cdot T \Leftrightarrow C_i = \frac{P_i}{R \cdot T}$$ Equation 1.3

$R = 0.082\ {}^{L \cdot atm}/_{mol \cdot K}$: $ideal\ gas\ constant$

Arrhenius equation: $$k = A \cdot \exp\left(-\frac{E_a}{R \cdot T}\right)$$ Equation 1.4

A: $frequency\ factor\ dependent\ on\ reaction$

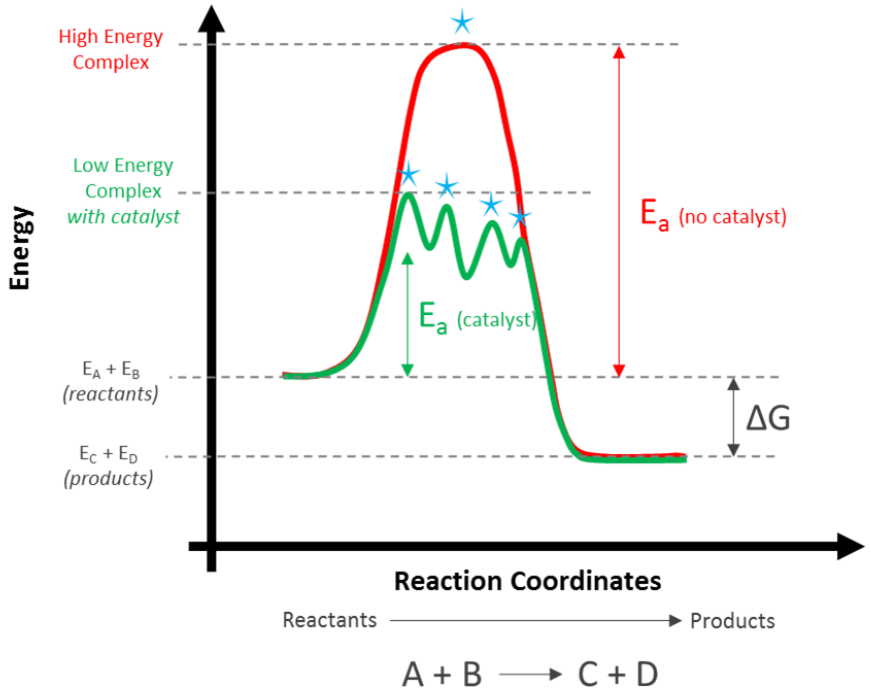

Figure 1.1 Characteristic energy diagram of a reaction $A + B \rightarrow C + D$ occurring with (green) and without (red) a catalyst. Peaks remarked with stars represent transition states.

From Arrhenius equation, it becomes apparent that both activation energy and temperature are defining parameters for the rate of the reaction. High activation energies mean that reactions are very sensitive to the changes of temperature. In simple collision theory, the increase of the temperature causes increase of the kinetic energy of the molecules, which can be interpreted as more collisions or, better, higher possibility of successful collisions among the molecules. Simultaneously, a temperature rise results in higher molecular internal energy through increased bending and stretching of bonds. Then the bonds become more vulnerable to cleave and rearrange for new molecules to form. Hence, the number of molecules with energies higher than the activation energy increases and the reaction occurs faster. Yet, the reactive pathway includes the transition between different states, until the formation of final products takes place. In this case, a catalyst would stabilize the intermediates at lower temperatures, enabling a less energy-demanding and more stable reaction pathway, which overall translates into faster kinetics.

The reactions can be homogeneously or heterogeneously catalysed if the catalyst and the reactants form a common or a different phase respectively. Typically, homogeneous catalysts are in liquid form (e.g. acids) or miscible in the reactants

solution (e.g. salts, complexes), while heterogeneous catalysts are considered usually solids (e.g. metals, oxides) in a separate form from the liquid or/and gas phase of the reaction mixture. Further classification of catalytic reactions depends on dominant parameters or conditions, such as transfer of electrons between electrodes (electrocatalysis), activation with light irradiation (photocatalysis) or use of microorganisms or enzymes (biocatalysis). Nowadays, even more terms, such as environmental and green catalysis, have emerged to describe the purpose of the catalytic reactions, as in environmental remediation or protection, or to highlight the green dimension of the catalytic systems via benign conditions and high selectivity for a specific product.

Each system, homogeneous or heterogeneous, has specific advantages and disadvantages. In homogeneous reactions, the catalysts are usually well-determined species (molecules, ions, enzymes etc.), in which case it becomes easier to make conclusions about the mechanism and the concentration of the catalyst and thus, control the chemical environment. While homogeneous catalysis limits the reaction to the liquid phase, it allows better contact and diffusivity among the reactants and the catalyst. However, it is neither easy nor cheap to separate, regenerate and reuse a homogeneous catalyst from the mixture.

On the other hand, the main benefits that heterogeneous catalysis affords are the non-costly or energy-sustainable ways to separate and recover the catalyst and the possibility to partake in all different phases of reaction.[2,3] Of course, the use of solid catalytic bodies can decrease the diffusion rates and the nature of the catalytically active sites is not easy to define or control,[4] leading possibly to smaller activities than the liquid homogeneous catalytic bodies give. However, solid materials can provide the potential for the implementation of a wide range of conditions, such as temperature, pressure, solvents, radiation etc., due to the fact that the solid catalysts are usually more stable in various thermal and chemical conditions.

Historically, the term catalysis exists since 1835 and is owed to Berzelius,[5,6] after reviewing the work of his contemporary chemist Mitscherlich.[5,6] The latter studied how solids accelerate and enable reactions and introduced the term contact catalysis, which was replaced after a century from the term heterogeneous catalysis. With these two pioneering scientists having already prepared the scientific community for the new discipline of catalysis, Ostwald work's upon catalysis was awarded a Nobel prize in 1909[6] and after that, new catalytic

processes were discovered, established and industrialized. The synthesis of ammonia, commercialized by BASF (Haber-Bosch process)[5,6] and the Fischer – Tropsch process in Germany[7] are considered great innovations of the era before the end of WW II.

Since then, the development of catalytic processes grew immensely and nowadays, the modern chemical and pharmaceutical industry is almost entirely reliant on catalysis, with heterogeneous catalysis finding greater applicability. While the petrochemical sector exhibits the most representative heterogeneous catalytic technologies of the last 50 years, the fine chemicals industry has a lot of examples to demonstrate as well. For instance, the Mallinckrodt Corporation has patented 70 years ago and has improved since then its catalytic process for the production of p-aminophenol from the hydrogenation of nitrobenzene[8] over a catalyst containing platinum and a divalent sulphur compound.[9]

More interestingly, the field of solar photocatalysis has also been commercialised since the mid-90s, starting from Japan and expanding in America and Europe. In fact, the global market of photocatalytic products accounted US$ 1.5 billion in 2014 and is estimated to reach a value of US$ 2.9 billion by 2020.[10] The first industrial photocatalytic process was established in Germany in 1945, which used light and chlorophyll for the large-scale production of ascaridole,[11] a veterinary drug for intestinal worms treatment and a solar photocatalytic facility was built in 1989 in Albuquerque of New Mexico (U.S.A).[12]

Most industrialised photocatalytic processes regard environmental remediation and mainly water decontamination. A large solar plant of water cleansing operates in Almeria and processes of air purification activity have emerged.[13] The photocatalytic water detoxification, such as dyes and agricultural poisons removal, is also one of the main technologies which are tested in pilot scale.[14,15]

1.1.2 Heterogeneous catalysts for sustainable chemistry and engineering

The value of the products of catalysis is indisputably huge. With more than 85% of the current chemical processes having been established as catalytic[16], the business of catalysts is equivalently remarkable. According to various projections, the demand for catalysts is following increasing trends[17] and is expected to grow by 4.8% to reach a value of USD 20.6 billion in 2018.[18] Chemical, petrochemical and environmental sector constitutes this demand by approximately 1/3 each, with refinery and environmental catalysts accounting for the largest shares[19,20] and

chemical synthesis catalysts being a developing field.[17] The industrial development of catalysts requires extended experimental research at a laboratory and pilot scale levels as it involves a multi-stage analysis of the solids and their specific activity for one or more reactions, while the catalytic properties are entirely dependent on the preparation methods, the raw materials and the manufacturing practices.[18]

As a consequence, the design and the engineering of catalytic materials have become a separate research field. The main objective is to create an active catalyst that can effectively undergo one or more catalytic cycles. Shriver and Atkins[21] reproduce the concept that the catalyst is not consumed during the reaction and, hence, it can remain reactive after it facilitates one or more chemical transformations. Nevertheless, the catalyst is heavily involved in the reaction system and its deactivation is possible over seconds or years of use, due to chemical (poisoning, fouling) and thermal (volatisation, degradation) processes, which makes either their replacement or their regeneration necessary.

The catalytic activity of solid materials can be expressed via the change of the reaction rate per unit of surface area and apparent volume of the catalyst (Equation 1.5). Given that not the entire surface area of solids may be catalytically active, calculating the activity is not straightforward and depends on the type of the catalyst and the reactor. For example, the catalytically active sites at metals, metal oxides and metal alloys are found at a uniform and quite dense distribution, which can promote a set of reactions that need broadly varying electronic properties or abundance of binding sites.

Activity:

$$a = \frac{\Delta r}{S \cdot V} \times 100 \qquad \text{Equation 1.5}$$

$$S: catalyst\ surface\ area$$

$$V: catalyst\ volume$$

In contrast, reactants that are likely to form unwanted or competing products would require catalysts with isolated active sites, as they may offer a more controlled catalytic environment to favour a specific chemical transformation over another. In this case, the molar number of the sites can be approximated and it is useful to express the activity via turnover numbers (TON) and frequencies (TOF) (Equation 1.6 and Equation 1.7), as a measurement of catalytic efficiency. Similarly, another valuable measurement which indicates the ability of the catalyst to direct the reaction towards the desired product is selectivity (Equation 1.8).

Turnover Number: $$TON = \frac{molar\ conversion}{molar\ number\ of\ active\ sites}$$ Equation 1.6

Turnover Frequency: $$TOF = \frac{TON}{time}$$ Equation 1.7

Selectivity [%]: $$s = \frac{desired\ product\ quantity}{converted\ reactant\ in\ shortage} \times 100$$ Equation 1.8

Obviously, there are ways to quantify how effectual a catalytic process is, but the current environmental, social and economic situation puts pressure to also quantify how green processes are. With chemical industry having caused negative effects to the environmental and human health during the last decades,[22] there is need not only to restore the natural equilibrium, but also to rearrange the human industrial activities in order to prevent pollution, promote sustainability and protect the environment. Hence, the evaluation of any chemical process should contain the metric of environmental acceptability, which is introduced through a range of measures. Among these, the *E factor* (Equation 1.9), as Roger Sheldon defined it, constitutes a fundamental metric of Green Chemistry.[22,23]

E-factor: $$E = \frac{mass\ of\ waste}{mass\ of\ product}$$ Equation 1.9

Green, or sustainable, chemistry proposes a totally new philosophy which introduces the development and use of environmentally friendly procedures and materials, the elimination of chemical and energy waste and the utilization of renewable resources. The framework of this philosophy can be condensed in the 12 principles of green chemistry, which were developed by Anastas and Warner.[24] Recently, the concept of green chemistry gained dimensions of larger scale introducing the concept of green commercialization, as the 12 principles of green engineering summarize. This list, developed by Anastas and Zimmerman,[25] is presented in Table 1.1, expanding the reduction of environmental risk, fiscal expenses and energy waste to more levels.

Table 1.1 The principles of green engineering.

	Principle	Explanation
1	Inherent Rather Than Circumstantial	Design so that any input and output is non-hazardous as possible.
2	Prevention instead of Treatment	Better to avoid forming waste rather than treating it or cleaning it up.
3	Design for Separation	Minimize the energy and materials use for separation and purification use.
4	Maximize Efficiency	Design aiming for the maximum mass, energy, space and time efficiency.
5	Output-Pulled vs. Input-Pushed	Generate and consume only what is needed.
6	Conserve Complexity	Across the design and production process, balance between the invested material and energy with the reuse or recycling complexity.
7	Durability rather than Immortality	Design products that can sustain their commercial life avoiding to become a risk for the environment.
8	Meet Need, Minimize Excess	Do not overdesign, do not design globally. Plan along the requirements line.
9	Minimize Material Diversity	Design and produce functionally and integrally.
10	Integrate Material and Energy Flows	Arrange the production, designing the flow diagrams on the basis of reuse and recycle.
11	Design for Commercial “Afterlife”	Plan for recovery after end-of-life and design on the basis of remanufacturing.
12	Renewable rather than Depleting	Minimize use of depleting resources, make use of inexhaustible supplies.

All these principles reflect sustainability in each step of the design, process and use, to a smaller or larger degree. Catalysis is not only recommended as a discrete principle of green chemistry but is also implied through the rest of the

listings. For instance, the green chemistry principle for energy efficiency notes that "energy should be reduced and synthesis should be practised at ambient conditions", which implies the use of catalysts to reduce the need for high temperatures making it possible to save energy. An everyday example of this achievement lies in the addition of enzymes in the detergents, which have made possible the washing of clothes at temperatures lower than 40 °C. However, even if the green technology era began the very next day, a significant period of time would be needed to resolve the remaining ecological problems of the past. This demand can be met since catalysis can provide a number of powerful tools for the restoration of the environmental decay and a number of end-of-pipe solutions to limit the pollution of existing processes.

The industrial future that green chemistry and engineering suggest is made of milder conditions, friendlier products and less polluting processes. It will always be recognized that anthropogenic processes have an environmental impact. Yet, it is possible to control it or drastically minimize it, as green engineering bridges the gap between the ideal and the realizable, without lowering the standards. Green chemistry and engineering are supplementary fields; all the principles should not be seen as challenges but as hints and guidelines.

A recent example of the greener technologies is the new generation of oil-based paints manufactured by soya oil and sugar, reducing the toxic volatile organic compounds by 50%.[26,27] Another one is the pilot-scale photocatalytic acylation of quinone-based molecules for the production of tetracycline precursors.[28] Generally, the concept of heterogeneous photocatalysis is a successful fusion of green chemistry and green engineering principles combining perfectly the two fields and becoming a major branch of catalysis.

1.1.3 Heterogeneous photocatalysis in the visible spectrum

The core of each chemical reaction is governed by energy transfer through electrons, which activate the molecules to higher chemical energy intermediate states and eventually lead to new and more stable electron configurations and molecular rearrangements. As it has been described, catalysts mediate to drive the reactions through a less energy demanding pathway, inducing and facilitating this electron transfer and energy. However, this is often plausible when the molecules have particular groups easy to activate under specific chemical conditions. For instance, acidic environment can be achieved with the use of a

solvent, which in turn could behave as an oxidant and functionalize a specific position of the substrate.

In such cases, the absorbance of energy from an external source can help with this molecular activation reducing the demands for prefunctionalization that specific chemical conditions could realize. However, using external energy is not considered less sustainable than using a solvent, (which in the end may be partially recovered and reused), unless the energy source is widely accepted to be renewable, non-hazardous and economical. Ultimately, such a source of power is the light, because it carries limitless quantities of energy. The different frequencies v or wavelengths λ of light define the quanta of photonic energy, hv or $\frac{hc}{\lambda}$ and when absorbed in the chemical reactions, they can lead to electronic ionizations (X-rays, UV spectrum) or electronic transitions (visible spectrum) or vibrational transitions (IR spectrum).

If light can activate a substrate to modify the rate of a reaction, then the light itself catalyses the reaction and this is considered a photoreaction. Often, an additional substance may be used as a photosensitizer which can absorb the light energy and transfer it to the substrates to activate them from a low energy state to a higher and reactive one. Chlorophyll, a substance found in the leaves of the plants and the most well-known natural photosensitizer, is able to capture the sunlight and activate the water and carbon dioxide, which react to release oxygen and glucose. In photocatalysis, the catalyst selectively absorbs quanta of the photonic energy and transits from a ground to an excited state, with the latter being considered the reactive one.

As in conventional catalysis, the classification of heterogeneous photocatalysis refers to the physical state of the catalytic material (solid) and the reaction mixture (liquid or gas) and the term was first introduced in 1970 to name an oxidation of hydrocarbons catalysed by TiO_2 under ultra-violet light.[29] TiO_2 is the most successful and widely reported among the mostly common heterogeneous photocatalysts,[30] which are in general bulk transition metal oxides. These oxides make good semiconductors, which become active when they absorb quanta of energy equivalent or bigger than the difference between the ground and the excited state, known as band gap energy.[31] However, the bandgap energy of TiO_2 is $3.2\ eV$, corresponding to the wavelength $\lambda = 390\ nm$, which is found in the ultraviolet spectrum.

While the photonic energy corresponds to the energy bandgap, it creates pairs of valence band (filled energy levels) holes and conduction band (unfilled energy levels) electrons, which behave respectively as strong oxidizers and reductants. Defects of the semiconductors materials can cause significant failures to this mechanism. A common example is the lattice imperfection, which can trap the electrons in energy depths from where they can be excited with much higher energy quanta (Figure 1.2a). Other failures may stem from poisoning, which may be a result of excess but deliberate contamination with impurities or other functional components.

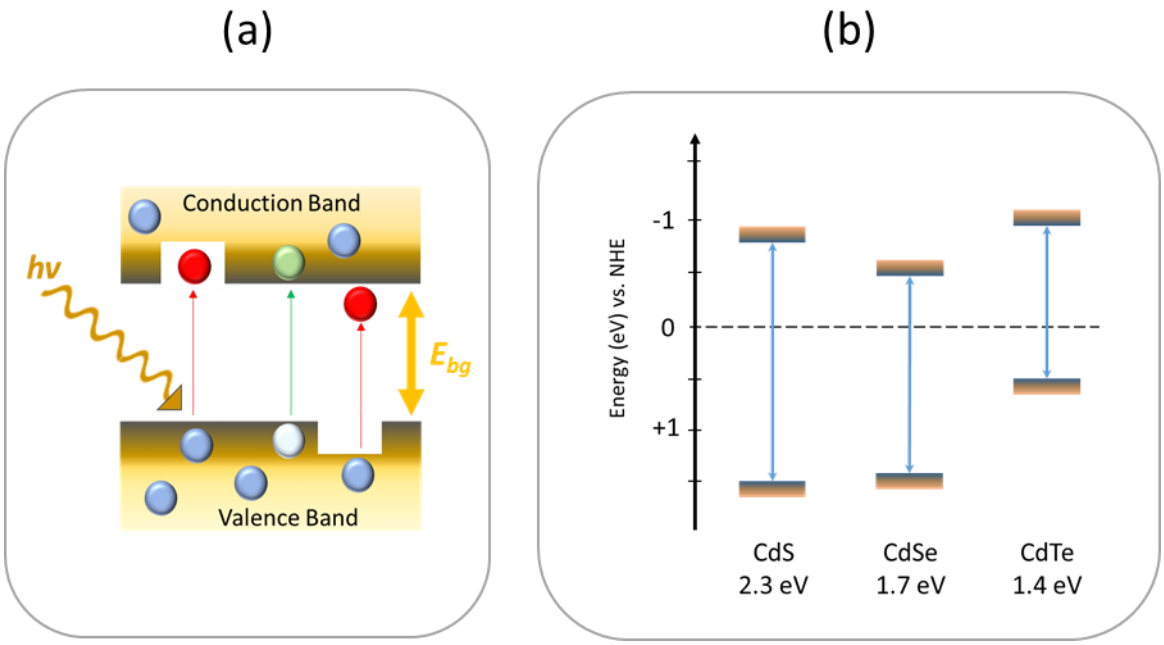

Figure 1.2 Illustration of (a) the successful (green) and unsuccessful (red) excitations of mobile (blue) electrons between the valence and conduction band of a semiconductor and of (b) the different energy levels of the bands performed by the incorporation of S, Se, Te in Cd.

The addition of non-metals, such as N or P, or other elements, can create an increase of photoresponse in the visible spectrum (400-800 nm), which corresponds to energy bandgaps from 1.6 eV to 3.1 eV. These impurities introduce energy levels within the larger bandgap of materials that typically respond to UV light, permitting lower energy levels that serve as “stepping stones” for the electrons to move from the valence band to the conduction band and make use of the visible light. In Figure 1.2b, for example, mixing different semiconductors may facilitate the photoresponse. Cadmium selenide, an electron acceptor, can move the conduction band lower, while cadmium telluride, an

electron donor, can move the valence band higher. Hence, the cooperation of CdSe and CdTe in CdS can create paths of smaller bandgap energy.[32] In other cases, the semiconductors may just serve as suitable supports of chromophores or nanoparticles, in an attempt to heterogenise molecular dyes known for their ability of capturing visible photons or to host nanomaterials or heavier atoms which can cause a rise of excited electrons.[33]

While the photonic energy and the crystallinity of the semiconductors are presented as important conditions for successful semiconductor photocatalysis, the rate of the recombination of the electron-hole pairs is possibly the most significant for molecular photocatalytic reactions. For instance, a very fast charge carrier recombination does not allow enough time for the material to remain at an excited and reactive state and a very slow recombination may lead to energy or even electron losses.[30] An adequately long lifetime of the photoexcited electrons, along with a high crystallinity could give the material the ideal charge mobility. This means that the electrons would have both the energy and the time to travel to the surface of the photocatalyst particles and react with the substrates, before recombining with the holes.

Hence, the two essential concepts that have been introduced are the intensity and the lifetime of the emission achieved, which are connected with the strong light absorption and the triplet state yield. It is known that the delocalized valence band of the transition metal complexes or inorganic semiconductors may give intense photonic absorbance close to or in the visible spectrum, but short-lived excited states on the order of nanoseconds. On the contrary, due to the delocalized orbitals of extended π-conjugated frameworks, light irradiation can excite organic molecules to higher states for longer time periods, on the order of microseconds, but occur at shorter wavelengths.

The physics behind this feature describes the phenomenon of photophosphorescence. Two paired electrons that occupy the same orbital have opposite spins and refer to the ground state S_o. Once an electron is excited from the highest occupied molecular orbital (HOMO) to the lowest unoccupied molecular orbital (LUMO), the spins may be antiparallel (excited singlet state, S_1) or parallel (excited triplet state, T_1) and, according to Hund's rule, the parallel spins are at a lower and more favourable energy state. However, in molecules, the triplet energy levels frequently overlap with the singlet excited states, which raises the possibility for the change in spin and for intersystem crossing from the S_1 to the T_1 state to take place. While the change of spin is prohibited during a

transition, this gives longer lifetime to the electron, before it withdraws back to the ground state levels to recombine (Figure 1.3).

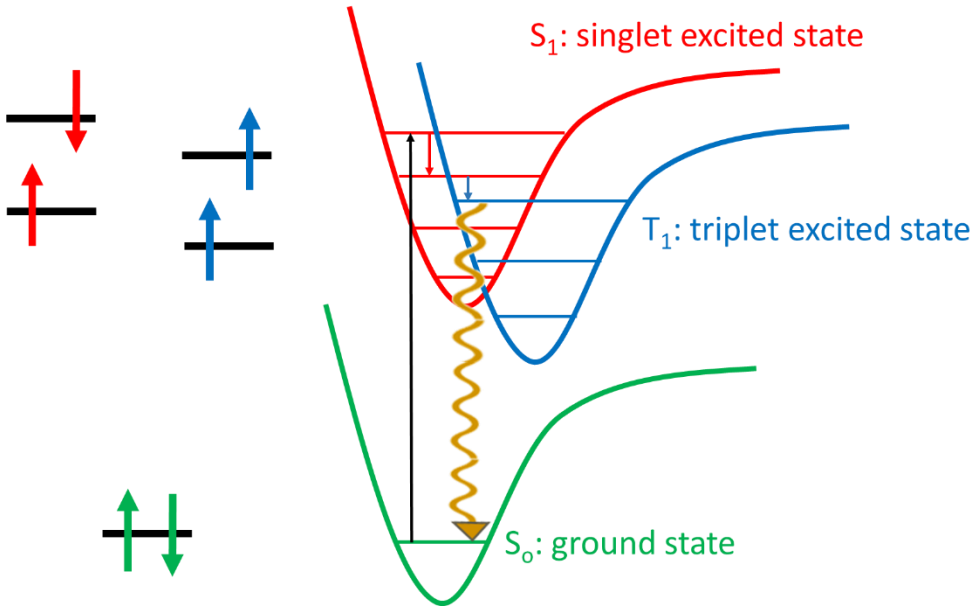

Figure 1.3 Representation of the excitation of an electron to a singlet state with antiparallel spins, passing to a triplet excited state with parallel spins and relaxing back to the ground state emitting phosphorescence (yellow wave).

Doping suitable organic systems with transition metals seems an auspicious method for molecular photocatalysis, as it can enable both strong and longer excitations close to or within the visible area. Such systems are already found in nature (e.g. haemoglobin, a Fe-porphyrin found in blood) and have inspired the synthesis of photoresponsive materials for a range of applications, where strong ligand-metal-ligand interactions are able to give intense and long photoexcitations. However, heterogeneous photocatalysis is a demanding research area, where the list of criteria for the promising candidate heterogeneous photocatalysts combines requirements from different fields.

In particular, as most heterogeneous catalysts, the candidate materials need to afford large surface areas, suitable porosity, chemical robustness, access to active sites, reusability and rational-cost and low-hazard manufacturing. As photocatalysts, they need to allow intense photogeneration of holes and electrons, slow relaxation of the photo-excited states and adequate charge mobility. Except for the aforementioned requirements, the abundance and innocuousness of the visible light photons, which allow ambient temperatures and prevent unwanted photothermal reactions, grows bigger the interest to

design reactive to the visible light materials. Overall, the field of heterogeneous photocatalysis becomes more challenging and more interesting at the same time, attracting more attention from different disciplinaries, in order to eventually harness the solar energy and efficiently convert it into chemical.

1.2 Porous Materials: Zeotypes and Coordination Polymers

1.2.1 Zeolite-like molecular sieves as catalytic materials

One of the best known and most extensively studied class of microporous materials is constituted by the naturally occurring and artificially synthesized zeolites. These materials are three-dimensional crystalline silicates or aluminosilicates, built from SiO_4 tetrahedra or alternate SiO_4 and AlO_4, generally referred as T atoms or TO_4 blocks. The TO_4 blocks are further organized or combined to several different 3D assemblies, which include ring-like arrangements to form pores, opes and cages. Despite the diversity of the structural properties in terms of porosity and channel system, their main and common property is that the tetrahedra assemble networks of uniformly sized pores, while the controlled artificial synthesis allows fewer structural defects. More properties occur with the presence of Al^{3+}, which gives an anionic charge to the framework balanced by cations (Na^+, K^+, NH_4^+, H^+ etc.) located in the pores and voids of these scaffolds. Hence, zeolites are unique porous materials full of possibilities for applications, like ion-exchange, adsorption and catalysis, due to these cations that afford interesting properties. However, the isomorphous substitution of heteroatoms for silicon or aluminium affords more specific and long-lasting features, but it is not an easy case, due to the ionic nature and the size of the T atoms, which strictly govern the zeolitic framework.

With the introduction of the phosphate tetrahedron PO_4, a new family of zeolite analogues, called aluminophosphate (AlPOs) or silicoaluminophosphate (SAPOs) was created.[34] In AlPOs, the strict alternation of AlO_4 and PO_4 blocks (due to Löwenstein's rule, that does not allow the thermodynamically non-favoured Al-O-Al bond) creates net of charge frameworks and the Al-O-P tetrahedral geometry becomes a more flexible platform for isomorphous substitution by a number of atoms. The P-O-P and Al-O-Al bridges and the Si-P vicinity are thermodynamically non-favoured, while the Si-O-Si bonds are considered very stable links, leading to three possible substitution mechanisms.

The first substitution mechanism (SM I) describes the replacement of aluminium, usually by a mono-, di- or tri-valent metal.[35,36] With the Si-P-Si linkages being non-favoured, this mechanism is not expected to occur for silicon substituting for aluminium. The second substitution mechanism (SM II) stands for the replacement of phosphorus, usually by tetra- or penta-valent elements. Silicon and titanium are good examples, due to the similar atom-size substitution. The combination of SM I and SM II is labelled as the third substitution type (SM III), according to which Al and P sites can be simultaneously replaced. While SM III can theoretically regard any tetravalent metal, it usually appears for Si and its potential is dependent on the concentration of silicon.[35] Substitution between similar size atoms causes low framework disorder, but difference in their oxidation states disturbs the total network charge. In these cases, the bridging oxygen atoms at the vicinity of the substitution will need to attract a proton to compensate for the electron excess caused and restabilise the framework.[35] Typical illustrative examples of the substitution mechanisms are given in Figure 1.4.

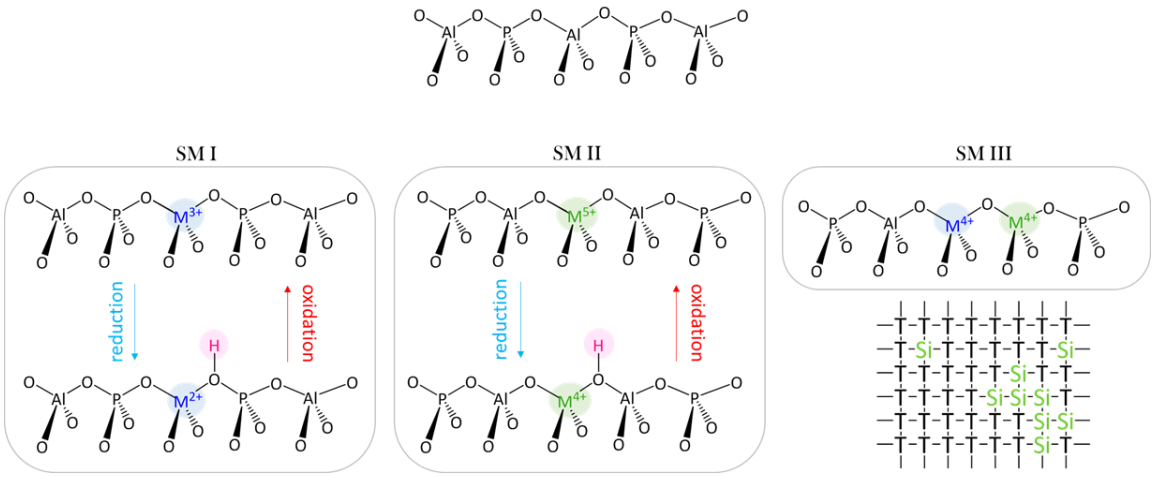

Figure 1.4 Substitution Mechanism I, II and III and illustration of silicon islands occurring when Si replaces Al and P sites. Substituting metal M may have various oxidation states in the framework depending on conditions of treatment.

These hydrogen atoms create Brönsted acidity on the surface of the zeolites and zeotypes,[37] which can be stronger at the edges of extended Si areas (silicon islands) that SMIII suggests.[35] Nonetheless, Lewis acidity may also be present, deriving from missing oxygen atoms, extra-framework aluminium and transition metals substitution.[38] The distinction between Brönsted and Lewis acidity can mainly help understand the catalytic mechanism that favours a reaction. In cases,

a very strong acidity might reduce the desorption rate of a reactant or a mild acidity well- dispersed on the surface can promote the catalytic performance, making the strength or the number of the acid sites a big contributor.[39] The acidity is additionally dependent on other factors. Different zeotypic architectures have different Al/Si ratios or allow different silicon uptake or have different T-O-T angles, which affect the strength of the hydrogen attachment.[37,40,41]

Apart from the acidic nature that zeolites and zeotypes possess, they can also convey redox behaviour, generated by the metal doping or substitution. A metal ion with more than one oxidation state, when exposed to the right conditions that allow its reduction or oxidation, it will be found in the framework at a specific oxidation state. Apparently, such a redox couple can initiate redox reactions and introduce active sites in the crystals of different character. This way, zeotypes gain a much more versatile character and can be both considered as acid solids and redox catalysts (Figure 1.4).

Obviously, the metal substituted (silico)aluminophosphates afford the possibility to design, determine, control and combine the types of active sites and correlate them to the catalytic performance in various applications. As a consequence, these materials serve significantly for research cases. In most studies of catalytic transformation, the reported materials appear reactive, but the inability to offer a platform for various designs and engineering of the reactive sites does not help understand what makes the materials reactive and how they can be improved.

The framework of (silico)aluminophosphates with code 5 (AlPO-5 and SAPO-5) is a commonly used structure, known as AFI, frequently chosen for its robustness and easy substitution with various metals. In this project, this framework is employed in different applications and is being tested along with substitution with cobalt and copper. The introduction of copper in the aluminophosphate is not a typical substitution reported in the literature, while the introduction of cobalt provides the possibility to test two different oxidation states (Co II and Co III) in the same tetrahedral configuration and content. Moreover, the silicosubstituted AFI framework offers an adequate prospect to realise whether acidity is a parameter of interest in the specific project.

The presence of copper and cobalt in the AFI framework introduces the materials named as CuAlPO-5 and CoAlPO-5, which are described in detail in Chapter 3. Since the metals are copper and cobalt with oxidation states +1, +2 for Cu and +2, +3 for Co, the most probable substitution mechanism is SM I, which governs

the replacement of Al sites. This gives the opportunity to realise how their redox behaviour affects the catalytic results. On the other hand, keeping the Si introduction at low content helps avoid the SM III and, therefore, control better the type of acidity in the reaction.

Furthermore, although metal substituted (silico)aluminophosphates have been widely reported in various catalytic applications, they have been reported in limited photocatalytic studies, with most of them regarding dye degradation processes.[42,43] This project submits CuAlPO-5 and CoAlPo-5 in visible light catalysing C-C bond formation and 4-nitrophenol reduction. However, due to the range of metals that can be inducted in the framework, it is not clear whether their limited photocatalytic performance and references are due to the type of metal, type of structure or the nature of the material itself. Thus, adding photocatalytic applications in the references of CuAlPO-5 and CoAlPO-5 should enhance the possibility to answer such questions in the future.

Zeolites and zeotypes, as they have been described here, have a vast and diverse set of possibilities. They can be designed in different architectures, allowing various cage and channel systems, which can force the reactants and products to undergo different molecular delivery and nanoscale confinement. Their acidic nature and metal functionality can be adjusted accordingly. Seemingly, they are considered as physically inorganic materials, chemically robust, but partially adaptable, as the tetrahedral coordination is a necessary, almost axiomatic, condition. Attempts to enhance their catalytic activity with an organometallic character have been reported by tethering catalytically active organic molecules and grafting organic-metallic entities.[44] However interesting these concepts are, the inability of isomorphous substitution, in this case, makes them vulnerable to leaching and deactivation, shifting the interest to a different class of porous materials that may allow the co-existence of organic compounds in their frameworks.

1.2.2 Coordination polymers: metal-organic frameworks properties

Inspired by the principles of coordination chemistry, solid, crystalline and porous materials can be generated with the repetition of coordination complexes. Metal cation centres or clusters (nodes) linked with mono- or poly-dentate organic ligands are called coordinative complexes and these entities have the ability to extend to an array of one, two or three dimensions, by self-assembly under specific conditions. Based on the electron density around the metals, the

coordination of the metals with the ligands may vary from 2 to 10 and depends on the angles between the metal centres and the linkers. The dimensionality of these inorganic-organic hybrid materials, known as metal-organic frameworks (MOFs), ranges from 1 to 3 as MOFs may develop in chains, layers or three-dimensional structures, creating a grid of metals bonded with organic molecules, as Figure 1.5 shows.[45]

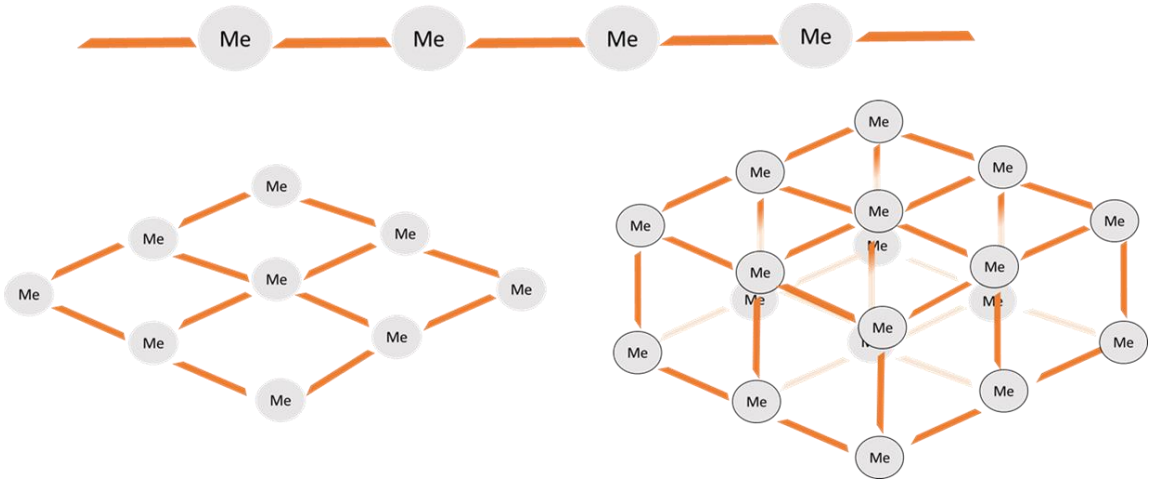

Figure 1.5 Metal nodes (grey) linked together with organic molecules (orange) forming 1-D, 2-D and 3-D MOFs.

The mostly common metals used in MOFs come from the group of transition metals. The ones with partially filled d orbitals, such as Co and Cu, make excellent candidates, due to the high degree of orbital hybridisation that they can undergo. This favours multiplicity of well-distinguished structures, molecular secondary building units,[46] where the 4-fold coordination is not necessary. Doping with different metals or metal clusters in order to create a multi-metallic network is also possible, although not yet widely reported.[47]

Apart from the metals, the variety of the organic ligands leads to a great range of structures of different rigidity or flexibility, pore sizes and topologies,[48] with isoreticular chemistry being one of the main reasons of MOFs diversity. The most common ligands are polycarboxylate anions, such as the trimesic acid of HKUST-1, a widely known copper-based MOF. The carboxyl groups afford a good linkage of nodes and their multiplicity along with other groups, such as hydroxyl groups, raises the degree of connectivity. Other types of ligands widely reported are pyridines and amines derivatives, while sulphates and phosphates are less described. The bonding between the metal centres and the linkers is characterized as an acid-base connection of a Lewis type, because of the electrons exchange.[49]

Apparently, the ligands affect MOFs' geometry, porosity and crystallinity, which in turn influence highly their functionality. Consequently, more techniques were proposed to enhance and diverse MOFs' functionality. Post-synthetic modification of ligands is the most widely applied and primarily reported technique, especially for MOFs which have ligands that can be amino-functionalized.[45] Ligand exchange is another technique which has been described but has not led to very stable MOFs. The review of Wang and Cohen elaborates on this research area and outlines a series of interesting examples up to 2009.[50]

A special set of organic ligands leads to the formation of an interesting sub-class of the MOFs. Imidazolate derivatives tend to coordinate with the metal centres via the nitrogen atoms and the transition metals are tetrahedrally coordinating to the imidazole linkers. The angle between the metal and the imidazole-based ligand (Figure 1.6) is comparable to the Si-O-Si angle (approximately 145°) found in zeolites. As a consequence, the accruing architectures adopt a zeolitic topology and the possibility to form chains or layers is reduced, since the type and shape of bonding between the nodes mathematically provide 3D structure.

This family of MOFs is recognized as Zeolite-Imidazolate Frameworks (ZIFs) and gets increasing attention because of the highly strong structures, rigid coordination, porosity, thermal stability and chemical resilience.[51] ZIF-8 is a zinc-imidazolate framework which responds more frequently in the literature. The change of the ligand to benzimidazole forms ZIF-7, which has the same topology but difference in the size of pores. The change of the metal to cobalt affords a novel structure, ZIF-9, which has recently been applied in various applications.

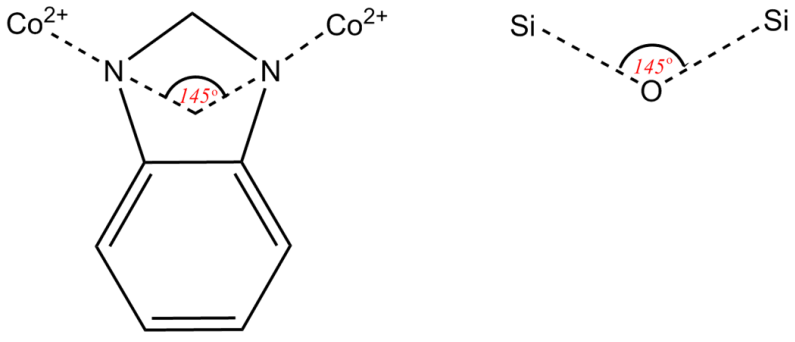

Figure 1.6 Similarity between the bonding angles of ZIFs and silicoaluminates.

MOFs afford particularly high surface areas and big pore dimensions. They can be designed applying principles of reticular and coordination chemistry and their development relies on tuning their properties by changing metals and the linker

molecules in terms of length, shape or functionality. Unlike zeolitic materials, they contain organic parts as part of their framework, which can be used as an advantage of affinity with organic transformation. They are characterized by high metal density and Lewis acid activity but lack thermal stability. While the advantages and disadvantages of MOFs may be reversely be read as disadvantages and advantages of zeolitic materials, ZIFs fuse together properties from both categories, aspiring to become a possible platform for competent applications.

1.2.3 Typical industrial and scientific applications of zeolitic materials and metal-organic frameworks

The surface properties and the various shapes of zeolites and zeotypes give them a lot of possibilities of use. Ion-exchange applications are quite exclusively driven by the unique features that the surface of the zeolites has. The protons or metal cations which compensate the anionic charge of the Al-O-Si network are found near the oxygen atoms, but they are not bound onto them. In this way, the cations are adjusted accordingly in the cages or pores near the framework. The bonding has a loose and ionic character, which makes cation-exchange usually easy. This, naturally, makes these materials very useful in water purification applications or in the industry of detergents (for example, as washing powders or filters).

Moreover, the zeolites are typically found in adsorption and separation processes, because of their surface and shape characteristics, which provide a variation in the interactions of different substrates with the crystals. The contact between the different compounds and the zeolites is dependent on the surface and shape of the materials, causing differences in the migration and the adsorption-desorption rates. This is why the zeolites are then found in sieving applications, like purifications of organic chemicals.

However, the shape and the size of the void system of these materials promote the shape-selectivity, due to the confinement of the reactants or products. Kinetic diameters matching the size of the pores easily diffuse in or out of the material. Bulky molecules can be excluded or trapped in, while inappropriately branched molecules are actually subjected to rearrangement, with the help of electrostatic forces applied in the narrow spaces of the materials.[52,53] Combining the shape-selectivity with the chemistry explains why zeolites and zeolite analogues find a lot of applications in catalysis and, even more, in refining and chemical

processes, where they have the biggest economic impact. As catalysts, zeolites have proven effective in terms of cost and performance in catalytic crude oil cracking, isomerization and other refinery processes.

Zeolite Y is a good example, known for its activity and selectivity. It is the commercial Fluid Catalytic Cracking (FCC) catalyst, while it is also used in short-chain alkanes alkylation and isomerization with zeolite-β.[53] H-ZSM-5 is mostly used for conversions of methanol to gasoline (MTG), while research revealed that the length of the ZSM-5 channels does not allow chains longer than maximum 11 carbons.[54] Methanol to olefins (MTO) reactions are principled by strong acidity, which facilitates the dehydration and by the steric diffusional effects, which hinder the production of high molecular weight alkenes. The chabazite analogue SAPO-34 has proven a very efficient catalyst for the MTO process.[55]

The introduction of heteroatoms (transition metals) in zeolites has also found commercial applications, with titanium silicate (TS-1) accounting for one of the most valuable catalysts for a range of industrial reactions with hydrogen peroxide, established by big firms, like Mobil, Sumitomo and Enichem. TS-1 is a Ti-substituted pentasil catalyst with non-acidic character, due to the partial substitution of Si(IV) for Ti(IV) and has been successfully applied for the oxidation of phenol to catechol and hydroquinone and to selectively epoxidise propylene to propylene oxide. TS-1 and Ti-ZSM-5 have been used productively for the production of ε-caprolactam, a precursor of the “greener” nylon.[56] Except for titanium, iron and copper have also been proven reliable dopants for a number of reactions. Fe-ZSM-5 catalyses the oxidation of benzene to phenol and Cu-ZSM-5 and Cu-FER have lately been reconsidered for the reduction of nitrogen oxide molecules.[57–59] The metal-substituted AlPOs and SAPOs constitute good potential for olefin isomerization and other applications that require weaker acidity, as is Pt-SAPO-11 used in the wax isomerization, developed by Chevron USA.

The Lewis acidity, the potential of open metal sites, the high metal content, the lack of dead volume alongside to the high pore volume makes MOFs interesting for chemical applications of different nature, where zeolites and zeotypes have been proven less effective. Gas related activities are the mostly discussed in the literature.[60] Briefly, the unsaturated sites of MOFs can chemisorb traces of unwanted gases, while the change of coordination of the sites may alter the colours of MOFs, which gives them the potential to function as sensors. The pressure or thermal swing adsorption –desorption is usual in MOFs, giving them a good potential for gas separations and gas storage, with the latter being

enhanced by the breathing effect some coordination polymers of this family demonstrate.[61] While CO_2 capture is one of the most typical examples, hydrogen storage remains a main challenge.[62,63]

However, MOFs have also emerged in the field of catalysis, considering the increasing number of publications during the last decade. An extensive review for the heterogeneous supramolecular catalysis with MOFs has been published recently and covers in many details the research which has been conducted with MOFs as catalytic materials.[64] Oxidations, hydrogenations, epoxidations, cyanosilynations, addition and coupling reactions, Knoevenagel condensations and many more types of reactions have been realized with MOFs, each of them indicating one of the main three characteristic principles of catalysis with MOFs.[65] First, the active site is part of the framework, which can be either the metal site or, less typically, the ligand. Second, the active species are encapsulated in the structure, rendering the framework a suitable support. Last, the active species is attached covalently to the framework units, which usually happens with the post-synthetic modification. In the latter case, specified homogeneous catalysts can be heterogenized. Furthermore, a new, theoretical approach shows that these materials can be viewed as semiconductors and isolators,[66–68] while some MOFs have been reported to be good photosensitizers.[69–71]

Despite their great potential and interesting applications, the 30 year long MOFs experience displays little commerciality, mainly due to the non-optimized technology for large-scale MOFs production and their ongoing research. However, as soon as companies, like BASF, committed and optimized massive preparation of MOFs and scaled up their production from laboratory quantities to tons manufacturing, the first worldwide announcement for their commercial application took place by DECCO in 2016, where MOFs are used to absorb the released 1-methyl cyclopropene in the storage places of fruits and vegetables.[72] Other application that is going commercial is their utilization in fuel tanks for vehicles to secure and boost the storage of natural gas.[73] It seems that the first applications that are being commercialized with MOFs regard their excellent interaction with gases, which justifies other recent agreements that have been on the news.[74] However, the continuous advancements in MOFs applications may soon create a breakthrough in commercial heterogeneous catalytic applications.

Zeolites have not been regarded traditionally as photocatalysts and MOFs have mainly responded to uses that deal with gases. However, in scientific research, there are a number of references that show the potential of zeolites and MOFs in

different fields and Table 1.2 enlists these applications along with the catalytic materials used. It should also be remarked that Ag and Cu exchanged zeolites used to appear promising for the photodecomposition of NO_x and N_2O.[75–79]

Table 1.2 Examples of zeolites and MOFs applied in specific applications of removal of water pollutants.

Application[REFERENCE]	Material	Comments
Photocatalytic decomposition of 4-nitrophenol[80]	TS-1	mesoporous titanosilicate Ti^{4+}, coordination number 4
Photocatalytic decomposition of monoethanolamine[81]	TS-1	mesoporous titanosilicate Ti^{4+}, coordination number 4
Degradation of phenols[82]	ETS-10	mesoporous titanosilicate Ti^{4+}, coordination number 8
Photodegradation of azo-dyes[83]	Ag-$CoFe_2O_4$-Y	Ag exchanged zeolite Y Ag^{1+} (extraframework), $CoFe_2O_4$ (magnetic nanocomposites)
Photocatalytic degradation of methyl violet[84]	$Co_2(L)(H_2O)_2$(4,4′-bipy)]·$3CH_3CN$	3D MOF, paddle wheel motives, Co^{2+}, coord. num.: 5
	$Mn_2(L)$(1,10-phen)$(H_2O)]\cdot H_2O$	2D MOD, non-equivalent sites (square pyramidal and octahedral), Mn^{2+}, coord. num.: 5 and 6
Photooxidation of methyl orange, methyl blue, methylene blue, neutral red, safranine T[85]	Cd(bpba)H_2bptc)$_{1/2}$ H_2O	3D mesoporous MOF, (pentagonal bipyramid) Cd^{2+}, coord. num.: 7
	Co(bpba)$(bdc)_{1/2}$	2D stacked layers, mesoporous MOF, (paddle wheel motif) Co^{2+}, coord. num.: 5
Removal / Degradation of bisphenol A as water pollutant[86]	Zr-(tetrakis-(4-carboxyphenyl))-porphyrin	3D mesoporous MOF with 1D cylindrical channels Zr^{4+}, coord. num.: 8

Application[REFERENCE]	Material	Comments
		active site: TCCP ligand

It is obvious that the type of MOFs frequently employed are particularly complex and demanding in preparation. Moreover, the ion-exchanged zeolites found in the literature involve noble metals or Ti, making the use of either expensive materials or exclusively UV light. These findings constitute a good motivation for further experimentation with simpler and less expensive materials, which respond to visible spectrum light and incorporate the metals into the framework.

1.3 Heterogeneous catalysis for green organic synthesis and environmental applications

1.3.1 The C-C bond formation

Chemical organic synthesis constitutes a special and important branch of chemistry because it regards and studies the transformation of chemical bonds into new structures intended to have specific targets and functionality. It is a very broad field with many applications, from catalysis to biochemistry and medicine and responds typically in the context of fine chemicals industry. The development of these complex and multifunctional molecular entities is compelled to produce them with high yield and purity. However, these processes are usually associated with excess of solvents, lacking eco-friendliness and becoming a chief source of waste, with the E-factors of this industrial division being high.[87]

As it has been described in the previous sections, catalysis becomes a very useful tool, which can offer benign conditions and cleaner production when applied in organic synthesis. In fact, homogeneous catalysis with organometallic or enzymatic complexes or dyes has already found application.[88] Although this is a positive step, the hurdle of recovery and separation becomes a considerable limitation. Subsequently, the use of solids, such as porous solids, molecular sieves and metal catalysts, are highly regarded, while organic synthesis can benefit from the shape functionality and metal incorporation in solids.

The suitability of each solid catalyst depends on the reactions of organic synthesis, with the C-C bond formation being one of the most representative and

significant types,[89,90] mainly because it serves as a means to extend the carbon grid of the molecules and raise their complexity. The use of organometallic complexes or organic bases for C-C bond formation significantly reduced the prefunctionalisation of the carbon positions with solvents. In the 1960s, the immobilisation of these organic catalysts on stable supports like mesoporous silica and alumina was considered a novel and sustainable process.[91] Nowadays, despite the deeper understanding of tethering organocatalysts, leaching, deactivation and lower selectivity remain some of the basic issues. This shifted the interest to using other efficient solids, such as metal oxides.[92]

Today, the generation of C-C bonds in organic synthesis with heterogeneous catalysis continues being a hot topic in chemistry and there is a lot of interest in the reported catalytic systems regardless the type of reaction of C-C bond. Table 1.3 is indicative of zeolites and MOFs that have been used for the study of a range of cross-coupling reactions. Palladium heterogeneous catalysts[93,94] have been broadly discussed and, as shown from the table, practically monopolise this research field. Other metals have also drawn the attention of scientists, such as ruthenium and [95–97] rhodium, [98,99] alongside copper[100–105] and cobalt.[106] Transition-metal-free systems have also attracted interest.[107,108]

Table 1.3 Examples of catalytic systems reported in the literature for a range of cross-coupling reactions for the formation of C-C bonds.

Application[REFERENCE]	Material	Comments
C-C coupling reaction[109]	SnBEA, ZrBEA, TiBEA	ion exchanged zeolite BEA Sn^{4+}, Zr^{4+} (extra-framework) Ti^{4+}
Suzuki coupling reaction[110]	Pd USY	zeolite Y Pd^{0} in 6-member ring
Suzuki coupling reaction[111]	[Pd (2-pymo)$_2$] $3H_2O$	microporous 3D MOF, SOD Pd^{2+} (isolated ions), coord. number: 4
Mizoroki-Heck coupling reaction[112]	Pd/ED-MIL-101	microporous 3D MOF Pd nanoparticles supported on MIL-101

Application[REFERENCE]	Material	Comments
Sonogashira coupling reaction[113]	Pd / Y - MOF	bimetallic MOF Pd^{2+}, coord. number: 4 Y^{3+}, coord. number: 8

Overall, the related published work is indicative of its importance and the attention it gains is rising due to the applicability of the C-C reactions in modern chemistry. The scientific and practical significance of this field justifies the increasing investigation of these reactions in terms of materials, parameters and substrates. However, the vast majority of catalysts are MOFs and involve palladium, or, otherwise, the MOFs serve only as hosts and supports of other active metals or complexes. This grows bigger the need to enquire and examine simpler systems, which can lead to a less expensive and possibly a more versatile alternative.

1.3.2 The presence of nitro and azo groups in the environment

Environmental catalysis field aims to use catalytic technology in order to reduce the pollution caused by anthropogenic activities, by applying catalytic technologies for environmental protection or remediation. Green Chemistry and Green Engineering aim to the development of sustainable and friendlier processes and materials, but the impact on the environment will still occur, even reduced and the remediation will still be necessary. The problem in remediation techniques is the unfriendly environment of the waste, which entails different molecules and reactive species. The diversity of the waste can deactivate a catalyst quickly or slow down significantly its function. For this reason, catalytic systems used for environmental applications need to be robust, sustainable, active and characterized by a low cost and relatively easy manufacturing technique.

Environmental toxicity in liquid body receptors is one of the main problems caused by industrial activities and aromatic nitro compounds are a considerable toxic hazard. These compounds constitute the biggest class of industrial chemicals and usually stem from the pesticide, explosive and pharmaceutical industry (Figure 1.7).[114] Their negative effects depend on a range of parameters, such as the number or the position of the nitro groups, number of aromatic rings

and presence of heteroatoms. The ecological disturbance is big[115], if one considers that they do not occur naturally, thus, there is not a natural defence mechanism. Similarly, they are dangerous for the human health[115] and they belong at the top of the list regarding pollutants for remediation.[116]

Another class of chemicals which can be found in big amounts in the wastewater contaminating the soil and underground water is constituted by azo compounds. Since azo dyes are approximately the 65-70% of the dyes used in total,[117] the azo groups are mainly found in textile colourants, but are not restricted in the dye industry (Figure 1.7). Their presence in water has dramatic impact on human and environmental health,[118] affecting life with mutagenic and carcinogenic effects, liver risks, skin irritations, nausea and other complications. Consequently, it is rather obvious and important to enhance the existing technologies employed for water remediation from these compounds, which range from advanced oxidation processes to chemical and biochemical destruction.

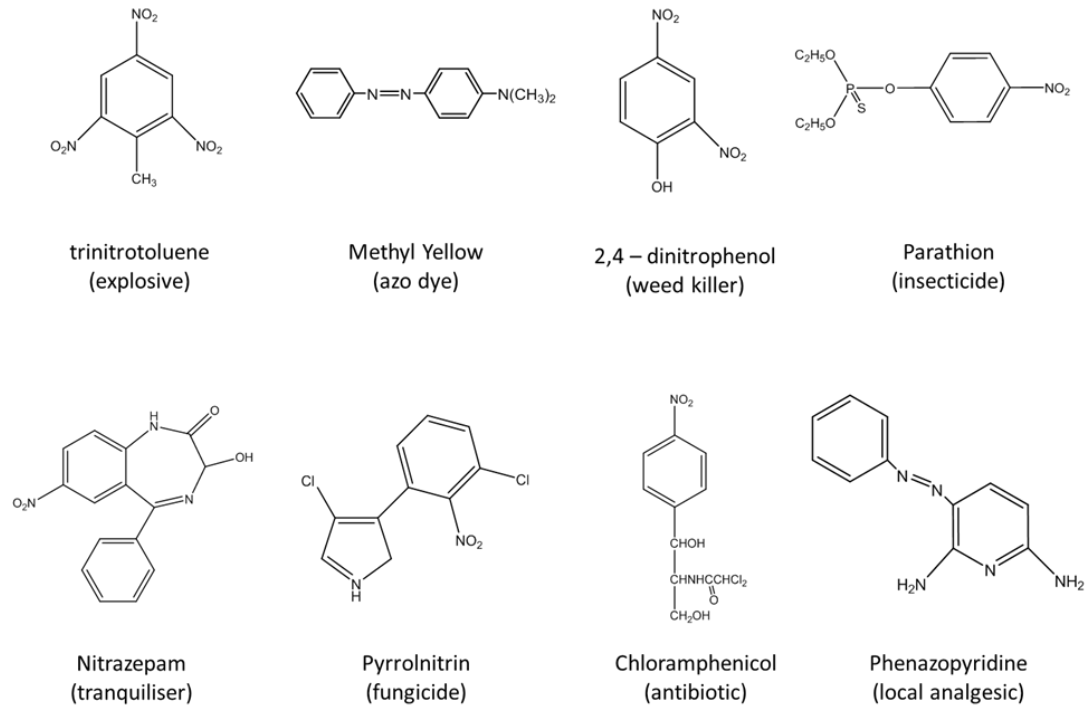

Figure 1.7 Examples of nitro- and azo-based molecules which are found in industrial products.

Denitrification of waters is applied in large scale nowadays, but they mainly regard the removal of nitrates. Some new technologies regard the reduction of nitrates with zero-valent iron walls at low pH values and electrokinetics.[119] Nitrogen in water bodies is also found as ammonium ions and the use of bacterial enzymes and microorganisms is possible to convert them into nitrites and

eventually nitrates.[120] However, the industrial removal of nitroaromatics and azo compounds is a challenging and demanding procedure, since neither microbial nor chemical degradation is complete or even feasible. As such, the proposal of the reduction of these nitro and azo-based chemicals to amino- and aniline-based molecules as an overall prior step may be the beginning of a sustainable solution.[119]

For this reason, the research community has turned towards methods of reduction of nitro and azo compounds. Noble metals, such as Pd, Ag, Au in the form of nanoparticles draw the attention due to the fast completion of the reaction.[121–125] However, considering the large scale remediation that removal of water pollutants demand, such technologies are not practical and are expensive. For this reason, research with more abundant materials and more economical methods is a necessity.

1.4 Aims and Objectives of the project

1.4.1 Porous catalysts based on copper and cobalt for a range of applications

In the most recent works, metals of particularly high cost, such as gold, silver, palladium, platinum, ruthenium, rhodium, gallium etc. tend to appear more frequently, as shown in Tables 1.2 and 1.3. It is true that such metals frequently promise a high catalytic activity, while the noble character of some adds other characteristics, such as better formation of nanoparticles, longer lifetime, better interaction with reducing gases. However, it is important that less hazardous metals and/or more abundant on earth are studied in terms of applicability in catalytic systems. Copper and cobalt are metals that fulfil these criteria and are not expensive and, thus, are shortlisted for their activity to be tested in a range of applications.

Catalysts have indeed specific functionality, but developing one catalyst per process is not always sustainable. On the contrary, designing catalysts which can be applied in more than one applications should be considered as an advantageous process. It is also important to take into consideration the methodology proposed in the synthetic protocols of the catalysts, since complex synthesis may not be well-controlled, may be difficult to scale up and reproduce and may rise significantly the cost of their manufacturing. Equivalently, catalysts should respond to a range of applications from different chemistry divisions

responding to different problems. This makes their scientific study more interesting because it enhances their applicability and understanding of different catalytic mechanisms.

On these lines, main focus of this project is the development of well-ordered copper and cobalt-based catalysts, with crystallinity and porosity in order to facilitate the examination of the nature and position of the atoms and active sites in particular. AlPOs and MOFs are perfect candidates due to their well-established properties, while their synthetic methodologies are not greatly demanding. Moreover, copper and cobalt are transition metals with photoresponse in the visible area of light. This is one more of the reasons why these metals are chosen, since aim is to synthesise catalysts with photocatalytic activity. As described in sectors 1.2.3, 1.3.1 and 1.3.2, most materials responsive to light have on their basis TiO_2 or metals, such as ruthenium, well-known for their photoactivity or photosensitization. However, these catalysts usually are supports (titania) or include metal particles hosted on supports, while aim is to create materials that incorporate the photoactive sites on the framework.

The range of applications is found from the area of organic synthesis and environmental remediation. A representative reaction of C-C bond formation should be an excellent platform to test catalytic and photocatalytic activity, while reduction of nitro groups and azo dyes have also been considered essential. Complex catalytic systems, as presented in Tables 1.2 and 1.3 are avoided, since aim is to examine simpler structures and understand how basic properties can benefit the study of applications, such as a Cross Dehydrogenative Coupling reaction, the reduction of 4-nitrophenol to 4-aminophenol and the degradation of azo dyes in aqueous and non-aqueous solutions.

Summing up the project objectives, cobalt and copper-based crystalline materials from the family of AlPOs and MOFs are being evaluated as catalysts and visible light photocatalysts in reaction systems of cross-coupling, 4-nitrophenol reduction and azo dyes degradation. Characterisation of these materials in terms of structure, porosity and nature of active sites will reveal additional information that should help with the design and engineering of simpler and inexpensive catalysts intended to be used in this range of applications. New properties will be attributed to the successful performance of the materials, which enhances the comprehension of these systems and may elucidate other similar ones.

1.4.2 Characterisation and correlation of properties with catalytic performance

Copper and cobalt AlPOs and MOFs of different morphologies and nature of active sites are probed catalytically and photocatalytically. The correlation of their properties with their performance is achieved via thorough structural and spectroscopic examination. Basic structural investigation is performed with PXRD technique to ensure phases and crystallinity. SEM is used to understand the morphology of the particles and as a medium of evaluating their uniformity. EDX and ICP analyses are employed to provide information regarding the metal incorporation. BET is used to ensure porosity of the materials. This basic characterization is a good starting point to ensure that the materials are structurally adequate to be used as solid catalysts.

Probing the materials in catalysis and photocatalysis applications, deeper understanding of the properties of the high-performance materials is desired, especially regarding their active sites. XPS is applied for characterisation of the oxidation state and EPR can reveal the environment of a metal site. Diffuse Reflection UV-VIS demonstrates the photoabsorbance of the materials, while it can also be used as a method for coordination geometry. More Cyclic Voltammetry is also employed in order to assess any electric conductivity, which might take part in the photocatalytic mechanism. Basic structural characterisation is also taking place post-catalysis, in order to evaluate the distortion the materials have undergone. Heterogeneity of the materials is also evaluated and used to supplement their sustainability. Sums up the mentioned techniques and the information that is likely to be extracted.

Table 1.4 List of applied characterisation techniques and brief reference on the information extracted from each one.

Characterisation method	Information
PXRD	Crystallinity and phase purity
BET	Porosity and surface area
SEM	Surface morphology and particles size and shape
EDX	Metal incorporation and content
ICP	Metal incorporation and content

Characterisation method	Information
XPS	Metals' oxidation state
EPR	Metals' coordination environment
DR UV-VIS	Photoresponse and coordination geometry
Cyclic Voltammetry	Electrochemical behaviour

1.5 References

1 R. A. van Santen and J. W. Niemantsverdriet, Springer US, Boston, MA, 1995.

2 G. Busca, in *Heterogeneous Catalytic Materials*, ed. G. Busca, Elsevier, Amsterdam, 2014, pp. 1–7.

3 G. Busca, in *Heterogeneous Catalytic Materials*, ed. G. Busca, Elsevier, Amsterdam, 2014, pp. 37–56.

4 G. O. Spessard and G. L. Miessler, *Organometallic chemistry*, Oxford University Press, New York, 2010.

5 M. Boudart, B. H. Davis and H. Heinemann, in *Handbook of Heterogeneous Catalysis*, eds. G. Ertl, H. Knözinger and J. Weitkamp, WILEY-VCH, Weinheim, 1997, pp. 1–49.

6 A. J. B. Robertson, *Platin. Met. Rev.*, 1983, **27**, 31–39.

7 M. E. Dry, in *Handbook of Heterogeneous Catalysis*, eds. G. Ertl, H. Knözinger and J. Weitkamp, WILEY-VCH, Weinheim, 1997, pp. 1879–1882.

8 R. A. Sheldon and H. van Bekkum, in *Fine Chemicals through Heterogeneous Catalysis*, WILEY-VCH, Weinheim, 2007, pp. 553–587.

9 D. C. Caskey and D. W. Chapman, 1986.

10 M. M. Gagliardi, *BCC Res. Rep.*, 2015.

11 G. O. Schenck, *Angew. Chemie*, 1952, **64**, 12–23.

12 J. E. Pacheco, M. Prairie, L. Evans and L. Yellowhorse, 1990, pp. 141–145.

13 A. Mills and S.-K. Lee, *J. Photochem. Photobiol. A Chem.*, 2002, **152**, 233–

247.

14 I. Oller, W. Gernjak, M. I. Maldonado, L. A. Pérez-Estrada, J. A. Sánchez-Pérez and S. Malato, *J. Hazard. Mater.*, 2006, **138**, 507–517.

15 J. García-Montaño, L. Pérez-Estrada, I. Oller, M. I. Maldonado, F. Torrades and J. Peral, *J. Photochem. Photobiol. A Chem.*, 2008, **195**, 205–214.

16 K. P. de Jong, in *Synthesis of Solid Catalysts*, ed. K. P. de Jong, WILEY-VCH, Weinheim, 2009, pp. 3–11.

17 S. James, *Global catalyst market by product (heterogeneous, homogeneous), by material (zeolites, metals, chemical compounds), by application (refinery, chemical synthesis, polymer, environment) expected to reach USD 27.59 billion by year 2020.*, San Francisco, California, 2014.

18 *World Catalysts - Demand and Sales Forecasts, Market Share, Market Size, Market Leaders*, Cleveland, Ohio, 2014.

19 *Emission Control Catalyst Market by Type, Application, and Geography - Regional Trends & Forecast to 2019*, 2014.

20 *Refinery catalysts market worth over $6 billion*, 2014.

21 D. F. Shriver and P. W. Atkins, *Inorganic Chemistry*, Oxford University Press, Oxford, 3rd edn., 1999.

22 R. A. Sheldon, *Chem. Soc. Rev.*, 2012, **41**, 1437–1451.

23 R. A. Sheldon, *Green Chem.*, 2007, **9**, 1273–1283.

24 P. T. Anastas and J. C. Warner, *Green chemistry: theory and practice*, Oxford University Press, New York, 2000.

25 P. T. Anastas and J. B. Zimmerman, *Env. Sci. Tech.*, 2003, **37**, 94A–101A.

26 *Eco-Friendly Dyes for Biodegradable Plastic Developed*, 2007.

27 *Chempol MPS Wins the 2009 Presidential Green Chemistry Challenge Award*, 2009.

28 C. Schiel, M. Oelgemoller, J. Ortner and J. Mattay, *Green Chem.*, 2001, **3**, 224–228.

29 M. Formenti, F. Juillet and S. J. Teichner, *Comptes Rendus l' Académie des*

Sci. Paris, 1970, **270**, 138–141.

30 T. L. Thompson and J. T. Yates, *Chem. Rev.*, 2006, **106**, 4428–4453.

31 A. Mills and S. Le Hunte, *J. Photochem. Photobiol. A Chem.*, 1997, **108**, 1–35.

32 W. Wu, C. Jiang and V. A. L. Roy, *Nanoscale*, 2015, **7**, 38–58.

33 A. O. Ibhadon and P. Fitzpatrick, *Catalysts*, 2013, **3**, 189–218.

34 S. T. Wilson, B. M. Lok, C. A. Messina, T. R. Cannan and E. M. Flanigen, *J. Am. Chem. Soc.*, 1982, **104**, 1146–1147.

35 H. O. Pastore, S. Coluccia and L. Marchese, *Annu. Rev. Mater. Res.*, 2005, **35**, 351–395.

36 N. Rajic, *J. Serb. Chem. Soc.*, 2005, **70**, 371–391.

37 J. Chen, P. A. Wright, S. Natarajan and J. M. Thomas, in *Zeolites and Related Microporous Materials: State of the Art 1994 - Proceedings of the 10th International Zeolite Conference, Garmisch-Partenkirchen, Germany, 17-22 July 1994*, eds. J. Weitkamp, H. G. Karge, H. Pfeifer and W. Hölderich, Elsevier, 1994, vol. 84, pp. 1731–1738.

38 F. Corà, I. Saadoune and C. R. A. Catlow, *Angew. Chem. Int. Ed.*, 2002, **41**, 4677–4680.

39 A. Corma, *J. Catal.*, 2003, **216**, 298–312.

40 Y. Jeanvoine, J. G. Ángyán, G. Kresse and J. Hafner, *J. Phys. Chem. B*, 1998, **102**, 5573–5580.

41 R. A. van Santen, in *Advanced Zeolite Science and Applications*, eds. J. C. Jansen, M. Stöcker, H. G. Karge and J. Weitkamp, Elsevier, 1994, vol. 85, pp. 273–294.

42 B. V. Kumar, C. P. Cajan, K. M. L. Rai and K. Byrappa, *Indian J. Chem. Technol.*, 2010, **17**, 191–197.

43 A. K. Paul, M. Prabu, G. Madras and S. Natarajan, *J. Chem. Sci.*, 2010, **122**, 771–785.

44 V. D. Santo, M. Guidotti, R. Psaro, L. Marchese, F. Carniato and C. Bisio, *Proc. R. Soc. A*, 2012, **468**, 1904–1926.

45 C. Janiak and J. K. Vieth, *New J. Chem.*, 2010, **34**, 2366–2388.

46 D. J. Tranchemontagne, J. L. Mendoza-Cortes, M. O'Keeffe and O. M. Yaghi, *Chem. Soc. Rev.*, 2009, **38**, 1257–1283.

47 N. Ahmad, H. A. Younus, A. H. Chughtai, K. Van Hecke, M. Danish, Z. Gaoke and F. Verpoort, *Sci. Rep.*, 2017, **7**, 832.

48 M. Eddaoudi, J. Kim, N. Rosi, D. Vodak, J. Wachter, M. O'Keeffe and O. M. Yaghi, *Science (80-.).*, 2002, **295**, 469–472.

49 I. Luz, F. X. L. i Xamena and A. Corma, *J. Catal.*, 2010, **276**, 134–140.

50 Z. Wang and S. M. Cohen, *Chem. Soc. Rev.*, 2009, **38**, 1315–1329.

51 S. K. Park, Z. Ni, C. P. Adrien, Y. J. Choi, R. Huang, F. J. Uribe-Romo, H. K. Chae, M. O'Keeffe and O. M. Yaghi, *Proc. Natl. Acad. Sci.*, 2006, **103**, 10186–10191.

52 B. Smit and T. L. M. Maesen, *Nature*, 2008, **451**, 671–678.

53 A. Corma and A. Martinez, *Adv. Mater.*, 1995, **7**, 137–144.

54 M. Stöcker, *Microporous Mesoporous Mater.*, 1999, **29**, 3–48.

55 L. Travalloni, A. C. L. Gomes, A. B. Gaspar and M. A. P. da Silva, *Catal. Today*, 2008, **133**, 406–412.

56 G. Bellussi and C. Perego, *CATTECH*, 2000, **4**, 4–16.

57 M. Piumetti, S. Bensaid, D. Fino and N. Russo, *Catal. Struct. React.*, 2015, **1**, 155–173.

58 T. Nanba, A. Sultana, S. Masukawa, M. Haneda, J. Uchisawa, A. Obuchi and H. Hamada, *Top. Catal.*, 2009, **52**, 1766.

59 T. Jiang, W. Wang and B. Han, *New J. Chem.*, 2013, **37**, 1654–1664.

60 A. U. Czaja, N. Trukhan and U. Muller, *Chem. Soc. Rev.*, 2009, **38**, 1284–1293.

61 C. M. Simon, E. Braun, C. Carraro and B. Smit, *PNAS*, 2017, **114**, E287–E296.

62 N. L. Rosi, J. Eckert, M. Eddaoudi, D. T. Vodak, J. Kim, M. O'Keeffe and O. M. Yaghi, *Science (80-.).*, 2003, **300**, 1127–1129.

63 G. Ferey, *Chem. Soc. Rev.*, 2008, **37**, 191–214.

64 J. Liu, L. Chen, H. Cui, J. Zhang, L. Zhang and C.-Y. Su, *Chem. Soc. Rev.*, 2014, **43**, 6011–6061.

65 M. Ranocchiari and J. A. van Bokhoven, *Phys. Chem. Chem. Phys.*, 2011, **13**, 6388–6396.

66 D. Farrusseng, S. Aguado and C. Pinel, *Angew. Chem. Int. Ed.*, 2009, **48**, 7502–7513.

67 A. Kuc, A. Enyashin and G. Seifert, *J. Phys. Chem. B*, 2007, **111**, 8179–8186.

68 M. Fuentes-Cabrera, *J. Chem. Phys.*, 2005, **123**, 124713.

69 Z.-M. Zhang, T. Zhang, C. Wang, Z. Lin, L.-S. Long and W. Lin, *J. Am. Chem. Soc.*, 2015, **137**, 3197–3200.

70 L. Zhang, P. Cui, H. Yang, J. Chen, F. Xiao, Y. Guo, Y. Liu, W. Zhang, F. Huo and B. Liu, *Adv. Sci.*, 2016, **3**, 1500243–n/a.

71 S. Pullen and S. Ott, *Top. Catal.*, 2016, **59**, 1712–1721.

72 J. Urquhart, *World's first commercial MOF keeps fruit fresh*, 2016.

73 J. A. Mason, J. Oktawiec, M. K. Taylor, M. R. Hudson, J. Rodriguez, J. E. Bachman, M. I. Gonzalez, A. Cervellino, A. Guagliardi, C. M. Brown, P. L. Llewellyn, N. Masciocchi and J. R. Long, *Nature*, 2015, **527**, 357–361.

74 A. Scott, *Chem. Eng. News*, 2017, 95, 10.

75 M. Anpo, Y. Shioya, H. Yamashita, E. Giamello, C. Morterra, M. Che, H. H. Patterson, S. Webber and S. Ouellette, *J. Phys. Chem.*, 1994, **98**, 5744–5750.

76 M. Anpo, T. Nomura, Y. Shioya, M. Che, D. Murphy and E. Giamello, in *New Frontiers in Catalysis - Proceedings of the 10th International Congress on Catalysis, Budapest, 19-24 July 1992*, eds. F. S. L. GUCZI and P. TÉTÉNYI, Elsevier, 1993, vol. 75, pp. 2155–2158.

77 K. Ebitani, Y. Hirano and A. Morikawa, *J. Catal.*, 1995, **157**, 262–265.

78 S. M. Kanan, M. A. Omary, H. H. Patterson, M. Matsuoka and M. Anpo, *J. Phys. Chem. B*, 2000, **104**, 3507–3517.

79 M. Anpo, S. G. Zhang, H. Mishima, M. Matsuoka and H. Yamashita, *Catal. Today*, 1997, **39**, 159–168.

80 G. D. Lee, S. K. Jung, Y. J. Jeong, J. H. Park, K. T. Lim, B. H. Ahn and S. S. Hong, *Appl. Catal. A Gen.*, 2003, **239**, 197–208.

81 T. Ban, S. Kondoh, Y. Ohya and Y. Takahashi, *Phys. Chem. Chem. Phys.*, 1999, **1**, 5745–5752.

82 P. Calza, C. Paze, E. Pelizzetti and A. Zecchina, *Chem. Commun.*, 2001, 2130–2131.

83 D. Ghanbari, S. Sharifi, A. Naraghi and G. Nabiyouni, *J. Mater. Sci. Mater. Electron.*, 2016, **27**, 5315–5323.

84 L. Lu, J. Wang, S.-L. Cai, B. Xie, B.-H. Li, J.-H. Man, Y.-X. He, A. Singh and A. Kumar, *J. Coord. Chem.*, 2017, **70**, 3409–3421.

85 L. Qin, H.-Z. Chen, J. Lei, Y.-Q. Wang, T.-Q. Ye and H.-G. Zheng, *Cryst. Growth Des.*, 2017, **17**, 1293–1298.

86 A.-N. Meng, L.-X. Chaihu, H.-H. Chen and Z.-Y. Gu, *Sci. Rep.*, 2017, **7**, 6297.

87 R. A. Sheldon and H. van Bekkum, in *Fine Chemicals through Heterogeneous Catalysis*, WILEY-VCH, Weinheim, 2007, pp. 1–11.

88 B. Cornils and W. A. Herrmann, Eds., *Applied Homogeneous Catalysis with Organometallic Compounds*, Weinheim, Wiley-VCH., 2002.

89 A. Suzuki, *Angew. Chem. Int. Ed.*, 2011, **50**, 6722–6737.

90 E. Negishi, *Angew. Chem. Int. Ed.*, 2011, **50**, 6738–6764.

91 C. C. Leznoff, *Chem. Soc. Rev.*, 1974, **3**, 65–85.

92 M. Rueping, J. Zoller, D. C. Fabry, K. Poscharny, R. M. Koenigs, T. E. Weirich and J. Mayer, *Chem. – A Eur. J.*, 2012, **18**, 3478–3481.

93 Yin and J. Liebscher, *Chem. Rev.*, 2007, **107**, 133–173.

94 J. Sołoducho, K. Olech, A. Świst, D. Zając and J. Cabaj, *Adv. Chem. Eng. Sci.*, 2013, **3**, 19–32.

95 V. M. Marx, M. B. Herbert, B. K. Keitz and R. H. Grubbs, *J. Am. Chem. Soc.*, 2013, **135**, 94–97.

96 F. Shibahara, J. F. Bower and M. J. Krische, *J. Am. Chem. Soc.*, 2008, **130**, 6338–6339.

97 J. R. Zbieg, J. Moran and M. J. Krische, *J. Am. Chem. Soc.*, 2011, **133**, 10582–10586.

98 H. Li, Y. Li, X.-S. Zhang, K. Chen, X. Wang and Z.-J. Shi, *J. Am. Chem. Soc.*, 2011, **133**, 15244–15247.

99 T. Seiser, O. A. Roth and N. Cramer, *Angew. Chem. Int. Ed.*, 2009, **48**, 6320–6323.

100 J. H. Montoya, A. A. Peterson and J. K. Nørskov, *ChemCatChem*, 2013, **5**, 737–742.

101 L.-M. Tan, Z.-Y. Sem, W.-Y. Chong, X. Liu, Hendra, W. L. Kwan and C.-L. K. Lee, *Org. Lett.*, 2013, **15**, 65–67.

102 H. Cao, H. Jiang, G. Yuan, Z. Chen, C. Qi and H. Huang, *Chem. – A Eur. J.*, 2010, **16**, 10553–10559.

103 P. Drabina, J. Svoboda and M. Sedlák, *Molecules*, 2017, **22**.

104 B. Karimi, F. Mansouri and H. M. Mirzaei, *ChemCatChem*, 2015, **7**, 1736–1789.

105 J. T. Kozlowski and R. J. Davis, *ACS Catal.*, 2013, **3**, 1588–1600.

106 G. Cahiez and A. Moyeux, *Chem. Rev.*, 2010, **110**, 1435–1462.

107 J. Qiu and R. Zhang, *Org. Biomol. Chem.*, 2014, **12**, 4329–4334.

108 S. Roscales and A. G. Csaky, *Chem. Soc. Rev.*, 2014, **43**, 8215–8225.

109 D. Palagin, V. L. Sushkevich and I. I. Ivanova, *J. Phys. Chem. C*, 2016, **120**, 23566–23575.

110 K. Okumura, T. Mushiake, Y. Matsui and A. Ishii, *Chemphyschem*, 2015, **16**, 1719–1726.

111 F. X. L. i Xamena, A. Abad, A. Corma and H. Garcia, *J. Catal.*, 2007, **250**, 294–298.

112 Y. K. Hwang, D.-Y. Hong, J.-S. Chang, S. H. Jhung, Y.-K. Seo, J. Kim, A. Vimont, M. Daturi, C. Serre and G. Férey, *Angew. Chem. Int. Ed.*, 2008, **47**,

4144–4148.

113 J. Huang, W. Wang and H. Li, *ACS Catal.*, 2013, **3**, 1526–1536.

114 P. Kovacic and R. Somanathan, *J. Appl. Toxicol.*, 2014, **34**, 810–824.

115 S. S. Talmage, D. M. Opresko, C. J. Maxwell, C. J. E. Welsh, F. M. Cretella, P. H. Reno and F. B. Daniel, in *Reviews of Environmental Contamination and Toxicology: Continuation of Residue Reviews*, ed. G. W. Ware, Springer New York, New York, NY, 1999, pp. 1–156.

116 K.-S. Ju and R. E. Parales, *Microbiol. Mol. Biol. Rev.*, 2010, **74**, 250–272.

117 V. Glezer, *Patai's Chem. Funct. Groups*, 2009, **1861**.

118 Farah Maria Drumond Chequer, G. A. R. de Oliveira, E. R. A. Ferraz, J. C. Cardoso, M. V. B. Zanoni and D. P. de Oliveira, ed. M. Günay, 2013.

119 H. R. Monsef, D. A. Michels, J. K. Bewtra, N. Biswas and K. E. Taylor, in *Emerging Technologies in Hazardous Waste Management 8*, eds. D. W. Tedder and F. G. Pohland, Springer Science & Business Media, 2007, pp. 141–152.

120 L. D. McMullen, in *Nitrogen in the Environment: Sources, Problems and Management*, eds. R. F. Follett and J. L. Hatfield, Elsevier Science, Amsterdam, 2001, pp. 455–460.

121 A. Hatamifard, M. Nasrollahzadeh and J. Lipkowski, *RSC Adv.*, 2015, **5**, 91372–91381.

122 P. Zhao, X. Feng, D. Huang, G. Yang and D. Astruc, *Coord. Chem. Rev.*, 2015, **287**, 114–136.

123 C. Wang, H. Zhang, C. Feng, S. Gao, N. Shang and Z. Wang, *Catal. Commun.*, 2015, **72**, 29–32.

124 J. Shu, Z. Wang, G. Xia, Y. Zheng, L. Yang and W. Zhang, *Chem. Eng. J.*, 2014, **252**, 374–381.

125 T. Bhowmik, M. K. Kundu and S. Barman, *RSC Adv.*, 2015, **5**, 38760–38773.

Chapter 2: Experimental Part

2.1 Synthesis of materials

2.1.1 Hydrothermal synthesis

The hydrothermal preparation of porous materials usually refers to zeolites and zeolite-like materials and is widely reported and acknowledged.[1] During the hydrothermal synthesis, a typical array of processes take place, which is kinetically and thermodynamically favoured and principled by high temperatures and pressures. In fact, the naturally occurring zeolites respond as geological reserves all over the world, frequently present in geographical areas with volcanic activity. They are found especially in rocks, that part of them have volcanic origin, where the hydrothermal alteration of various aluminosilicate minerals, such as asterios, has taken place.[2]

The lab-based synthesis of zeolites and zeotypes requires the use of raw materials which typically would be sources of Al, P and Si, in solid or liquid form, such as alumina, phosphoric acid and silica. Initially, these materials would be dissolved in water to form a random hydrogel, which can accommodate the nucleation stage occurring after. The nucleation is possible as soon as an organic compound is added, which is able to release organic cations for the ingredients to arrange themselves around. These organic molecules play the role of the template.

In rare occasions, the template can be true, which means that the voids of the molecular sieves are constructed exactly according to the shape of the organic molecule and this shape is kept after the removal of the template. A good example is methyldicyclohexylamine which can specifically produce AFI frameworks. More frequently, the templates work as structure directing agents and, as their name reveals, they offer the cations for an electronic direction of the atoms. They also facilitate crystal form, preventing them from interacting with water, by filling their empty spaces. Typically, the pH is kept around 7 or a little basic, to ensure that these organic (usually amine based) molecules are stable.

The following stage of the crystallization requires high pressures and temperatures. This usually happens with autogenous pressure being built up within the vessel of synthesis and at temperatures higher than the boiling point

of water, typically ranging from 150-250 °C. These conditions help the formation of the first crystals and create an environment where they can grow mimicking the order of the first ones. The period of time that these gels need to stay under autogenous pressure and high temperatures obey the law of Ostwald of successive transformations of one phase to another. The longer the gels are kept in these conditions, the more thermodynamically favoured phases are shaped. Thus, by withdrawing a gel from the synthesis environment at different timings, earlier metastable phases can be isolated.

The isomorphous metal substitution usually requires a metal precursor, such as a metal salt, to be added in the prenucleation stage. This technique is particularly advantageous and known as "one-pot" synthesis. However, other techniques also allow the introduction of metals, such as impregnation and ion-exchange, but in these cases, the metal is not part of the framework substituting for a site but stays as an extra-framework ion. While there are advantages and disadvantages which govern the applications in which the materials prepared by these methods can be used, ion-exchange is possible when the framework is strongly ionic, like in zeolites. AlPOs and SAPOs are not frequently reported to be modulated in this way.

The usual vessel which hosts the crystallization is a PTFE-lined stainless steel autoclave. Obviously, steel autoclaves are able to withhold the high pressures that are present during the crystallization at high temperatures. The PTFE liners are used because they are hydrophobic and, unlike glass, they cannot be etched or broken at the extreme conditions, while they serve as good hosts of crystal seeds, which can help with the formation of the initial crystals. After a specific amount of time, the autoclaves are allowed to cool down to ambient temperatures and the crystals are collected with the help of filtration or centrifugation and multiple washings with water to remove unreacted reagents or impurities.

As mentioned in the beginning, zeolites and zeotypes are hydrothermally synthesised, almost exclusively following a generic mechanism. It begins with the dilution of the precursors in water to form an initial gel of complexes. The rise of temperature and pressure starts the nucleation stage, permitting the clusters to be arranged in an ordered manner. Out of crystal habit and imitation, the layers of atoms, molecules and complexes add up on the formed surfaces and macroscopically grow into three-dimensional structures. Figure 2.1 illustrates a simplified scheme of the crystallization procedure of zeolitic materials.

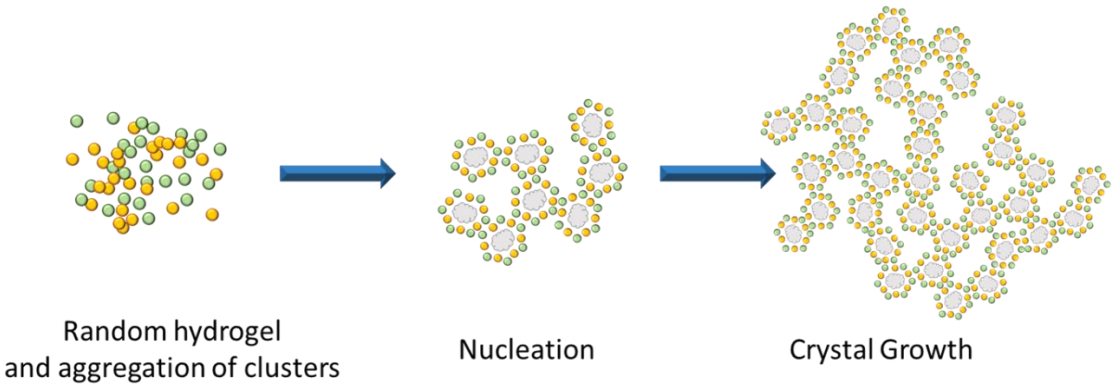

Figure 2.1 Schematic illustration of the phases through which the synthesis of zeolitic materials consists of. Green and yellow stand for the ingredients of raw materials and grey stands for the template molecules.

2.1.2 Solvothermal synthesis and activation of metal-organic frameworks

Solvothermal synthesis is a wider term that encompasses hydrothermal synthesis, where the solvent used is specifically water. When a solvent other than water is used, then organic and organometallic molecules can be easier dissolved, which is why solvothermal synthesis is linked with MOF preparation. Experienced by the know-how of zeolitic preparation, the usual process requires autogenous pressures and responds often with “one-pot” methodology. With solvothermal synthesis being the most conventional process, it takes place in closed vessels for time periods from 48 to 96 hours. The use of solvents may not allow the rise of the temperature above 150 °C, while the MOF preparation generally can happen also at lower or even ambient temperatures. This makes the use of glass bottles also possible.

Except for a possible medium for the precursors to dissolve, another role of the solvents is that of the “filler” or “spacer”. In detail, the solvent molecules uptake the space of the cavities of the MOFs, while they, rarely, have a directing role.[3] The preferred solvents are usually aprotic molecules, which provide a relatively inert electronic environment to avoid strong bonds with the organic ligands, and small and flexible molecules, to aid their successive removal from the pores of MOFs. On these grounds, dimethyl formamide (DMF) and diethyl formamide are frequently reported. However, polar molecules such as water and ethanol are also common solvents and they can be used individually or in combination, depending on the precursors' solubility and their molecular size.

The formation of MOF crystals is affected by the temperature conditions. Hence, the control of the temperature is very important during their synthesis. The microwave-assisted synthesis is gaining ground as it can accelerate the procedure, when the temperatures do not exceed 130 °C. The microwave irradiation usually decreases the crystallization time in the order of minutes or a few hours.[4] Seemingly, the microwaves provide a better local heating in the mixture, which helps the crystal growth, with the distribution of particle size being smaller and the phase more consistent.[5] There are also other processes, such as the sonochemical technique and the electrochemical techniques, which offer different advantages, such as phase homogeneity, production yield, lower temperatures etc.[4,5]

Regardless how MOFs are synthesized, filtration or centrifugation takes place, essentially to remove unreacted substrates and excessive solvent to be washed out. The procedure that follows is considered one the most important, which is recognized as activation of MOFs. During the activation phase, MOFs reveal their porosity and expose their active sites. Usually, this would entail heating of the solids under vacuuming conditions, to help the solvent leave the inside of the scaffold and from the sides of the metals, generating uncoordinated sites. On a few occasions and prior to vacuum heating, ageing the material in a new solvent (like methanol and chloroform) makes the exchange between them possible facilitating overall solvents' removal.

Nevertheless, the crystallisation procedure of MOFs may again be schematised (Figure 2.2) and described generically. Although it does not diverge significantly from this of zeolitic materials, there are some specific differences. Unlike zeolites, the dissolution of the precursors occurring in a solvent does not form a gel, although it provides a suitable environment for a preliminary arrangement of the clusters into small organised arrays. Depending on the thermodynamic conditions, these arrays increase in size slower or faster, as they attract more groups that imitate the former organised compositions. Time allowed, the previously random solution is being transformed into a crystalline framework.

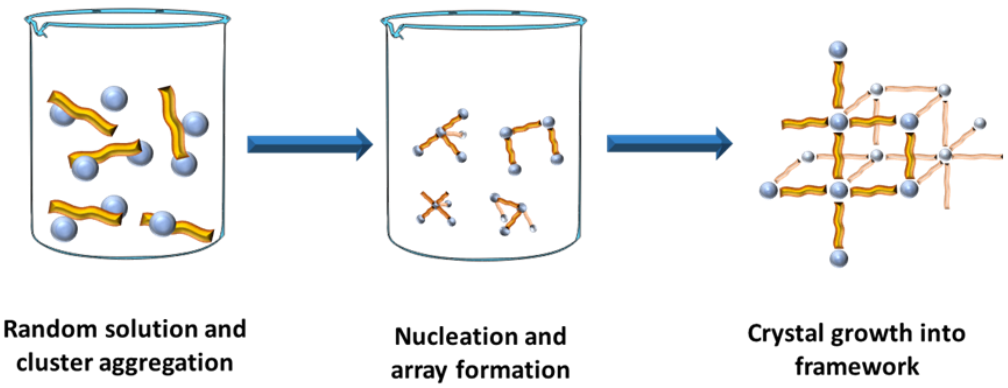

Figure 2.2 Schematic illustration of the phases through which the synthesis of MOFs consists of. Blue spheres stand for the metal clusters and yellow rods stand for the organic molecules of the framework.

2.2 Techniques for characterization and analysis

There is a wide range of instrumental analysis methods that can be applied for characterizing the materials and understanding in depth their physical and chemical properties. At the same time, some of these instrumental techniques can be also used for the purpose of quantitative analysis in order to monitor the progress of a catalytic reaction. Generally, the techniques are categorized into optical (spectroscopic or non-spectroscopic), electric, chromatographic, thermoanalytical and combinatory, according to the measured magnitude.

A number of these techniques were applied to this project and are described synoptically hereinafter, in terms of importance and information bestowed by each experimental method. Table 2.1 summarises all the techniques applied and the intention they were used for in the projects of this thesis. A briefing of the information that each technique is likely to infer is also available.

Table 2.1 Summary of the applied instrumental techniques applied in this thesis, along with each one's aim of use and sort of information.

Instrumental Technique	Aim of use	Information
PXRD	Solid characterisation	Phase purity and crystallinity
SEM	Solid characterisation	Surface morphology and particles size and shape
BET	Solid characterisation	Porosity and surface area
EDX	Solid characterisation	Metal incorporation and elemental stoichiometry
ICP-OES	Solid characterisation	Elemental content ratio
	Liquid characterisation	Metal content in solution (potential of catalyst to leach)
UV-VIS	Liquid characterisation	Monitoring of catalytic reactions sensitive in the visible light
DR UV-VIS	Solid characterisation	Photoresponse in the visible spectrum, d-d transitions as an indication of oxidation state and coordination geometry
H^1 NMR	Liquid characterisation	Monitoring of catalytic products of reaction

Instrumental Technique	Aim of use	Information
FTIR	Solid characterisation	Detection of removal or formation of functional groups and bonds
Cyclic Voltammetry	Solid characterisation	Registration of electrochemical behaviour
XPS	Solid Characterisation	Analysis of oxidation state of metals
EPR	Solid Characterisation	Analysis of coordination geometry

2.2.1 Powder X-Ray Diffraction (PXRD) and Rietveld Refinement

The PXRD technique is based on the interaction of the X-rays with matter, as a phenomenon of emission absorbance and diffraction of the rays. The X-Ray pattern of a crystal is constituted by the reflections of the X-rays, which are analysed in terms of relative intensity and position. The incident X-rays on an inner shell electron excites it to higher energy levels, leaving a vacancy, which is quickly filled by another electron of a higher shell. While the most intense (and possible) electron transitions regard the K and L shells, the energy differences when the atom is reset to its ground state are identical for each atom.

The wavelength range of X-rays starts from 0.1 Å and can reach up to 100 Å. In diffraction, the range 0.1-10 Å is sufficient, because these lengths are comparable to the crystallographic distances and the radii of atoms, which is why it is useful for zeolites and analogues or metal-organic frameworks. The XRD analysis is principled by Bragg's Law, according to which the angle ϑ of incidence of the known wavelength irradiation λ determines the spacing d between the planes of the crystals, revealing the crystalline structure.

Figure 2.3 explains schematically the principle of measurement. If the diffracted waves are in phase, they will give amplified signals. This is possible only for certain wavelengths which are integer divisors of the green and orange lengths on the scheme. Also, since the matter is crystalline, these distances ought to be equal and the distance d can then be measured using simple trigonometry (Bragg's Law).

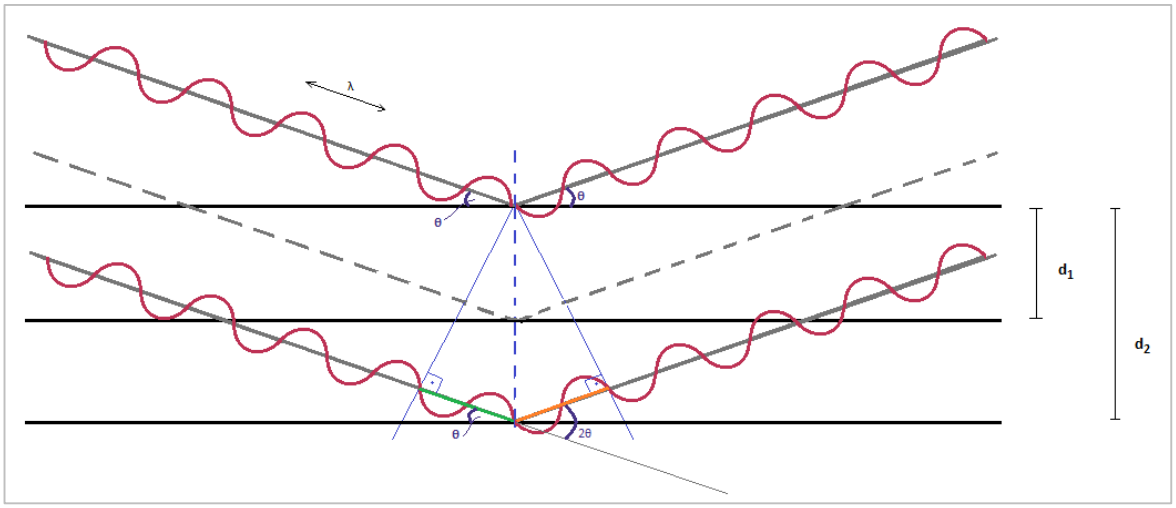

Figure 2.3 Illustrating the diffraction of X-Rays on a crystalline material. The red waveform lines stand for the X-Rays and the d1 and d2 distances depict the spacing between the layers of the atoms. The distance λ stands for wavelength and the ϑ value is the angle of incidence of the ray.

The formula for Bragg's law (Equation 2.1) involves the coefficients as follow: n is the order of the radiation, d is the space between the planes of the crystal, ϑ is the angle of incidence of the rays on the plane of the crystal and λ is the wavelength of the irradiation.

Bragg's law: $n\lambda = 2 \cdot d \cdot sin\theta$ Equation 2.1

The raw data spectrum from a set of 2ϑ values has a form of concentric circles of spots of different size. Transformation of polar to x-y coordinates (2ϑ, Intensity) is important, for a set of qualitative and quantitative information can be withdrawn. The XRD patterns reveal the identity of the phase of the solid sample because the peak positions are determined only by the geometry of the planes and the lattice parameters, with each peak representing reflections with high symmetry degrees or crystallographic resemblance. As it is obvious from the

picture, the 2ϑ values are related to the spacing between the planes, which in turn define the size and the shape of the unit cell, characterized by "indexing reflections" or "Miller indices" (hkl values). Deviation of the expected 2ϑ values can indicate a distortion of the unit cell. The relative intensities are related to the atoms that make up the unit cells, as their size and type affects the direction and the degree of the reflection and thus, they can present any structural modifications.[6]

The crystalline quality is another information which can be disclosed by the XRD patterns, taking into consideration the widths of the peaks. Broad peaks are usually indications of poorer crystallinity, due to high scattering degree. Except for the quality of the crystal, the ratio of the width between peaks of a specific orientation may also be used to visualize the direction of formed channels within the crystal in respect to the unit cell directions. Additional information regarding the crystallinity is also found in the background, with high levels being associated with the presence of amorphous phases. More specific information is associated with the effects observed in the low-angle regions, which can show hierarchical order or extra-framework species, which are mainly due to profound changes of the electron density inside the voids.[7]

The Rietveld Refinement[8,9] process is a widely used numerical model applied between the experimental and the simulated XRD data. It is used for confirmation of the phase and extraction of the parameters to describe accurately the crystalline structure. The mathematical process followed is based on the least-squares method for non-linear regression and its result is a set of coefficients of statistical value for the evaluation of the refinement. The most important ones are the R values (residuals), the x^2 and the ratio of shift of the peaks over the estimated standard deviation (e.s.d.).[9,10]

Between the R values, the R_{wp} (weighted profile R value) is minimized during the fitting to express the precision of the fitting of the experimental data on the simulated, with emphasis on the intense peaks (Equation 2.2). For a complex phase (monoclinic to triclinic) a maximum accepted value would be around 15%, whereas for a simple phase (cubic) a value of 8% would be more appropriate.

$$R_{wp} = \left[\frac{\sum_i \left(\left(y_i^{exper} - y_i^{simul}\right)^2 \cdot w_i\right)}{\sum_i \left(\left(y_i^{exper}\right)^2 \cdot w_i\right)}\right]^{1/2} \qquad \text{Equation 2.2}$$

$$\text{where } w_i = \left(y_i^{exper}\right)^{-1/2}$$

Other R values or interest, the Rp is an unweighted metric of the quality of the fitness of the experimental curve on the computed and the R_{exp} is the statistically expected R value (Equation 2.3). The latter is used as an evaluation of the quality of the experimental data and should be smaller than the R_{wp} value to consider the experimental XRD pattern able to provide good refining data.

$$R_{wp} = \left[\frac{N-P}{\sum_i \left(\left(y_i^{exper}\right)^2 \cdot w_i\right)}\right]^{1/2}$$

Equation 2.3

where $N = number\ of\ points$ and

$P = number\ of\ parameters$

The ratio $\frac{R_{wp}}{R_{exp}}$ is called x^2 and is known as goodness-of-fit (GoF); the closer to 1, the better the fitting between the data is. The ratio of the shifts over the e.s.d. is a metric of oscillation among the peaks and can be used to extract information for the presence of impurity phases.[11] If there is a convergence, the maximum accepted value is about the value of 0.10. Generally, one should keep in mind that the Rietveld Refinement and the coefficients mentioned depend on how well-fitted the background is, how poorly or adequately the shapes are described and how significant the disagreement between the calculated and the experimental patterns is. Finally, the convergence of the method is prerequired in order for the results to be considered useful indicators.

2.2.2 Scanning Electron Microscope (SEM) and Energy Dispersive X-Ray Spectroscopy (EDX)

When the dimensions of materials become much smaller than the light wavelengths, the most advanced technology of lenses is not enough to reveal detailed information. In this case, the interaction of electrons with the surface of such materials can produce a number of signals, due to their much shorter wavelengths, and collected by appropriate detectors, they can be combined for comprehensive and thorough analysis. As a beam of primary electrons is directed with high energy on the surface of a sample, it induces scattering of the sample electrons from different depths, ranging from the surface (Auger electrons), through the small depth of around 20 nanometers (secondary electrons) and medium depth (backscattered electrons), to depths much higher than 1 μm

(diffracted photons and characteristic X-Rays, visible light photons and cathodoluminescence, heat). The energy of the primary electrons dominates the scattering and the type of the electrons.

In SEM, the electroconductivity of the samples is of high importance and for this reason, non-conductive samples are thinly sputtered with gold and stabilized on a carbon tape and the chamber is controlled to develop high vacuum. In another case, the chamber may be of low vacuum, samples may not be coated and electroconductivity would result from the controlled presence of moisture in the chamber. Then, the beam can effectively interact with the material samples and detectors can efficiently collect the signals.

The secondary electrons are caused by inelastic scattering of the beam at high angle degrees and excitation of the inner shells. The detection of secondary electrons is mostly responsible for creating the three-dimensional images of the surfaces, because their morphology, such as valleys, edges and anomalies, impacts on the angles of the scattering. The detection of backscattered electrons, which are of higher energy and lower angle scattering, is mostly responsible for the brightness and contrast effects on the image, due to the fact that backscattering is pronounced for higher atomic numbers and generates brighter images. The emission of X-rays is characteristic for each element, as a result of the well-defined energy difference between the shells of each element. The detection of X-rays governs the technique of EDX.[12] Figure 2.4 illustrates the relative depth from which the electrons are emitted.

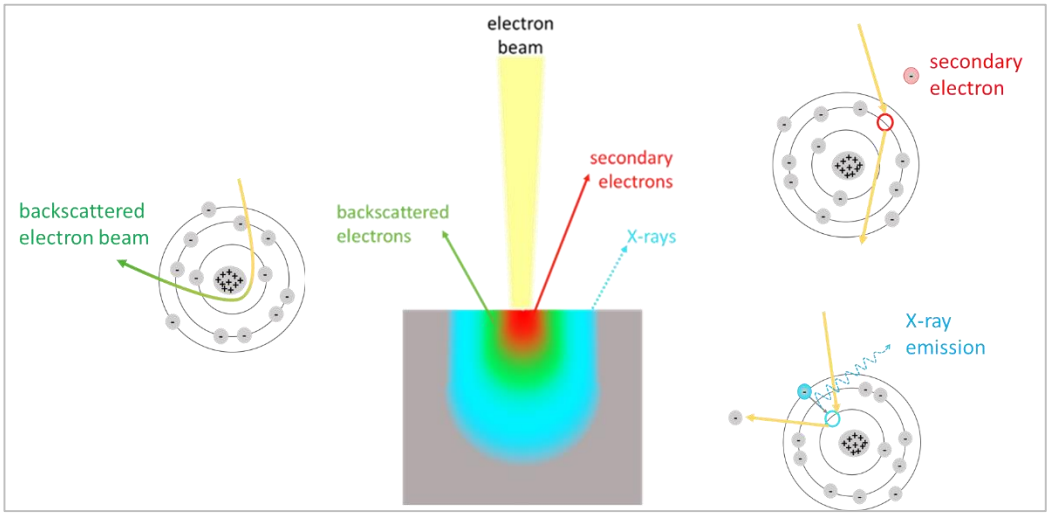

Figure 2.4 Illustration of the depth of the ejected electrons.

It is apparent that SEM is a very strong technique which provides purely morphological information and when coupled with EDX, it can provide

information relative to elemental composition. For porous materials, the image data of SEM can be used to depict the size and shape of particles and the type of the surface.[12,13] The open framework topologies usually fold particles to specific shapes and, in older times, the shape of the particle was an indication of the phase, while the uniformity of the size was indication of successful synthesis. In catalysis and photocatalysis, the size and the shape of the particles along with the smoothness or roughness of a surface can be connected to the reactivity of the materials.

2.2.3 Ultraviolet-visible spectroscopy (UV-VIS) and Diffuse Reflectance Ultraviolet-visible spectroscopy (DR UV-VIS)

In UV-VIS spectrophotometry, the samples absorb the electromagnetic irradiation of wavelengths from 200 to 800 nm, while there are instruments which can go deeper to the IR spectrum. If in this range of wavelengths the samples respond, they contain groups of atoms sensitive to electron transitions from the visible and the near ultraviolet light. These atoms have usually electrons, which transit from low energy orbitals to higher energy orbitals. The orbital energy increases in the order: σ (bonding orbital) > π (bonding orbital) > n (non-bonding orbital, valence electrons) > π^* (antibonding orbital) > σ^* (antibonding orbital) and the biggest the energy difference between the orbitals, the closer to the near UV area the atoms absorb light.

The main types of interaction between light and a material in solid or liquid phase are the transmission, the absorbance and the reflection of light (Figure 2.5). Usually, the absorbance occurs when electrons are found in the non-bonding and bonding orbitals, which absorb the light and transit to the antibonding orbitals of higher energy levels. Molecules of high conjugation absorb light of relatively high energy, which involves short wavelengths, closer to the UV region. In the case of transition metals, the d (unpaired) electrons are usually the candidate electrons, requiring lower energy, giving characteristic peaks in the visible region.

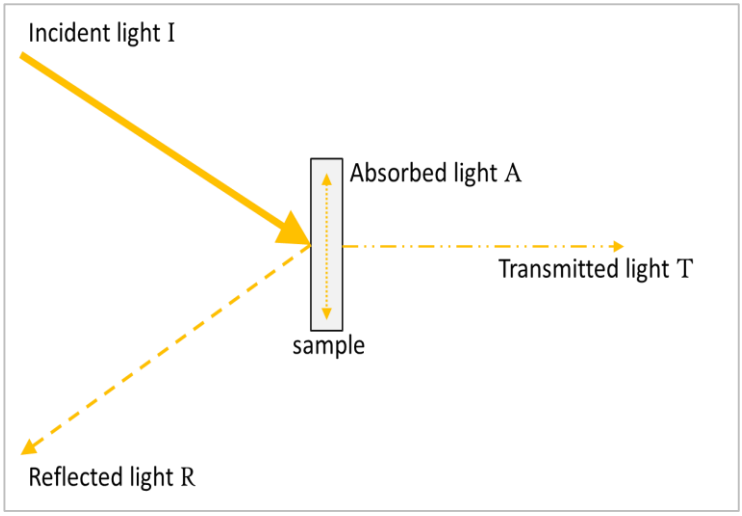

Figure 2.5 Possible paths of incident light

The collected data is a simple spectrum on a plot with horizontal axis the wavelength range and vertical axis the absorbance (A) or irradiation intensity (I) or irradiation permeability (T). The best parameter to be measured depends on the physical form or colour or shininess of the sample. For liquid samples, the method can be quantitative, based on Beer-Lambert law (Equation 2.4), according to which the absorbance is dependent proportionally to the concentration (C) of the sensitive group and the length of the cell (b), while the molar absorptivity coefficient (ε) is wavelength-dependent. Solid samples in powder form, consist of small particles, which would cause multiple reflections in a random distribution. The solid UV-VIS instruments are equipped with mirrors and lenses that enable the collection and measurement of reflected scattered light, usually referred as Diffuse Reflectance UV-VIS (DR UV-VIS).

Beer-Lambert Law: $$A = log\frac{I_o}{I} = log\frac{1}{T} = \varepsilon \cdot C \cdot b$$ Equation 2.4

In DR UV-VIS, the Schuster-Kubelka-Munk theory is fundamental for the measurement of the optical absorbance of a sample by approximation of its reflectance, taking into consideration the main phenomena of absorption and scattering of light. The ratio $F(R_\infty)$ between the absorbance coefficient (k) and the scattering coefficient (s) depends on the quantity of the sensitive groups and the thickness of the layer. Given that the particles size is much smaller than the thickness of the sample, then that ratio is similar to the Beer-Lambert law. Given that the absolute reflectance R_∞ is not possible to be measured, the relative

reflectance R'_∞ of the sample against a standard (usually $BaSO_4$) is used as Equation 2.5 shows.[14]

Kubelka-Munk function: $$F(R'_\infty) = \frac{(1-R'_\infty)^2}{2R'_\infty} = \frac{k}{s}$$ Equation 2.5

The information that the UV-VIS technique reveals can be both qualitative and quantitative. The presence of metal ions or sensitive groups is often discerned with naked eye, since the samples are coloured (reflectance of the opposite colour that corresponds to the slot of spectrum they absorb). These ions or groups have characteristic maximum interaction wavelengths λ_{max}, but more than one of them may absorb at the same or similar wavelengths, thus it is not a method to identify the atoms but to confirm their presence. However, the above laws show that there is proportionality between the concentration of the sensitive groups and the intensity of the absorbance, hence a set of standards can be used to quantify the measurement of a sample.[15]

Except for the presence of a specific group, the wavelength can be linked in certain occasion to the coordination and then, UV-VIS can also be used supplementary as a characterization of geometry. Differences in coordination according to ligand theory are determined with different energy orbital splitting. Since each photon carries a quantum of energy corresponding to a wavelength, the electrons in high or low spin complexes will give characteristic peaks to shorter or longer wavelengths respectively.

2.2.4 Inductively Coupled Plasma – Optical Emission Spectroscopy (ICP-OES)

The method of emission spectroscopy is considered one of the most important methods of instrumentation analysis. It is principled by the registration of the emitted electromagnetic radiation from excited atoms and ions in a form of spectrum of variant intensity and wavelengths. The intensity is indicative of the concentration of the elements under examination in the samples, whereas the wavelengths are characteristic for each element. Typically, the optical emission spectroscopy techniques are applied for the determination of metals and semimetals, like Si and non-metals, like P and the range of wavelengths is usually limited up to near ultraviolet spectrum. Generally, the method is considered accurate and very sensitive, while it can give results for elements in traces.

The ICP-OES analysis requires liquid samples, which implies that solid samples need to be in solutions and the elements in complete dissociation. This is achieved through the digestion of the solids in acids, like HNO_3, H_2SO_4, HCl and HF, depending on the sort of the analysis conducted (organometallic, inorganic, trace etc.). The liquid sample is sprayed in the torch to interact with the plasma (up to 8000 °C), which has been inductively coupled as argon goes through strong magnetic field. These conditions force the sample to undergo vaporization and ionization, since the geometry of the torch usually allows long contact times, due to which the method is considered very effective.[16]

Both qualitative and quantitative information is obtained from the ICP-OES. Briefly, from a scanning of the spectrum (normally 170 nm – 800 nm) the principal spectral lines are picked and compared to reference tabulated spectral lines of elements and ions for ICP with argon as carrier gas. A certain width can then be decided for each spectral line in order to avoid spectral interferences. The intensity of the optimum spectral lines is then taken into account through the calibration curves prepared using a set of standard solutions of known concentrations and elements, in order to determine the unknown concentrations of the samples in weight %. This is particularly useful for a catalytic reaction, in order to trace leaching of the metal active sites in the reaction or for a catalytic material, in order to identify the actual incorporation of the metal active sites in the bulk in comparison to the theoretical calculations.

2.2.5 Nuclear Magnetic Resonance Spectroscopy (NMR)

NMR is a technique based on the specific orientation of the nuclear spins upon the appliance of an external magnetic field. The exposure of a sample to a strong magnetic field leads to the absorbance of radiation of radio frequency and the spins of the nuclei of the atoms tend to flip in the presence of the external magnetic field and from parallel it becomes antiparallel. The inversion of the spin is accompanying, therefore, the transition of the nuclei from the state of low energy to a state of high energy. This is observed when the number of the neutrons or/and the protons are not even, allowing for an integer spin or a half-integer spin.

The electronic environment of the protons is significant for the assignment of the peaks. The shielding of the nuclei from the electrons causes a shift in the signal (chemical shift). In simple words, the more electrons are removed from around the nucleus, the more the nucleus is exposed to the neighbouring groups and the

higher the shift is expected. At the same time, the multiplicity of a peak is of great importance. For example, in proton NMR (^{1}H against ^{2}D, with the former resonating at 400 MHz and the latter at 60 MHz) the splitting of a peak is often related to the number of protons attached to the neighbouring atom under examination (with oxygen and nitrogen being excluded). This is known as the "n+1" rule, where n is the number of the accounted neighbouring protons.[17]

Evidently, the presence or absence of certain peaks functions as adequate qualitative information. However, NMR can also provide quantitative information, given that the intensity of the signal is proportional to the number of species producing the signal. For proton NMR, the integration under the peaks corresponds to the ratio of hydrogens and not absolute number of hydrogens, since the equivalence of hydrogens may result to higher intensities instead of new peaks, as for instance in symmetrical molecules. Consequently, the quantitative data accruing from NMR have a relative rather than an absolute base.

2.2.6 Cyclic Voltammetry

The technique of cyclic voltammetry is based on the redox electrochemical activity that a material demonstrates, by measuring the current produced upon the change of the potential in an electrochemical cell. Typically, a waveform of potential against current is formed when a reaction on the surface of the electrodes occurs over a certain potential range. The plot of current (I) versus potential (V) regards two directions of scanning the potential (positive and negative) and its shape determines the stability of the products from the electron transfer and the formation of reversible and irreversible electroactive species.

The main instrumentation required for the performance of the method include a suitably designed electrochemical cell, a working, a counter and a reference electrode, an electrolytic solution and a potentiostat along with a data acquisition system. Obviously, the technique depends on a number of parameters which can influence the performance, such as potential limits, scan rate, electrodes and electrolyte. However, the method is reasonably accurate and reproducible, which makes the study of an electrochemical system feasible, the identification of the occurring reactions easy and the comparison between the responses of different electrochemical species simple.

In order to achieve the aforementioned objectives, one should observe the cyclic voltammograms for specific characteristics. Initially, it is the number and the

shape of the peaks that appear on every scan which are of great importance. This actually proves that an electrochemical reaction is taking place and one can judge whether it represents a reversible or an irreversible reaction. A general and qualitative rule requires that smaller and wider peaks correspond to irreversible processes, whereas steeper peaks observed over a shorter time correspond to reversible processes. Another set of information that one can draw out of a voltammogram is associated with the potential values of the peaks. This can be used for the elimination or determination of expected known redox couples present in the reaction or for simply probing the kinetics of the electron transfer, as greater distance between the peaks is an evidence of slower transfer phenomena.

Moreover, a cyclic voltammogram exhibits interest when multiple scans take place. The differences between them constitute a qualitative feature which usually can be used in order to determine if an essential decay of the reversible reactions over time occurs. Naturally, fundamental deviations between the scans show significant changes of the electrochemical profiles of the species and should not be expected, as a certain level of equilibrium should be achieved on each scan. Finally, the area under the response relates to the charge transfer for the process from the reduction to the oxidation and vice versa. From a qualitative point of view, this magnitude is linked to an expression of conductivity of the species and from a quantitative point of view, this magnitude can be used to estimate or calculate the electron stoichiometry of the redox reactions.

2.2.7 X-Ray Photoelectron Spectroscopy (XPS)

The electrons of each orbital have a characteristic binding energy, BE, which is mainly affected by the orbital energy level, the number of electrons in the atom and the atom nucleus. Photons of specific wavelength, typically from 0.1 to 25 Å (soft X-rays), have enough energy hv to interact with electrons of core levels and induce their emission, with a specific kinetic energy, KE. Consequently, the magnitude of the kinetic energy is dependent on the electron's binding energy, according to Equation 2.6, which is simplified omitting the less contributing factors of Fermi energy level, relaxation energy of the atom and other effects.

$$KE = BE - hv \qquad \text{Equation 2.6}$$

The XPS spectra consist of peaks which correspond to the number of the photoelectrons as a function of their kinetic energy. The position of each peak determines the binding energy of the electrons of the elements after particular calibrations, while the area below the peak is proportional to the number of atoms of the elements. Moreover, the range of the peaks (full width at half maximum) can reveal qualitative information about the coexistence of more than one oxidation states of the same element. It is usually expected that the background will present a relative increase towards the area of the lower energy values, which is due to secondary electrons and the Auger electrons. The secondary electrons have low kinetic energies because they have been generated by the random scatterings of the excited electrons in the solid. The Auger electrons are usually noted as LMM peaks. Satellite peaks (shake-up / shake-off) are frequently present for transition metals with *3d* and *4s* unpaired electrons. These peaks appear at discrete binding energies of higher values than the main peaks, due to electrons that lost a percentage of their energy and transferred it to another electron.

The XPS analysis is considered as one of the most appropriate methods of surface characterization.[18–20] The depth of the information reaches the order of 15 Å and, provided the equipment, it can reach deeper surfaces. It gives information about the energy levels of the conduction bands and it finds applications mainly in the qualitative analysis of surfaces and the investigation of the chemical nature of the system under study. The nomenclature of the peaks is based on the electron configuration, which corresponds to the quantum numbers as table shows.

Table 2.2 Correspondence between energy levels, electron configuration and quantum numbers as used in XPS peaks nomenclature.

Energy level	Electron configuration	Quantum numbers
K	1s	[1, 0, ½]
L_1	2s	[2, 0, ½]
L_2	2p ½	[2, 1, ½]
L_3	2p ³⁄₂	[2, 1, ³⁄₂]
M_1	3s	[3,0, ½]

Energy level	Electron configuration	Quantum numbers
M_2	3p ½	[3,1, ½]
M_3	3p $^3/_2$	[3,1, $^3/_2$]
M_4	3p $^3/_2$	[3,2, $^3/_2$]
M_5	3p $^5/_2$	[3,2, $^5/_2$]
N_1	4s	[4, 0, ½]

2.2.8 Fourier Transform Infrared (FTIR)

As the name of the spectroscopic technique reveals, the FTIR[21] technique makes use of infrared light. A source generates a beam of IR light of a range of frequencies, with the most typical window of measurements ranging from 12 to 120 THz (Mid IR). This is usually given as wavenumbers (4000 to 400 cm^{-1}) and sometimes as wavelengths (2.5 to 25 μm). The technique relies on the interaction of the IR spectrum with the matter and on the fact that the IR spectrum frequencies are of the same order of magnitude with the vibrational frequencies of most molecules. As a consequence, the molecules absorb the radiation and resonate at these frequencies.

This resonance is expressed with a range of behaviours stemming from the bonds of the molecules, none of which includes the breaking of the bond. In particular, the interaction of the IR spectrum with the molecules results into stretching and other oscillations of the bonds, depending on the type of the functional groups and what movement their positioning allows. Generally, the oscillations observed are of vibrational and rotational nature, caused from the absorbance of the light.

With a percentage of energy of the beam being absorbed, a detector can measure the transmittance of the light through the sample and generate a spectrum, based on the Fourier transformation of the electric signal. Since all bonds differ in terms of length, strength and direction, the recorded bands become a fingerprint of the existing functional groups, as each one will show interaction with the IR spectrum at a specific frequency with a specific intensity.

Wavenumbers from 4000 to 3000 cm^{-1} usually correspond to bonds with hydrogen, such as N-H, O-H and C-H. Triple bonds between carbon atoms or carbon and nitrogen atoms manifest within 2250-2000 cm^{-1}, while bands of double bonds appear as stronger peaks in the narrower window of 1680 to 1650 cm^{-1}. Single bonds of carbons with oxygen atoms appear below 1200 cm^{-1}. Apparently, the identification of the groups relies on the combinatory interpretation of the peaks of the spectrum, since IR spectra can have broad peaks. Similarly, the intensity of the peaks can be indicative of the number of the groups. Consequently, FTIR can serve as a satisfying technique for the identification of structures and the detection of changes happening at a molecular level.

2.2.9 Electron Paramagnetic Resonance (EPR)

The technique of EPR[22–24] relies on the microwave electromagnetic energy of frequencies 9-10 GHz, which interact with the magnetic moments of the unpaired electrons of atoms. The absorbance of the electromagnetic energy by the system under study is possible if the quantum energy of the irradiation ($\Delta E = |E_i - E_k| = h\nu$)[1] is equal with the difference of the two (quantum) energy levels of the system. Since there are only two possible spin states ($m_s = \pm\frac{1}{2}$), the projection of the spin of the electrons in the direction of the magnetic field B has only two possible states too, the parallel ($E_\uparrow = +\frac{1}{2} g_e \beta_e B$) and the antiparallel ($E_\downarrow = -\frac{1}{2} g_e \beta_e B$)[2] and the difference between the two states is equal to one energy quantum ($\Delta E = |E_\uparrow - E_\downarrow| = g_e \beta_e B_{res} = h\nu$), which the electron absorbs and resonance occurs (Figure 2.6). The g-factor, g_e, is independent of the frequency applied and for the spin of one unpaired electron, it is equal to the value of 2.0023. The divergence of g is affected by the electronic configuration; thus in systems with p or d electrons, a value of $g \neq 2.0023$ is expected.

[1] $h = 6.626076 \times 10^{-34}\ J\ sec$
[2] $\beta_e = 9.2742 \times 10^{-24}\ J\ T^{-1}$, $1\ Gauss = 10^{-4}\ Tesla$

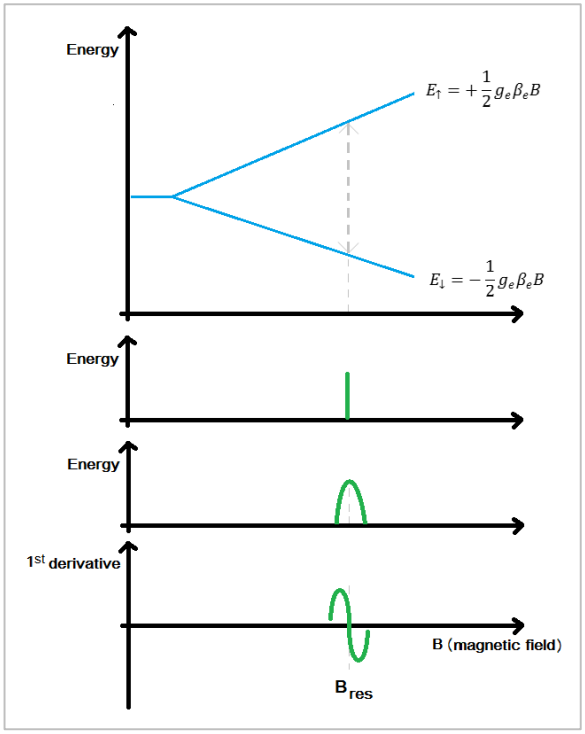

Figure 2.6 From top to bottom: (a) Split energy levels for a simple system with one unpaired electron, (b) Ideal monochromatic absorbance, (c) Absorbance over a distribution of magnetic fields, (d) Modulation of signal to its 1st derivative.

Interactions with nuclei spin contribute to further split of the energy levels (Hyperfine Coupling). The number of splits depends on the nuclei spin I according to the rule $2n(I + {}^1/_2)$ and the relative intensities of the corresponding peaks match the Pascal triangle. The hyperfine interaction is expressed by the hyperfine constant a. Unlike *s* electrons, *p* or *d* orbitals display low electron density at the centre of the atom and their spin resonance depends upon the direction of the external magnetic field applied, which results into anisotropic and low hyperfine coupling. Due to the random orientations of the centres, the a_{aniso} can be analyzed to x, y, z components and, in combination with the spins, it leads to either three ("rhombic", $g_x \neq g_y \neq g_z$) or two different directions of resonance ("axial", $g_x = g_y = g_{//} \neq g_z = g_\perp$). Interpretation of the EPR spectra can reveal information about the geometry of the systems. Strong and weak ligand fields influence the value of the energy differences and total spins, which are reflected on the g-factors values. Figure 2.7 shows how the symmetry of the local environment of the paramagnetic centres can be characterized.

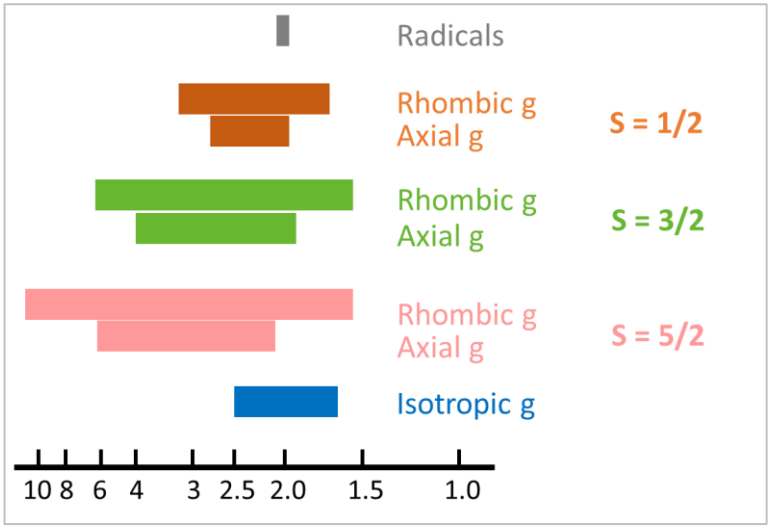

Figure 2.7 Range of values of the g-factor for characteristic symmetries and spins, as they are calculated from the EPR spectra.

2.2.10 Brunauer-Emmett-Teller model for gas absorption (BET)

Porosity and surface areas are typically delivered by gas adsorption measurements. In particular, an inert gas molecule (for example nitrogen or argon) under specific conditions is adsorbed in the void system of a solid. The more gas is adsorbed, the more available adsorption sites exist and the more the partial pressure of the gas change. According to the theoretical model of monolayer adsorption of the gas molecules on the surface area of the solids (Langmuir theory), the rate of adsorption (and desorption) of the gas is proportional to the number of available sites and the partial pressure of the gas.

The BET model takes into consideration that the adsorption is multilayer and that the first layer of gas molecules is different and the interaction between the upper gas layers resembles liquids interaction. Subsequently, the rates of adsorption and desorption are corrected accordingly and the gas volume adsorption isotherm can reveal information about the type and energy of interaction (adsorption or chemisorption or low or high energy) and the type of porosity (non-porous, mesoporous, macroporous, ordered materials). Assumptions such as absence of interactions between the adsorbate molecules define the idealistic nature of the measurements, but its wide application makes it a standard technique.[25]

Additionally, the model has small applicability to microporous crystalline solids, where the multilayer formation is closer to a filling effect than layer formation. In these cases, the surface area magnitudes are indications of a well-ordered

crystallinity and a well-determined void system, while the values are a useful tool of comparison of available active surfaces of different frameworks or of different metal substitutions or between the fresh and the spent solid material.

2.3 Instrumentation

Powder X-Ray Diffraction patterns (broad angle) were obtained on a Bruker D2 diffractometer using Cu source K_{α_1} and λ=1,54056 Å, in the premises of the University of Southampton. The patterns were compared with simulation patterns and were refined with the Rietveld method.

Diffuse Reflectance UV-VIS measurements were conducted using a Shimadzu 2600 spectrometer with integrated sphere in the premises of the Research Complex at Harwell (Catalysis Hub) and a Shimadzu 3600 UV-VIS-NIR spectrophotometer with integrated chamber in the premises of IMRE/A-STAR. All the catalysts were measured in different sample holders, depending on the nature of the material, while the sample holders were preliminarily tested for the background. The reference standard used was $BaSO_4$. The UV-VIS measurements were typically obtained for the range of wavelengths from 200 to 800 nm.

UV-VIS spectra of liquid solution were collected from a Shimadzu 3600 UV-VIS-NIR spectrophotometer in the premises of IMRE/A-STAR, using a pair of identical quartz cuvettes for the reference and the sample.

The BET measurements were conducted with N_2 adsorption/desorption at 77 K, using a Micrometritics Gemini 2360 Surface area analyser in the University of Southampton and a Micrometritics ASAP 2020 Surface area and porosity analyser in the premises of IMRE/ A-STAR.

Details upon the morphology of the surface and the size and shape of the particles were obtained with an XL30 ESEM D6849 instrument (University of Southampton), operated with Microscope Control software. The energy of the electron beam was set at 10.0 kV, the vacuum of the chamber was set between 0.6-0.9 Torr and the magnification was set for measurements ranging from 5-500 μm. Images of used catalysts were collected from an FE SEM 6700F, in the premises of IMRE/A-STAR, with energy beam at 10.0 kV, vacuum chamber at 5.14E-4 mbar and magnification up to 1 μm

For the cyclic voltammograms of the materials the Metrohm Autolab PGSTAT101 potentiostat was used and was coupled with a reference (Pt), a counter (Ag/AgCl)

and a working electrode (glassy carbon / ID: 3 mm and OD: 3 mm), along with a Nova Autolab software (version 1.18) for current-to-voltage conversions and data acquisition. The electrolyte used was a buffer solution of phosphates (pH=7, C=0.1 M). It was bubbled with nitrogen for oxygen removal prior to each measurement and fresh solution was used for each material.

Continuous wave X-band EPR experiment was performed on a Bruker EMX spectrometer with microwave frequency 9.86 GHz, with an inbuilt microwave frequency counter at ambient temperature and pressure, in the premises of the University of Southampton. A microwave power of 1.8 mW, a modulation amplitude of 0.1 mT and a modulation frequency of 100 kHz were used. Spectra were recorded with Bruker Xenon software and fittings were done using the Matlab-based EPR simulation package EasySpin.

XPS analysis of fresh materials was performed at the University of Newcastle, using a Thermo-Scientific Theta Probe instrument equipped with monochromated Al Kα source in NEXUS facility and collected spectra were analysed using the CasaXPS software. XPS analysis of spent materials took place in IMRE/A-STAR, using a Thermo Scientific Theta Probe XPS and applying the analysis software ThermoAvantage. Monochromatic Al Kα X-ray (hν=1486.7 eV) was employed for analysis with an incident angle of 30° with respect to surface normal. Photoelectrons were collected at a take-off angle of 50° with respect to surface normal. The analysis area is approximately 400μm in diameter while the maximum analysis depth lies in the range of 4 - 10nm. Survey spectra were captured for element identification, while high-resolution spectra were acquired for chemical state analysis. Charge compensation was performed by means of low-energy electron flooding and further correction was made based on adventitious C1s at 285.0 eV using the manufacturer's standard software. The error of binding energy is estimated to be within ±0.2eV.

The ICP-OES measurements were conducted with a Varian Vista MPX CCD Simultaneous axial ICP-OES instrument, based in the MEDAC LTD laboratories.

Proton (^{1}H) NMR was performed on a Bruker A400 FT-NMR spectrometer (University of Southampton), using $CDCl_3$ as solvent.

Finally, the visible light photocatalysis experiments were conducted in the University of Southampton with a strip JSG 5M 300 LEDs 3528 SMD Neutral/ Day white colour and in the premises of IMRE/A-STAR a Hamamatsu white light illuminator LIGHTINGCURE LC8 was used with a UV cut-off filter below 400 nm.

2.4 Experimental Methodology

2.4.1 Preparation of materials and characterization

The catalytic materials that have been used for this project are copper and cobalt-based zeotypes and MOFs. There a few reasons that justify the choice of these two metals for applications of organic synthesis and environmental control. Copper is a transition metal of low toxicity and hazard and of relative abundance. Its unique electron configuration makes copper (II) a difficult ion to coordinate with a variety of ligands, but it responds in naturally occurring biocomposites and enzymes. Conversely, cobalt is a metal of high abundance in nature which justifies its low cost and with an electron configuration that makes it easy to be found in different coordination environments. Cobalt in oxidation state 2+ and 3+ is also widely reported for its catalytic properties. Both copper and cobalt demonstrate absorbance in the visible region of light, which could be used for their development in photocatalytic systems.

The preparation of the catalytic materials has been optimized via basic characterization before the materials are catalytically probed. Among the zeotypes, the AFI framework (code 5) has been selected for its robustness and quick preparation. CoAlPO-5 and CuAlPO-5 have been synthesized according to the rules of sol-gel chemistry. Their exact synthetic protocol is discussed thoroughly in Chapter 3. CoAlPO-5 has been widely discussed in literature for a number of catalytic reactions,[26,27] unlike CuAlPO-5.[28] In both cases, the interest lies in cobalt's and copper's substitution for a framework site.

According to the rules of conventional solvothermal synthesis, CoMOF-74, HKUST-1 (copper-based MOF) and ZIF-9 (cobalt-based ZIF) have been prepared under an optimized synthetic protocol, reported in Chapter 3. HKUST-1 is among the most popular MOFs for its topology and one of the copper-based ones, while it has been reported for its catalytic performance in the Knoevenagel condensation reaction.[29] The electron configuration of cobalt allows the element's coordination with a range of ligands and this is why cobalt is frequently found replacing the most usual metal found in the MOFs, zinc. Unfortunately, zinc MOFs are not good candidates for catalysis or visible light photocatalysis, due to their sensitivity to ambient conditions and their white colour. CoMOF-74 is a Co^{2+} based material with a complex and interesting structure. CoMOF-74 has been reported for gas applications[30,31] and some catalytic uses.[32] ZIF-9 is one of the zeolitic imidazole-

based materials. It is made out of benzimidazolate ions in coordination with Co^{2+} ions. ZIF-9 formerly reported applications include mostly gas adsorption and separation.[33–35] Zakzeski et al. have reported it as an oxidative catalyst of aromatic oxygenates,[36] while Wang et al. employed it in water oxidation electrocatalysis.[37]

The optimization of the synthesis has taken place after trials with different ratios of reagents, different time and temperature crystallisations. PXRD is the main criterion that applies to the phase purity of the materials. SEM images are a good indication of crystallinity and successful synthesis methodology. BET measurements apply as a proof of porosity. Where applicable or important, characterization of the nature of the active site, in terms of oxidation state and coordination, is performed via XPS, DR UV-VIS and EPR. Further characterization is applied for specific elucidation of properties.

2.4.2 Batch catalytic reactions at ambient conditions

It is important to be able to control applications of organic synthesis kinetically and thermodynamically at ambient pressure and temperature. The ambient temperature reactions are very appealing in organic synthesis, due to the fact that organic molecules can become vulnerable at high temperatures and thermal effects can drive the reactions through paths that are not easily controlled, while this depends on the desired product and its selectivity. For this reason, homogeneous synthetic applications are preferred for the high yields and the one-phase systems that simplify the chemical reactor design. By the same token, they are often characterized by excess use of solvents or oxidants such as H_2O_2, the elimination of which happens to be one of the main aims of green chemistry and engineering. However, the separation of these components at the end of a synthetic process is energy and time-consuming. As in organic synthesis, it is also usual for application of environmental nature to preferably occur at ambient conditions for they usually take place on a large scale.

The organic synthesis and environmental applications that are being studied in this project take place at ambient conditions, in the darkness and under the irradiation of white light. The small quantities of substrates used make a glass vial ideal for these reactions, which can remain on a stirring plate without the need of being held (often the vial was simply taped on the stirring plate). A tape of LED lights is being adhered on the inside of a glass cylinder of diameter comparable to the diameter of the stirring plate so that the light surrounds the vial-reactor (Figure 2.8a). In a different setup, the glass vial may be required to

remain in the dark (Figure 2.8b). When irradiated by white light illuminator, a cut-off filter has been adjusted, to allow wavelengths only from 400 to 800 nm (Figure 2.8c). In both cases, LEDs and illuminator do not raise the temperature of the reaction mixture significantly or enough to induce thermal reactions. In some experiments, the glass vials were put in small water baths to ensure that any heat produced is absorbed. The glass vial behaves as a batch reactor that accommodates the catalyst (solid powder) and the reaction mixture (liquid). After specific time of reaction, NMR or UV-VIS is used to monitor the degree of conversion achieved, depending on the type of reaction under study.

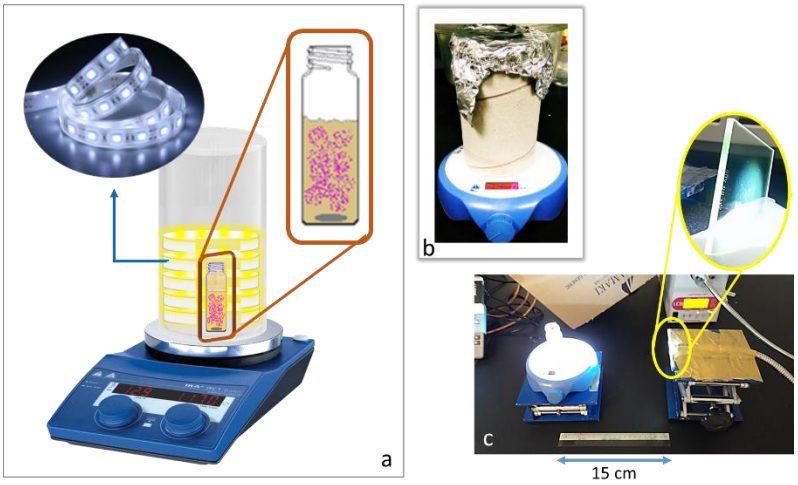

Figure 2.8 (a) Illustrative representation of batch reactor for organic synthesis under the irradiation of light with LEDs tape on a stirring plate. The magnification of the batch reactor shows the reaction mixture with the powder catalyst and the magnetic stirrer. (b) Picture of the layout to achieve conditions of darkness. (c) Picture of setup of batch reactor for 4-NP reduction and dye solution decolouration. The magnified picture depicts the cut-off filter.

2.4.3 Progress of reactions and quantitative analysis

In this project, each analytic technique is used according to a set of parameters that may limit or favour its application to observe the progress of the reactions. In organic synthesis, the transformation of organic molecules can be easily monitored by looking at the differences of the protons attached to the organic carbon atoms. The small quantities of the samples and the use of deuterium facilitates this observation employing ^{1}H NMR. The use of dyes or molecules with sensitive groups in the visible area makes liquid UV-VIS a suitable analytic technique. As soon as the appropriate method is found according to the

sensitivity related to the system of study, the quantitative analysis takes place with calibration curves.

It is frequent that internal standards are used, which are molecules inactive to chemical environments and their concentration remains the same throughout the reaction. The concentration of the substrates is then measured against the internal standards. However, in reactions where the conversion of a reactant leads to one product, selectivity stops playing an important role and internal standards are not necessary for the quantitative analysis since the difference of intensity of the signals are connected to the conversion achieved.

Quantifying the conversion using ^{1}H NMR, the starting material and product material are initially characterized and their peaks are located. The difference of the area under a peak of interest before and after a reaction time determines the conversion of the starting material to the product because the intensity (area below the peak) of the absorption band is proportional to the number of hydrogen atoms that give a signal at the specific frequency. This way, the measurement is direct, as long as the bands do not overlap. The total integral area A_t can be calculated, as in Equation 2.7, where k is the constant of proportionality, $H\%$ is the percentage of hydrogen atoms and n refers to the moles of the solution, which can be calculated by its weight and concentration. The percent difference between two integral areas at a specific frequency regards the percent conversion of the starting material over reaction time. For high selectivity and one final product, the peak of the product is used supplementary.

$$A_t = k \cdot H\% \cdot n \qquad \text{Equation 2.7}$$

Similarly, in the UV-VIS analytic technique, the intensity (height) of an absorption band at a specific wavelength is proportional to the concentration of the sensitive group (Lambert-Beer law). Unlike NMR and other analytic techniques, the absorption bands in UV-VIS are broader and for this reason, it is preferable to calibrate using the intensity at the wavelength of maximum absorbance. A set of standard solutions, hence of known concentrations, are measured using a quartz cuvette (1cm path) and their absorption intensities at a specific wavelength are registered against the known concentrations. Plotting the concentrations C against the intensities A allows the estimation of the linear correlation between the two magnitudes (Equation 2.8), which is used for the calculation of the unknown concentration of a sample from the signal of intensity.

$$A\ (a.u.) = k \cdot C \qquad \text{Equation 2.8}$$

Due to linearity, the percent difference between intensities of the same wavelength corresponds to the percent conversion of the starting material. However, it is important to mention that more parameters of interest and significance are examined in UV-VIS, such as shift of peaks towards the UV or the IR area, baseline and absorbance intensities. Regarding the latter point, the absorbance intensities are very important and are very dependent on the instrument's sensitivity, as very high concentrations usually give significant noise or very low concentrations may not be adequate, which makes only a specific range of concentrations appropriate for the calibration curve and the functional operation of the instrument.

2.5 References

1 E. J. P. Feijen, J. A. Martens and P. A. Jacobs, in *Preparation of Solid Catalysts*, ed. J. W. G. Ertl, H. Knözinger, WILEY-VCH, Weinheim, 1999.

2 A. Corma, *J. Catal.*, 2003, **216**, 298–312.

3 M. P. Suh, Y. E. Cheon and E. Y. Lee, *Coord. Chem. Rev.*, 2008, **252**, 1007–1026.

4 C. Dey, T. Kundu, B. P. Biswal, A. Mallick and R. Banerjee, *Acta Crystallogr. Sect. B*, 2014, **70**, 3–10.

5 Y.-R. Lee, J. Kim and W.-S. Ahn, *Korean J. Chem. Eng.*, 2013, **30**, 1667–1680.

6 C. Hammond, *The Basics of Crystallography and Diffraction*, Oxford University Press, 2nd edn., 2008.

7 L. B. McCusker and C. Baerlocher, in *Introduction to Zeolite Science and Practice*, eds. P. A. J. van Bekkum E.M. Flanigen and J. C. Jansen, Elsevier, 2001, vol. 137, pp. 37–67.

8 G. Will, *Powder Diffraction: The Rietveld Method and the Two Stage Method to Determine and Refine Crystal Structures from Powder Diffraction Data*, Springer New York, 2006.

9 R. A. Young, Ed., *The Rietveld Method*, International Union of Crystallograhy, Oxford University Press, New York, 1993.

10 L. B. McCuske, R. B. Von Dreele, D. E. Cox, D. Louër and P. Scardi, *J. Appl. Cryst.*, 1999, **32**, 36–50.

11 W. I. F. David, *J. Appl. Cryst.*, 2003, **34**, 691–698.

12 J. Goldstein, D. E. Newbury, P. Echlin, D. C. Joy, C. Fiori and E. Lifshin, *Scanning Electron Microscopy and X-Ray Microanalysis*, Springer US, New York, 1st edn., 1981.

13 P. J. Goodhew, J. Humphreys and R. Beanland, *Electron Microscopy and Analysis*, Taylor & Francis, London, 3rd edn., 2000.

14 J. H. Nobbs, *Rev. Prog. Color. Relat. Top.*, 1985, **15**, 66–75.

15 R. S. McDowell and J. F. Kelly, *Kirk-Othmer Encycl. Chem. Technol.*, 2000.

16 J. R. Dean, *Kirk-Othmer Encycl. Chem. Technol.*, 2007.

17 D. Kiemle J. and W. T. Winter, *Kirk-Othmer Encycl. Chem. Technol.*, 2000.

18 C. C. Chusuei and D. W. Goodman, in *Encyclopedia of Physical Science and Technology (Third Edition)*, ed. R. A. Meyers, Academic Press, New York, Third Edit., 2003, pp. 921–938.

19 D. Cahen and A. Kahn, *Adv. Mater.*, 2003, **15**, 271–277.

20 R. Matzdorf, *Surf. Sci. Rep.*, 1998, **30**, 153–206.

21 P. R. Griffiths, in *Transform Techniques in Chemistry*, ed. P. R. Griffiths, Springer US, Boston, MA, 1978, pp. 109–139.

22 L. Kevan, *Electron Spin Resonance*, Academic Press, New York, Third Edit., 2003.

23 E. Garribba and G. Micera, *J. Chem. Edu.*, 2006, **83**, 1229–1232.

24 N. J. Bunce, *J. Chem. Edu.*, 1987, **64**, 907–914.

25 G. Attard and C. Barnes, *Surfaces*, Oxford University Press, New York, 2011.

26 J. M. Thomas, R. Raja, G. Sankar and R. G. Bell, *Nature*, 1999, **398**, 227–230.

27 L. Zhou, J. Xu, C. Chen, F. Wang and X. Li, *J. Porous Mater.*, 2008, **15**, 7–12.

28 Q. Ke, M. Wu, H. Yu and G. Lu, *ChemCatChem*, 2017, **9**, 733–737.

29 S. A. Sotnik, K. S. Gavrilenko, A. S. Lytvynenko and S. V Kolotilov, *Inorg. Chim. Acta*, 2015, **426**, 119–125.

30 T.-L. Hu, H. Wang, B. Li, R. Krishna, H. Wu, W. Zhou, Y. Zhao, Y. Han, X. Wang, W. Zhu, Z. Yao, S. Xiang and B. Chen, *Nat. Commun.*, 2015, **6**, 7328–7336.

31 Y. He, R. Krishna and B. Chen, *Energy Environ. Sci.*, 2012, **5**, 9107–9120.

32 H.-Y. Cho, D.-A. Yang, J. Kim, S.-Y. Jeong and W.-S. Ahn, *Catal. Today*, 2012, **185**, 35–40.

33 F. Cacho-Bailo, I. Matito-Martos, J. Perez-Carbajo, M. Etxeberría-Benavides, O. Karvan, V. Sebastián, S. Calero, C. Téllez and J. Coronas, *Chem. Sci.*, 2017, **8**, 325–333.

34 L. S. Lai, Y. F. Yeong, K. K. Lau and M. S. Azmi, *Sep. Sci. Technol.*, 2014, **49**, 1490–1508.

35 Y. Huang, D. Liu, Z. Liu and C. Zhong, *Ind. Eng. Chem. Res.*, 2016, **55**, 7164–7170.

36 J. Zakzeski, A. Dębczak, P. C. A. Bruijnincx and B. M. Weckhuysen, *Appl. Catal. A Gen.*, 2011, **394**, 79–85.

37 S. Wang, Y. Hou, S. Lin and X. Wang, *Nanoscale*, 2014, **6**, 9930–9934.

Chapter 3: Preparation of crystalline porous catalytic materials and their characterization

3.1 Architectures of zeolitic materials and metal-organic frameworks

The list of zeolitic topologies and metal-organic frameworks is very long and the database is being enriched as the successful synthesis of new architectures is reported. Industrially, only a small percentage of these architectures is employed and it would be an oversight to omit a reference to some very important and interesting zeolitic materials and metal organic frameworks. Besides, their unique features are the main reason why these materials have been distinguished. Some of them are illustrated in Figure 3.1.

Starting from zeolites, the faujasite (FAU) framework is one of the most important for the oil industry. Its sodalite cages with the hexagonal apertures of 7.4 Å and interconnected pores has proven unique in the fluid-catalytic cracking technology. MFI or ZSM-5 is a zeolite of historical importance in the hydrocarbon reactions, since it was patented for the conversion of methanol to gasoline by Mobil Oil. The 5-membered MFI ring is the opening of a 5.5 Å pore, due to which it affords distinct microporosity. It is also known for high selectivity, due to its rare zig-zag 1-D channels. Modernite (MOR) is one of the most abundant minerals with applicability in isomerisation reactions, attributed to its 1-D channels of 6.5 Å diameter. Chabazite (CHA) is another common type of zeolite with very uncommon structure. Three rings of 8 atoms have a 3.8 Å diameter and permit the entrance to the cages of the material from three different axes, characteristic of its high degree of dimensionality.

Unlike zeolites, the distinction of certain MOFs does not regard their commercial applicability. MOF-5 is one of the most displayed examples of the implementation of the reticular chemistry for their synthesis. Made out of zinc nodes and 1,4-benzodicarboxylate ligands, it affords high porosity in the arrangement of 14 Å cubic pores, along with high moisture sensitivity. MOF-74 is considered a stable material with most typical metal nodes being zinc, cobalt, nickel and manganese, linked up via 2,5-dioxidoterephthalate ions. This results into hexagonal 1-D

channels of 7 Å diameter. HKUST-1, made up of copper nodes and trimesic acid ligands, is well-known for its unique paddle-wheel motifs, the 3 interconnected pores ranging from 10 to 14 Å and the multidimensionality of the cages. ZIF-8 responds most frequently in zeolitic imidazolate frameworks applications and is commercially available as Basolite Z1200. Based on zinc nodes connected via imidazolate, it adopts a sodalite topology with an opening diameter of 3.4 Å, leading into a 10 Å cavity.

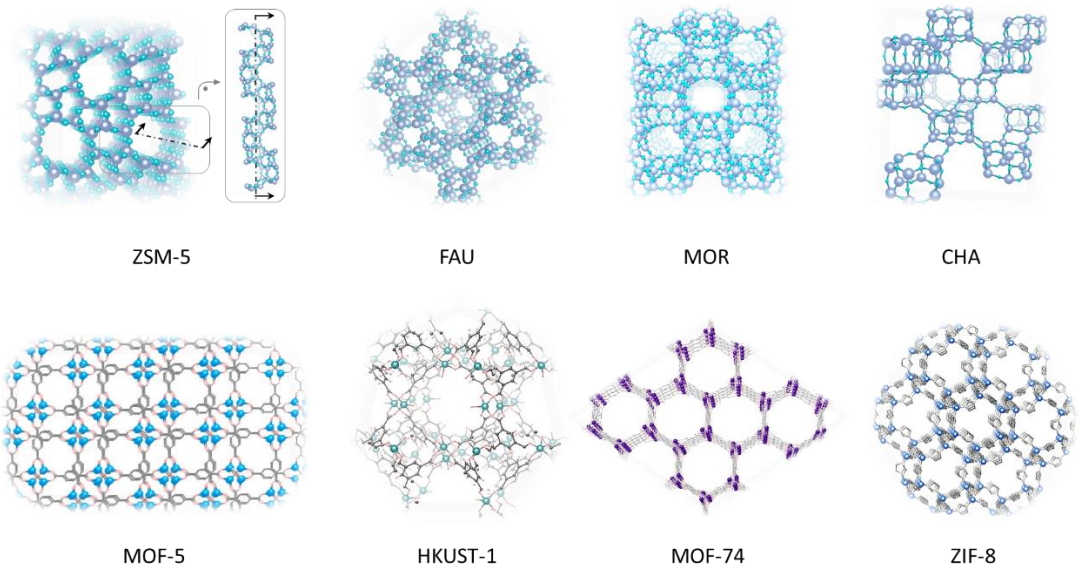

Figure 3.1 View of representative zeolites and MOFs.

Apparently, the choice of the materials is based on the type of research carried out in this thesis, for which cobalt and copper metals has been decided, due to their abundance, photoresponse, catalytic activity and inexpensive use. Employing zeolite analogues which are better controlled and permit metal substitution, the AFI aluminophosphate is an exceptional candidate for its simple preparation and its fast crystallization. It affords a good platform for Cu and Co incorporation in the framework and it is known for its robustness and microporosity. Silicon substitution is also feasible, leading to higher acidic charge of the framework. CuAlPO-5 and CoAlPO-5 are described extensively in the following sector.

AlPO-5, as a zeotype, does not allow an overly high metal loading. MOF-74, on the other hand, affords a similar channel shape and orientation and as a MOF, it permits a high metal content. However, the difference of the geometry of the metal sites in AlPO-5 and MOF-74 will be taken into consideration. HKUST-1 is selected for its high dimensionality and pore size, while ZIF-9, a cobalt based

framework constitutes an alternative choice of a material with zeolitic topology, hence tetrahedral coordination, and high metal content.

3.2 Topology and Preparation of metal-substituted zeotyped and metal-organic frameworks

3.2.1 Topology and Synthetic Protocol of CuAlPO-5 and CoAlPO-5

CuAlPO-5 and CoAlPO-5 belong in the category of zeotypes under the AFI framework with code 5. The AFI architecture consists of one-dimensional long tubular channels across the z axis. The diameter of the AFI opes, namely the diameters of the cross sections of these channels, are 7.3 Å with 12 T atoms building the ope ring. The AFI structure is not naturally occurring. Its crystallization is short, which is indicative of the fact that AFI is an early metastable phase. Copper or cobalt metals are expected to substitute for an aluminium site, because of their oxidation states. Two illustrations of the copper and cobalt substituted AlPO-5 are shown in Figure 3.2.

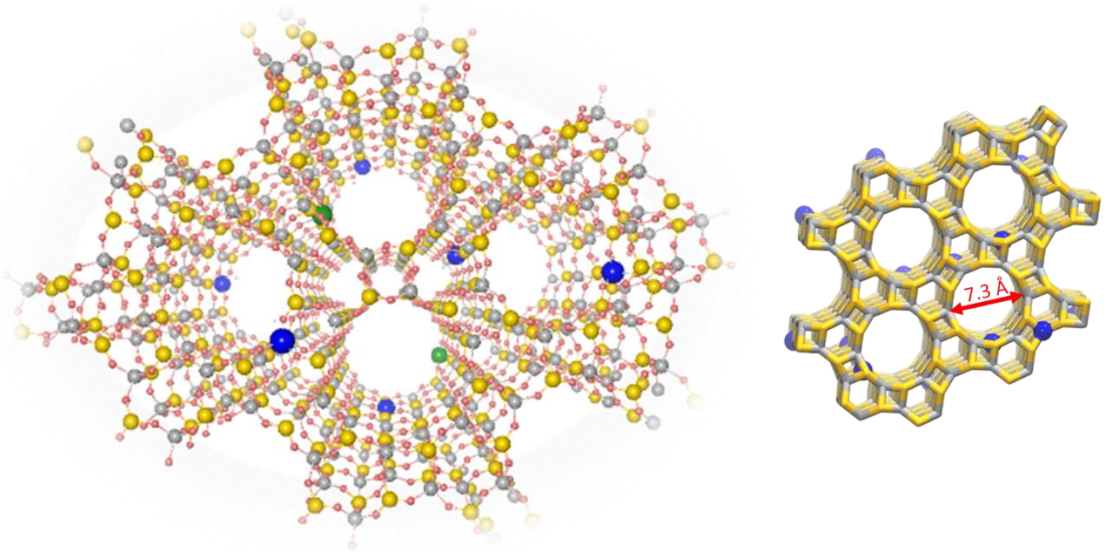

Figure 3.2 MeAlPO-5, where Me: Cu or Co, depicted with green or blue heteroatoms. Oxygen atoms are in pink, aluminium atoms are in grey and phosphorus atoms appear in yellow. On the left, the AFI framework with perspective where the isolated copper and cobalt sites are visible. On the right, the AFI framework with emphasis on the tetrahedral building units.

CuAlPO-5 synthesis was based on the work of Muñoz et al.[1], with a molecular ratio 0.5Al : 0.41P : 0.3SDA : 7.1H_2O : 0.04Cu and is described thoroughly hereinafter: copper II oxide (0.4 g) is stirred with deionized water (9.1 mL) and orthophosphoric acid (85% w/w, 3.4 mL) under heating (80 ˚C) until the solution is blue-turquoise and the copper oxide is completely dissolved. After the solution has cooled down, it is stirred vigorously with alumina (3.1 g) in a teflon beaker until a homogeneous mixture is obtained. Tetraethylammonium hydroxide (35% w/w, 9 mL) is added dropwise and is left stirring until the gel is completely homogenized. The resulting gel-mixture has a turquoise-blue colour. The gel charges immediately Teflon-liners up to 1/3 of their volume, which are sealed in stainless-steel autoclaves. The autoclaves are transferred in a preheated oven, left at 150 ˚C for 24 hours and are cooled down in an ice-bath. The material is filtered under vacuum, washed with deionized water and left to dry overnight at 80 ˚C. The light blue-turquoise crystalline powder is ground and calcined at 550 ˚C for 16 hours under flow of air. The final material has a light green-pistachio colour and is kept in a desiccator to prevent moisture absorption until it is used.

CoAlPO-5 was synthesized in a similar manner with a molecular ratio 0.5Al : 0.8P : 0.4SDA : 1.9H_2O : 0.04Co and is described here: orthophosphoric acid (6.7 g) is stirred with deionized water (25 mL) until complete dissolution. Aluminium hydroxide (3.9 g) is added into the mixture under vigorous stirring. Solution of cobalt acetate (0.7 g) in deionized water (10 mL) is added dropwise into the mixture under stirring. Finally, N,N-Dicyclohexylmethylamine is added dropwise under stirring until the gel is completely homogeneous with a light purple colour. The gel charges immediately Teflon-liners up to 1/3 of their volume, which are sealed in stainless-steel autoclaves. They are transferred in a preheated oven, left at 200 ˚C for 2 hours and are cooled down. The material is filtered under vacuum, washed with deionized water and left to dry overnight at 80 ˚C. The blue crystalline powder is ground and calcined at 550 ˚C for 16 hours under flow of air. The final material has a light green-yellow colour and is kept in a desiccator to prevent moisture absorption until it is used.

3.2.2 Topology and Synthetic Protocol of HKUST-1 and CoMOF-74

HKUST-1 has been named after the “Hong Kong University of Science and Technology” and is known for its paddle-wheel shaped secondary building unit ($Cu_2(CO_2)_4$). It is made out of copper II nodes linked via 1,3,5-benzenetricarboxylate (BTC), with an empirical formula $Cu_3(BTC)_2(H_2O)_3$, while it is

also known as MOF-199.[2] Copper exists as a dimer in the second oxidation state (Cu^{2+}). As Figure 3.3 depicts, each copper atom coordinates with four atoms of oxygen from two carboxylates and with one oxygen that belongs to a water molecule. The removal of the water oxygen from copper is possible through prolonged degassing through heating under vacuum, which turns the material from a blue-green colour to dark blue and exposes the Cu^{2+} site.[3,4]. Upon this change, the copper site changes coordination and from a square pyramidal initial phase, it becomes almost square planar. HKUST-1 has a complex architecture, with a 3-dimensional channel system. The pores are square shaped with the largest one being approximately 11 Å wide.

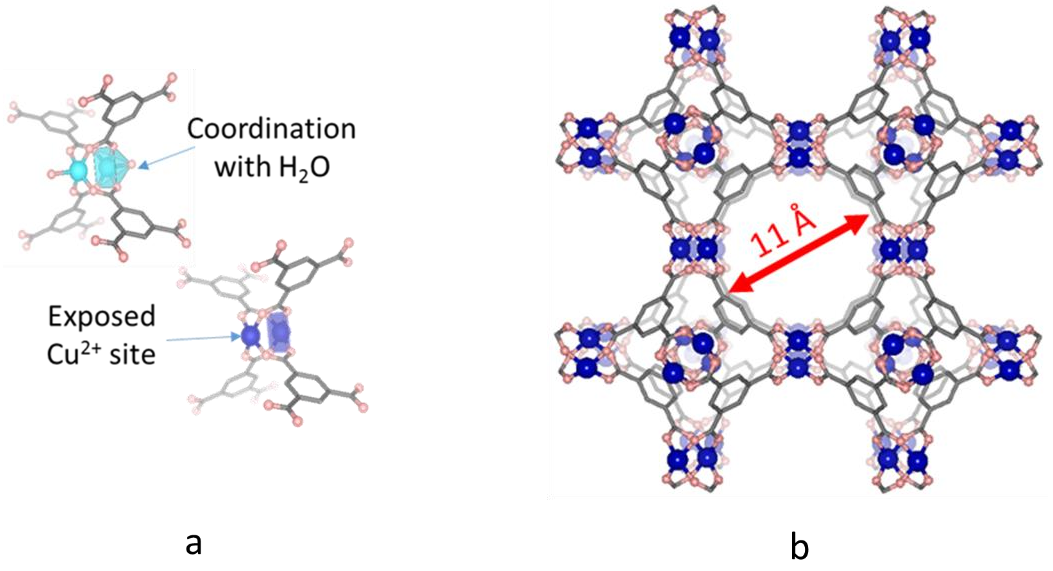

Figure 3.3 Paddlewheel secondary units of HKUST-1 before (a, top) and after (a, bottom) removal of water molecule from the framework. Representation of HKUST-1 framework with exposed Cu^{2+} sites (b).

For synthesis of HKUST-1, copper nitrate trihydrate (2.188 g) is added in 30 mL of deionized water and benzene-1,3,5-tricarboxylic acid (btc / trimesic acid, 1.05 g) is added in a mixture of 15 mL of ethanol and 15 mL deionized water. The two solutions are mixed together and the final solution of light blue-turquoise colour is placed in Teflon lined stainless steel autoclaves by filling half their volume. The autoclaves are heated in an oven at the temperature of 110 ˚C for 18 hours and they are left to cool down in room temperature. The crystals have an intense green-turquoise colour and are collected by filtration under vacuum with a 1:1 (v/v) mixture of ethanol and deionized water and then with deionized water only. The material is left overnight to dry at 80 ˚C and it is possible that during the drying procedure, it will change to a blue colour, while it will regain its initial

green-turquoise colour, as soon as it is exposed to the ambience. The MOF crystals are then ground and the powder is heated at 120 ˚C under vacuum for 16 hours (this procedure turns the material to dark blue) and kept in a desiccator to prevent its contact with the moisture of the environment. The methodology was based on the work of Alaerts et al.[5]

CoMOF-74[6] is an symmetric and rigid MOF with open metal sites and an empirical formula (Co_2(dhBDC). The organic ligand that holds together the cobalt sites is 2,5-dihydroxy-terephthalate (dhBDC) and each cobalt site coordinates with three carboxyl and two hydroxyl groups (Figure 3.4) from four organic ligands and a water molecule. Upon heating under vacuum, the cobalt site loses the water molecule and obtains a square pyramidal coordination. The structure of MOF-74 is interesting with long uniform channels, 1.1-1.2 nm wide with hexagonal shape, due to which the framework resembles to an 1-dimensional honeycomb (Figure 3.4).

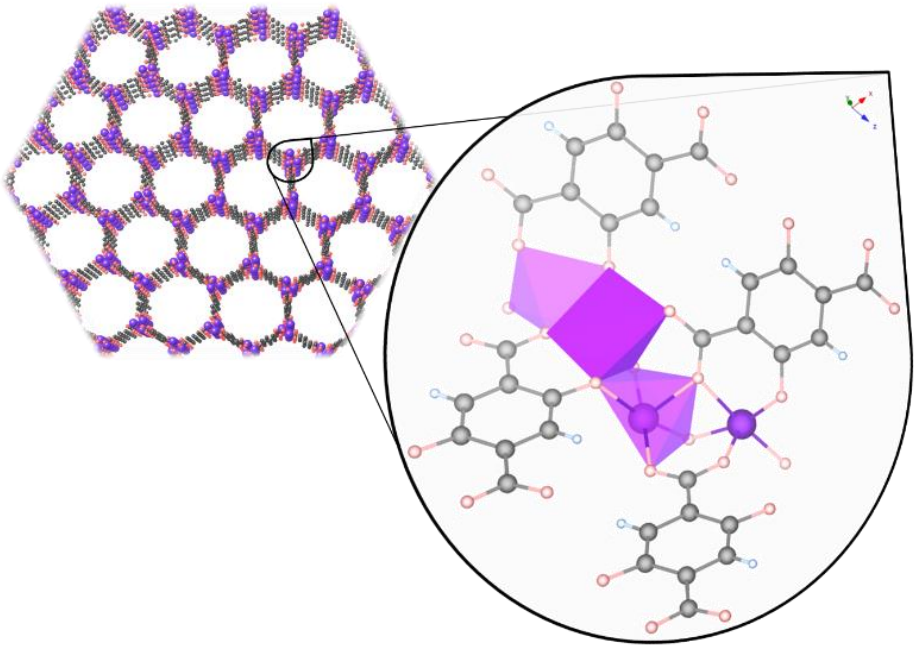

Figure 3.4 CoMOF-74: hexagonal pore channels and connectivity between the cobalt ions and the ligands (Co: purple, C: grey, O: pink, H: light blue).

Synthesis of CoMOF-74 has been beased on the work of Wang et al.[6] and is described hereinafter: cobalt nitrate hexahydrate (0.57 g) and 2,5-dihydroxyterephthalic acid (0.12 g) are added in a mixture of dimethylformamide (16 mL), ethanol (16 mL) and water (16 mL). The solution is left under stirring at room temperature until solids are completely dissolved. The solvent mixture is loaded in glass bottles (of 100 mL) and placed in an oven at 100 ˚C for 24 hours

and, then, left to cool down at ambient temperature. Brown crystals are collected by decanting the mother liquor. The collected solid is washed several times with DMF and, next, with methanol, by decanting and replenishing the solvent 4 times over two days. At the final stage, the solvent is removed with rotary vacuum and the solid remains under vacuum at 150 ˚C for 1 day. A purple –brown powder is then collected, ground and stored in a desiccator.

3.2.3 Topology and Synthetic Protocol of ZIF-9

ZIF-9 is a cobalt based framework with a zeolitic topology and empirical formula $Co(PhIm)_2$. It keeps the nature of a MOF, as it consists of inorganic (the cobalt sites) and organic parts (the imidazole based molecules). The organic molecules in ZIF-9 are benzimidazolate (PhIm) and the nitrogen atoms of PhIM coordinate with the Co^{2+} ions. Cobalt coordinates tetrahedrally with the nitrogen atoms of four ligands (Figure 3.5a). The benzyl ring of the ligands create sphere-like cavities (Figure 3.5b) and their presence reduces the opening of the pores from 11 Å, which is the internal diameter, to approximately 3.5 Å (Figure 3.5c). The benzyl ring of the ligands is responsible for the hydrophobicity of this microporous structure. ZIF-9 is also known for its high rigidity and stability, probably due to the sodalite topology it adopts,[7-9] although it is usually represented from another direction (Figure 3.5d).

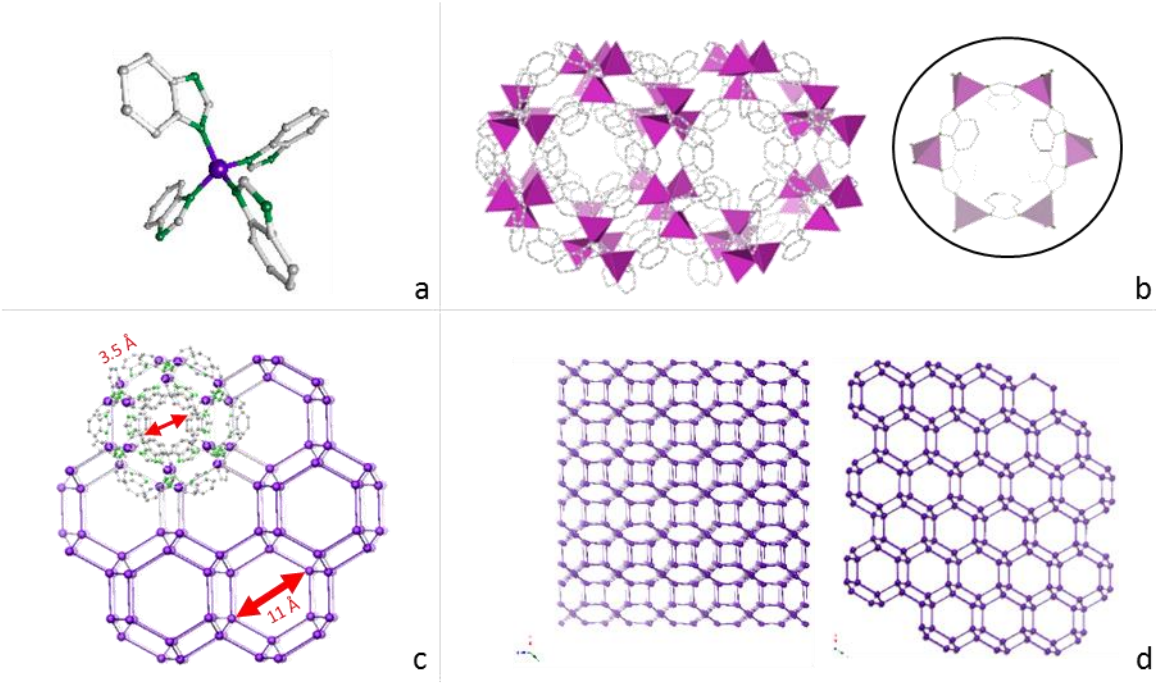

Figure 3.5 (a) Tetrahedral coordination of cobalt (purple) with four benzimidazole ligands, (b) Sphere-like cavities of ZIF-9 shaped from the benzyl ring of the ligand, (c) Representation of the metal grid of ZIF-9 and the internal diameter of the void, in contrast to the confinement of the opening due to the ligands, (d) Sodalite view of ZIF-9 and typical view of ZIF-9 parallel to axis c.

For the synthesis of ZIF-9, cobalt nitrate hexahydrate (0.5 g) and benzimidazole (0.15 g) are added in dimethylformamide (45 mL). The solution is left under stirring at room temperature until the solids are completely dissolved in the solvent, gaining an intense magenta colour. NaOH or KOH tablets are added for pH stabilization around 7-8. The crystallization is taking place in glass bottles, (100 mL) at 130 ˚C for 48 hours. The bottles are then left to cool down at ambient temperature and deep magenta and purple crystals are collected by centrifugation. The collected solid is washed with DMF and then methanol several times, by decanting the solvent. The solid is next immersed in chloroform, changed four times during two days. Finally, the solid is collected by rotary evaporation and is left to dry overnight at 80 ˚C. The crystals are ground and the purple powder is heated under vacuum for 5 hours at 130 ˚C to ensure removal of solvent molecules from the structure. The procedure was based on the work of Li and Kim[10] and improved by the work of Öztürk et al.[11]

3.3 Basic structural and porosity characterization results of the prepared porous solids

The preparation information of the materials used in this thesis, as described in the previous section, are summarised in Table 3.1. Following the preparation of the solids, their structural properties are examined applying instrumental characterization, to ensure crystallinity and porosity, before probing the materials catalytically.

Table 3.1 Summary of preparation information of CuAlPO-5, CoAlPO-5, CoMOF-74, HKUST-1 and ZIF-9.

Material	Molar ratio	Sources	Crystallization (time / T)	Recovery method	Activation (method, time / T)
CoAlPO-5	0.5Al : 0.8P : 0.4SDA : 1.9H_2O : 0.04Co	Al(OH), H_3PO_4, MDCHA (SDA), H_2O, $(CH_3COO)_2Co$	2 h / 200 °C	Filtration, drying	Calcination, 16 h / 550 °C
CuAlPO-5	0.5Al : 0.41P : 0.3SDA : 7.1H_2O : 0.04Cu	Al_2O_3, H_3PO_4, CuO, TEAOH (SDA), H_2O	24 h / 150 °C	Filtration, drying	Calcination, 16 h / 550 °C
CoMOF-74	3Co : 0.6dhBDC, (V DMF : V EtOH : V H_2O)	$Co(NO_3)_2$, dhBDC	24 h / 100 °C	Decanting, rotary evaporation	Vacuum Heating, 24 h / 150 °C
HKUST-1	1.17Cu : 0.5btc, (V EtOH : V H_2O)	$Cu(NO_3)_2$, btc	18 h / 110 °C	Filtration, drying	Vacuum Heating, 16 h / 120 °C
ZIF-9	3Co : 1.3PhIm, (V DMF)	$Co(NO_3)_2$, PhIm	48 h / 130 °C	Decanting, solvent exchange with $CHCl_3$, rotary evaporation	Vacuum Heating, 5 h / 130 °C

Starting with PXRD, a range from 5° up to maximum 40° angle is representative for the microporous materials. General observations regard the low background,

proof of absence of amorphous phase and a uniform width of peaks. The PXRD pattern of each solid is compared to the simulated pattern generated from cif files of single crystal data, found in databases or software libraries. As Figure 3.6 reveals, the major peaks of each XRD pattern associate well with the hkl values of the simulated pattern and show phase purity, high crystallinity and good agreement. Although shift of the major peaks is not observed, the relative intensities of the peaks within the area of 19 to 23 degrees slightly vary. In detail, the relation between the intensities of the peaks 210, 002 and 211 of the CuAlPO-5 and CoAlPO-5 XRD patterns is not the same as the relation of the corresponding peaks of the simulated AFI XRD pattern. This intensity variation can be probably due to the metal substitution, the type of substitution and the positions of the atoms in the cell.

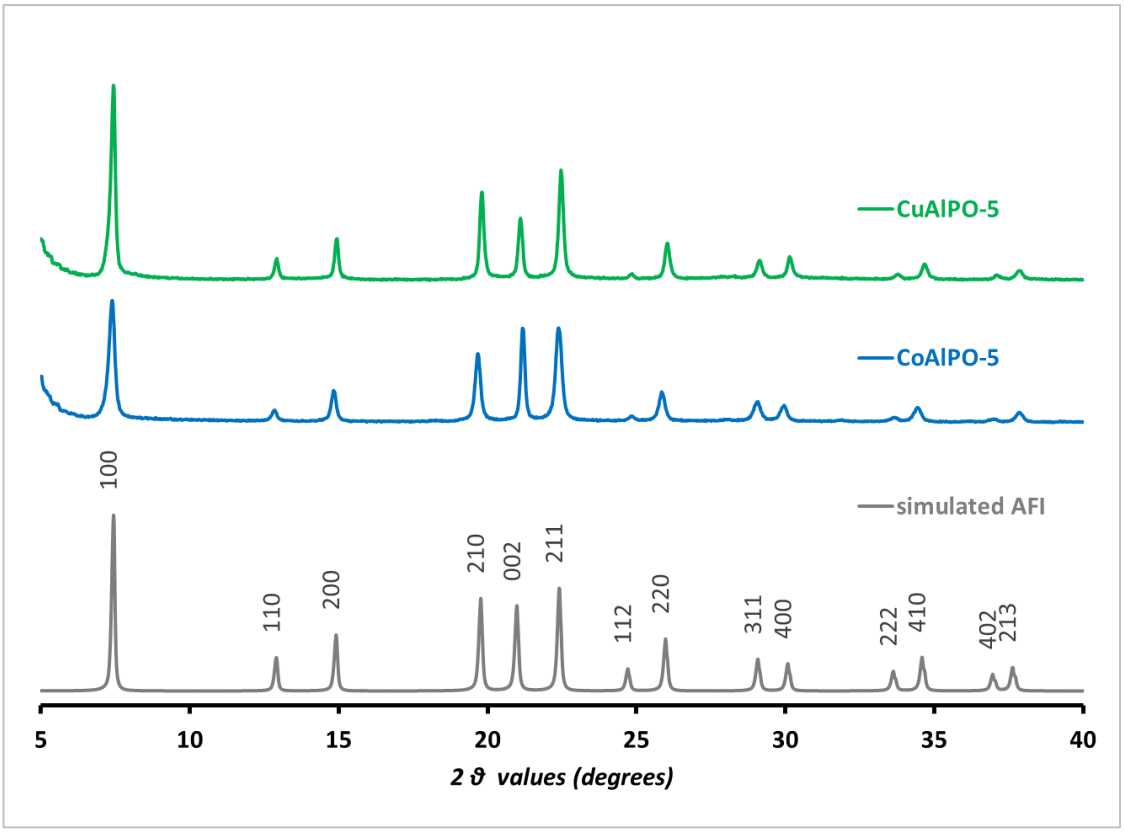

Figure 3.6 PXRD patterns of experimental data of CoAlPO-5 and CuAlPO-5 in comparison with the simulated AFI pattern.

The Rietveld refinement elucidates any cell distortion effects of the metal substitution for AlPOs and is used for the evaluation of the crystalline information. Cell distortion can become apparent by significant relative shifts of peak positions, but for minor disturbance or quantification of the distortion caused, it is possible to calculate the lattice parameters from the XRD patterns of the samples with the Rietveld Refinement technique. The refinement of the

experimental data is shown in Table 3.2 and the quality of the refinement is fine as the statistic coefficients, found in Appendix A.1, are within acceptable limits.

Table 3.2 Comparison between the simulated AFI lattice parameters and the refined experimental data of CoAlPO-5 and CuAlPO-5.

Cell parameters	Simulated data	Refined experimental data	
	AFI	CoAlPO-5	CuAlPO-5
a (Å)	13.71	13.76	13.77
b (Å)	13.71	13.76	13.77
c (Å)	8.46	8.38	8.39
$\widehat{\boldsymbol{\alpha}}$ $(\boldsymbol{deg.})$	90	90	90
$\widehat{\boldsymbol{\beta}}$ $(\boldsymbol{deg.})$	90	90	90
$\widehat{\boldsymbol{\gamma}}$ $(\boldsymbol{deg.})$	120	120	120
$\boldsymbol{\rho}\left(^{\boldsymbol{g}}/_{\boldsymbol{mL}}\right)$	1.76	1.76	1.76

Similar work has been performed for the MOFs employed in this project. As MOFs are hybrid materials, the crystals formed are not as big and well-defined as for inorganic materials and thus the XRD patterns can be of lower quality. Comparing the theoretical patterns with the experimental ones, it is obvious that HKUST-1 experimental and calculated data are in good agreement (Figure 3.7). The peaks are sharp enough to determine crystallinity, phase purity and absence of amorphous phase, but peaks have broader bases, a sign of smaller crystal sizes.

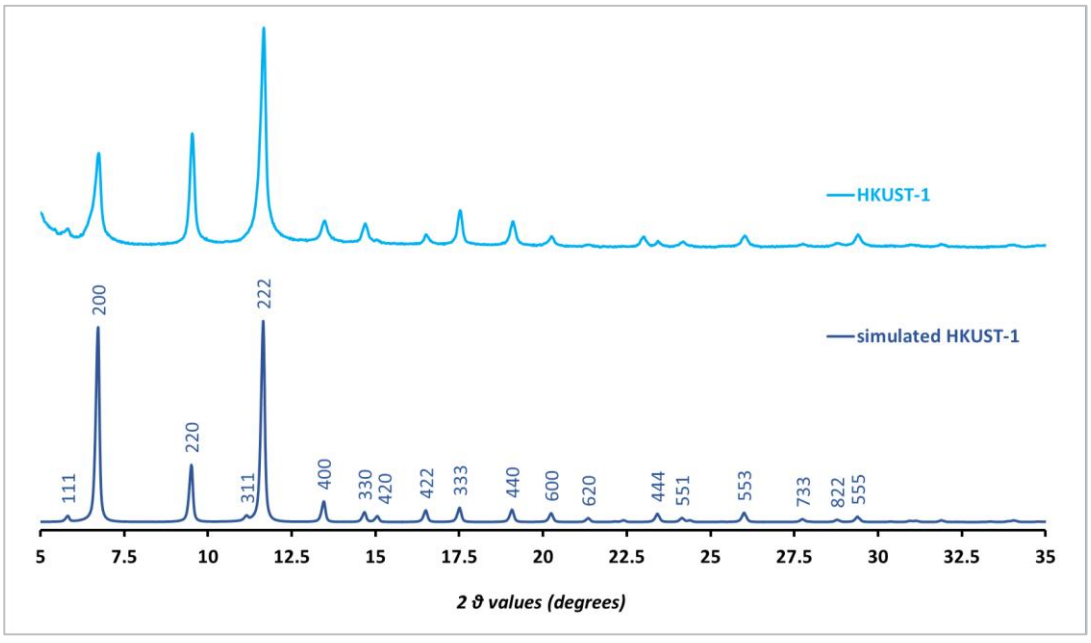

Figure 3.7 PXRD patterns of experimental data of HKUST-1 in comparison with the simulated pattern.

The CoMOF-74 XRD pattern appears in relatively good agreement with the simulated data, with decent crystallographic information, low background and correct positions of major peaks (Figure 3.8). However, the experimentally collected pattern appears poorer, with the intensities of the peaks appearing low. However, in terms of relative intensities the experimental pattern of CoMOF-74 follows the simulated one, as peaks with indices 011, 300 and 140 have comparable relation.

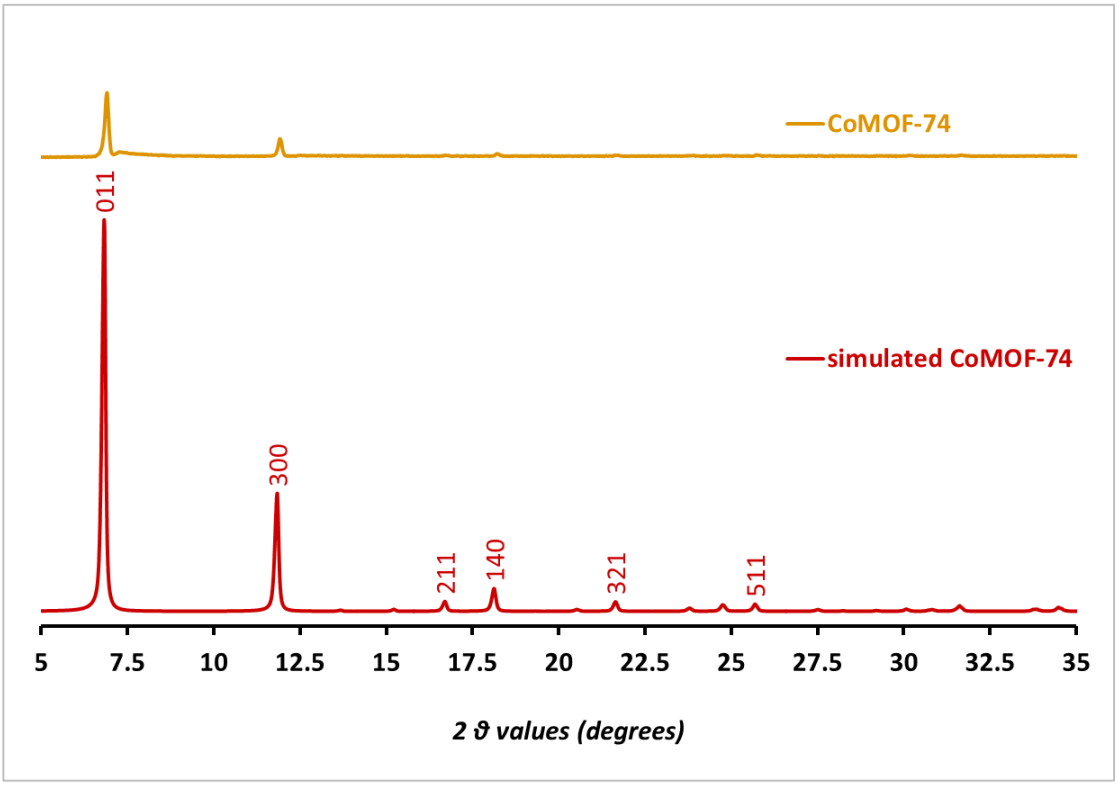

Figure 3.8 PXRD pattern of experimental data of CoMOF-74 in comparison with the simulated pattern.

ZIF-9 synthesis has been the hardest to control since it is pH dependent. The PXRD pattern of ZIF-9 in Figure 3.9 shows increased noise in the background, but relatively sharp peaks to define purity and crystallinity of the phase. The differences between the experimental and the theoretical pattern can be discerned through existence or absence of reflections and shift of the peaks. In detail, the (2,0,-1), (3,0,0) and (2,0,2) hkl reflections which are calculated in the simulated pattern appear with very low intensity in the experimental pattern, while two small extra peaks are present between the angle 12.5° and 15°. These findings could be indications of lower crystallinity or existence of impurity.

Öztürk et al. published their work on the controlled synthesis of phase-pure ZIF-9 and they reported the formation of another phase when pH is not alkaline during

synthesis.[11] They named the new phase cobalt formate coordination polymer and according to their XRD simulations, cobalt formate XRD pattern lacks the two major peaks with indices 101 and 2-10, which appear only for ZIF-9, while the new phase diffracts intensely in the angle area between 10 and 15 degrees. The present experimental pattern that has been acquired and is depicted in Figure 3.9 does not necessarily indicate the presence of cobalt formate in ZIF-9.

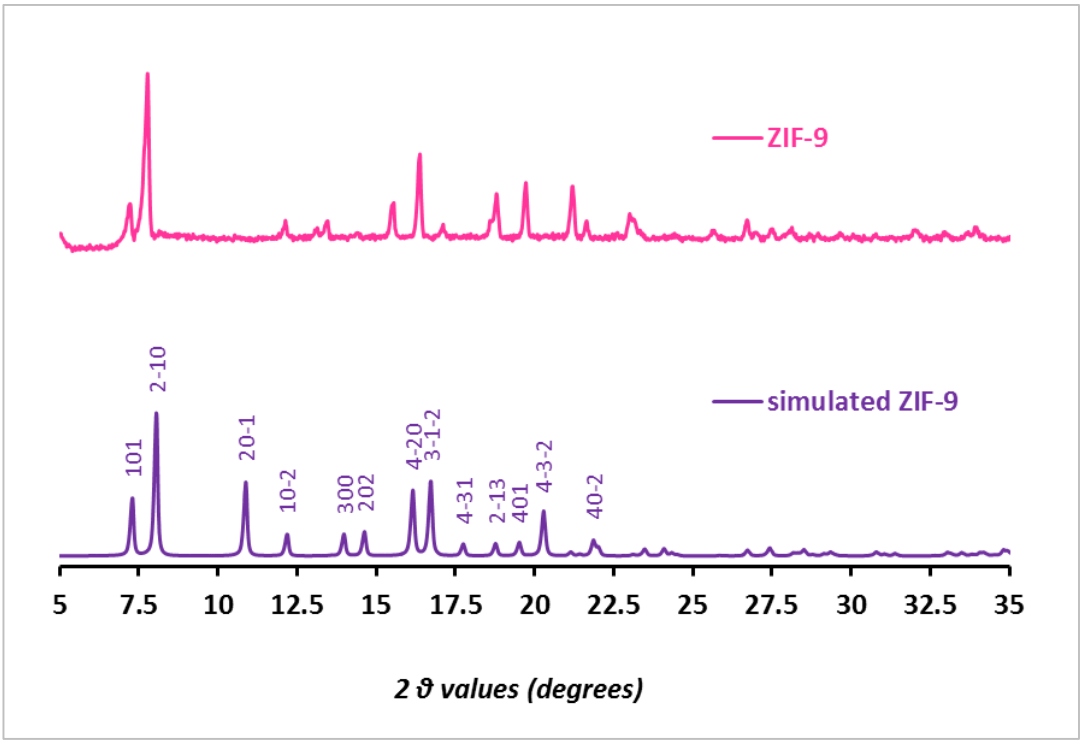

Figure 3.9 PXRD pattern of experimental data of ZIF-9 in comparison with the simulated pattern.

Rietveld refinement has been applied for the MOFs' cell parameters and, as expected, ZIF-9 cell has experienced the biggest distortions, as Table 3.3 demonstrates. However, the statistical values as shown in Appendix A.1 show that the XRD pattern corresponds to the ZIF-9 phase and data are adequately well-fitted.

Table 3.3 Comparison between the simulated lattice parameters of the MOFs and their refined experimental data.

Cell parameters	HKUST-1		CoMOF-74		ZIF-9	
	Simulated data	Refined exper. data	Simulated data	Refined exper. data	Simulated data	Refined exper. data
a (Å)	26.303	26.291	25.885	25.869	21.926	21.649
b (Å)	26.303	26.291	25.885	25.869	21.926	21.649
c (Å)	26.303	26.291	6.806	6.864	15.704	15.744
$\widehat{\boldsymbol{\alpha}}$ (***deg.***)	90	90	90	90	90	90
$\widehat{\boldsymbol{\beta}}$ (***deg.***)	90	90	90	90	90	90

Cell parameters	HKUST-1		CoMOF-74		ZIF-9	
	Simulated data	Refined exper. data	Simulated data	Refined exper. data	Simulated data	Refined exper. data
$\hat{\gamma}\,(deg.)$	90	90	120	120	120	120
$\rho\left(^{g}/_{mL}\right)$	1.032	1.039	1.181	1.178	1.340	1.352

The porosity of the materials is evaluated applying the BET method using nitrogen. The BET values are found in Table 3.4 and are indicative, while they serve comparatively. MOFs are expected to have higher surface areas and the tabulated values confirm that. The particularly low BET value of ZIF-9 though has been reported in the literature[12] and is rationalized as a result of entrapment of organic molecules in the cavity-like voids. These organic molecules may come from either or both solvent and ligands. This entrapment can be due to the aromatic rings of the organic ligands which narrow considerably the opening to the pores. This makes it hard for the confined molecules to be removed and for the nitrogen molecules to fill up the voids.

Table 3.4 BET values of surface areas of cobalt and copper substituted AlPO-5s, HKUST-1, CoMOF-74 and ZIF-9

	Surface Area / BET (m^2 / g)		Surface Area / BET (m^2 / g)
$Co_{0.04}$AlPO-5	263	HKUST-1	830
$Cu_{0.04}$AlPO-5	290	CoMOF-74	623
$Cu_{0.02}$AlPO-5	281	ZIF-9	5
$Cu_{0.08}$AlPO-5	262		

SEM images give a better impression of the morphology of the materials. The particles are adequately defined in terms of size and shape for all cases at high magnifications, while lower magnifications allow the acquisition of data, such as uniformity of particles and agglomerates. CuAlPO-5 and CoAlPO-5 are expected to form spherical crystals.[13,14] As shown in Figure 3.10, the diameters of the spherical particles range from 10 to 30 μm. The surface of CuAlPO-5 appears rough (Figure 3.10b), while the CoAlPO-5 surface is even and smoother (Figure 3.10a). High consistency and low degree of agglomeration can be deduced from the observation of the SEM images of lower magnification (Appendix A.2.1 and A.2.2).

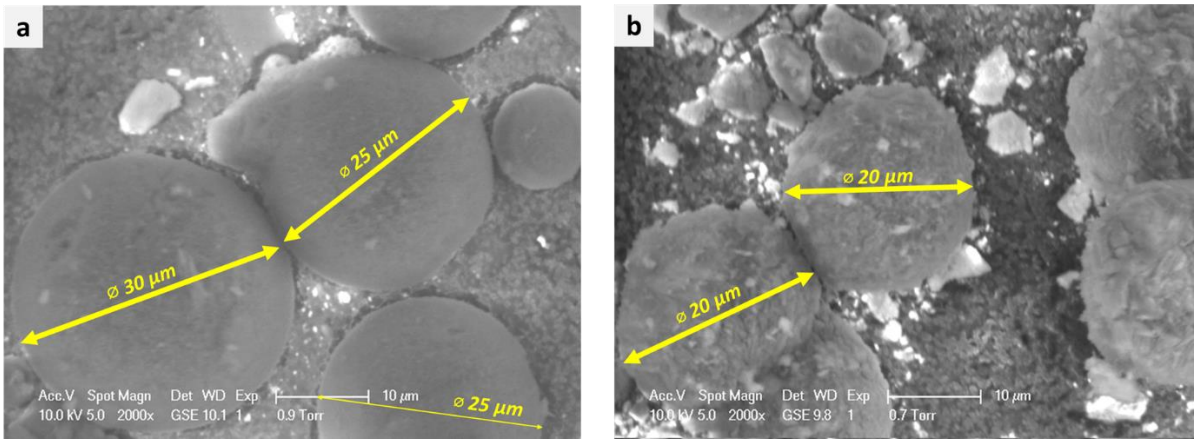

Figure 3.10 SEM images of CoAlPO-5 (a) and CuAlPO-5 (b).

HKUST-1 particles take a diamond-like shape.[15] Indeed, Figure 3.11a shows an isolated pyramidal crystal from the top and the size is below 10 µm. In Appendix A.2.3, more SEM pictures for HKUST-1 are found and regard wider areas which portray a good distribution of particles size, while the formation of agglomerates has taken place to a small extent. The SEM pictures of CoMOF-74 (Figure 3.11b) are of better quality due to the size of the particles, which have a length of 100 µm. The fibre-like shape of the particles is again in good accordance with the reported data[12] and the image of lower magnification (Appendix A.2.5) shows a controlled synthesis with a size and shape regularity and a little extent of aggregation. Finally, the shape of the CoZIF-9 particles can be described as cylindrical rods of 5 µm length, as depicted in Figure 3.11c. The SEM pictures reveal a controlled synthesis (also obvious in the pictures at Appendix A.2.4). However, ZIF-9 crystals are reported differently in the literature and there are no references with good agreement between the reported images. However, in most cases, the SEM images of ZIF-9 reveal random particles[11,16,17] rather than organized arrangements, like in this case.

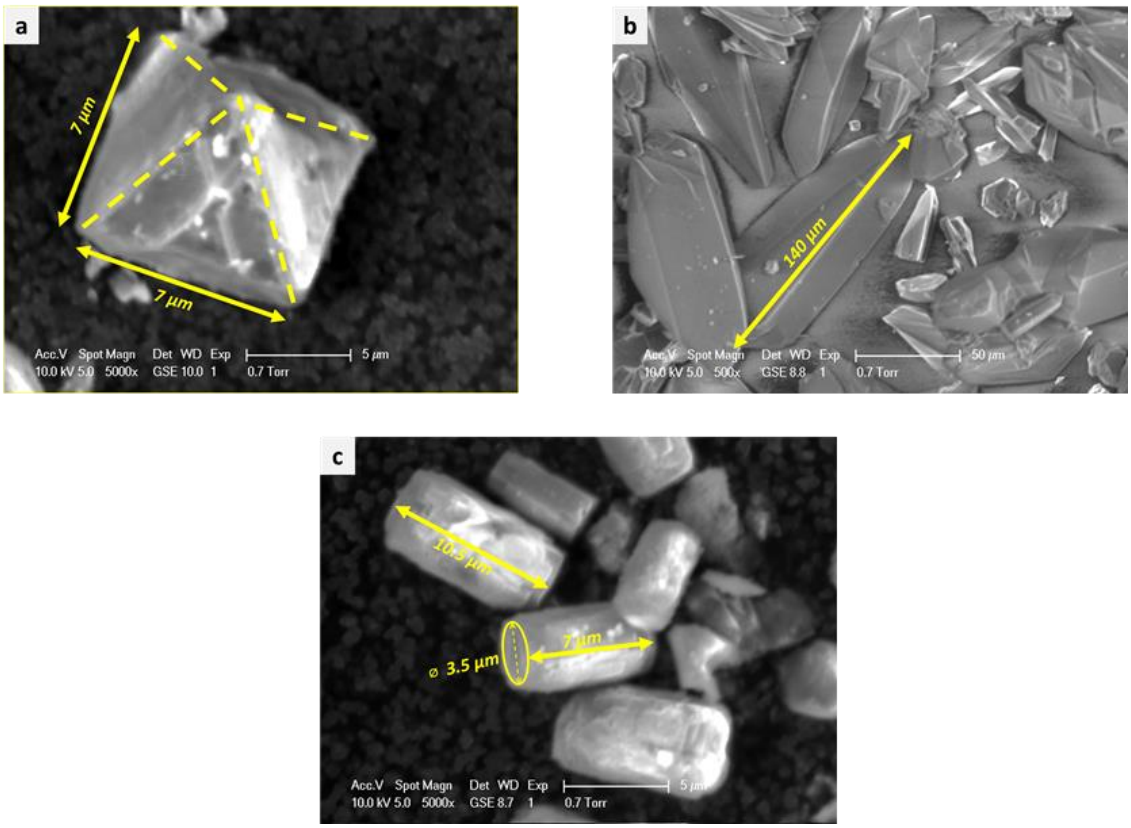

Figure 3.11 SEM images of HKUST-1 (a), CoMOF-74 (b) and ZIF-9 (c).

SEM coupled with EDX was used to confirm the incorporation of the metal in the framework. The EDX spectra were collected from more than 2 points and from areas where an agglomeration of particles was observed and surfaces seemed flat. For MOFs have a higher content of metal in the frameworks, the associated errors were lower, as tables in Appendix A.1.3 display. Representative spectra along with the image depicting the points of spectra collection are found below (Figure 3.12 and Figure 3.13).

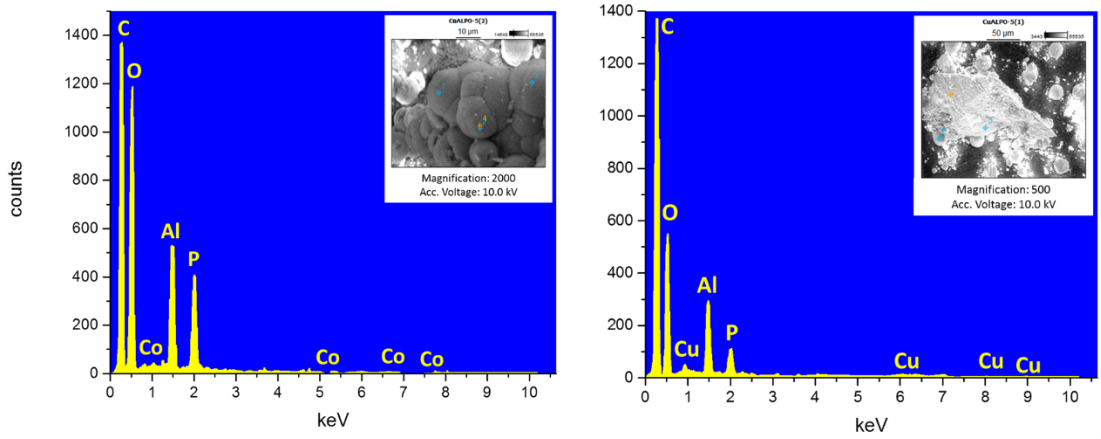

Figure 3.12 Representative EDX spectra of CoAlPO-5 (left) and CuAlPO-5 (right). Inset images regard the locations EDX data were obtained from.

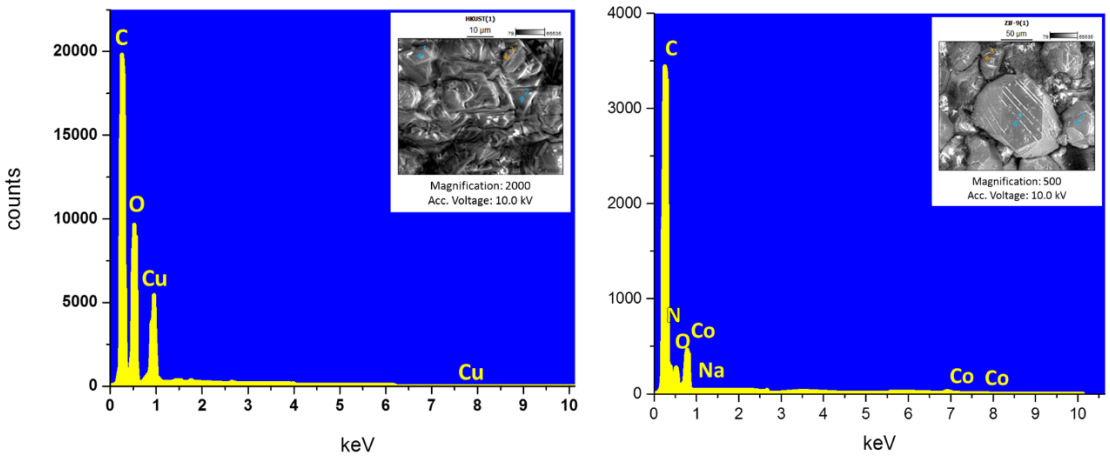

Figure 3.13 Representative EDX spectra of HKUST-1 (left) and ZIF-9 (right). Inset images regard the locations EDX data were obtained from.

As PXRD patterns are not sensitive to the incorporated metal of the materials due to low content, ICP-OES analysis is also employed to determine metal integration in the framework. ICP analysis can be used for accurate composition, which is useful for the comparison between the theoretically expected and the experimentally achieved elemental ratios. Consequently, ICP has been used to evaluate the synthesis procedure, while the elemental analysis it affords is the starting point for other techniques used further on (e.g. XPS). The ICP values are found in the Appendix A.1.4. The values tabulated in Table 3.5 highlight the differences between the experimental and theoretical ratios of some of the materials employed, as the latter have been calculated by the empirical formulas of the materials and the incorporation of metal during synthesis. It is interesting that HKUST-1 shows a higher presence of copper, while ZIF-9 shows a bigger content of carbon and nitrogen. This could be attributed to entrapment of the organic molecules (ligands and/ or solvent) inside the framework as mentioned above. The tabulated values include the calculations from the EDX data, while both techniques are used comparatively and supplementary, qualitatively and quantitatively.

Table 3.5 Elemental analysis calculations with EDX and ICP and deviation from the theoretically expected values.

	Elemental Ratio	Theoretical	EDX	ICP	Differences - EDX	Differences - ICP
$Cu_{0.04}AlPO_4$	Cu/P	0.004	0.176	0.059	340%	-47.5%
	Al/P	0.960	1.932	0.971	-101.3%	-1.2%

	Elemental Ratio	Theoretical	EDX	ICP	Differences - EDX	Differences - ICP
$Co_{0.04}AlPO_4$	Co/P	0.04	N.A.	0.039	N.A.	-2.5%
	Al/P	0.96	N.A.	1.073	N.A.	-11.8%
HKUST-1 / $Cu_3(btc)_2$	Cu/C	0.167	0.100	0.181	-40%	8.4%
CoZIF-9 / $Co(PhIm)_2$	Co/C	0.071	0.079	0.068	11.3%	-4.2%
	Co/N	0.250	0.238	0.233	-4.8%	-6.8%

3.4 Conclusions and Discussion

The basic characterization techniques of the materials consisted of PXRD, BET, SEM coupled with EDX and ICP-OES to ensure crystallinity, porosity and metal incorporation into the framework. The characterization results are a good assurance that the optimized synthetic protocols constitute recipes with correct standards for the synthesis of highly crystalline and porous materials. Having this basic characterization, the materials can be probed catalytically in the range of applications that are of interest.

Although in industrial scales, high quality of crystallinity of materials may not be as important, in science it helps understand the structural geometry and the exact positions of the atoms that may give a low or high performance. The structural and other properties before and after catalysis may reveal information about the catalytic mechanism, the nature of the active sites and possible ways to enhance the catalytic performance through the correlation of the characterization information with the catalytic behaviour. Characterization results are also useful in cases of scaling-up of synthetic methods, since it is typical for a lower degree of diffusion and mixing to occur when the quantities of the ingredients are bigger. This can be prevented by designing better how the synthesis takes place.

The synthetic protocols mentioned in this chapter produced quality materials. Overall, the accordance between the theoretical and the experimentally achieved crystalline phase is good, with satisfying porosity. All measured values appear in agreement with the values reported in the literature, as cited in the previous section. Further characterization is presented in the following chapters and

regards more specific analyses, coupled with the catalytic performance of the materials in the various applications. However, the materials properties, as measured so far, are considered able to catalyse a reaction. In particular, CoAlPO-5 has multiply been reported in catalytic applications for its oxidizing ability with molecular oxygen. Some of the substrates probed are linear alkanes,[7] cyclohexane[18] and dyes[19], where the cobalt sites appear in tetrahedral geometry, highly active and accessible due to the material's porosity, topology and highly crystalline AFI structure.

CuAlPO-5, on the other hand, has not been broadly used in catalysis or other applications. Most possible reason must be the range of different microscopic and macroscopic characteristics reported, along with the various synthetic protocols published by different research groups. The diversity of the findings reading the nature of the copper sites discourages scientists to probe its catalytic activity. However, as copper is a very useful transition metal for catalysis,[20,21] CuAlPO-5 figures as a very attractive material for oxidations in benign conditions.[22] The preparation procedure of Muñoz et al,[1] as described in the previous sections and followed in this thesis, has afforded a material with strong argumentation for an isomorphously substituted AlPO-5 with copper, as the results of XRD, XPS, SEM, ESP, FTIR support.

Moreover, HKUST-1 has been used and reported widely in catalysis.[23–26] The big surface area and porosity of the material allow access to the copper active sites and facilitate the diffusion, which makes it highly attractive for catalytic processes. The wide 1-D channels of CoMOF-74, along which chains of cobalt sites which function as open Lewis acid sites are found, has also attracted interest in applications of cycloadditions in mild conditions[12] and deNO_x processes.[27] Finally, the tetrahedral geometry of the cobalt open sites of ZIF-9 along with its stability and high metal content has drawn interest for catalytic reductions[17,28] or oxidations,[29] while its breathing effect has been proven unique for CO_2 adsorption and CO_2 catalysis.[30,31]

Summing up, the selected materials have been synthesised and characterised successfully. The copper and cobalt sites appear in different coordination or are linked with different elements in the framework, which is a useful feature to examine, along with the different topologies. The metals are known for their photoresponse in the visible spectrum and as such, photocatalytic probing with visible light is considered feasible. The former catalytic performance of all the selected materials is a strong motivation to use them in new reactions and

examine which characteristics play a more significant role or which characteristics are prone to change post-catalysis.

3.5 References

1 T. Muñoz, A. M. Prakash, L. Kevan and K. J. Balkus, *J. Phys. Chem. B*, 1998, **102**, 1379–1386.

2 D. J. Tranchemontagne, J. R. Hunt and O. M. Yaghi, *Tetrahedron*, 2008, **64**, 8553–8557.

3 C. Prestipino, L. Regli, J. G. Vitillo, F. Bonino, A. Damin, C. Lamberti, A. Zecchina, P. L. Solari, K. O. Kongshaug and S. Bordiga, *Chem. Mater.*, 2006, **18**, 1337–1346.

4 C. Dey, T. Kundu, B. P. Biswal, A. Mallick and R. Banerjee, *Acta Crystallogr. Sect. B*, 2014, **70**, 3–10.

5 L. Alaerts, E. Séguin, H. Poelman, F. Thibault-Starzyk, P. A. Jacobs and D. E. De Vos, *Chem. – Eur. J.*, 2006, **12**, 7353–7363.

6 L. J. Wang, H. Deng, H. Furukawa, F. Gándara, K. E. Cordova, D. Peri and O. M. Yaghi, *Inorg. Chem.*, 2014, **53**, 5881–5883.

7 P. Zhao, T. D. Bennett, N. P. M. Casati, G. I. Lampronti, S. A. Moggach and S. A. T. Redfern, *Dalton Trans.*, 2015, **44**, 4498–4503.

8 J. C. Tan, T. D. Bennett and A. K. Cheetham, *Proc. Natl. Acad. Sci. U.S.A*, 2010, **107**, 9938–9943.

9 S. K. Park, Z. Ni, C. P. Adrien, Y. J. Choi, R. Huang, F. J. Uribe-Romo, H. K. Chae, M. O'Keeffe and O. M. Yaghi, *Proc. Natl. Acad. Sci. U.S.A*, 2006, **103**, 10186–10191.

10 Q. Li and H. Kim, *Fuel Process. Technol.*, 2012, **100**, 43–48.

11 Z. Öztürk, J. P. Hofmann, M. Lutz, M. Mazaj, N. Z. Logar and B. M. Weckhuysen, *Eur. J. Inorg. Chem.*, 2015, **2015**, 1625–1630.

12 H.-Y. Cho, D.-A. Yang, J. Kim, S.-Y. Jeong and W.-S. Ahn, *Catal. Today*, 2012, **185**, 35–40.

13 V. Naydenov, L. Tosheva, O. N. Antzutkin and J. Sterte, *Microporous*

Mesoporous Mater., 2005, **78**, 181–188.

14 D. G. Nicholson and M. H. Nilsen, *J. Mater. Chem.*, 2000, **10**, 1965–1971.

15 M. Shoaee, J. R. Agger, M. W. Anderson and M. P. Attfield, *CrystEngComm*, 2008, **10**, 646–648.

16 M. He, J. Yao, Q. Liu, Z. Zhong and H. Wang, *Dalton Trans.*, 2013, **42**, 16608–16613.

17 L. T. L. Nguyen, K. K. A. Le, H. X. Truong and N. T. S. Phan, *Catal. Sci. Technol.*, 2012, **2**, 521–528.

18 L. Zhou, J. Xu, C. Chen, F. Wang and X. Li, *J. Porous Mater.*, 2008, **15**, 7–12.

19 D.-J. Chang, I.-P. Chen, M.-T. Chen and S.-S. Lin, *Chemosphere*, 2003, **52**, 943–949.

20 J. Clavadetscher, S. Hoffmann, A. Lilienkampf, L. Mackay, R. M. Yusop, S. A. Rider, J. J. Mullins and M. Bradley, *Angew. Chem. Int. Ed.*, 2016, **55**, 15662–15666.

21 S. R. Chemler, *Beilstein J. Org. Chem.*, 2015, **11**, 2252–2253.

22 Q. Ke, M. Wu, H. Yu and G. Lu, *ChemCatChem*, 2017, **9**, 733–737.

23 R. Yépez, J. F. Illescas, P. Gijón, M. Sánchez-Sánchez, E. González-Zamora, R. Santillan, J. R. Álvarez, I. Ibarra and J. Aguilar-Pliego., *J Vis Exp.*, 2016, e54054.

24 C. G. Piscopo, M. Schwarzer, M. Herrmann, A. Affini, P. Pelagatti, G. Maestri, R. Maggi and S. Loebbecke, *ChemCatChem*, 2016, **8**, 1293–1297.

25 A. Nagaraj and D. Amarajothi, *J. Colloid Interface Sci.*, 2017, **494**, 282–289.

26 A. Dhakshinamoorthy, M. Alvaro and H. Garcia, *Catal. Commun.*, 2017, **97**, 74–78.

27 H. Jiang, Q. Wang, H. Wang, Y. Chen and M. Zhang, *ACS Appl. Mater. Interfaces*, 2016, **8**, 26817–26826.

28 F. Bai, H. Huang, C. Hou and P. Zhang, *New J. Chem.*, 2016, **40**, 1679–1684.

29 J. Zakzeski, A. Dę bczak, P. C. A. Bruijnincx and B. M. Weckhuysen, *Appl. Catal. A Gen.*, 2011, **394**, 79–85.

30 S. Wang, J. Lin and X. Wang, *Phys. Chem. Chem. Phys.*, 2014, **16**, 14656–14660.

31 T. Toyao, M. Fujiwaki, K. Miyahara, T.-H. Kim, Y. Horiuchi and M. Matsuoka, *ChemSusChem*, 2015, **8**, 3905–3912.

Chapter 4: Cross Dehydrogenative Coupling reaction between tetrahydroisoquinoline and nitromethane

This chapter includes collaborated work with colleagues, whose contribution is appreciated and acknowledged.

Cameron P. Ross was an undergraduate project student at the University of Southampton during the academic year 2014-15 and contributed significantly to this work with the preparation of tetrahydroisoquinoline and the ^{1}H NMR analyses. Stuart J. Elliot, a PhD student at the University of Southampton, who helped with the EPR experiment performance. Peter Richardson, a research fellow in Electrochemistry at the University of Southampton during the academic year 2014-15, advised how to operate the cyclic voltammetry setup and demonstrated how to prepare and run the analysis. Arran M. Gills, a 2nd year PhD student at the University of Southampton during the academic year 2014-15, helped with the processing of the XPS data with CasaXPS software.

Part of the work described in this chapter has been drafted for publication of a paper and has been orally presented in the 18th International Zeolite Conference, in June 2016 in Rio de Janeiro, Brazil.

4.1 Cross Dehydrogenative Coupling reactions: Brief Literature Review

4.1.1 The importance of C-C couplings and transition metals

The expansion of chemical and biological molecular networks and the construction of new, stable and functional molecules for specific applications is one of the main principles and aims of organic synthesis. For this reason, a

number of reactions have been discovered and developed, which obey the main codes of addition, substitution, redox reactions etc. and have their fundamentals in the context of electrophilic, nucleophilic and radical mechanisms. Among these reactions, the formation of new C-C bonds is of great significance.

Friedel-Crafts reactions represent one of the first attempts to create new C-C bonds. Since then, the progress in this field is remarkable and its significance keeps being highlighted and was notably stressed in the two Nobel lectures of Suzuki[1] and Negishi.[2] Akira Suzuki focused on the types of C-C bonds formed in terms with the carbon orbital hybridization, emphasizing the interest in regio-, enantio- and stereo-selectivity. Ei-ichi Negishi especially focused on the cross-coupling schemes that the transition metal catalysis has realised. However, despite the magnitude of the C-C coupling reactions, the need to pre-activate and de-activate the materials in multiple steps and perform several procedures to synthesize the desired molecule inhibits the efficiency and increases chemical waste.

On the contrary, a direct coupling of two carbon atoms, without intricate pre-functionalization and addition/removal of groups on the substrates to activate these carbon atoms, would significantly reduce the synthesis steps, the chemicals used and the waste produced. This is particularly desired for carbon atoms formerly bonded to hydrogen atoms, because the C-H bonds are rather idle and difficult to activate, due to the lower electron density. This explains why the Csp^3-Csp^3 bond formation demonstrates a challenging selectivity[1] and how the use of oxidants facilitates the activation of the hydrogen atoms. Consequently, the cleavage of two C-H bonds and the concomitant C-C formation (Scheme 4.1) attracts attention and is categorized under the term of the Cross-Dehydrogenative-Coupling (CDC).

$$C-H \quad + \quad H-C \quad \xrightarrow{catalyst,\ [O]} \quad C-C \quad + \quad H_2O$$

Scheme 4.1 Simple illustration of the Cross-Dehydrogenative-Coupling.

The CDCs are usually transition-metal catalysed reactions, with the transition metals functionalizing *in situ* the C-H bonds.[3,4] Palladium, rhodium, ruthenium and copper are the most commonly reported transition metals and they are typically used as simple salts. Palladium is the most widely used in the form of

$Pd(OAc)_2$ and $PdCl_2$, probably due to its high activity and diversity[5]. In many cases, Pd is used to activate aromatic C-H bonds and Csp^2-H bonds, with the Fujiwara-Moritani coupling[6] being the most representative scheme. A more recent example is the work of Li and partners,[7] who developed an acylation reaction in the presence of $Pd(OAc)_2$ and tBHP (tertiary butyl hydroperoxide), with molecular ambient oxygen as terminal oxidant at 120 ˚C.

Rhodium and ruthenium also demonstrate good catalytic performance and have achieved high yield along with high selectivity.[8,9] Rhodium(I) and (III) have been reported to achieve couplings with Cu(II) oxidants[8,10–12] and Ag-based co-catalysts.[12] Ruthenium was successfully reported for achieving selectivity and yield for an oxidative cross-coupling reaction at 140 ˚C[12] and for a challenging activation of Csp^3-H bond of simple alkanes.[13–15] Both rhodium and ruthenium are in the forms of complexes and salts and are reported at lower stoichiometric equivalents than palladium.

Copper is more preferred for its cost and abundance.[16] This transition metal has successfully achieved couplings in the form of complexes[17] and salts,[18,19] which makes copper highly promising. Copper, as in CuBr, $CuBr_2$, CuCl, $CuCl_2$, has been extensively and effectively used for C-H activation of carbon atoms adjacent to nitrogen in the presence of tBHP.[19,20] Similar results have also been reported for the less reactive carbon atoms adjacent to oxygen with copper mainly as CuOTf[21] and $Cu(OAc)_2$.[22] CuBr and $CoCl_2$ catalytic synergy have also been reported for Csp^3-H bond activation.[23]

The reactivity of copper in the presence of molecular dioxygen urged scientists to render the reactions even greener. The problem is that copper or other metal salts and complexes cannot be recovered or easily separated from the reaction mixtures, but the use of iron nanoparticles[24] or CuBr in ionic liquid made this possible.[25] By the same token, ionic liquids,[25] electrochemical environments[26] and visible light irradiation[27] have been employed successfully and promoted electric conductivity and radical mechanisms. There are also examples of CDC reactions catalysed by non-metal systems, using hypervalent iodonium salts.[28]

With this practice, the green dimension of the cross-couplings is enhanced, because toxicity and cost are reduced. However, the problems of recovery of the catalytic system and separation of the product remain. In fact, the recovery and separation for reasons of cost and purity become urgent when transition or noble metals are included. One solution lies in the application of heterogeneous metal-

based catalysts. There are research attempts that report the use of solid materials in C-C coupling reactions and as mentioned before, Pd based heterogeneous systems are the most prominent. Table 1.3 (Chapter 1) gathers some Pd-based cross-couplings, while Table 4.1summarizes a few examples regarding CDC reactions with heterogeneous metal-based systems.

Table 4.1 Examples of C-C couplings with heterogeneous catalytic systems.

Application[REFERENCE]: (reaction, oxidant, conditions)	Catalyst system	Performance
Aldol condensation towards benzacetone[29] (90 °C, 5 h)	Hf^{4+}, Zr^{4+}, Sn^{4+} tetrahedral isolated sites on zeolite BETA	Hf^{4+}: 91% (conv.), 97% (select.) Zr^{4+}: 32% (conv.), 90% (select.) Sn^{4+}: 94% (conv.), 98% (select.)
C-C coupling between p-bromoanisole and phenylboronic acid towards p-methoxybiphenyl[30] (solvent: o-xylene, base: K_2CO_3, oxidant: atm. air, 150 °C, 5 h)	Pd^{2+} MOF	1st use: 85 % (conv.), 99% (select.) 2nd use: 74 % (conv.), 99% (select.)
C-C coupling between acetylacetone and iodobenzene towards phenylacetone[31] (solvent: o-xylene, base: K_2CO_3, oxidant: atm. air, 6 h, 60/80/100 °C)	HKUST-1	60 °C: 11% (conv.), 33% (sel.) 80 °C: 11% (conv.), 33% (sel.) 100 °C: 11% (conv.), 33% (sel.)
C-C coupling between nitroethane and aldehydes towards β-nitroalkanols[32] (solvent: H_2O or EtOH, oxidant: atm. air, 24 h, room temperature, 4-benzaldehyde A, benzaldehyde B and 4-methoxybenzaldehyde)	MOFs: Cu-dmpzc Zn-dmpzc Co-dmpzc Pd-dmpzc Cd-dmpzc (nature of active sites unavailable)	Conversion for A, B, C in H_2O/EtOH: Cu: 73/78%, 75%, 60/69% Zn: 93/98%, 86/88%, 63/67% Co: 79/81%, 71/74%, 51/52% Pd: n.a., 48/41%, 30/33% Cd: n.a., 86/79%, 68/69%

Generally, the shift towards the heterogeneous or heterogenised systems is important and precise characterisation of the active sites is useful, in relation with the diversity of the systems (supported particles, zeolites, MOFs etc.), which provides a range of different types of activity. While Pd appears in the majority of these applications, efforts to promote different metals are considerable, as shown in Table 4.1. In the heterogeneous systems, the structure and the transition metals are in close relation. Copper and zinc are attractive as metals, but their electron configuration makes it more difficult to work with zeolitic systems (Cu: [Ar] $3d^{10}$ $4s^{1}$ and Zn: [Ar] $3d^{10}$ $4s^{2}$), while MOF structures enable their use. Cobalt is one of the least responding metals in the C-C reactions, although it finds a wide catalytic applicability as a transition metal.

4.1.2 The cross-dehydrogenative aza-Henry reaction

A carbon atom found adjacent to a nitrogen atom can be easily deprotonated in the presence of a base. As the base can attract the proton attached to the carbon, the anion formed will target any acidic proton (for example, hydrogen atom of a carbonyl group) present and a coupling between the two carbons can occur (Scheme 4.2) resulting eventually in an aldol. This type of reaction is known as a Henry reaction, named after the chemist who discovered it.[33] Several variations of this type of scheme which involve nitroalkanes have been discovered since then,[34-36] with the aza-Henry reaction being one of the most important.

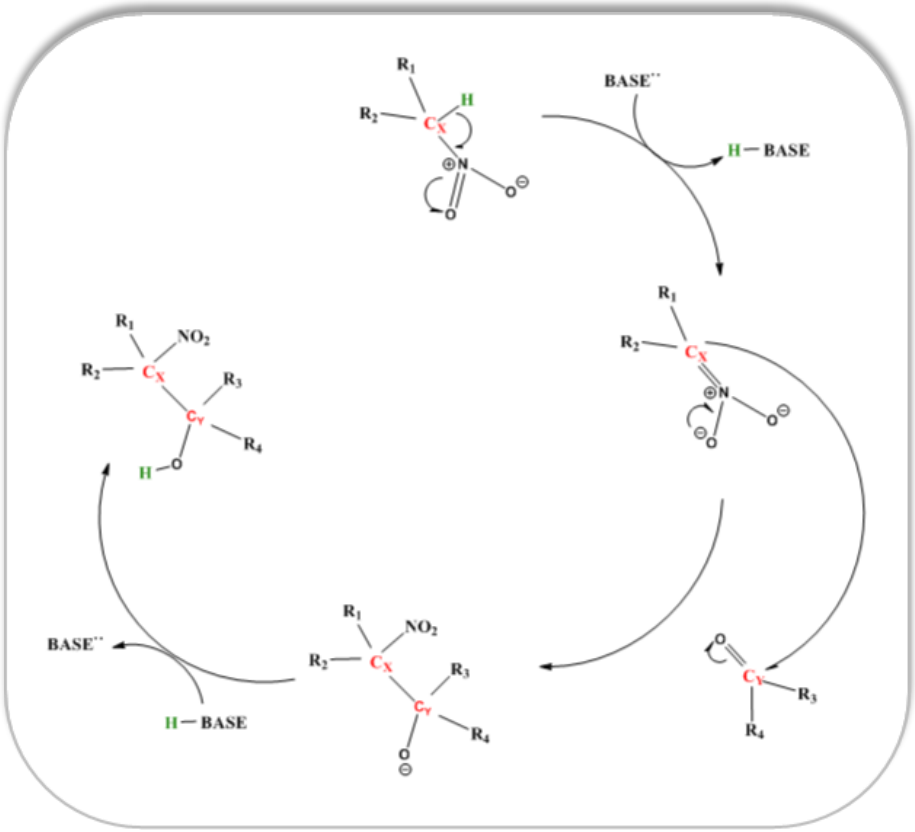

Scheme 4.2 Simple mechanistic illustration of a Henry reaction.

The aza-Henry reaction involves nitroalkanes and imines and results in the formation of β –amino acids and nitro-amines, which are fundamental functional molecular units of pharmaceutical and agrochemical value.[37,38] Most examples regard the reaction between tetrahydroisoquinolines (THIQs) and nitroalkanes; the enantioselectivity, the challenging Csp^3-H activation and the pharmaceutical activity of the THIQ derivatives[39–42] make these reactants interesting and attractive to study. The reactions usually proceed in the presence of CuBr and tertiary butyl hydroperoxide (tBHP) or molecular oxygen, ambient conditions and give a good yield of products after 6-12 hours.[43,44] Several studies in organic synthesis show interesting results, using $CuCl_2$ or $Cu(NO_3)_2$ or $Cu(OAc)_2$ for phenyl-substituted THIQ.[43,45,46]

Evidently, copper has a unique catalytic effect on this type of reaction, functionalizing the α carbons of imines and tetrahydroisoquinolines and activating the nitroalkanes simultaneously, but the exact role of the catalytic species has not been identified.[47,48] Furthermore, ruthenium has demonstrated analogous activity under aerobic conditions,[49–51] while other metals have also been positively evaluated.[52–54] The reason lies in the fact that metals can work as redox catalysts, which are highly efficient in reactions based on electron transfer.

These reaction processes are also fundamental in photochemistry, which explains why the phenyl-THIQ systems became exemplary platforms to assess photocatalysts.[27] Generally, photochemical CDC reactions have been reported widely with Ir and Ru complexes,[55–61] because these molecular entities absorb strongly in the visible light and become excited to oxidize an electron donor, such as an amine, or reduce an electron acceptor, such as oxygen, promoting redox reactions.[62] Porphyrins and organic dyes are also photoreactive, due to the strong conjugation and long excited-state lifetimes, capable of performing electron transfer and photosensitisation.[60,63–66] Some literature examples of visible-light assisted homogeneous systems are tabulated in Table 4.2

Table 4.2 Homogenous photocatalytic systems of the aza-Henry reaction (between PhTHIQ and nitromethane with atmospheric air as oxidant) reported in the literature.

Ref.	Type of catalyst and light source	Catalyst system (active sites	Catalyst quantity, % mol. substrate	Conversion / Time
[64]	Dye Green LED	Rose Bengal (n.a.)	5	100 % 10 h
[67]	Dye Green LED	Eosin Y (n.a.)	2	80 % 8 h
[61]	Transition metal complex Visible light: standard household fluorescent bulb	$Ru(bpy)_3Cl_2$ (Ru^{2+})	1	100 % 20 h
		$Ir(ppy)_2(dtbbpy)PF_6$ (Ir^{3+})	1	100 % 10 h
[58]	Transition metal complex Blue LED	Platinum (II) tertpyridyl complex (Pt^{2+})	0.25	90 % n.a.
[59]	Transition metal complex Visible light, Common fluorescent bulb, 26 W	$Ru(bpy)_3Cl_2$ (Ru^{2+})	0.2	85 % 8 h
		$Ir(ppy)_2(dtbbpy)PF_6$ (Ir^{3+})	0.2	99 % 8 h

Ref.	Type of catalyst and light source	Catalyst system (active sites	Catalyst quantity, % mol. substrate	Conversion / Time
[60]	Transition metal complex / Porphyrin complex Visible light, Xe lamp, 300 W, λ>400 nm	Palladium (II) meso-tetrakis (2,3,4,5,6-penta fluorophenyl) porphyrin (Pd^{2+})	0.05	100 % 3 h

Semiconductors have also been attractive for their properties, cost and heterogeneous nature. As expected, TiO_2 has been widely used in combination with other semiconductors to enhance visible light photoresponse. THIQ derivatives have successfully undergone photocatalytic aerobic CDCs with TiO_2 and ZnO[68] and TiO_2 and CdS.[69–71] However, not many heterogenised catalysts have been reported. Shi et al. supported ruthenium polyoxometalates on porous copper metal-organic frameworks and suggested photoactivity and synergy between Ru^{2+} and Cu^{2+}.[72] Wu et al. heterogenised $CoCl_2$ with dimethylglyoxime (dmgH), reporting it as an *in situ* photosensitizer and highly photoactive in water.[73] Other groups used successfully Au(III) on carbene[74], Pt(II) with terpyridyl[53] and Pd(II) with porphyrin,[60] establishing high-cost metals and pyridyl or porphyrin complexes for light-assisted CDCs of THIQs. Yet, the progress in this field is significant and as the interest remains high, more extensive scientific research can be achieved.

4.2 Experimental Approach

4.2.1 Objective and experimental methodology

The evaluation of porous solids based on transition metals of low cost, eco-friendliness and catalytic activity for a CDC application is under study. In detail, the aza-Henry type reaction between N-Phenyl-tetrahydroisoquinoline and nitromethane has been chosen as a representative and highly selective CDC reaction. The materials that probe the reaction are porous and crystalline, with diversity in topology and variety of active sites in terms of coordination type. CuAlPO-5, CoAlPO-5, HKUST-1, CoMOF-74 and ZIF-9 were examined in darkness and under the irradiation of white light from LEDs and were compared with the performance of other analogous heterogeneous systems, presented in Table 4.3.

Table 4.3 Heterogeneous systems for the photocatalysis of PhTHIQ and nitromethane with atmospheric air as oxidant reported in the literature.

Ref.	Type of catalyst and light source	Catalyst system (active sites	Catalyst quantity, % mol. substrate	Conversion / Time
[59]	Transition metal complex Visible light, Common fluorescent bulb, 26 W	Ru-PCP (Ru^{2+})	0.2	90 % 8 h
		Ir-PCP (Ir^{3+})	0.2	94 % 8 h
[68]	Semiconductor Halogen lamp, 11 W	TiO_2 (P25)	100	93 % 40 h
[71]	Semiconductor Blue light, λ=440 nm	CdS	n.a.	97 % 24 h
[75]	Semiconductor Visible light, Philips cool daylight energy-saving bulb, 60 W	Mesoporous graphitic carbon nitride (mpg-C_3N_4)	28.7 % wt.	100 % 22 h

Semiconductors and supported reactive metals are the usual protagonists for the photocatalysis of aza-Henry reactions. Although reactive, these materials do not answer questions regarding the structure, architecture and the nature of the active sites that the reaction may be sensitive to. It is, thus, important to test materials that provide this possibility of experimentation and characterisation for a few reasons. First, this will elucidate further the reactive species needed for this type of reaction. It will give the possibility to investigate the catalytic and photocatalytic properties of materials traditionally used as catalysts and of materials known for different uses. Testing these materials in a new application of fundamental importance in organic chemistry (with applications in the industrial sector) can give an insight whether it is necessary to shift towards new materials. Second, testing these materials in new applications may well explore and in turn expand their list of applications.

The experimental methodology followed is described thoroughly. N-phenyl-tetrahydroisoquinoline (PhTHIQ) was prepared according to the procedure described by Li et al.[76] Details of the preparation and characterization of the material are found in the Appendix B.1. All reactions were performed at room temperature and ambient pressure between 1 eq. of PhTHIQ (0.11 mmol), 1 eq. of nitromethane (1 mL) and 10% wt. of the substrate PhTHIQ (2 mg) catalyst, unless reported differently. The reaction vessels were capped glass vials and stirring is performed with simple stirrer bars at ca. 750 rpm.

The reactions in the dark were performed with 1.5 eq. tert-butyl hydroperoxide (tBHP) (0.15 mmol), while the reaction under irradiation of LED light was performed only with molecular oxygen. In the latter case, vials were capped with a rubber septum penetrated by a syringe needle to avoid the depletion of the atmospheric air, while no bubbling of oxygen had taken place. The irradiation of light was achieved with an LED strip wrapping the glass vials, as described in chapter 2.4.2 and illustrated in Figure 2.8. During all tests, samples were taken at 6 hours and 24 hours and were tested via ^{1}H NMR. The solvent (nitromethane) of the samples was removed in a rotory evaporator and $CDCl_3$ as solvent was then added.

The range of metals considered for this reaction included iron, cobalt, copper and zinc. All of the metals were used in the form of salts: $Fe(Ac)_2$, $Fe(NO_3)_3 \cdot 9H_2O$, $Co(NO_3)_2 \cdot 6H_2O$, CoF_3, $Cu(NO_3)_2 \cdot 3H_2O$, $Zn(NO_3)_2 \cdot 6H_2O$. Based on the performance of Co and Cu, as will be shown, CuAlPO-5, CoAlPO-5, HKUST-1, CoMOF-74 and ZIF-9 were being evaluated for the CDC reaction. The fresh catalysts were fully characterised, to elucidate the nature of the atoms in the materials and correlate it with the catalytic performance. Further characterisation was performed on used catalysts, to evaluate the structural distortion caused by the involvement of the solids in the reactions.

The catalysts were also evaluated in terms of recyclability and reusability. Isolation and washing of the catalytic materials had taken place before the materials were used again. In another scenario, scale-up of the reaction by 5 times was performed to eliminate catalyst loss, while recovering and reactions were left running under the typical conditions for 24 hours. Centrifugation was performed to achieve collection of the solid and separation of the supernatant liquid phase. The process was repeated 5 times and the activity of the catalysts was tested and compared after each cycle.

4.2.2 Catalytic and photocatalytic results of the CDC reaction

The catalytic reaction between PhTHIQ and nitromethane refers to ambient conditions, absence of light and presence of tBHP, along with catalytic material (Scheme 4.3). As explained, a range of salts was used for screening the best-performing metals and set against the blank reaction. The blank reaction refers to a catalyst-free reaction, in order $Fe(Ac)_2$, $Fe(NO_3)_3 \cdot 9H_2O$, $Co(NO_3)_2 \cdot 6H_2O$, CoF_3, $Cu(NO_3)_2 \cdot 3H_2O$, $Zn(NO_3)_2 \cdot 6H_2O$ against the background reaction (blank).

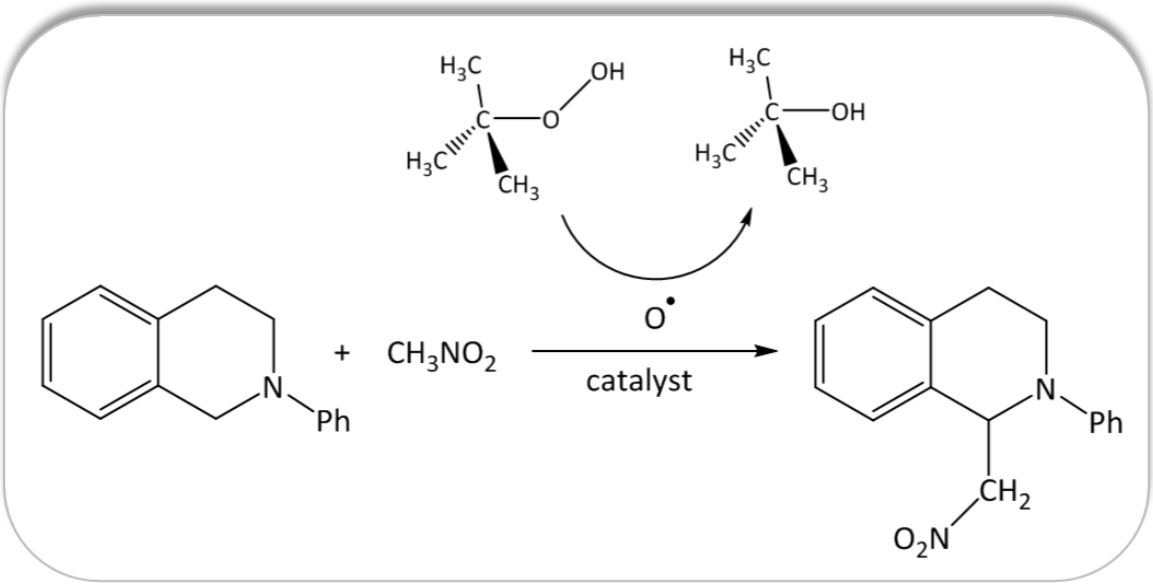

Scheme 4.3 CDC reaction between PhTHIQ and nitromethane in the presence of tBHP.

The results regard the conversion achieved after 6 hours and 24 hours of reaction in darkness and it is obvious that all metals except for zinc have performed well. Among the metals, cobalt(II) performs best achieving 45% conversion after 6 hours and 90% conversion after 24 hours. Interestingly, zinc(II) and iron(II) achieve the smallest conversions for 6 and 24 hours, while copper(II) performed better than cobalt(III) after 24 hours even though their performance at 6 hours was comparable.

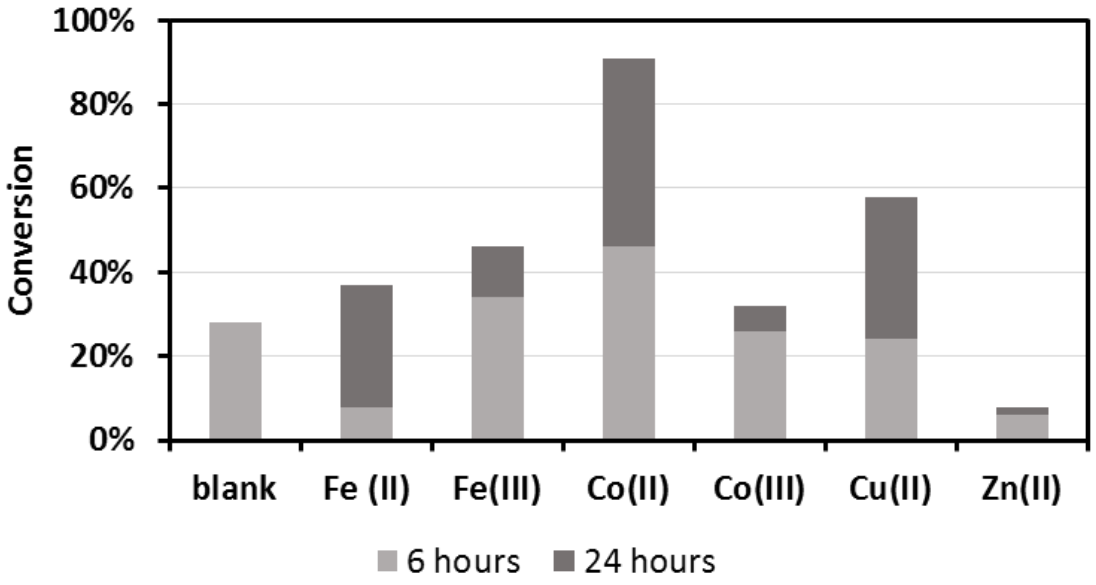

Figure 4.1 Catalytic activity of $Fe(Ac)_2$, $Fe(NO_3)_3 \cdot 9H_2O$, $Co(NO_3)_2 \cdot 6H_2O$, CoF_3, $Cu(NO_3)_2 \cdot 3H_2O$, $Zn(NO_3)_2 \cdot 6H_2O$ in the reaction between PhTHIQ and nitromethane, in dark with the presence of tBHP.

Iron(III) and copper(II) achieve respectively 34% and 24% after 6 hours of reaction, but iron stops being as active after 24 hours, achieving overall 46% of conversion against the value of 58% that the copper catalysed reaction reaches. The blank reaction shows conversion of ca. 30% over 6 hours.

While iron(III) seems active for this reaction, the ambiguous nature of iron-based porous materials from the family of AlPOs is an inhibiting parameter to opt for it. The incorporation of iron, unlike copper and cobalt, in the AlPOs in specific oxidation states is not easy to control and this can impact the characterization and analysis, despite its low hazardous character and low cost. Consequently, the shortlisted metals to examine in porous materials are copper and cobalt.

Cobalt(III) was tested as calcined CoAlPO-5 and cobalt(II) was tested as reduced CoAlPO-5 and ZIF-9. The CoAlPO-5s did not follow the trend of the corresponding salts and Co^{II}AlPO-5 performed poorly after 6 hours, thus the experiment was not carried out further using Co^{II}AlPO-5. It should be noted that the incorporation of cobalt in the AlPO-5 has been adjusted to 4%. The activity of ZIF-9 though outperforms the rest of the cobalt materials, as Figure 4.2 shows. After 6 hours of reaction, the conversion has overridden the value of 60% and after 24 hours the conversion is almost 85%.

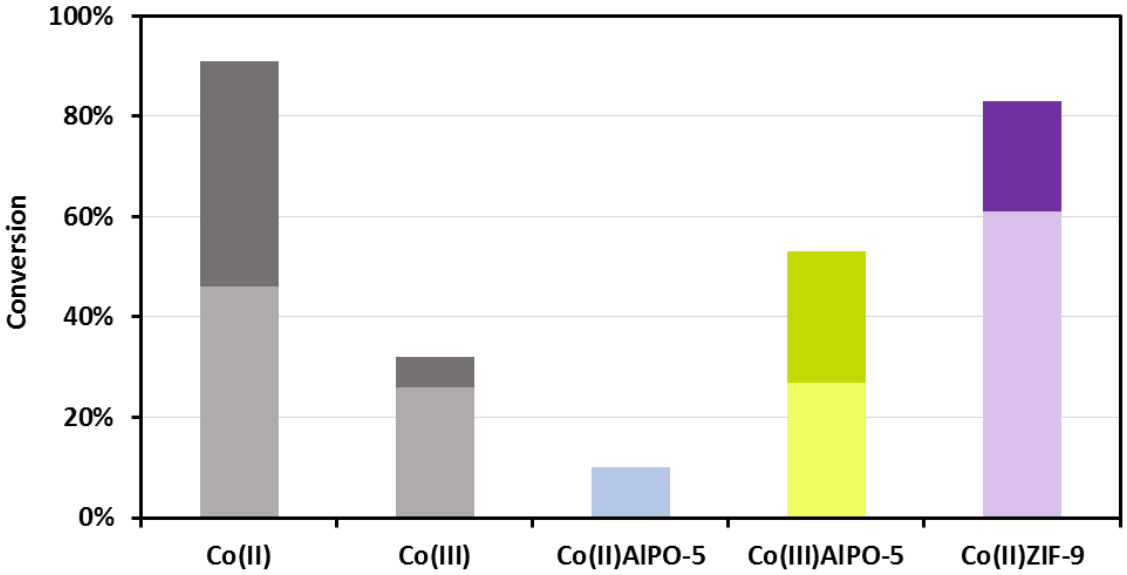

Figure 4.2 Conversions achieved with CoAlPO-5 and ZIF-9 in the reaction between PhTHIQ and nitromethane, in the dark with the presence of tBHP. Conversions are collated with the ones achieved by the salts $Co(NO_3)_2 \cdot 6H_2O$, CoF_3. The lighter shade of colours corresponds to results of 6 hours and the darker shade to results of 24 hours.

Unlike the case of cobalt, copper materials achieved higher conversions than the corresponding salts, but the values are comparable. In particular, while the copper salt achieved less than 30% after 6 hours, CuAlPO-5 achieved slightly more than 50% after 6 hours and reached a conversion of ca. 80% after 24 hours. HKUST-1 reached 80% conversion after 6 hours. Both copper based solids demonstrated ca. 80% conversion, while the copper salt approaches a conversion of 60%. Again, it should be noted that the copper incorporation in the AlPO-5 has been adjusted to 4%. The activity is depicted in Figure 4.3.

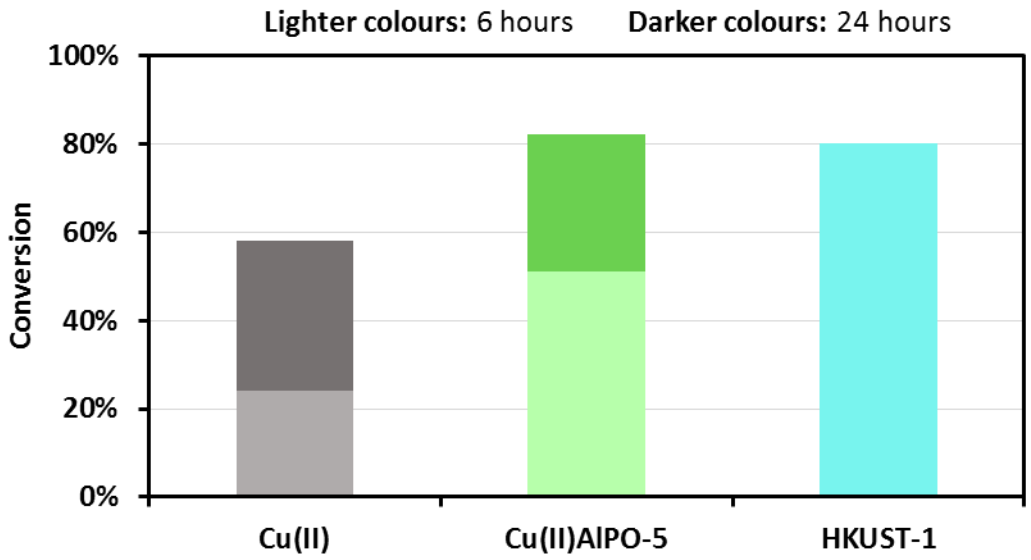

Figure 4.3 Conversions achieved with CuAlPO-5 and HKUST-1 in the reaction between PhTHIQ and nitromethane, in dark and in the presence of tBHP. Conversions are collated with the ones achieved by the salt $Cu(NO_3)_2 \cdot 3H_2O$ after 6 hours and after 24 hours.

Comparing the results among the metal-substituted AlPO-5s, CuAlPO-5 has performed best and for this reason, it is useful to understand how the copper loading may affect the activity. In the AlPO materials, the catalytic performance should be assessed in dependence on the loading of copper and cobalt as this is an adjustable quantity. Some reactions may require metal isolation or adjacent metal sites for a better performance. For this reason, molar loadings of 2%, 6% and 8% are included in the tests as Figure 4.4 demonstrates. The preparation of these materials follows the same procedure as described in Chapter 3, where the only change regards the quantity of copper precursor used. Details are given in the Appendix B.2.

However, one important point should be made here. Copper appears more reactive than cobalt in the AFI zeotype, while other zeotype structures have not been taken into consideration, such as CHA (framework code 34). However, attempts to test other zeotypic topologies, such as CHA, in order to answer better a question regarding the role of the structure, have been made as it will be introduced in the following section. However, the achievement of copper incorporation in zeotypes, as mentioned in Chapters 2 and 3, is not a common practice and the synthesis procedure followed was not trusted due to reproducibility issues. Apart from this, AlPO-34, a CHA aluminophosphate,

requires the use of HF and due to its hazard, it was preferred to omit it from the materials under study.

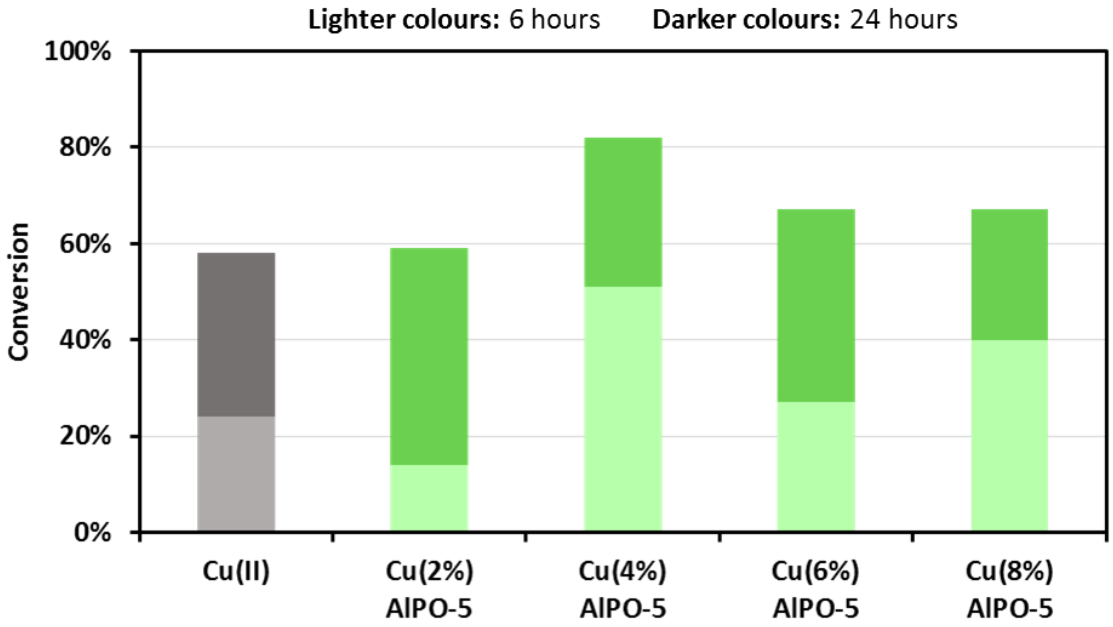

Figure 4.4 Conversions achieved with CuAlPO-5 of different metal loadings in the reaction between PhTHIQ and nitromethane, in dark and in the presence of tBHP. Conversions are collated with the ones achieved by the salt $Cu(NO_3)_2 \cdot 3H_2O$ after 6 hours and after 24 hours.

The metal loading of 4% seems optimal among the tested loadings. While there is a trend of results of 24 hours, the trend is not the same for the results that regard the conversions at 6 hours. However, in both time samplings, Cu(4%)AlPO-5 achieves the highest conversion, indicative of the fact that the activity of metal-substituted AlPOs does not depend on the metal incorporation, although one would expect that more metal content would turn the material more active. On the contrary, in AlPOs the site isolation and dispersion can make the material more effective. Similarly, the lower concentration (2%) of copper in the CuAlPO-5 may be indicative of the non-sufficient number of metal sites.

Summing up the observations, the differences between copper and cobalt materials for the reaction of PhTHIQ and nitromethane in the dark and in the presence of tBHP are interesting. Both transition metals achieve high conversions but in different contexts. In link with literature results,[47,48] copper performs well for this reaction. CuAlPO-5 is more active than Co^{III}AlPO-5, HKUST-1 achieves in only 6 hours the same conversion that CuAlPO-5 achieves after 24 hours. ZIF-9 is definitely more active than Co^{III}AlPO-5 and its performance after 6 and 24 hours is

comparable to CuAlPO-5. Putting all results together (Figure 4.5), Co^{III}AlPO-5 performs the least well. CuAlPO-5 and ZIF-9 follow in order of performance achieving conversions above 80% after 24 hours. HKUST-1 outperforms both of these achieving similar results in only 6 hours.

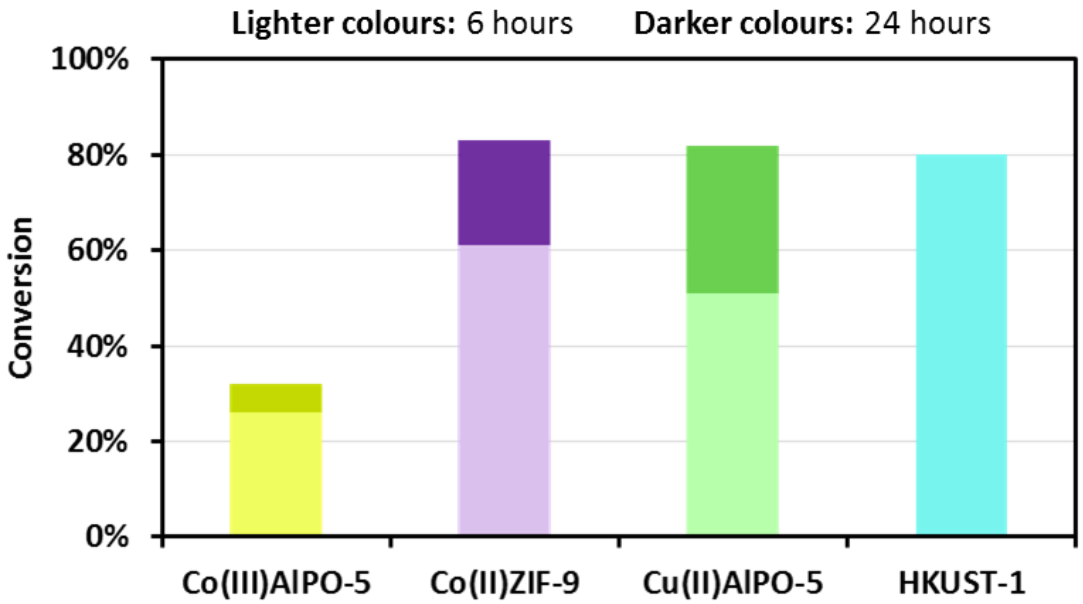

Figure 4.5 Conversions achieved with CoAlPO-5, ZIF-9, CuAlPO-5 and HKUST-1 after 6 and 24 hours of reaction between PhTHIQ and nitromethane in dark with the presence of tBHP.

The deeper investigation of the nature of the active sites of these catalysts should elucidate the properties that make HKUST-1 the best catalyst for this reaction and CuAlPO-5 and ZIF-9 good candidates. However, the interest focuses also on the photocatalytic reactivity of the materials, in order to gain a more concrete impression of their performance. The photocatalytic results follow in this section and are plotted similarly.

The photocatalytic reaction between PhTHIQ and nitromethane refers to ambient conditions, irradiation of LED white light and absence of tBHP, along with 10% of weight of PhTHIQ substrate of catalytic material (Scheme 4.4). The focus of this part of the project is the further evaluation of the previously screened catalytic solid materials in terms of photocatalytic activity. Another cobalt-based MOF (CoMOF-74) is added in order to gain a better insight of the properties in terms of comparison and to replace the poorly performing CoAlPO-5.

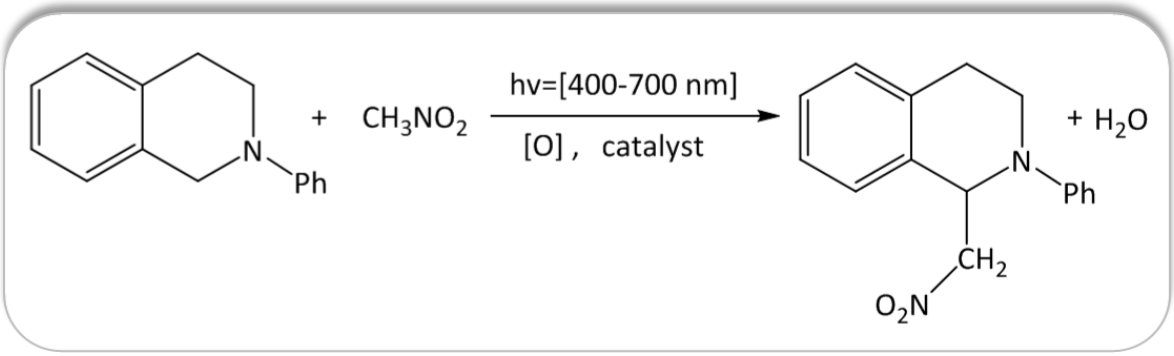

Scheme 4.4 CDC reaction between PhTHIQ and nitromethane in the absence of tBHP, in the irradiation of white light and using ambient air as oxidant.

The use of tBHP in the previous section has confirmed that the reaction proceeds with oxygen species into the reaction system. In the photocatalytic system, the oxygen source is atmospheric air, which gives the reaction a much greener dimension. A sophisticated and more complex experimental setup would possibly allow high pressure of air so that the oxygen would be dissolved in the liquid phase of the reaction and more molecular oxygen might be available in the mixture. However, this project does not provide for pressurized air in combination with light irradiation. Subsequently, a typical aerobic photocatalytic reaction is under study.

As CDC reactions respond to the need for new C-C bonds, the use of visible light is the most appealing and useful, because the organic compounds absorb minimal energy in the visible spectrum. This way, ambient temperatures are ensured and undesired photochemical or photothermal transformations that UV and IR light could cause are prevented. For this reason, it is considered important to collect the spectrum of the LED lights and ensure the absence and presence of wavelengths of interest. As Figure 4.6 demonstrates, IR and UV spectra are not included and a narrow band between the blue and green light (around 480 nm) is absent. In addition to this, regular temperature measurements during the reactions took place and excessive temperature rise was not recorded.

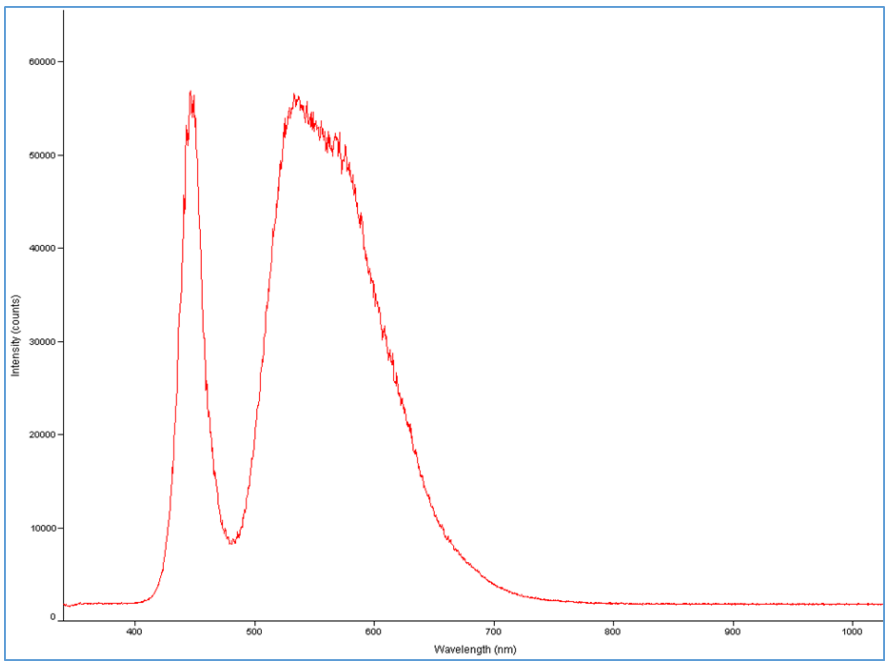

Figure 4.6 White LED light spectrum.

For the evaluation of the photocatalytic activity of the materials CuAlPO-5, HKUST-1, ZIF-9 and CoMOF-74, a blank reaction is again performed. This time, the blank reaction is performed in ambient conditions, under light irradiation and in the absence of any catalyst and of course tBHP. The blank reaction demonstrates conversion of 14% after 6 hours. Therefore, it cannot be considered that the light enhances significantly the background reaction and if enhanced activity of the catalysts is observed, then it should be attributed to the photocatalytic properties of the materials. The photocatalytic results of the materials are plotted in Figure 4.7 and regard only 6 hours of reaction.

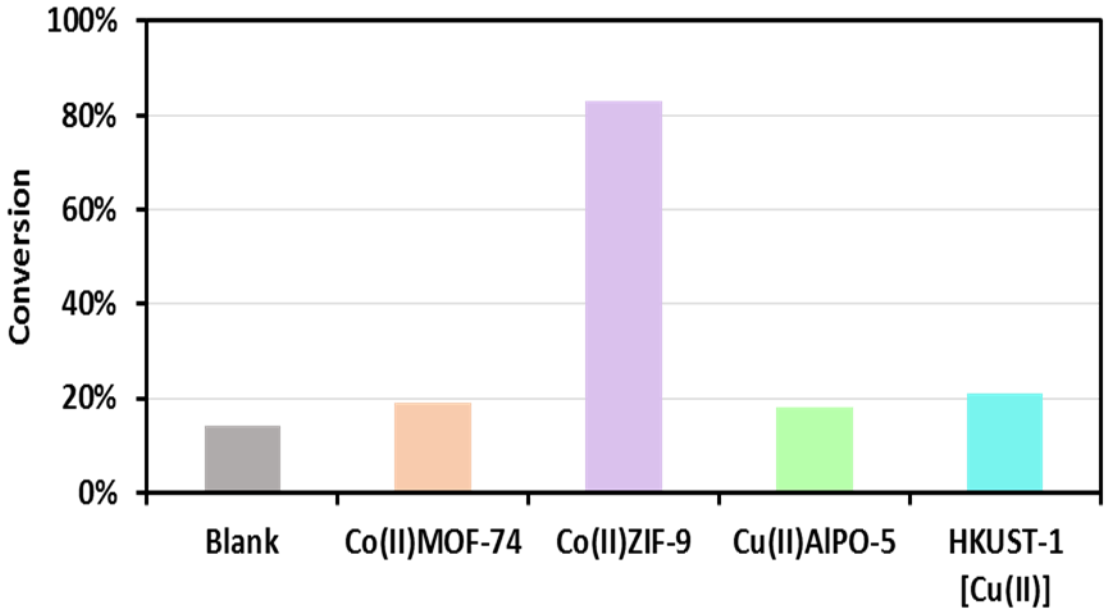

Figure 4.7 Conversions achieved with CoMOF-74, ZIF-9, CuAlPO-5 and HKUST-1 in 6 hours of reaction between PhTHIQ and nitromethane under the irradiation of visible white light and with ambient air as oxidant.

It is apparent from Figure 4.7 that ZIF-9 outperforms the rest of the materials. For ZIF-9, sampling at 6 hours shows conversion of around 80%, while it reached this level of performance in the dark with tBHP after 24 hours. The rest of the materials perform poorly in the absence of tBHP. After 6 hours, CuAlPO-5 achieves 18% in light and comparable results are obtained for CoMOF-74 and HKUST-1, with the latter performing slightly better. Focusing on ZIF-9, HKUST-1 and CuAlPO-5, a comparative plot of conversions achieved after 6 hours of reaction in the presence of tBHP in the dark and in the absence of tBHP in the light is given in Figure 4.8.

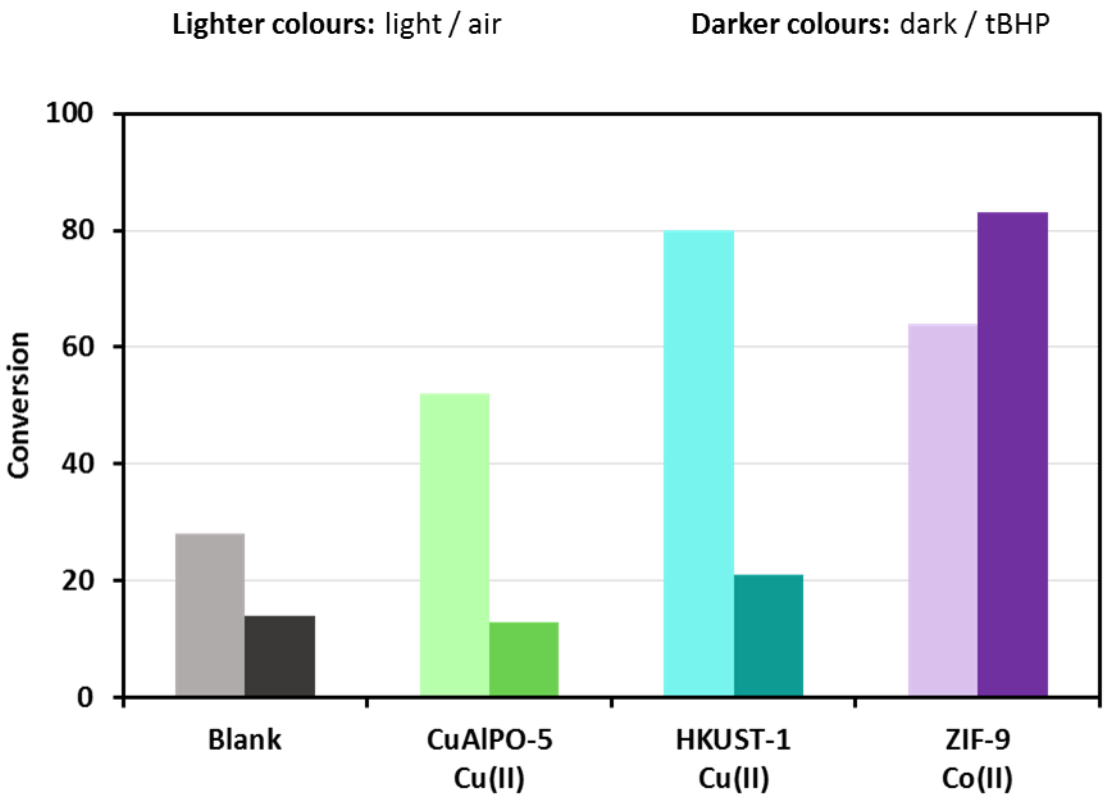

Figure 4.8 Comparative plot of conversions achieved with ZIF-9, CuAlPO-5 and HKUST-1 after 6 hours of reaction between PhTHIQ and nitromethane, in the absence tBHP with light and air (left) against dark with tBHP (right).

While HKUST-1 performs in conditions of darkness and in the presence of tBHP better than ZIF-9 and CuAlPO-5 by ca. 20% and 35% respectively, ZIF-9 proves itself a true photocatalyst, performing better than HKUST-1 and CuAlPO-5 by 60% and 70% respectively in conditions of white light and absence of tBHP. To understand further how tBHP, air, light and dark affect the performance of the catalysts, the catalysts were further submitted into the CDC reaction under different conditions. Initially, an experiment took place in the dark in the absence of tBHP, to understand whether the catalysts are able to activate PhTHIQ and nitromethane in the absence of light and readily available oxidant species from tBHP. Another experiment was carried out in the light and with tBHP in order to understand which catalyst performs best when all conditions are optimal. The results are compared in form of plot in Figure 4.9.

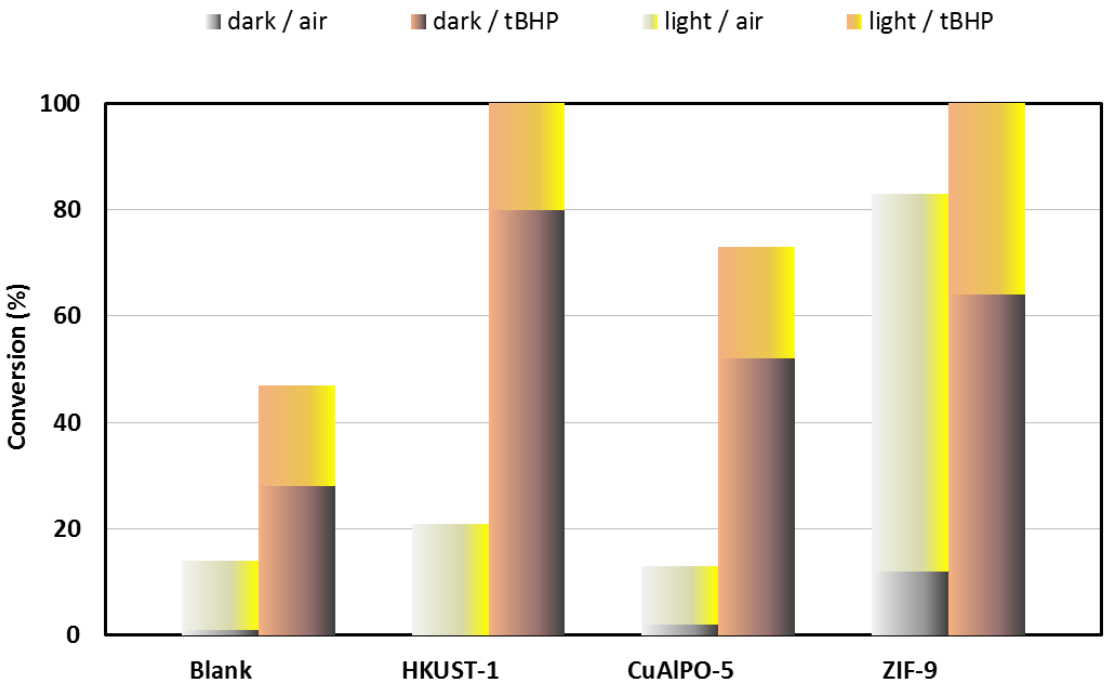

Figure 4.9 Comparative plot of conversions achieved with HKUST-1, CuAlPO-5 and ZIF-9 after 6 hours of reaction between PhTHIQ and nitromethane, tested in conditions of tBHP in dark and light and in conditions of air in dark and light.

Among the catalysts, CuAlPO-5 fails to achieve 100% of conversion when there is adequate availability of oxidant (tBHP) and light, reaching an overall maximum of 73%. HKUST-1 and ZIF-9 have finished the reaction after 6 hours when both tBHP and light are available. Impressively, ZIF-9 achieves the best conversion of over 10% in the worst conditions (absence of tBHP and darkness) among the catalysts, when the blank reaction is only 1%. Interestingly, HKUST-1 and CuAlPO-5 do not register any special activity under these conditions.

4.2.3 Investigation of different aspects of the CDC reaction

Working with MeAlPO and MOF materials affords a range of catalytic parameters that one should look into. Regarding MeAlPOs, the main catalytic properties are redox activity and Brönsted acidity. Regarding MOFs, the organic ligands may also affect the catalytic activity of the material. In order to realise whether these aspects should be taken into consideration in the performance, a set of materials are catalytically probed, in order to evaluate if acidity and organic ligands may favour the CDC reaction between PhTHIQ and nitromethane.

Initially, silicon substitution in the AlPOs and MeAlPOs is known to afford acidity, either in terms of strength or number of acidic sites. AlPO-5 is considered ideally a framework net of charge and, in the absence of any metal, no conversion is expected with tBHP in the dark. However, experimentally it is possible for the neutral AlPO-5 to have crystalline defects, which could afford a little acidity on the surface of AlPO-5.

The rule of thumb is that the less crystalline a material is the less acidity it displays, which explains why amorphous materials, like silica, are considered non-acidic. However, in crystalline materials, the ratio between the Si and Al influences the acidity. Generally, the silicon substitution leads to catalytically active Brönsted acidity, since the alteration of Si, Al, P tetrahedral requires a charge compensating proton. According to this, the incorporation of silicon in AlPO-5 is expected to raise acidity and SAPO-5 is expected to turn more acidic than AlPO-5.

The parameter of the topology also plays a significant role here. In crystalline materials, the T-O-T links influence the energy of the hydrogen attachment on the oxygen and the bigger the angle is, the easier the deprotonation occurs, which increases the acidity of a material, [77,78] while the Si/Al ratio is also linked with the geometry.[77] In detail, the AFI topology is supposed to uptake more silicon than the CHA topology. The former framework is expected to favour higher silicon substitution in contrast to the isolated acid sites of the CHA framework.[79] Employing FTIR spectroscopy, the distinction between the intermediate acidity of SAPO-5 and the higher acidity of SAPO-34 has been measured.[80]

Apart from the level of acidity, which is connected with the number of the acid sites, the strength of acidity is also affected. For example, a very strong acidity may reduce the desorption rate of a reactant, a mild acidity well-dispersed on the surface can promote the catalytic performance and a weak acidity can eliminate the selectivity.[81,82] For example, an extensive Si substitution may lead to lower number of acid sites, but stronger local acidity at the edges of the Si islands, due to defected silanol species, such as terminal, vicinal, geminal or nest.

As explained before, SAPO-34 is a silicoaluminophosphate of CHA architecture, which permits the isolated silicon sites and thus, stronger acidity is expected. Finally, if acidity or combination of acidity and redox properties play a significant role, silicon substituted CoAlPO-5 should afford higher conversions. In that case,

the performance should be enhanced significantly and this would lead to the assumption that the specific CDC reaction is largely benefitted by this parameter.

Subsequently, AlPO-5, SAPO-5, SAPO-34, Co^{II}AlPO-5, Co^{III}AlPO-5 and Co^{II}SAPO-5 are synthesised with the silicon-substituted materials arranged to have a comparable Si content. All materials are structurally characterized and employed for the catalysis of the reaction between PhTHIQ and nitromethane, in the dark and in the presence of tBHP at ambient conditions. Details concerning the synthesis and the characterisation are found in the Appendix A.5 and B.3. The results are plotted in Figure 4.10 and evaluated qualitatively.

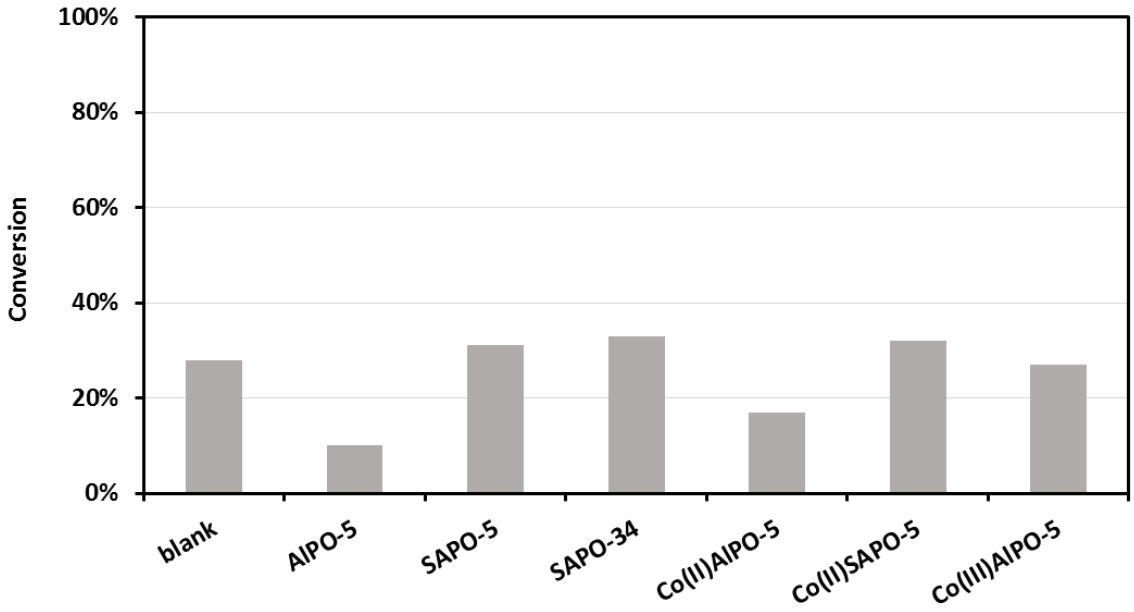

Figure 4.10 Conversions achieved after 6 hours with AlPO-5, SAPO-5, SAPO-34, Co^{II}AlPO-5, Co^{III}AlPO-5 and Co^{II}SAPO-5 in the reaction between PhTHIQ and nitromethane in dark and in the presence of tBHP, plotted for qualitative reasons.

It can only be inferred that Brönsted acidity is helpful for the CDC reaction under study since the observed benefit in terms of conversion is not significant comparing between the silicon-substituted materials and the blank reaction. However, the difference between SAPO-5 and SAPO-34 is not important, thus intermediate or stronger Brönsted acidity does not have a great impact. Thus, there is not a valid reason to look deeper into the number of acid sites or their strength. Similarly, the combination of silicon and cobalt does not prove a strong parameter that could boost the performance, since CoAlPO-5s and CoSAPO-5 perform similarly. Generally, the fact that Brönsted acidity plays its role in the reaction has been reported previously[83–85] and its ascertainment may prove useful

for mechanistic comprehension. Supplementary to this, MOFs are characterised by Lewis acidity and therefore, it is useful to take into consideration that the CDC reaction may discriminate between the two different types.

The shortlisted MOFs employed in the reaction in conditions of darkness and in the presence of tBHP for their performance are ZIF-9 and HKUST-1. The organic ligands of ZIF-9 and HKUST-1 are phenyl imidazolate or benzimidazolate (PhIm) and 1,3,5-benzene tricarboxylate (BTC), respectively. The ligands have been weighed at 10% of the substrate of PhTHIQ and been added in the reaction mixture, in ambient conditions of darkness and tBHP presence. The results for 6 hours are plotted in Figure 4.11 and are juxtaposed with the results of the respective MOFs.

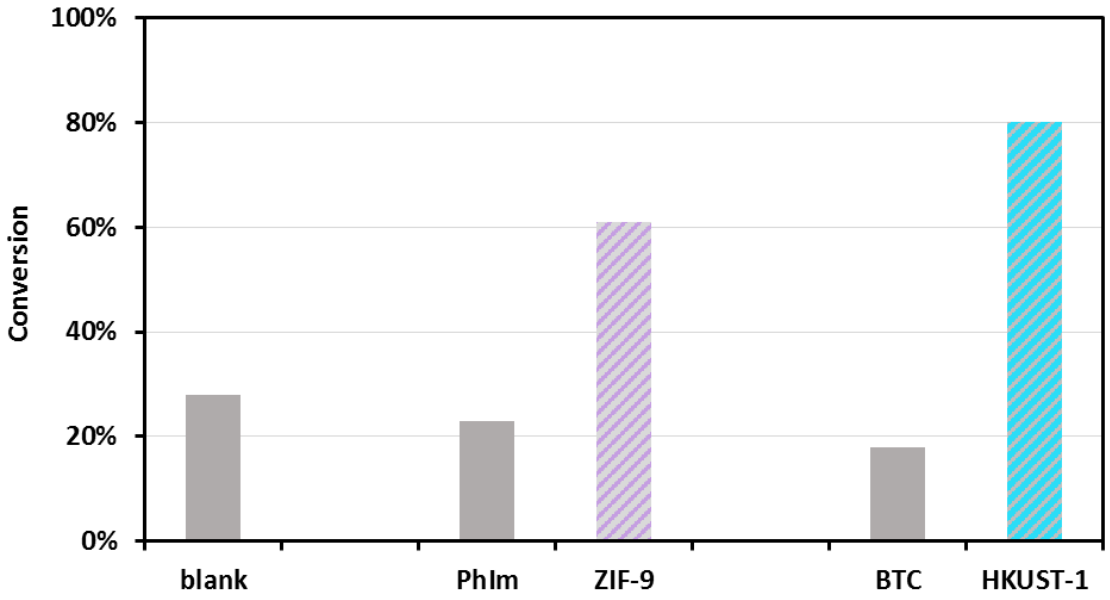

Figure 4.11 Conversions achieved by the ligands of ZIF-9 (PhIm) and of HKUST-1 (BTC), contrasted to the conversions achieved by ZIF-9 and HKUST-1 after 6 hours of reaction between PhTHIQ and nitromethane in dark and in the presence of tBHP.

It is obvious that the catalytic effect of the ligands is not considerable, compared with the effect that the MOFs cause. ZIF-9 achieves 61% conversion in 6 hours whereas the ligand PhIm achieves just over 20%, comparable with the background reaction in dark and with tBHP. The results of HKUST-1 and its ligand also lead to the same conclusion, with the ligand BTC achieving 60% less conversion than HKUST-1. Hence, the organic molecules do not enhance considerablhy the CDC reaction under study. However, since ZIF-9 performed excellently as a

photocatalyst, further experiments were carried out with PhIm and the results are plotted in Figure 4.12.

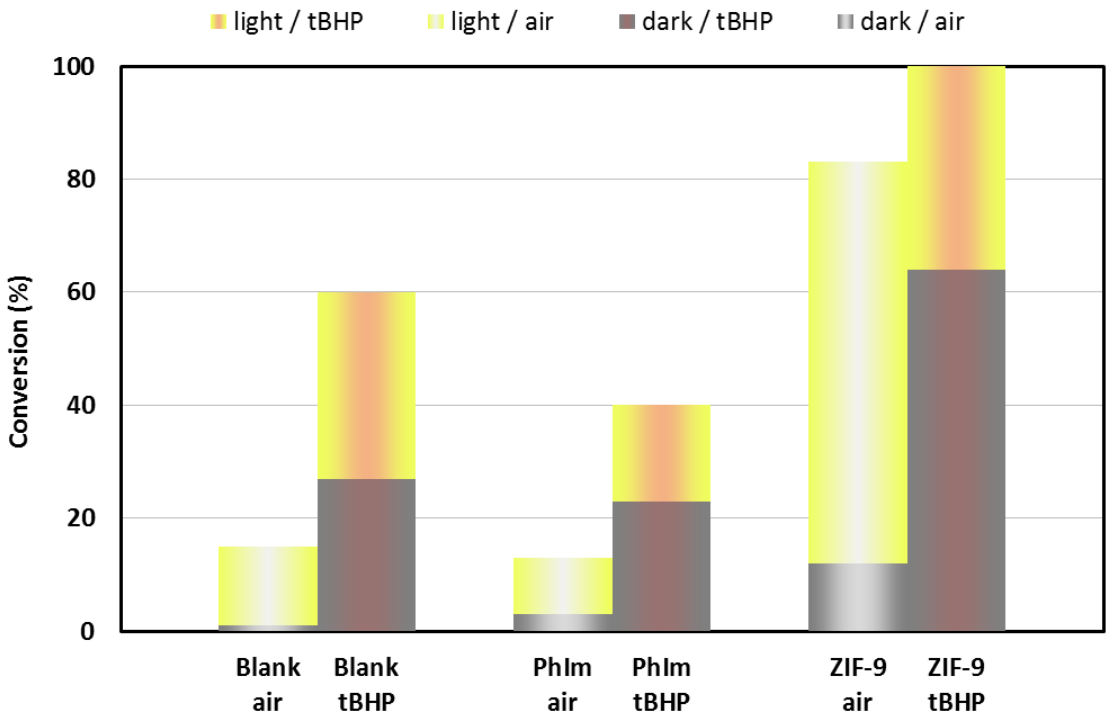

Figure 4.12 Conversions achieved with PhIm and ZIF-9 in dark and light, air and tBHP after 6 hours of reaction between PhTHIQ and nitromethane.

Values of Figure 4.12 confirm that PhIm should not be considered as taking active part in the reaction. Conversion achieved with PhIm when conditions are optimal (tBHP and light) does not exceed 40% while conversion achieved in the worst conditions (dark and air) are comparable with the blank reaction. By the same token, ZIF-9 converts PhTHIQ by ca. 60% in tBHP and dark, while PhIm exhibits similar results as the blank in the same conditions. Overall, PhIm along with BTC is not catalytically active for the CDC reaction between PhTHIQ and nitromethane and both organic molecules play the role of ligand of metallic sites in HKUST-1 and ZIF-9. Therefore, they only achieve heterogeneity of the MOFs, which is being tested in the next section.

4.2.4 Heterogeneity and reusability of the catalytic materials

The heterogeneity and reusability of the catalytic materials are of major importance. One of the main advantages of heterogeneous porous solids used as catalysts is their ability to be recovered and recycled in the reaction, without the loss of activity being an obstacle to their usage. As mentioned in section 4.2.1, two experimental methods are followed; either isolation after one reactive cycle,

washing and reuse of catalysts or continuous use for 24 hours repeated 5 times in a row. The focus remains on the best-performing catalysts: ZIF-9, CuAlPO-5 and HKUST-1.

In the case of reactions in the dark and in the presence of tBHP, the catalysts were collected by centrifugation, washed several times with solvents, filtered and let dry. CuAlPO-5 was washed with deionized water, HKUST-1 was washed with ethanol and water and ZIF-9 was washed with methanol. The choice depends on the solvents used in the synthesis of the catalysts. The MOFs were additionally heated under vacuum to restore the porosity by removing solvent molecules and to expose copper sites in the case of HKUST-1. The catalytic results of the materials regard the first and the second cycle and are plotted in Figure 4.13.

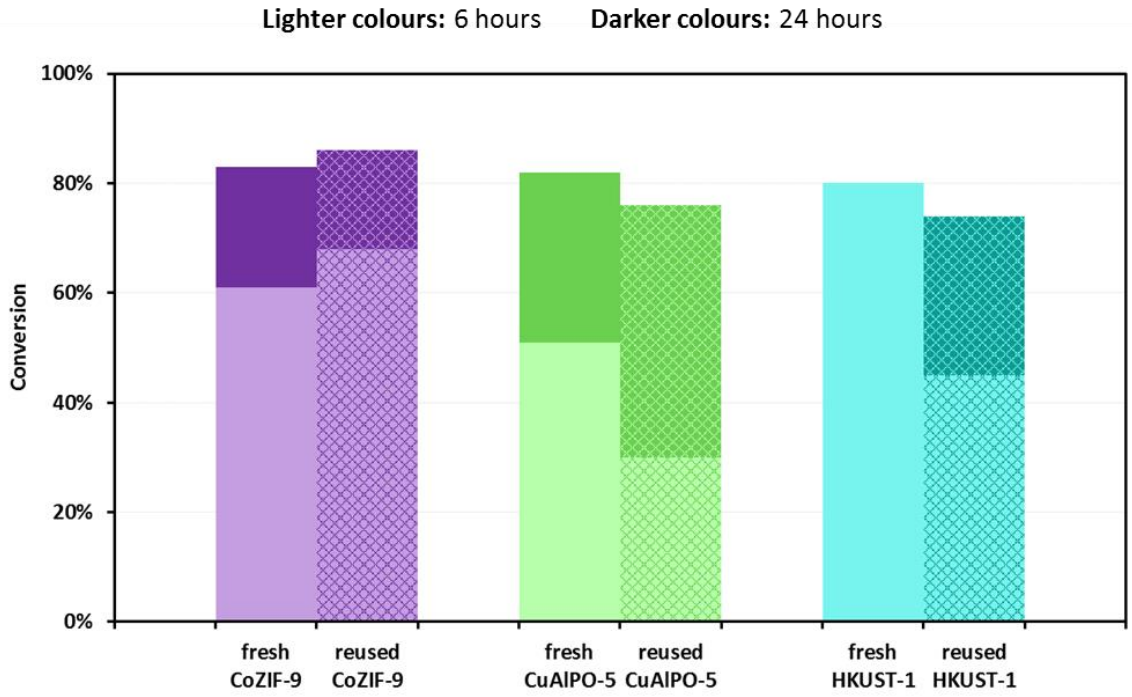

Figure 4.13 Reusability test of ZIF-9, CuAlPO-5 and HKUST-1 regarding the CDC reaction between PhTHIQ and nitromethane, in the presence of tBHP and in the dark. Conversion obtained from fresh and reused catalysts are collated.

The biggest loss of activity is observed for HKUST-1. After 6 hours during the second cycle, HKUST-1 and CuAlPO-5 achieve approximately half the conversion they achieved as fresh, but the overall loss is no more than 5%. Unlike CuAlPO-5 and HKUST-1, ZIF-9 seems to give enhanced results of conversion during the second cycle, for both sample timings at 6 and 24 hours. Although washing of

the catalyst took place, it is likely that further washing might be needed to remove active intermediates from the surface of ZIF-9.

Leaching of the metal after one use might be another factor to examine and HKUST-1 seems the best option to conduct analysis because it is a MOF with high copper content and after one use the material might dissociate and copper may escape into the reaction mixture. For this reason, the supernatant of the solution of the reaction with HKUST-1 was collected and submitted to ICP analysis after centrifugation. Processing of the ICP results showed a very low degree of metal leaching (ca. 5 μg of copper in 1 mL juxtaposed with the starting value of 550 μg of copper in 1 mL).

While the decay of the scaffolds is possible to occur mechanically due to grinding with the magnetic stirring, the process of regeneration might also affect the performance of the materials. For this reason, fresh HKUST-1 was submitted to the regeneration process (filtration and washing, drying, heating under vacuum) without having first taken place in the reaction and is called “processed”. The tabulated results in Table 4.4 suggest that the regeneration method for recovery may contribute to activity loss.

Table 4.4 Values of conversion obtained after 6 and 24 hours of the CDC reaction between PhTHIQ and nitromethane in the dark and in the presence of tBHP with fresh HKUST-1, processed HKUST-1 and reused HKUST-1.

	Conversion at 6 hours	Conversion at 24 hours
Fresh HKUST-1	80%	N.A.
Processed HKUST-1	49%	79%
Reused HKUST-1	45%	74%

For this reason, another approach was selected for testing the reusability of ZIF-9 in the case of LED light-assisted reaction and in the absence of tBHP. The reaction was scaled-up 5 times in terms of mass and volume. The catalyst was collected by centrifugation after 24 hours and was added to a fresh reaction mixture after each 24-hour cycle. This procedure was repeated 5 times and no regeneration of the catalyst took place. The results in Figure 4.14 regard the conversion obtained after the 5th cycle and is juxtaposed to the results obtained with the fresh ZIF-9.

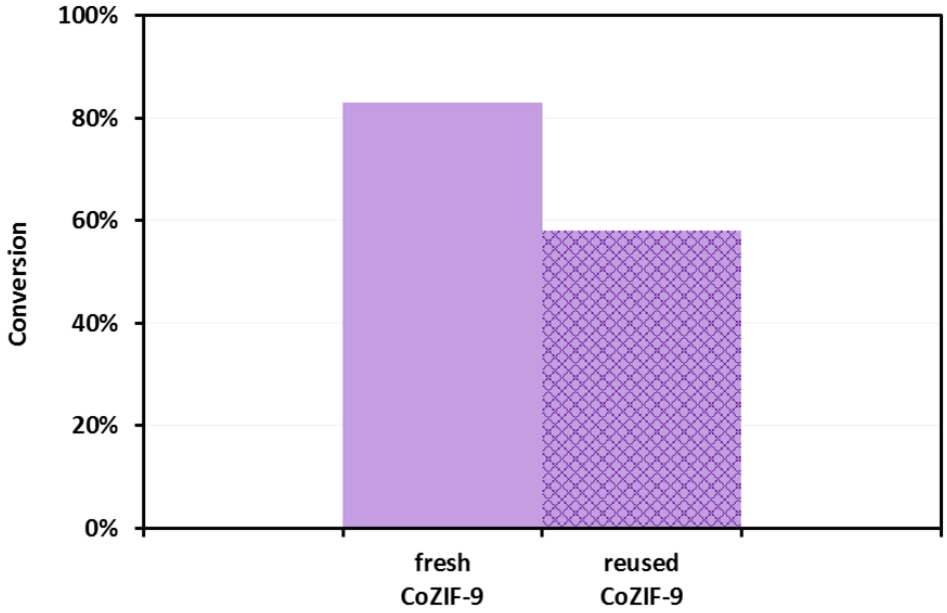

Figure 4.14 Reusability test of ZIF-9 regarding the CDC reaction between PhTHIQ and nitromethane, in the absence of tBHP and under the irradiation of white LED lights.

Impressively and interestingly, ZIF-9 shows a little over of 20% loss in the performance after 5 cycles in comparison after 24 hours of reaction. Overall, the results show that the catalytic materials can be reusable and are heterogeneous and remain active after use in the CDC reaction between PhTHIQ and nitromethane, in conditions of dark or light, in the presence or absence of tBHP. Post-catalysis characterization also takes place and observations are described in a following section, in order to evaluate the structural distortion of solids after the reaction. With ZIF-9, CuAlPO-5 and HKUST-1 having performed well in this CDC reaction, further characterisation of fresh materials is presented, in order to elucidate better the properties of the materials that may affect their catalytic and photocatalytic performance.

4.3 Characterisation of ZIF-9, HKUST-1 and CuAlPO-5

Focusing on the best performing catalytic materials, ZIF-9, HKUST-1 and CuAlPO-5, for the catalytic and photocatalytic CDC reaction between PhTHIQ and nitromethane, further characterisation takes place and is presented in this section. The elucidation of the nature of the metal sites relies on techniques such as DR UV-VIS, XPS and EPR, which reveal information regarding the oxidation state and the coordination of the atoms under examination. DR UV-VIS is also employed in order to recognise the differences in the photoresponse of the

materials. Intense or weak absorbance of photons of certain wavelengths will be used as information to explain the photocatalytic properties of these materials.

In the attempt to understand deeper the factors that make these materials photocatalytically active for the C-H activation, cyclic voltammetry is also employed. Redox potentials of the photocatalysts are frequently associated with redox potentials of processes of substrates and energy of bond cleavage. This information will constitute a much more thorough image of the properties of the materials and their connection with their performance. Additional structural characterisation of the used materials will be presented to evaluate the distortion that these scaffolds undergo.

4.3.1 Oxidation state investigation – XPS

High-resolution XPS spectra were obtained for ZIF-9, CuAlPO-5 and HKUST-1 in order to retrieve information about the oxidation states of the metallic sites. The analysed peaks regard the regions of photoelectrons ejected from the 2p electronic shells. As Figure 4.15 and Figure 4.16 demonstrate, presence of satellite peaks is intense which indicates the absence of metallic copper (Cu^0) and metallic cobalt (Co^0).

The satellite peaks for $Co^{2+}2p^3/_2$ and $Co^{2+}2p^1/_2$ are located around the binding energies of 787.1 and 803.7 eV. The main peaks for ZIF-9 are located at binding energies 781.7 eV and 797.7 eV for $Co^{2+}2p^3/_2$ and $Co^{2+}2p^1/_2$ respectively, which correspond to the doublet split of Co2p. The difference between the fitted splits is 16 eV (against 15 eV that literature indicates).[86] The pattern of the peaks shows symmetry and no Auger peak has been included in the fitting. Moreover, the pattern of the satellites indicates only one oxidation state in the solid system, which is Co^{2+}.[87–89]

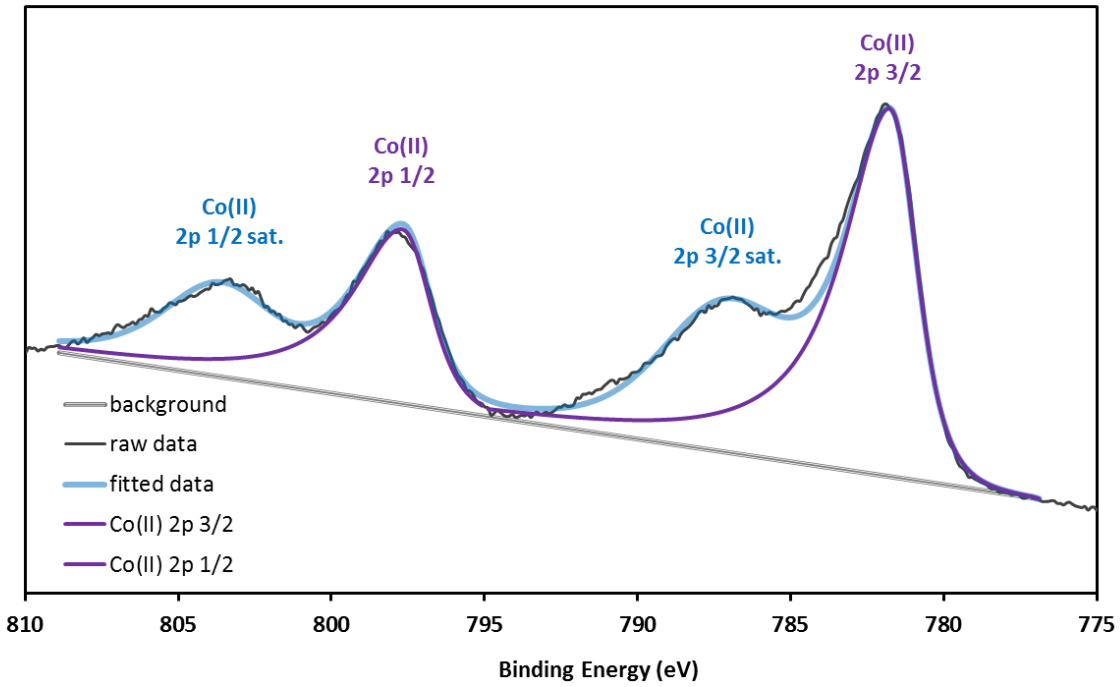

Figure 4.15 Experimental XPS spectra and fitting for ZIF-9.

Significant differences are observed between the spectra for the two copper-based materials (Figure 4.16). The main Cu2p peaks for HKUST-1 indicate the existence of one oxidation state. Although it is difficult to differentiate the oxidation state of copper only from XPS spectra, the juxtaposition with the spectrum of CuAlPO-5 is helpful to identify the presence of Cu^{2+} in HKUST-1 and Cu^{1+} and Cu^{2+} in CuAlPO-5.

In detail, it is clear from the spectrum of CuAlPO-5 that there are two main doublet splits. $Cu^{1+}2p^{3}/_{2}$ and $Cu^{1+}2p^{1}/_{2}$ are located at binding energies 934.4 eV and 954.4 eV, whereas $Cu^{2+}2p^{3}/_{2}$ and $Cu^{2+}2p^{1}/_{2}$ are located at binding energies 935.5 eV and 955.0 eV. These values are in relatively good accordance with the literature,[87–90] since the $Cu^{2+}2p^{3}/_{2}$ peak is shifted compared to the Cu^{1+} peak. HKUST-1 main doublet peaks are shifted to even higher binding energies, with the $Cu^{2+}2p^{3}/_{2}$ and $Cu^{2+}2p^{1}/_{2}$ located at binding energies 963.5 eV and 943.5 eV. This shift in relation to the location of the peaks in the spectrum of CuAlPO-5, along with the strong satellite peaks constitute a good indication that only Cu^{2+} is present in HKUST-1. Cu LMM peaks for CuAlPO-5 and HKUST-1 are found in the Appendix A.6 and are in good accordance with the literature.[88]

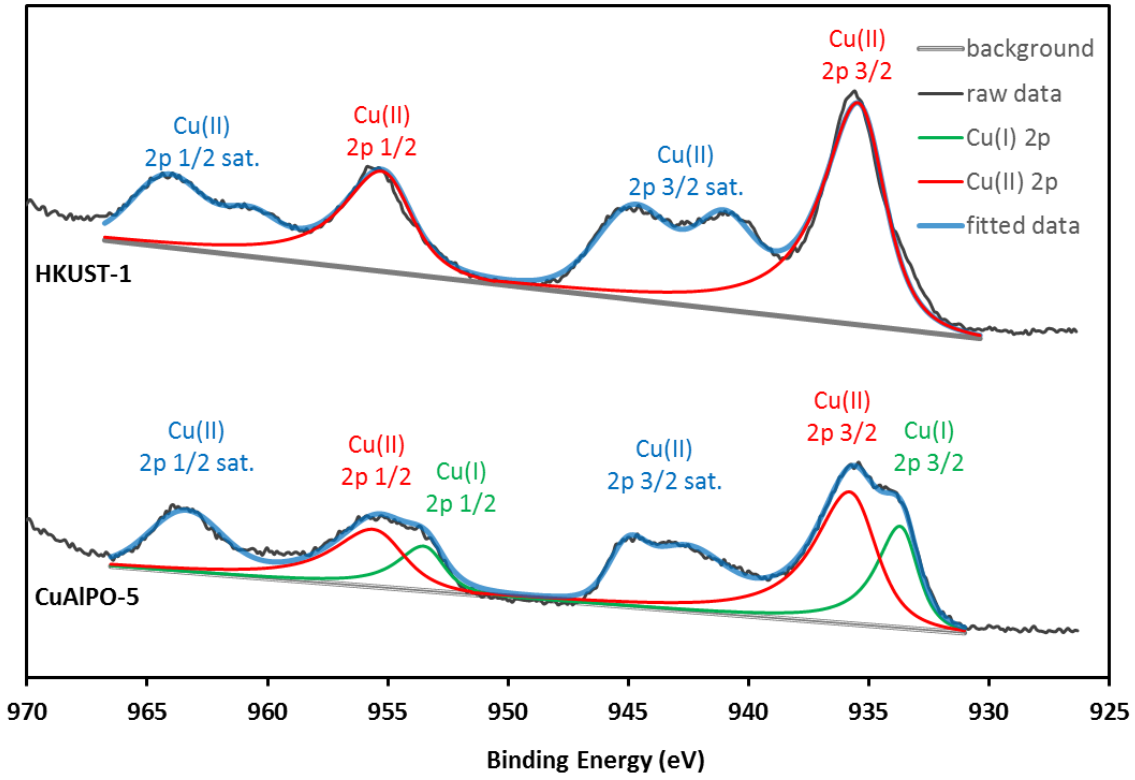

Figure 4.16 Experimental XPS spectra and fitting for CuAlPO-5 (bottom) and HKUST-1 (top).

It must be noted that the fitting of the data was performed with constraints that are advisable. As such, differences of split doublets were kept as close as possible to theoretical values and ratio between areas of $p^1/_2$ and $p^3/_2$ subshells was kept at 1:2 (for Cu, a ratio value of 0.508 is recommended).[91] Backgrounds were selected to be linear for the materials are not conductive, in contrast to Shirley background modelling which refers to conductive and metallic materials.[92] All spectra were shifted according to the difference between the experimental and theoretical C(1s) value.[91]

4.3.2 Coordination of metallic sites investigation – EPR and DR UV-VIS

Apart from the oxidation states of the metals in the materials, it is very useful to understand the coordination of the metals and whether the theoretical representation as given in Chapter 3 is close to the experimentally achieved. The coordination of the metals can reveal information about the stability of the metals in the architecture and the degree of exposure of the metallic site to the reaction substrates. Copper-based materials are sensitive to magnetic resonance, due to the d^9 electron configuration with one unpaired electron and thus, the EPR technique is considered appropriate.

The EPR spectrum of CuAlPO-5 (Figure 4.17) is typical and ideal to obtain g-factors and hyperfine constants A. An initial qualitative interpretation of the spectrum suggests a 4-fold coordination ($g_{//}$ area within 275-325 mT). No splitting in the $g_{\perp}$ area is observed (325-350 mT) and the peak is broad. The pattern is indicative of axial symmetry and anisotropy of the Cu^{2+} metal sites. The z-axis of the copper species is aligned to the magnetic field and only two g-factors are observed, corresponding to two magnetic orientations.[93–96]

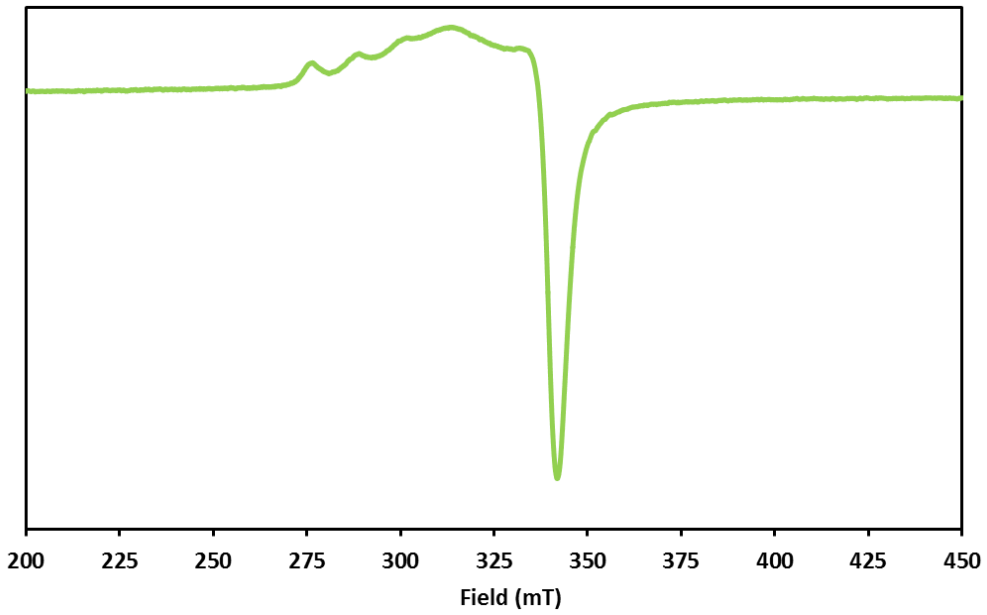

Figure 4.17 EPR spectrum of CuAlPO-5.

For the quantitative EPR information, the transformation of magnetic field B (Equation 4.1) is used to calculate the $g_{//}$ and $g_{\perp}$, using the values $B_{//}$ and $B_{\perp}$, where the operating microwave frequency is $f_v = 9.844798\,GHz$. The G ratio can be calculated from Equation 4.2 and represents the strength of the exchange interaction. The hyperfine parameters a are calculated with Equation 4.3. All values for CuAlPO-5 are found in Table 4.5.

$$B = \frac{h \cdot f_v}{g \cdot \beta_e} \Leftrightarrow g = \frac{h \cdot f_v}{B \cdot \beta_e} \Leftrightarrow \begin{cases} g_{//} = \dfrac{h \cdot f_v}{B_{//} \cdot \beta_e} \\ g_{\perp} = \dfrac{h \cdot f_v}{B_{\perp} \cdot \beta_e} \end{cases}$$ Equation 4.1

where $h = 6.626076 \times 10^{-34}\ J\ sec$ (Planck's constant) and
$\beta_e = 9.2742 \times 10^{-24}\ J\ T^{-1}$ (Bohr magneton)

$$G = \frac{g_{\parallel} - g_e}{g_{\perp} - g_e}$$ Equation 4.2

$$a\ (in\ 10^{-4}\ cm^{-1}) = A\ (in\ Gauss) \times g_e \times \beta_e$$ Equation 4.3

where A the differences between the peaks

Table 4.5 EPR parameters calculated for CuAlPO-5.

	$g_{\parallel}$	$g_{\perp}$	G	$a_{\parallel}\ (MHz)$	$a_{\perp}\ (MHz)$
CuAlPO-5	2.387	2.084	4.7	406	28

Interpreting the calculated values, the initial observation is the direction of the inequality $g_{\parallel} > g_{\perp} > 2.0023$, indicative of the pseudotetrahedral local structural of the copper centres and tetragonal distortion due to the unpaired electron at the $d_{x^2-y^2}$ orbital.[93-96] The opposite direction of the inequality would imply that the unpaired electron is found at the d_{z^2} causing a cubic distortion and compression along the z-axis with octahedral symmetry. Elaborating on the tetrahedral distortion, the cupric ion is possibly shifted from the local framework site keeping the 4-fold coordination.[93-96]

The G ratio is higher than 4, which is indicative of absence of electron exchange interaction and this means that the material lacks magnetic character. This is possible if the cupric ions have isolated positions in the framework. The hyperfine constants correspond to couplings A smaller than 150 Gauss, indicative of the

low symmetry, often observed for distorted tetrahedral complexes of copper ions.[93–96]

The EPR spectrum of HKUST-1 (Figure 4.18) agrees with the reported findings for rhombic symmetry and dimeric nature of the cupric ions. The broader peak observed for activated HKUST-1 (exposed copper ions after removal of water molecule) is in accordance with the literature.[97] The g-factors as calculated by the software were determined to be $g_{\perp} = 2.127$ and $g_{\perp} = 2.17$, for the non-activated and the activated HKUST-1 respectively.

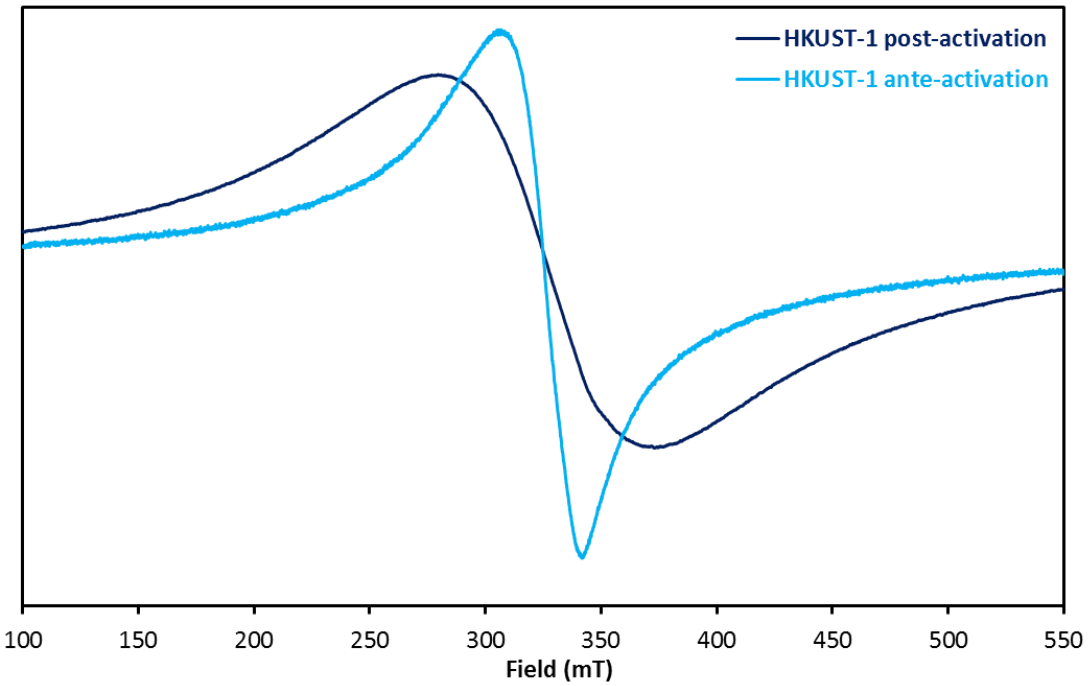

Figure 4.18 EPR spectrum of HKUST-1.

The main criterion for a compound to appear EPR sensitive is the existence of unpaired electrons. Cobalt (II) has a d7 electron configuration which should allow EPR signal. However, according to literature,[98–100] orbital splitting of cobalt is not easy to obtain with EPR at ambient temperatures. However, the strong purple colour of ZIF-9 implies strong photoresponse making the DR UV-VIS spectrum a good alternative for the characterisation of the geometry of the cobalt sites. Indeed, the DR UV-VIS spectrum (Figure 4.19) of ZIF-9 shows intense photoresponse within the range of 500-650 nm. The dominant peak around 588 nm and the shoulder at 540 nm can be assigned to d-d transitions of Co^{2+} tetrahedral species, as octahedral geometry and Co^{3+} are usually assigned to shorter wavelengths.[94,101–104]

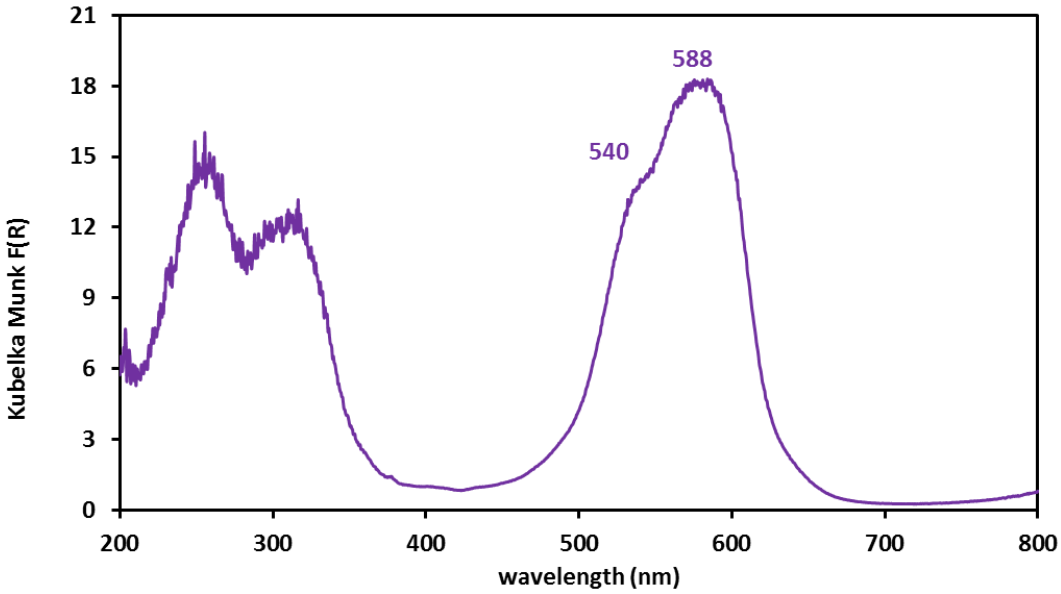

Figure 4.19 DR UV-VIS spectrum of ZIF-9.

4.3.3 Visible light response – DR UV-VIS

Except for site geometry that follows further down in the analysis, DR UV-VIS is useful in order to compare the photoresponse with the spectrum of the LED light, but, eminently, it is related to the transitions of electrons between bonding orbitals. The spectra of HKUST-1, CuAlPO-5 and ZIF-9 are found in Figure 4.20. The first observation regards the intensities of the main peaks. The bright intense colours are usually associated with the d-d transitions of the electrons of the transition metals. CuAlPO-5 exhibits the lowest absorption, which is justified by the pale green-blue colour of the material, opposed to the intense purple and blue/turquoise colours of ZIF-9 and HKUST-1.

Generally, the d-d transitions are of lower energy, which is why these peaks appear from 400 to 700 nm normally. Regarding these high intensity peaks of ZIF-9 and HKUST-1 in the visible spectrum, the maximum absorption wavelengths are indicative of the energy difference between the highest occupied molecular orbitals (HOMO) and the lowest unoccupied molecular orbitals (LUMO), given that the transition is allowed from the symmetry of the orbitals. The wavelength for the ZIF-9 and the HKUST-1 peak corresponds to an energy gap of 2.2 and 1.65 eV, respectively.

In inorganic materials, the ligand to metal charge transfer (LMCT) is similar to the metal to ligand process (MLCT). The ligand of HKUST-1 (trimesate ion) can be considered as a platform of extended pi bonds and delocalized electrons. Thus,

the charge transfer from the ligand to the metal can be strong. Similarly, the ligand of ZIF-9 (benzimidazolate ion) contains an aromatic ring and electron rich nitrogen atoms. This configuration can also explain LMCT for ZIF-9, while, in both cases, the partaking of the transition metals (Cu and Co) has a share, as charge carriers. The activity that is observed at shorter wavelengths (lower than 300 nm) is indicative of the pi-pi* transitions that organic compounds usually exhibit and is indicative of the MLCT and LMCT processes. The activity is more intense for the ZIF-9 and HKUST-1, due to the existence of aromatic molecules as part of their frameworks.

CuAlPO-5 absorbance is non-significant. However, as corroborated with the EPR technique, its broad peak near 790-800 nm suggests a pseudotetrahedral coordination, which agrees with the absorbance bands higher than 700 or 800 nm of such copper complexes.[105,106] Octahedral molecular geometry of copper (II) is expected at much shorter wavelengths.[107,108] The copper in the activated HKUST-1 exists in a square planar arrangement as a dimer $Cu^{2+}\cdots Cu^{2+}$. In the non-activated HKUST-1, each copper coordinates with an extra water molecule and dimer's geometry is best described as axial square pyramidal. In both cases, the copper dimer can be viewed as octahedral distorted species and the broad peaks in Figure 4.20 centralised around 700-710 nm can support this view.

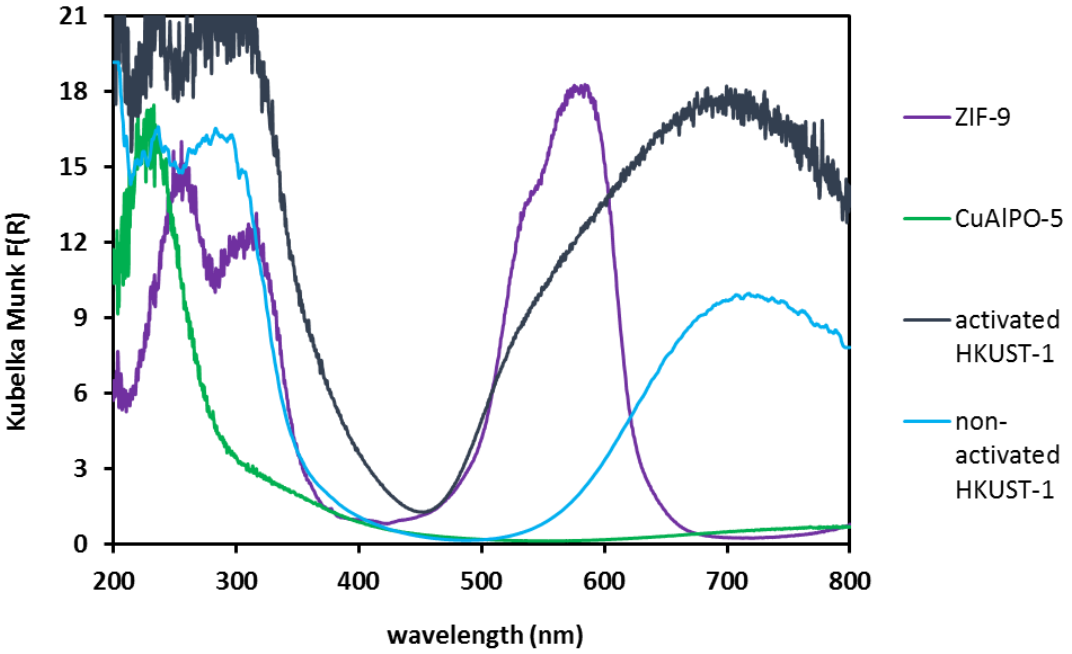

Figure 4.20 DR UV-VIS spectra of ZIF-9, CuAlPO-5 and HKUST-1 (activated and non-activated).

The activated HKUST-1 DR UV-VIS spectrum overlaps with the spectrum of ZIF-9, while the photoresponse of CuAlPO-5 is weak. Comparing though with the spectrum of the LEDs in Figure 4.6, ZIF-9 and HKUST-1 seem to make a good usage of the emitted photons, with ZIF-9 possibly exploiting the LED light better. Additional interest attracts the difference of intensity observed between the spectra of the non-activated and activated HKUST-1. The removal of the water molecule from the copper site upon activation with vacuum under heating turn the material to dark blue from a light turquoise colour and the absorbance bands reported here are characteristic.[109,110]

4.3.4 Redox potential values – Cyclic voltammetry

Cyclic voltammetry technique is applied in order to investigate the redox potential values of the materials. The redox potentials of a photocatalyst can be a useful feature, used as a tool to assess whether the material is suitable for the oxidation of a substrate. The rule of thumb is that a photocatalyst's redox potential should be more positive than the redox potential of the substrate. Generally, the C-H bonds are considered vulnerable to photooxidative conditions and the redox potentials can be relatively low. For amines, the reported values are around 0.7 V vs. SCE in hydrated solvents[111] and range from 0.3 to 1.0 V in acetonitrile.[112–114] For this reason, it is interesting to examine this property of ZIF-9, CuAlPO-5 and HKUST-1 and obtain a comparative view of their electrochemical behaviour. The cyclic voltammograms of the photocatalysts are plotted in Figure 4.21, Figure 4.22 and Figure 4.23.

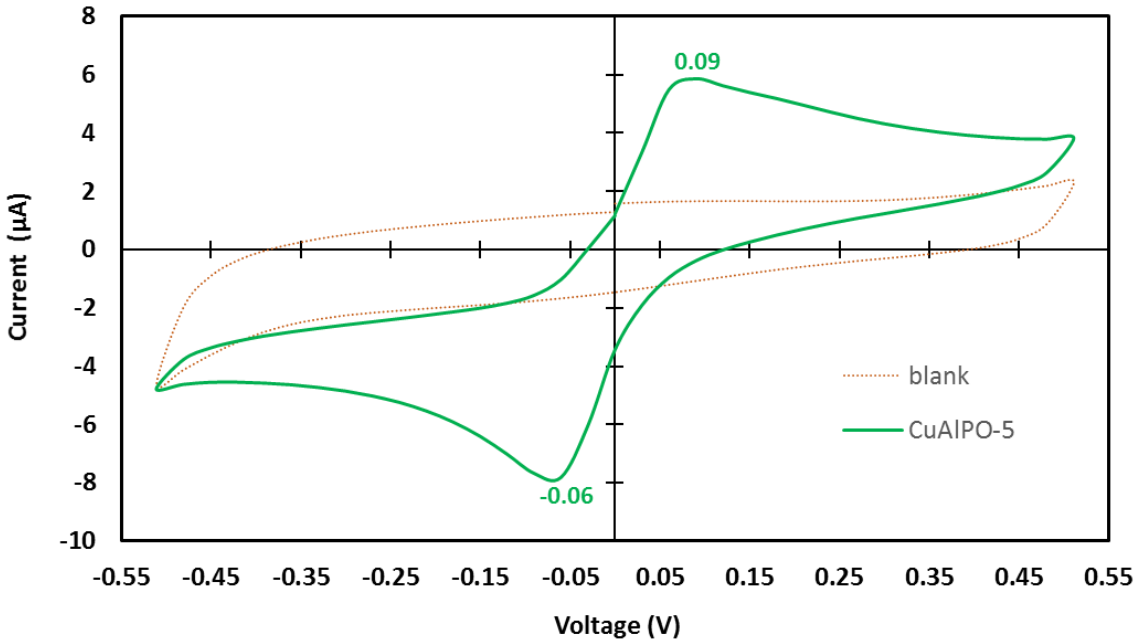

Figure 4.21 Cyclic voltammogram of CuAlPO-5.

Starting with CuAlPO-5, the collected cyclic voltammogram in Figure 4.21 follows a typical pattern of a reversible redox process. The reduction peak of CuAlPO-5 is located at -0.06 V and the oxidation peak is at 0.09 V, giving a redox potential equal to 0.15 V. From tables of standard electrode potentials,[115] the difference between the two peaks of 0.15 V is close to the standard potential for Cu^{+} to Cu^{2+} (0.16 V).

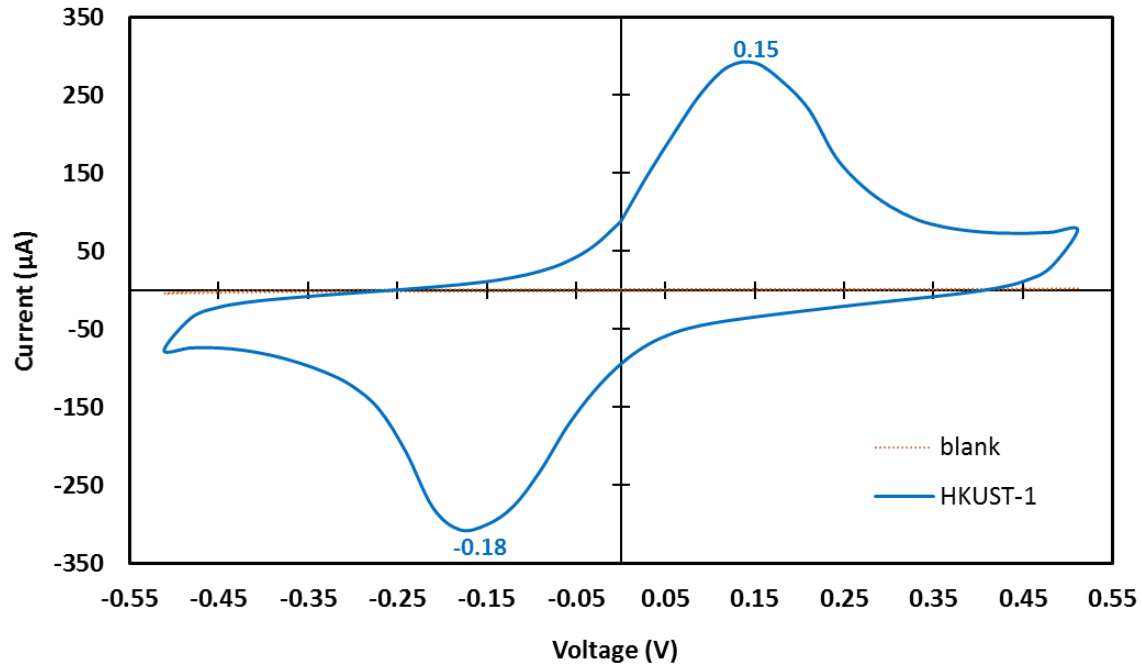

Figure 4.22 Cyclic voltammogram of HKUST-1.

The collected cyclic voltammogram of HKUST-1 in Figure 4.22 also follows a typical pattern of reversible redox process. The reduction peak of HKUST-1 is located at -0.18 V and the oxidation peak at 0.09 V. The difference between the two peaks is equal to 0.33 V and according to standard electrode potentials[115] it is close to the potential of the redox couple Cu^{2+}/Cu, which theoretically demands 0.34 V and corresponds to the transfer of two electrons in one step.

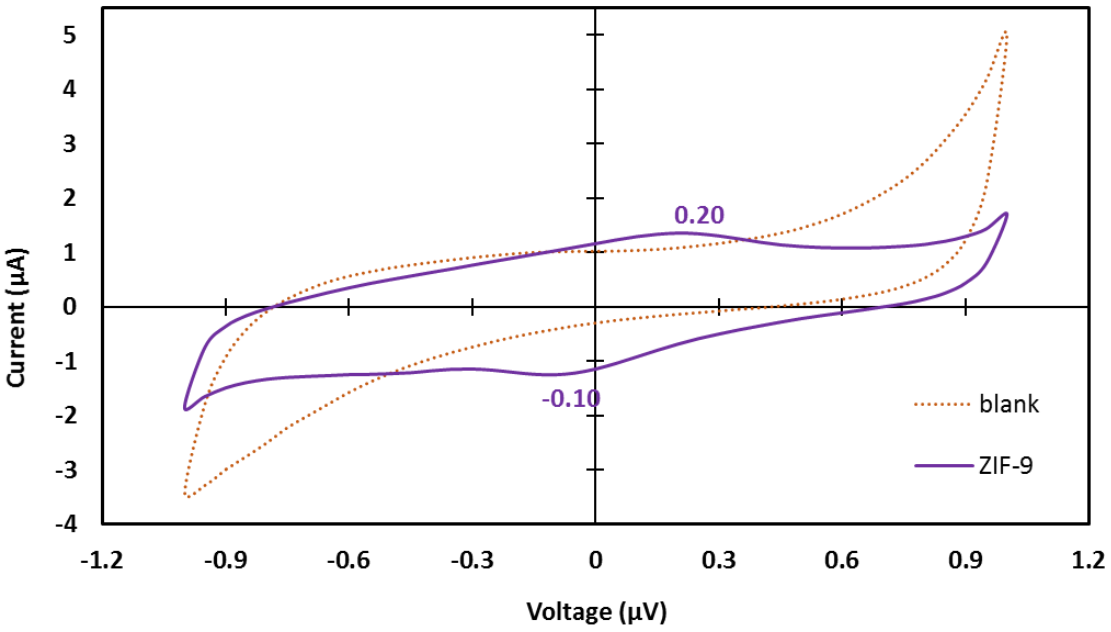

Figure 4.23 Cyclic voltammogram of ZIF-9.

ZIF-9's electrochemical behaviour is registered in Figure 4.23. The cyclic voltammogram of ZIF-9 corresponds to a reversible redox process like the previous materials demonstrated, due to the symmetry of the pattern. However, the intensity of the peaks is very low and the response is representative of materials with high resistivity, which could be due to the high stability that has been reported for ZIF-9[116] as the bonds between the cobalt sites and the nitrogen atoms are considered very strong. Observing the voltammogram of ZIF-9, two low redox peaks are distinguished which give a redox potential of 0.30 V.

A comparison of the calculated values shows that CuAlPO-5 has the smallest redox potential, while the two MOFs have similar values. However, none of the values is bigger than 0.7 V (the difference between Ag/AgCl and SCE is only 45 mV). There are a few explanations why the method cannot give concrete conclusions. The character of this approach is entirely qualitative because redox potentials are very sensitive to a number of parameters such as pH, temperature, solvent etc. Thus, a redox potential measured in acrylonitrile can be very different

to a redox potential measured in phosphate buffer solution. Moreover and judging from the extensive literature reported for $Ru(bpy)_3^{2+}$, the redox potential of the photocatalyst in the excited state can be significantly higher than the redox potential of the photocatalyst in the ground state. However, the technique can provide an initial comparative impression, while a method that measures that photoelectrochemical behaviour of the materials might be more revealing.

4.3.5 Post – catalysis PXRD characterisation

Post-catalysis characterisation is considered very useful in order to understand the degree of involvement of the material in the reaction and the degree of distortion that it has undergone. As it was mentioned, the powder catalysts can decay mechanically in the reactions due to excessive grinding from the magnetic stirrer. The PXRD performed on spent catalysts can reveal the degree of crystallinity reserved. Prior to the PXRD analysis on the spent materials, centrifugation was applied to separate the solid from the reaction mixture. The separated solid was dispersed in a small volume of isopropanol and was deposited on the PXRD sample holder for analysis.

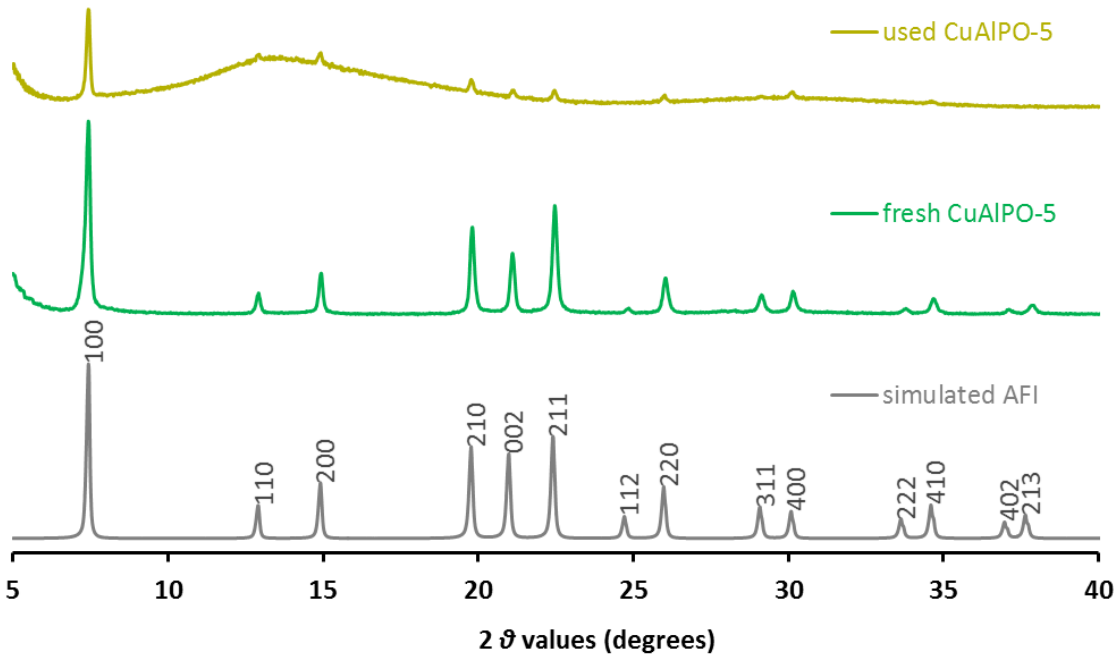

Figure 4.24 PXRD pattern of CuAlPO-5 used in one cycle of the CDC reaction between phenyl-tetrahydroisoquinoline and nitromethane in conditions of light irradiation.

In more detail, the peaks of the PXRD of used CuAlPO-5 remain in good accordance with the simulated pattern (Figure 4.24). The low content of copper metal in CuAlPO-5 makes the XRD technique non-sensitive to copper and thus peaks that could correspond to reduced copper cannot be detected. Similarly, copper oxide diffracts at higher angles, with strong peaks appearing between 25 and 40 degrees.[117] The PXRD pattern of the used HKUST-1 is of lower quality, with the intensity of the peaks being very low (Figure 4.25). The peaks of the used ZIF-9 catalyst are not well discerned (Figure 4.26) due to significant elevation of the baseline; however, neither shift of main peaks nor formation of new ones are observed.

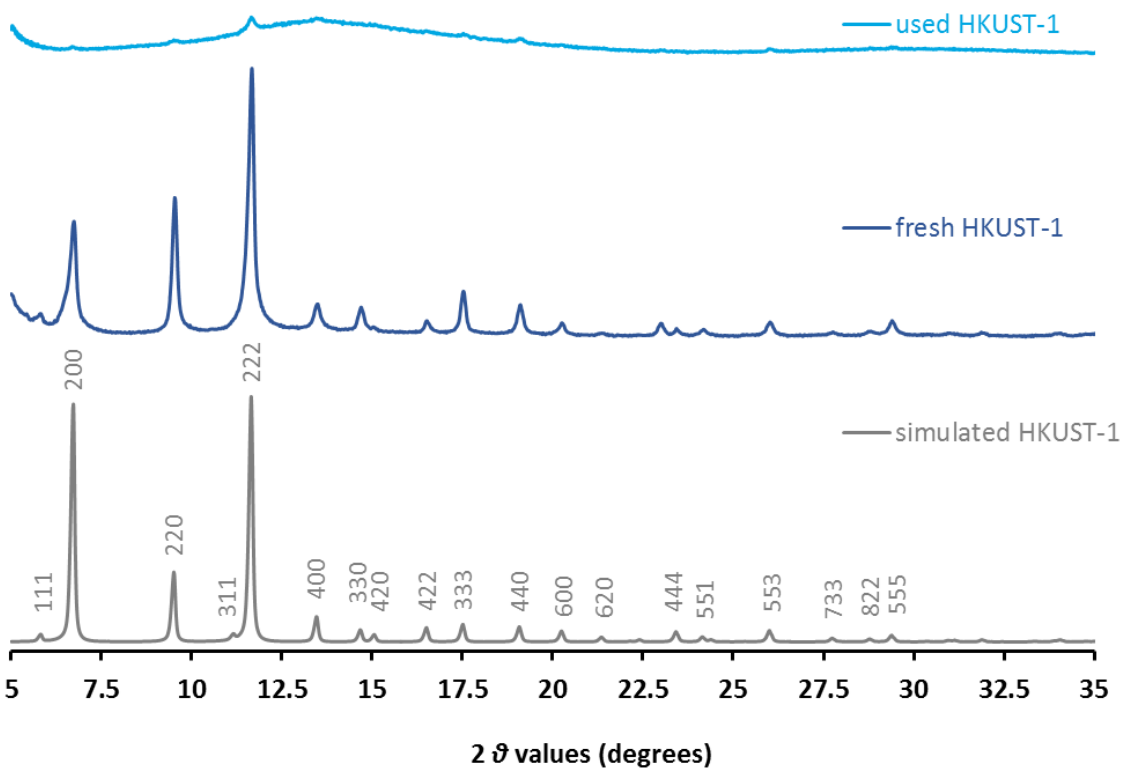

Figure 4.25 PXRD pattern of HKUST-1 used in one cycle of the CDC reaction between phenyl-tetrahydroisoquinoline and nitromethane in conditions of light irradiation.

The elevation of the baseline is a typical characteristic of amorphous phase. A significant elevation of the baseline is observed for all materials between 10 and 20 degrees. A slight elevation between 25 and 30 degrees is detected. Consequently, this can be attributed to reactants and intermediates that have remained on the surface of the catalysts and possible excessive washing of the used catalysts might remove this phase and reveal better-maintained crystallinity.

Wherever possible, migration of peaks has not been observed, which means that the planes of the crystals remain and low distortion could have been caused. Similarly, no extra peaks are present, which enhances this statement along with the possible peaks of metallic species, which might be possible for the case of HKUST-1 and ZIF-9, due to the higher metal content.

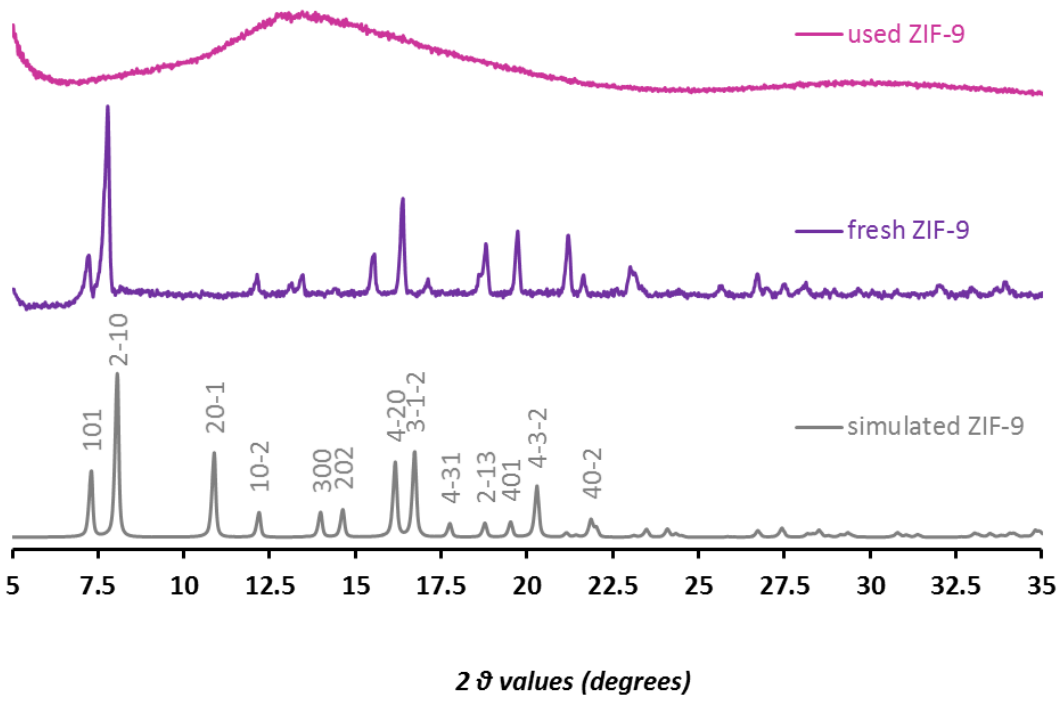

Figure 4.26 PXRD pattern of ZIF-9 used in one cycle of the CDC reaction between phenyl-tetrahydroisoquinoline and nitromethane in conditions of light irradiation.

In general, PXRD patterns show that microcrystallinity has been lost more for ZIF-9, less for HKUST-1, while CuAlPO-5 appears stronger. The AFI topology is known for its robust framework and its entirely inorganic character contributes to its heterogeneous role. The partial organic nature of HKUST-1 and ZIF-9 may turn them more susceptible to damage due to the mechanic grinding and friction, although both are MOFs known for their chemical and thermal stability.

PXRD technique is not enough to characterise the materials post-catalysis, but the relatively low quantity used along with the relatively low recovery efficiency made it impossible to analyse the used materials further with ICP, XPS, DR UV-VIS, EPR and SEM. These techniques would reveal information relevant to the structural

integrity of the materials, the maintenance of the chemical composition and the changes of the nature of the active sites.

HKUST-1 has been reported in another C-C coupling system as a successfully recovered and reusable catalyst.[118] Dang et al. performed structural characterisation and observed non-significant degradation, while the catalytic activity remained at the same levels. On the contrary, Garcia and co-workers used HKUST-1 in a hydrogenation reaction and their structural characterisation showed degradation of the material. Li and Kim used ZIF-9 in hydrogen production and reused the materials five times.[119] They reported higher activity after recovery and maintenance of the macrocrystallinity after structural characterisation. In a Knoevenagel reaction performed by the group of Phan, ZIF-9 was applied for 5 successive runs and only 3% reduction of activity was noted, while structural characterisation revealed slight distortion of the structure.[120] It must be noted that in these reported examples, the researchers indicate excessive washing with solvents to remove substrates and impurities and possibly amorphous phase.

Overall, the post-catalysis characterisation of CuAlPO-5, ZIF-9 and HKUST-1 performed and presented here is not indicative of the possibilities of the materials. Recovery method and quantity is not adequate for proper characterisation while the reusability tests indicated good performance. More characterisation techniques would be advantageous to realise the degree of structural disturbance and active sites changes.

4.4 Conclusions and Discussion

CuAlPO-5, HKUST-1 and ZIF-9 are able to catalyse successfully and similarly the CDC reaction between PhTHIQ and nitromethane in the presence of tBHP, whereas Co^{II}AlPO-5 and Co^{III}AlPO-5 perform poorly for this reaction. Reusability tests showed that all materials partially lose their activity in the presence of tBHP, performing though as true heterogeneous catalysts. In light of structural characterisation after the catalytic reaction, the materials appear less crystalline. Possible washing off of the substrates after the usage could reveal less amorphous phase and better crystallinity.

Photocatalytically, ZIF-9 outperforms the rest of the materials and preserves high activity after 5 cycles of reaction. Reported photocatalytic results of the same CDC reaction catalysed by Ru, Ir, Pt and Pd complexes, dyes such as Rose Bengal and Eosin Y, CdS and graphitic carbon nitride are tabulated in Table 4.3 for

reasons of comparison. Comparing them with the photocatalytic results of ZIF-9, it is clear that ZIF-9 can deliver the product after 6 hours of reaction in air and white light against the 10-40 hours reported. Overall, ZIF-9 is considered a remarkable heterogeneous catalyst and photocatalyst for this reaction, of low cost and relatively simple preparation.

In attempt of correlation between the structural features of the materials with their performance, ZIF-9 presents Co^{2+} sites in tetrahedral coordination. CuAlPO-5 also presents Cu isolated sites in tetrahedral coordination, but both Cu^{+} and Cu^{2+} are present in the material. Unlike CuAlPO-5, HKUST-1 hosts only Cu^{2+} metal sites in dimeric coordination. Unlike ZIF-9, CoAlPO-5 and CoMOF-74 did not perform well for this reaction system. CoAlPO-5 is also characterized by tetrahedral cobalt species while CoMOF-74 is characterised by a square pyramidal Co^{2+} coordination. Given this information, no concrete conclusion regarding the coordination geometry and oxidation state can be deduced. By the same token, silicon substituted AlPO-5 and CoAlPO-5 showed that Brönsted acidity may not be a strategic parameter for the CDC reaction.

Employing information from Chapter 3, the small size of the pores of all the materials is most probably not allowing entrance to the substrates. Thus, one can conclude that the reaction takes place on the external surface of the materials. Structurally, the two most performing MOFs, ZIF-9 and HKUST-1 afford the most complex channel and pore system, which could function protectively to the material during the reaction. In addition, the benzimidazolate ligands of ZIF-9 give a hydrophobic character to the material, while the nature of HKUST-1 and CoMOF-74 is hydrophilic, with the metal sites coordinating easily with a water molecule. Since the CDC reaction under study produces water as side product, it is likely that these materials deactivate easily losing quickly their performance. Simultaneously, the SEM pictures revealed that ZIF-9 particles were the smallest in size and small size of particles leads to higher external surface area, where the reaction is speculated to take place. This opinion is enhanced by the low porosity that ZIF-9 exhibits with BET analysis, implying that occupied pores or non-accessible pore system do not lower the performance of the material.

Furthermore, examining the electrochemical behaviour of the materials, CuAlPO-5 showed the smallest redox potential. ZIF-9 and HKUST-1 redox potential was higher and comparable, which could explain the better photocatalytic results. Moreover, the oxidation peak of ZIF-9 appears at 0.20 V whereas the oxidation peak of HKUST-1 appears at 0.15 V, which could imply a more electrochemically

active material. Redox potential values for PhTHIQ in similar conditions of measurement (phosphate buffer solution) could enhance the reasoning of good photocatalytic behaviour of these materials. However, the photoresponse obtained by the DR UV-VIS showed that HKUST-1 and ZIF-9 absorb intensively photons in the visible area, with ZIF-9 having a more tailored response to the emitted photons from the LED lights.

CuAlPO-5 redox activity is most probably corresponding to the general good activity of copper for this reaction, however, HKUST-1 seems more promising. Comparing between HKUST-1 and ZIF-9, the imidazole-based ligands of ZIF-9 may play a key role in the reaction. The electron rich nitrogen atoms are more likely to interact with the π-orbitals of aromatic rings enhancing the electron density and participating more intensively to photochemical transformations, which could explain the photoactivity of ZIF-9. In addition, the Co^{2+} coordination with the nitrogen atoms could potentially allow a better charge mobility, which is fundamental for photoredox reactions.

It is apparent that more characterisation is needed to reveal the exact reasons why ZIF-9 is performing best as a photocatalyst and catalyses the reaction in light and dark in the absence of tBHP, making use of molecular oxygen. A number of more sophisticated techniques can be applied to comprehend the deeper nature of the material in terms of photoconductivity (mobility of generated e^- / h^+) and excited states lifetimes, while electrochemical behaviour of ZIF-9 at excited state would be more interesting and useful. Moreover, study of its performance in other CDC systems can reveal its activity in different additions with other nucleophiles, its ability to functionalize more complex tetrahydroisoquinoline molecules and the selectivity profile it may afford in light or dark.

The system under study showed that CuAlPO-5 and HKUST-1, two copper-based scaffolds of different classes of porous materials, are able to perform using tBHP as oxidant. Simultaneously, it showed the interesting nature of ZIF-9, which indicates that a MOF with a well-known zeolitic topology is of notable potential and adds remarkable catalytic and photocatalytic applications in its list of uses.

4.5 References

1 A. Suzuki, *Angew. Chem. Int. Ed.*, 2011, **50**, 6722–6737.

2 E. Negishi, *Angew. Chem. Int. Ed.*, 2011, **50**, 6738–6764.

3 V. Ritleng, C. Sirlin and M. Pfeffer, *Chem. Rev.*, 2002, **102**, 1731–1770.

4 A. Lutz, in *Topics in Organometallic Chemistry*, ed. N. Chatani, Springer, Berlin, Heidelberg, 2007, pp. 35–60.

5 S. S. Stahl, *Angew. Chem. Int. Ed.*, 2004, **43**, 3400–3420.

6 S. Danno, I. Moritani and Y. Fujiwara, *Tetrahedron*, 1969, **25**, 4819–4823.

7 O. Baslé, J. Bidange, Q. Shuai and C.-J. Li, *Adv. Synth. Catal.*, 2010, **352**, 1145–1149.

8 N. Kuhl, M. N. Hopkinson and F. Glorius, *Angew. Chem. Int. Ed.*, 2012, **51**, 8230–8234.

9 T. Kawashima, T. Takao and H. Suzuki, *J. Am. Chem. Soc.*, 2007, **129**, 11006–11007.

10 J. Wencel-Delord, C. Nimphius, F. W. Patureau and F. Glorius, *Angew. Chem. Int. Ed.*, 2012, **51**, 2247–2251.

11 K. Morimoto, M. Itoh, K. Hirano, T. Satoh, Y. Shibata, K. Tanaka and M. Miura, *Angew. Chem. Int. Ed.*, 2012, **51**, 5359–5362.

12 J. Dong, Z. Long, F. Song, N. Wu, Q. Guo, J. Lan and J. You, *Angew. Chem. Int. Ed.*, 2013, **52**, 580–584.

13 G. Deng, L. Zhao and C.-J. Li, *Angew. Chem. Int. Ed.*, 2008, **47**, 6278–6282.

14 N. Chatani, Y. Ie, F. Kakiuchi and S. Murai, *J. Org. Chem.*, 1997, **62**, 2604–2610.

15 X. Guo and C.-J. Li, *Org. Lett.*, 2011, **13**, 4977–4979.

16 M. Kitahara, N. Umeda, K. Hirano, T. Satoh and M. Miura, *J. Am. Chem. Soc.*, 2011, **133**, 2160–2162.

17 A. Grandbois, M.-È. Mayer, M. Bédard, S. K. Collins and T. Michel, *Chem. – A Eur. J.*, 2009, **15**, 9655–9659.

18 H.-Q. Do and O. Daugulis, *J. Am. Chem. Soc.*, 2011, **133**, 13577–13586.

19 C.-J. Li and Z. Li, *Pure Appl. Chem.*, 2006, **78**, 935–945.

20 L. Zhao and C.-J. Li, *Angew. Chem. Int. Ed.*, 2008, **47**, 7075–7078.

21 Y. Zhang and C.-J. Li, *Tetrahedron Lett.*, 2004, **45**, 7581–7584.

22 W.-T. Wei, M.-B. Zhou, J.-H. Fan, W. Liu, R.-J. Song, Y. Liu, M. Hu, P. Xie and J.-H. Li, *Angew. Chem. Int. Ed.*, 2013, **52**, 3638–3641.

23 Z. Li and C.-J. Li, *J. Am. Chem. Soc.*, 2006, **128**, 56–57.

24 T. Zeng, G. Song, A. Mooresa and C.-J. Li, *Synlett*, 2010, **13**, 2002–2008.

25 N. Shankaraiah, R. A. Pilli and L. S. Santos, *Tetrahedron Lett.*, 2008, **49**, 5098–5100.

26 O. Baslé, N. Borduas, P. Dubois, J. M. Chapuzet, T.-H. Chan, J. Lessard and C.-J. Li, *Chem. – A Eur. J.*, 2010, **16**, 8162–8166.

27 L. Shi and W. Xia, *Chem. Soc. Rev.*, 2012, **41**, 7687–7697.

28 R. Fan, Y. Ye, W. Li and L. Wang, *Adv. Synth. Catal.*, 2008, **350**, 2488–2492.

29 J. D. Lewis, S. de Vyver and Y. Román-Leshkov, *Angew. Chem. Int. Ed.*, 2015, **54**, 9835–9838.

30 F. X. L. i Xamena, A. Abad, A. Corma and H. Garcia, *J. Catal.*, 2007, **250**, 294–298.

31 N. T. S. Phan, T. T. Nguyen, P. Ho and K. D. Nguyen, *ChemCatChem*, 2013, **5**, 1822–1831.

32 A. Tă bă caru, N. Xhaferaj, L. M. D. R. S. Martins, E. C. B. A. Alegria, R. S. Chay, C. Giacobbe, K. V Domasevitch, A. J. L. Pombeiro, S. Galli and C. Pettinari, *Inorg. Chem.*, 2016, **55**, 5804–5817.

33 L. Henry, *Comptes Rendus l' Académie des Sci. Paris*, 1895, **120**, 1265–1268.

34 W. Jin, X. Li and B. Wan, *J. Org. Chem.*, 2011, **76**, 484–491.

35 R. Ballini and G. Bosica, *J. Org. Chem.*, 1997, **62**, 425–427.

36 T. Arai, M. Watanabe and A. Yanagisawa, *Org. Lett.*, 2007, **9**, 3595–3597.

37 P. Spiteller, M. Rüth, F. von Nussbaum and W. Steglich, *Angew. Chem. Int. Ed.*, 2000, **39**, 2754–2756.

38 M. Namikoshi, K. L. Rinehart, A. M. Dahlem, V. R. Beasley and W. W.

Carmichael, *Tetrahedron Lett.*, 1989, **30**, 4349–4352.

39 M. Somei and F. Yamada, *Nat. Prod. Rep.*, 2005, **22**, 73–103.

40 M. Chrzanowska and M. D. Rozwadowska, *Chem. Rev.*, 2004, **104**, 3341–3370.

41 K. W. Bentley, *Nat. Prod. Rep.*, 2004, **21**, 395–424.

42 K. W. Bentley, *Nat. Prod. Rep.*, 2005, **22**, 249–268.

43 O. Basle and C.-J. Li, *Green Chem.*, 2007, **9**, 1047–1050.

44 Z. Li and C.-J. Li, *J. Am. Chem. Soc.*, 2005, **127**, 3672–3673.

45 M. Ghobrial, M. Schnürch and M. D. Mihovilovic, *J. Org. Chem.*, 2011, **76**, 8781–8793.

46 E. Boess, D. Sureshkumar, A. Sud, C. Wirtz, C. Farès and M. Klussmann, *J. Am. Chem. Soc.*, 2011, **133**, 8106–8109.

47 J. Yu, Z. Li, K. Jia, Z. Jiang, M. Liu and W. Su, *Tetrahedron Lett.*, 2013, **54**, 2006–2009.

48 Z. Li and C.-J. Li, *Org. Lett.*, 2004, **6**, 4997–4999.

49 Q.-Y. Meng, Q. Liu, J.-J. Zhong, H.-H. Zhang, Z.-J. Li, B. Chen, C.-H. Tung and L.-Z. Wu, *Org. Lett.*, 2012, **14**, 5992–5995.

50 S.-I. Murahashi, T. Nakae, H. Terai and N. Komiya, *J. Am. Chem. Soc.*, 2008, **130**, 11005–11012.

51 S.-I. Murahashi, N. Komiya and H. Terai, *Angew. Chem. Int. Ed.*, 2005, **44**, 6931–6933.

52 A. Tanoue, W.-J. Yoo and S. Kobayashi, *Adv. Synth. Catal.*, 2013, **355**, 269–273.

53 K. Alagiri, G. S. R. Kumara and K. R. Prabhu, *Chem. Commun.*, 2011, **47**, 11787–11789.

54 T. Tsuchimoto, Y. Ozawa, R. Negoro, E. Shirakawa and Y. Kawakami, *Angew. Chem. Int. Ed.*, 2004, **43**, 4231–4233.

55 G. Zhao, C. Yang, L. Guo, H. Sun, C. Chen and W. Xia, *Chem. Commun.*, 2012, **48**, 2337–2339.

56 M. Rueping, C. Vila, R. M. Koenigs, K. Poscharny and D. C. Fabry, *Chem. Commun.*, 2011, **47**, 2360–2362.

57 J. D. Slinker, A. A. Gorodetsky, M. S. Lowry, J. Wang, S. Parker, R. Rohl, S. Bernhard and G. G. Malliaras, *J. Am. Chem. Soc.*, 2004, **126**, 2763–2767.

58 J.-J. Zhong, Q.-Y. Meng, G.-X. Wang, Q. Liu, B. Chen, K. Feng, C.-H. Tung and L.-Z. Wu, *Chem. – A Eur. J.*, 2013, **19**, 6443–6450.

59 Z. Xie, C. Wang, K. E. DeKrafft and W. Lin, *J. Am. Chem. Soc.*, 2011, **133**, 2056–2059.

60 W.-P. To, Y. Liu, T.-C. Lau and C.-M. Che, *Chem. – A Eur. J.*, 2013, **19**, 5654–5664.

61 A. G. Condie, J. C. González-Gómez and C. R. J. Stephenson, *J. Am. Chem. Soc.*, 2010, **132**, 1464–1465.

62 J. Xuan and W.-J. Xiao, *Angew. Chem. Int. Ed.*, 2012, **51**, 6828–6838.

63 D. P. Hari and B. König, *Org. Lett.*, 2011, **13**, 3852–3855.

64 Y. Pan, C. W. Kee, L. Chen and C.-H. Tan, *Green Chem.*, 2011, **13**, 2682–2685.

65 G. Jiang, J. Chen, J.-S. Huang and C.-M. Che, *Org. Lett.*, 2009, **11**, 4568–4571.

66 P. Esser, B. Pohlmann and H.-D. Scharf, *Angew. Chemie Int. Ed. English*, 1994, **33**, 2009–2023.

67 H. J. Kim, L. Su, H. Jung and S. Koo, *Org. Lett.*, 2011, **13**, 2682–2685.

68 M. Rueping, J. Zoller, D. C. Fabry, K. Poscharny, R. M. Koenigs, T. E. Weirich and J. Mayer, *Chem. – A Eur. J.*, 2012, **18**, 3478–3481.

69 M. Cherevatskaya, M. Neumann, S. Füldner, C. Harlander, S. Kümmel, S. Dankesreiter, A. Pfitzner, K. Zeitler and B. König, *Angew. Chem. Int. Ed.*, 2012, **51**, 4062–4066.

70 Y. Zhang, N. Zhang, Z.-R. Tang and Y.-J. Xu, *Chem. Sci.*, 2012, **3**, 2812–2822.

71 T. Mitkina, C. Stanglmair, W. Setzer, M. Gruber, H. Kisch and B. Konig, *Org. Biomol. Chem.*, 2012, **10**, 3556–3561.

72 D. Shi, C. He, B. Qi, C. Chen, J. Niu and C. Duan, *Chem. Sci.*, 2015, **6**, 1035–1042.

73 C.-J. Wu, J.-J. Zhong, Q.-Y. Meng, T. Lei, X.-W. Gao, C.-H. Tung and L.-Z. Wu, *Org. Lett.*, 2015, **17**, 884–887.

74 W.-P. To, G. S.-M. Tong, W. Lu, C. Ma, J. Liu, A. L.-F. Chow and C.-M. Che, *Angew. Chem. Int. Ed.*, 2012, **51**, 2654–2657.

75 L. Möhlmann, M. Baar, J. Rieß, M. Antonietti, X. Wang and S. Blechert, *Adv. Synth. Catal.*, 2012, **354**, 1909–1913.

76 Z. Li, S. B. D. and C.-J. Li, *Proc. Natl. Acad. Sci. U.S.A*, 2006, **103**, 8928–8933.

77 R. A. van Santen, in *Advanced Zeolite Science and Applications*, eds. J. C. Jansen, M. Stöcker, H. G. Karge and J. Weitkamp, Elsevier, 1994, vol. 85, pp. 273–294.

78 Y. Jeanvoine, J. G. Ángyán, G. Kresse and J. Hafner, *J. Phys. Chem. B*, 1998, **102**, 5573–5580.

79 J. Chen, P. A. Wright, S. Natarajan and J. M. Thomas, in *Zeolites and Related Microporous Materials: State of the Art 1994 - Proceedings of the 10th International Zeolite Conference, Garmisch-Partenkirchen, Germany, 17-22 July 1994*, eds. J. Weitkamp, H. G. Karge, H. Pfeifer and W. Hölderich, Elsevier, 1994, vol. 84, pp. 1731–1738.

80 M. E. Potter, S. V Aswegen, E. K. Gibson, I. P. Silverwood and R. Raja, *Phys. Chem. Chem. Phys.*, 2016, **18**, 17303–17310.

81 E. Gianotti, M. Manzoli, M. E. Potter, V. N. Shetti, D. Sun, J. Paterson, T. M. Mezza, A. Levy and R. Raja, *Chem. Sci.*, 2014, **5**, 1810–1819.

82 A. Corma, *J. Catal.*, 2003, **216**, 298–312.

83 M. Rueping and A. P. Antonchick, *Org. Lett.*, 2008, **10**, 1731–1734.

84 F.-F. Wan, C.-P. Luo, G. Deng and L. Yang, *Green Chem.*, 2014, **16**, 2428–2431.

85 Q. Xia, Q. Wang, C. Yan, J. Dong, H. Song, L. Li, Y. Liu, Q. Wang, X. Liu and H. Song, *Chem. – A Eur. J.*, 2017, **23**, 10871–10877.

86 XPS Reference - Knowledge Base, *http://xpssimplified.com/periodictable.php*, (accessed September 2015).

87 Q. Luo, B. An, M. Ji, S.-E. Park, C. Hao and Y. Li, *J. Porous Mater.*, 2015, **22**, 247–259.

88 M. Tonigold, Y. Tu, B. Bredenkötter, B. Rieger, S. Bahnmüller, J. Hitzbleck, G. Langstein and D. Volkmer, *Angew. Chem. Int. Ed.*, 2009, **48**, 7546–7550.

89 A. A. Talin, A. Centrone, A. C. Ford, M. E. Foster, V. Stavila, P. Haney, R. A. Kinney, V. Szalai, F. El Gabaly, H. P. Yoon, F. Léonard and M. D. Allendorf, *Science (80-.).*, 2014, **343**, 66–69.

90 L. Wang, J. R. Gaudet, W. Li and D. Weng, *J. Catal.*, 2013, **306**, 68–77.

91 in *CasaXPS User's manual*, Casa Software Ltd., Wilmslow, UK, 2001, pp. 5–17.

92 in *CasaXPS User's manual*, Casa Software Ltd., Wilmslow, UK, 2001, pp. 55–69.

93 M. V Angeluş iu, G. L. Almă jan, D. C. Ilieş , T. Roş u and M. Negoiu, *Chem. Bull. „POLITEHNICA" Univ. Timisoara*, 2008, **53**, 78–82.

94 A. M. Beale and B. M. Weckhuysen, in *From Zeolites to Porous MOF Materials - The 40th Anniversary of International Zeolite Conference, Proceedings of the 15th International Zeolite Conference*, eds. R. Xu, J. Chen, W. Yan and Z. Gao, Studies in Surface Science and Catalysis, Elsevier, 1st edn., 2007, vol. 170, pp. 748–755.

95 Y. I. Kim, S. N. Choi and C. U. Ro, *Bull. Korean Chem. Soc.*, 1994, **15**, 533–549.

96 A. L. Porte, in *Electron Spin Resonance: Volume 7*, ed. P. B. Ayscough, The Royal Society of Chemistry, London, 1982, pp. 69–123.

97 O. Fleker, A. Borenstein, R. Lavi, L. Benisvy, S. Ruthstein and D. Aurbach, *Langmuir*, 2016, **32**, 4935–4944.

98 B. M. Weckhuysen, A. A. Verberckmoes, M. G. Uytterhoeven, F. E. Mabbs, D. Collison, E. de Boer and R. A. Schoonheydt, *J. Phys. Chem. B*, 2000, **104**, 37–42.

99 P. Pietrzyk, M. Srebro, M. Radoń , Z. Sojka and A. Michalak, *J. Phys. Chem.*

A, 2011, **115**, 2316–2324.

100 A. B. P. Lever and H. B. Gray, *J. Magn. Reson.*, 1978, **32**, 169–172.

101 A. P. Katsoulidis, D. E. Petrakis, G. S. Armatas, P. N. Trikalitis and P. J. Pomonis, *Microporous Mesoporous Mater.*, 2006, **92**, 71–80.

102 W. W. Wendlandt, *J. Therm. Anal.*, 1969, **1**, 469–472.

103 Q. Zhang, C. Chen, M. Wang, J. Cai, J. Xu and C. Xia, *Nanoscale Res. Lett.*, 2011, **6**, 586–592.

104 N. Carmona, V. Bouzas, F. Jiménez, M. Plaza, L. Pérez, M. A. García, M. A. Villegas and J. Llopis, *Sens. Actuator B-Chem.*, 2010, **145**, 139–145.

105 S. K. Kang, H. S. Kim and Y. I. Kim, *Bull. Korean Chem. Soc.*, 2004, **25**, 1959–1962.

106 R. M. Patil and M. M. Prabhu, *Int. J. Chem. Sci.*, 2010, **8**, 52–58.

107 S. M. Emam, A. S. El-Tabl, H. M. Ahmed and E. A. Emad, *Arab. J. Chem.*, 2014, DOI: 10.1016/j.arabjc.2014.05.019.

108 A. A. El-Sherif, *Inorg. Chim. Acta*, 2009, **362**, 4991–5000.

109 H. A. Bayoumi, A.-N. M. A. Alaghaz and M. S. Aljahdali, *Int. J. Electrochem. Sci.*, 2013, **8**, 9399–9413.

110 C. Prestipino, L. Regli, J. G. Vitillo, F. Bonino, A. Damin, C. Lamberti, A. Zecchina, P. L. Solari, K. O. Kongshaug and S. Bordiga, *Chem. Mater.*, 2006, **18**, 1337–1346.

111 J. R. L. Smith and D. Masheder, *J. Chem. Soc.{,} Perkin Trans. 2*, 1976, 47–51.

112 P. J. Smith and C. K. Mann, *J. Org. Chem.*, 1969, **34**, 1821–1826.

113 L. C. Portis, V. V Bhat and C. K. Mann, *J. Org. Chem.*, 1970, **35**, 2175–2178.

114 Y. L. Chow, W. C. Danen, S. F. Nelsen and D. H. Rosenblatt, *Chem. Rev.*, 1978, **78**, 243–274.

115 Standard Electrode Potentials in Aqueous Solution at 25˚C, *http://hyperphysics.phy-astr.gsu.edu/hbase/tables/*, (accessed December 2014).

116 K. S. Park, Z. Ni, A. P. Cote, J. Y. Choi, R. Huang, F. J. Uribe-Romo, H. K. Chae, M. O'Keeffe and O. M. Yaghi, *Proc. Natl. Acad. Sci. U.S.A*, 2006, **103**, 10186–10191.

117 S. L. Cheng and M. F. Chen, *Nanoscale Res. Lett.*, 2012, **7**, 119.

118 G. H. Dang, D. T. Nguyen, D. T. Le, T. Truong and N. T. S. Phan, *J. Mol. Catal. A-Chemical*, 2014, **395**, 300–306.

119 Q. Li and H. Kim, *Fuel Process. Technol.*, 2012, **100**, 43–48.

120 L. T. L. Nguyen, K. K. A. Le, H. X. Truong and N. T. S. Phan, *Catal. Sci. Technol.*, 2012, **2**, 521–528.

Chapter 5: Reduction of 4-Nitrophenol to 4-Aminophenol in ambient conditions

This chapter includes collaborated work with colleagues, whose contribution is appreciated and acknowledged.

Dr. Chen Chao, a scientist II in IMRE, provided helpful guidance regarding the experimental methodology followed in this chapter. Dr Zhang Zheng, a scientist II in IMRE, performed the XPS experiments of the used materials and his assistant and senior specialist II, Dr Seng Hwee Leng Debbie, gave me access and insight to the Thermoavantage software for the XPS data analysis.

Part of the work included in the chapter has been orally presented at the 5th International Conference in Engineering, Science, Technology and Waste Management, in August 2017 in Singapore.

5.1 4-Nitrophenol to 4-Aminophenol: From an environmental hazard to a commercially valuable molecule

Nitro-compounds constitute a class of dangerous pollutants of the environment. They are found in large quantities in the wastewaters and they can contaminate underground water and soil. The maximum acceptable limit in water has been set to 20 ppb. Nitrophenols, are the most representative molecules of this group of compounds and occur almost exclusively from human activity. Drug industry, dye synthesis factories, pesticides and explosives manufacturing plants originate great amounts in their effluents,[1] while nitrophenols are also formed in the exhausts of automobiles or in the troposphere due to NO_x pollution.[2]

Nitrophenols are known to significantly decay the environmental quality. The nitro-group and the aromatic ring make these compounds very stable physically,

chemically and biologically. EPA has classified them as persistent toxic compounds and possible carcinogen,[3] because the molecules cannot degrade via aerobic bacteria[4] and anaerobic degradation leads to carcinogenic hydroxylamines.[5] Studies have revealed that exposure to these compounds threatens the human and animal health, targeting organs like liver and kidneys and causing headaches and drowsiness. High levels in the blood impede the oxygen transfer, which can lead to cyanosis.

4-nitrophenol and 2-nitrophenol are the most typical products of the environmental degradation of nitrophenols. They are considered industrial pollutants, with 4-nitrophenol being more dangerous due to its greater solubility in water and the para-position of the nitro-group relative to the hydroxyl group. They cause ecological damage and for this reason, their removal from the environment and especially water bodies has always been an issue to tackle.

Initially, physicochemical techniques have been applied, such as adsorption and stripping and biological treatment.[6–9] However, these techniques do not solve the problem; they rather transfer the pollution to a different medium or create toxic intermediates. Other specific water treatment methods would be ozonation[10,11] and UV photodegradation,[12,13] which gradually shifted the interest to Advanced Oxidation Processes (AOPs).[14,15] AOPs degrade the pollutants by cleavage of aromatic rings, mineralization to H_2O and CO_2 and reduction of nitro-groups to amino-groups.

The reduction of 4-nitrophenol to 4-aminophenol has become a model reaction of environmental and catalytic interest. The high rate of the reaction and the absence of side-products make it useful for the evaluation of the catalytic efficiency of materials. While metal-exchanged zeolites are known for their catalytic properties, they have been reported only as adsorbing materials of 4-nitrophenol or in combination with noble metals and nanocomposites.[16–19] Similar data have been reported for mesoporous silica or nanocomposites on oxides.[20,21] In a few studies, oxidation with H_2O_2 is being reported as a method of mineralisation. Daneshvar et al. studied the degradation of 4-nitrophenol with hydrogen peroxide and UV-light,[22] while Umabala introduced $BiVO_4$ with UV light and supported successful mineralization of a mixture of 2-nitrophenol and 4-nitrophenol.[23] The literature findings are tabulated in Table 5.1 for reasons of comprehensive comparison.

Table 5.1 Literature examples of degradation processes of 4-nitrophenol.

Application [REFERENCE]	Catalyst concentration (mg/mL)	Molar ratio ($NaBH_4$:4-NP)	Performance	Time
Reduction with Ag / Natrolite (natural)[18]	0.1	100	100 %	160 s.
Reduction under UV-light with NiO / PbO on nanoclinoptilolite[17]	0.5	n.a.	40 %	200 s.
Photodegradation under UV-light with NiS / PbS on nanoclinoptilolite[17]			35 %	
Adsorption on Fe – nano/mesoporous zeolites, no reduction reported[16]	5	n.a.	n.a. Maximum capacity: 200 mg of 4-NP / g zeolite in 3 min.	180 s.
Reduction with Pd / Natrolite[19]	0.14	75	100 %	50 s.
Reduction on Co @ ZIF-67, with Co nanocrystals[24]	1	2000	100 %	180 s.
Adsorption and photodegradation on TiO_2 / SiO_2 mesoimprinted nanocomposites[21]	1.5	n.a.	100 %	30 min.
Adsorption and photodegradation on TiO_2 / SiO_2 nanoimprinted nanocomposites[21]				110 min.
Reduction on Pd @ ZIF-8[25]	1	200	100 %	300 s.
Reduction on Pd @ ZIF-8[26]	1	100	100 %	120 min.
Photooxidation with H_2O_2[22]	n.a.	n.a.	100 %	150 min.

Application [REFERENCE]	Catalyst concentration (mg/mL)	Molar ratio ($NaBH_4$:4-NP)	Performance	Time
Reduction on Au NP @ graphitic carbon[27]	1.7	1000	100 %	15 s.
Photooxidation of mixture of 2-NP and 4-NP with $BiVO_4$[23]	0.1	n.a.	100 %	210 min.
Photooxidation of mixture of 2-NP and 4-NP with $BiVO_4$ and H_2O_2[23]				120 min.
Adsorption on Nano-zero-valent Fe / SBA-15, no reduction reported[20]	5	n.a.	100 %, $([4NP]_o = 1.4\ mM)$	270 s.
			65 %, $([4NP]_o = 4.3\ mM)$	
Reduction with visible artificial light on AgCl @ Ag hydride[28]	2	n.a.	100 %	16 min.
Reduction with natural sunlight on AgCl @ Ag hydride[28]				10 min.
Reduction on Ni_xCo_{1-x} – Fe_2O_4 NP[29]	25	50	100 %	30-180 s.
		25		20-40 min.

Most frequently, kinetic studies of the reduction of 4-nitrophenol to 4-aminophenol have been carried out with noble metals and nanoparticles, such as Pd, Ag and Au,[19,25–28,30] supported on a range of substrates (zeolites, hydrides, graphitic carbon, oxides, MOFs or ZIFs), among which ZIF-8 (a zinc-based ZIF) is widely used and reported,[25,26] possibly due its large surface area, its potential to delay nanoparticles aggregation over time and its lack of photoresponse. Li et al. carry out a comparative survey of thirteen heterogeneous 4-nitrophenol reduction catalysts in relation to their kinetic performances[24] and, for first-order kinetics,

the reported rate constant varies from 0.0222 min^{-1} (Pt-reduced graphene oxide)[31] to 0.792 min^{-1} (Ni/graphene),[32] while they report enhanced kinetics corresponding to a constant of 1.024 min^{-1}.

Li et al. report an interesting approach of Co nanocrystals made via ZIF-67 (a cobalt-based ZIF), which reduces 4-nitrophenol in 3 minutes,[24] while Singhal's group synthesized Ni-doped cobalt ferrite nanoparticles,[29] using a nickel-cobalt alloy, which was fully effective within the first 3 minutes of the reaction. Focusing a little more on these findings, it is interesting to explore the reported investigation on the active sites. In most cases, the involvement of cobalt into the catalysts, as cobalt ferrite or cobalt nanocrystals, assigns the property of magnetisation to the material.

Therefore, the aforementioned research groups report cobalt, as an approach for efficient separation of the solid from the solution with a magnet, rather than an active metal and catalytic unity. Li et al. modified the cobalt-based ZIF-67 with pyrolysis and converted the tetrahedral Co II species to octahedral metallic Co entities achieving the synthesis of a magnetic material.[24] Singh et al. confirm that nickel ferrite and Ni^{+2} ions are active for the reduction of 4-nitrophenol and introduce Ni-cobalt ferrite to reduce the size of the particles and separate magnetically the catalyst, without characterising the cobalt species or excluding nickel from the study to test the potential of cobalt ferrite particles. Interestingly, nickel is not reported as frequently, although one commercial industrial technique to produce 4-aminophenol is the hydrogenation of 4-nitrophenol over Raney nickel.[33] To be more specific, Raney nickel is a Ni-Al alloy, which has been subjected to dealumination with strong NaOH, increasing the surface area and its capacity for hydrogen absorption.

This brings up the interesting topic of the industrialized methods for 4-aminophenol production. While the reduction of 4-nitrophenol to 4-aminophenol seems a straight-forward approach, 4-aminophenol is a reactive aminophenol isomer[34] and a few industrial approaches have been established to ensure 4-aminophenol production, but with a number of drawbacks following each. The downside of the aforementioned reduction of 4-nitrophenol over Raney nickel is the use of hydrazine, along with the fact that the catalyst is carcinogenic and pyrophoric, requiring particularly inert atmospheric conditions. The patented and industrialized Mallinckrodt process[35] refers to the catalytic hydrogenation of nitrobenzene with strong mineral acids, side-producing mainly aniline. Traditionally, a multi-step reduction of nitro-chlorobenzene or 4-nitrophenol over

iron-acid catalysts affords high quantities of Fe-FeO sludge,[36] rendering the method non-sustainable. In contrast, the hydrogenation of 4-nitrophenol over Pt is considered green, but of high cost.[37]

In research, a plethora of published works reports the attractive use of borohydrides with heterogeneous catalysts to reduce 4-nitrophenol to 4-aminophenol (Table 5.1). The high rate of the reaction and the range of conditions (pH, light intensity, dissolved oxygen availability, catalyst-substrate ratio) that affect the rate draw a lot of attention. From the comparative table (Table 5.1), a main observation regards the high molar ratios between $(BH_4)^-$ and 4-nitrophenol reported, which predominantly range between 50 and 100, while a couple of examples regard higher values. The smallest times required for 100% conversion are 15 sec, for molar ratio 1000 and Au nanoparticles on graphitic carbon[27] and 50 sec, for molar ratio 75 and Pd upon Natrolite,[19] but primarily reported times are 100-300 sec. and 10-20 min.

Although the reduction of 4-nitrophenol to 4-aminophenol with borohydrides appears as a model catalytic reaction, the production of 4-aminophenol is significant, because of its importance in organic synthesis as a precursor. Generally, aminophenols constitute backbone molecules of pharmaceuticals (largely analgesics and antipyretics) and intermediate molecules in the dye and pigment industry. They are also used in the development of photographic films, in the cosmetics industry for hair-dyes manufacturing and as anti-corrosion agents. In terms of market, the value of 4-aminophenol is projected to reach 1.7 billion USD in North America by 2022,[38] which demonstrates the demand for the chemical and the need to turn its production greener.

5.2 Experimental approach

5.2.1 Objective and experimental methodology

The catalytic evaluation of porous solids based on transition metals of low cost and high abundance for the reduction of 4-nitrophenol to 4-aminophenol is under study. The catalysts employed are ZIF-9, HKUST-1, CuAlPO-5 and CoAlPO-5 and are evaluated in conditions of a low molar ratio of reducing agent $(BH_4)^-$ to substrate 4-nitrophenol. To summarize briefly the nature of the active sites and topologies of the materials, the totally inorganic metal substituted AlPO-5s exhibit parallel channels with a pore opening of 7 Å and metal sites in +2 oxidation state and low content and a tetrahedral coordination. The hybrid

materials HKUST-1 and ZIF-9 exhibit complex structure of cavities and porosity, with multidimensional access to the pores. HKUST-1 is copper based, with copper paddlewheel motifs and open metal sites, sensitive to moisture, while ZIF-9 is built with cobalt nodes, in tetrahedral geometry with benzimidazolate ions linking through the nitrogen atoms.

The catalytic reaction is tested in darkness and the results afforded by the catalytic materials are compared. The best performing material or materials are examined in different molar ratios in order to assess their activity and next, are examined under white light. Reusability tests are also taking place in order to assess heterogeneity and deactivation. The aim of this project is the investigation of the reductive ability of the aforementioned materials in a model reaction. Details regarding the experimental methodology are given hereafter.

The substrate 4-nitrophenol (4-NP) is used as purchased by Sigma-Aldrich (Reagent Plus, >99%) and Sodium Borohydride ($NaBH_4$) is used as purchased by Fluka (>99%), without further purification. The experiments in darkness are designed to examine the effect of different molar ratios between the reductant $NaBH_4$ and substrate 4-nitrophenol and the effect of the catalyst concentration. The experiments in white light are designed according to the results obtained from the experiments in darkness, in order to evaluate whether the best performing catalyst is photocatalytically active. The experimental setup responds to the description given in chapter 2.4.2 and illustrated in Figure 2.8.

Studying published data (Table 5.1) and given the sensitivity of the employed instruments, the molar ratios selected for this reaction are 50, 25, 12.5 and 8. By the same token, the catalyst concentration varies between 0.5 mg/mL and 0.1 mg/mL. In detail, the starting concentration of 4-nitrophenol is 0.1 mM (aqueous solution) and, unless stated otherwise, the volume of the solution is 25 mL. It should be noted that the 4-nitrophenol solution used is freshly prepared. The catalyst is weighed according to the desired concentration. The reducing agent is weighed according to the desired molar ratio and is added to the solution as a solid and not as an aqueous solution. The reaction mixture is stirred at 750 rpm.

The sampling volume is 1mL to avoid severe disturbance of the mixture in terms of concentration and kinetics. The progress of the reaction is monitored spectroscopically with UV-VIS and the results are considered qualitatively and quantitatively. The kinetic analysis takes place to evaluate the catalytic activity and compare it with the reported data. Reusability tests of the best performing

catalyst are performed, without washing with solvents taking place. Post-catalysis characterisation is also presented in order to assess structural distortion and crystallinity maintenance.

5.2.2 Measurement preparation

The UV-VIS spectrum of 4-nitrophenol aqueous solution is characterised by a peak at $\lambda = 317\,nm$. The hydrolysis of 4-nitrophenol results in the 4-nitrophenolate anion and the solution is characterized by a strong yellow colour and a peak at $\lambda = 400\,nm$. A characteristic spectrum is given in Figure 5.1. The degree of the hydrolysis determines the intensity of the yellow colour of the solution and, subsequently, the intensity of the peak at 400 nm. The degree of the hydrolysis is not easily defined and for this reason, the measurement of the concentration of 4-nitrophenol in the solution is based on the peak at 317 nm of freshly prepared 4-nitrophenol aqueous solutions.

A set of standard aqueous solutions of different concentration of 4-nitrophenol was prepared and was used to create a calibration curve of the concentration of 4-nitrophenol in the solution versus the intensity of the absorption at 317 nm. Due to the high rate of the reduction of 4-NP, the separation of the catalyst from the reaction mixture which is submitted to UV-VIS analysis is realised with hydrophilic syringe filters. For this reason, the same set of standard aqueous solutions was filtered and submitted to UV-VIS to measure the effect of the filters to the registered UV-VIS intensity.

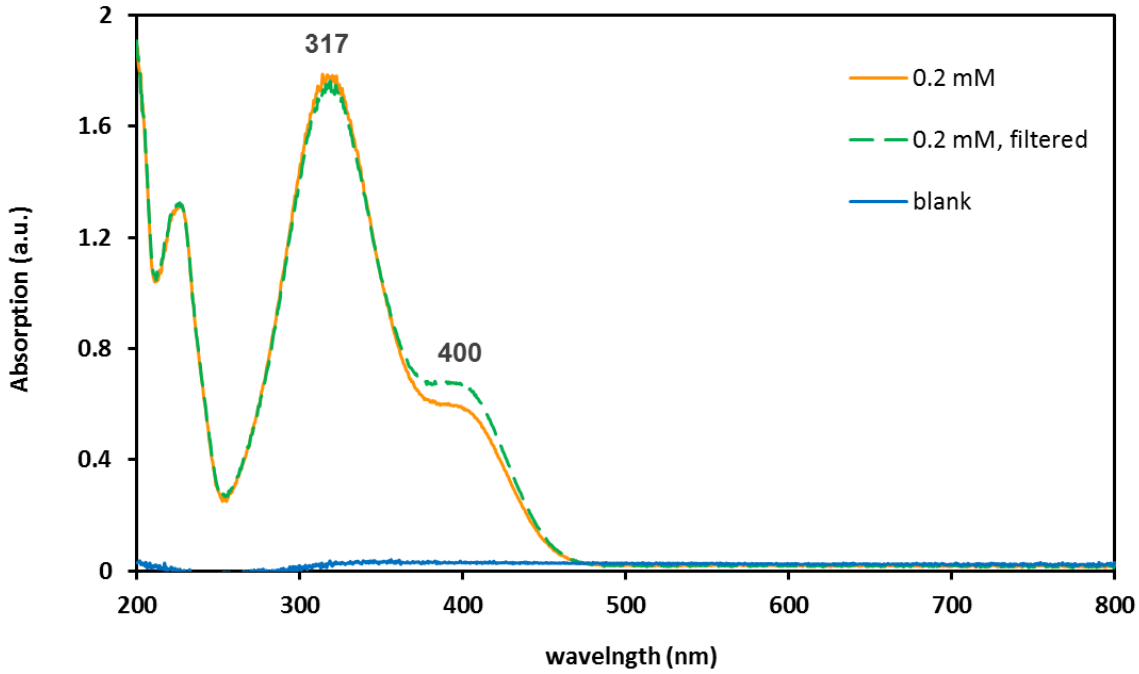

Figure 5.1 Typical UV-VIS spectra of 4-nitrophenol aqueous solution with and without filtering, where the peak of 4-nitrophenol appears intense at 317 nm and the shoulder at 400 nm corresponds to the 4-nitrophenolate anion. The blank shows the response of the instrument in the absence of a sensitive molecule (deionized water in quartz cuvette).

The dashed line in Figure 5.1 indicates the spectrum acquired after the filtration of the standard solution 0.2 mM. One can notice that passing the solution of 4-nitrophenol through a syringe filter, the intensity of the main peaks differ. As such, a second calibration curve was created and used accordingly. For example, the fitting of the non-filtered data was used for the measurement of the starting solutions, as the sampling occurred before the addition of the catalyst. Similarly, progress of the reactions of blank solutions was measured in the same way. Samples of solutions with catalyst were measured after filtering and, naturally, they were analysed using the curve corresponding to the filtered solutions. The calibration curves are linear fittings of the intensity as Lambert-Beer law predicts. They are plotted in Figure 5.2 and correspond to the inset figure of spectra.

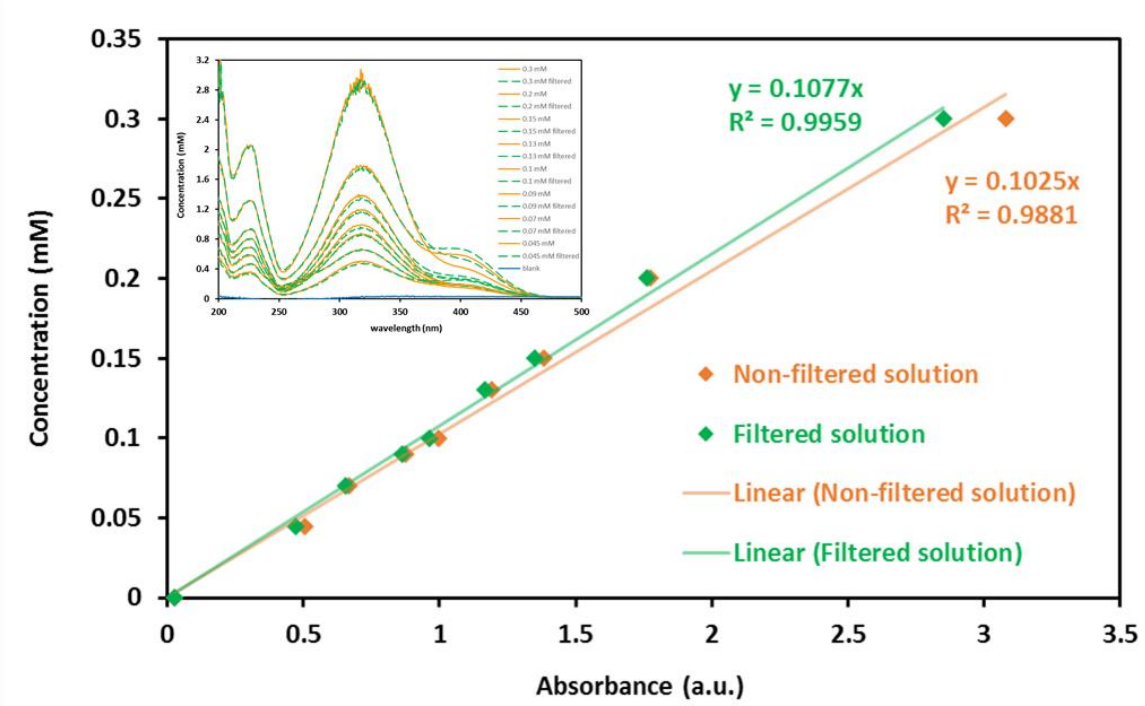

Figure 5.2 Calibration curve for the correlation between the absorption intensity and the concentration of 4-nitrophenol in aqueous solutions. The inset plot corresponds to the spectra obtained for the standard solutions ranging from 0.045 mM to 0.3 mM.

It should be noted that 4-aminophenol is reported to be sensitive via UV-VIS at 300 nm. In the lack of 4-aminophenol, a calibration curve for the product of the reduction was not obtained. However, the appearance of a peak at 300 nm is attributed to the formation of 4-aminophenol.

5.2.3 Catalytic results of the conversion of 4-nitrophenol to 4-aminophenol

Although the type of the reaction under study in this project (reduction of 4-nitrophenol to 4-aminophenol) is different from the type or the reaction studied in Chapter 4 (CDC reaction between PhTHIQ and nitromethane), the catalyst first employed for the current project is ZIF-9, because it was the best performing photocatalyst and a good performing catalyst for the CDC application. The catalyst was added at 0.5 mg/mL. From observations, the effect of the catalyst in the absence of the reducing agent is interesting. After the addition of the catalyst, the peak at 400 nm becomes very intense, which means that the hydrolysis of 4-nitrophenol to 4-nitrophenolate anion is being enhanced or accelerated. However, it is not obvious whether ZIF-9 has another effect on 4-nitrophenol or the ion. For this reason, it was opted to run first a long

experiment, where 4-nitrophenol aqueous solution was mixed with ZIF-9 at the concentration of 1 mg/mL and was let in the dark for 75 hours. Regular sampling was performed and the results are plotted in Figure 5.3.

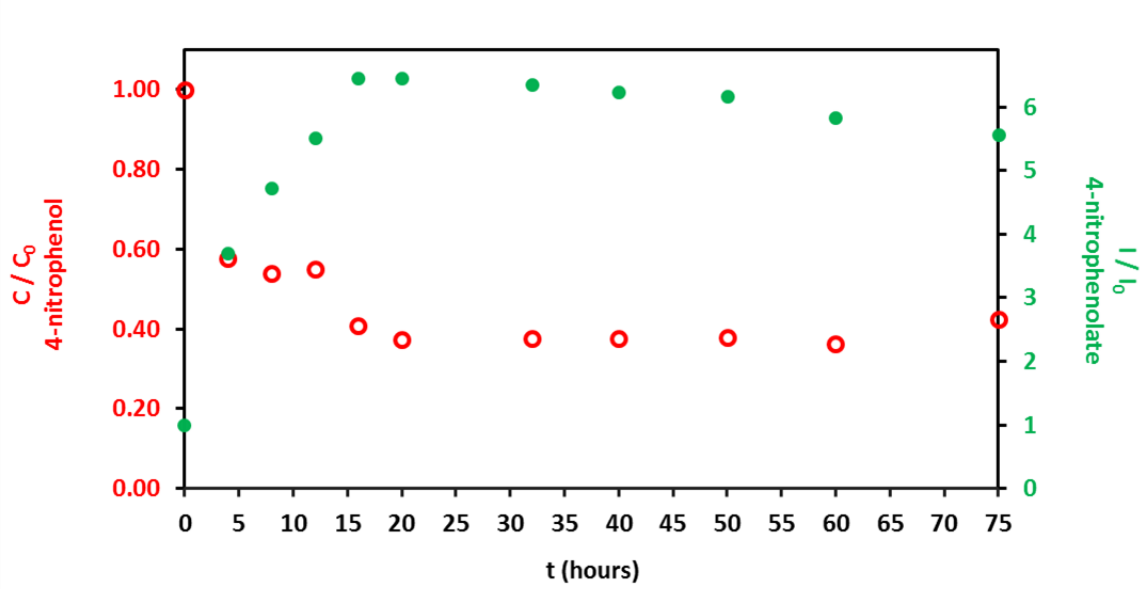

Figure 5.3 Drop of concentration of 4-nitrophenol and increase of intensity of peak of 4-nitrophenolate over 75 hours of stirring ZIF-9 with 4-nitrophenol aqueous solution in the dark.

Having established from the previous experiment that the catalyst is not able to reduce in the dark the peak of 4-nitrophenolate at 400 nm without the presence of the reductant ($NaBH_4$), the following experiment was designed so that the catalyst is added at 0.5 mg/mL and is kept under stirring at ambient conditions in the dark for 1-2 minutes. Then, $NaBH_4$ was added as a solid and stirring is kept between 700 and 750 rpm. From the moment of the addition of the reducing agent, the progress of the solution was monitored regularly.

The first sampling regards the starting solution before the addition of the catalyst at wavelength 317 nm. The second sampling regards the solution after the addition of the catalyst in the absence of the reducing agent, in order to register the effect of the catalyst in the solution during the phase of the dispersion of the solid in the mixture. The wavelength of interest for the second sampling is 400 nm. With the addition of $NaBH_4$, the reaction starts and the activity of the catalyst is being evaluated, with $NaBH_4$ at different molar ratios. The wavelengths of interest regard the peak at 317 nm (4-nitrophenol), but primarily the peaks at 400 nm (4-nitrophenolate) and at 300 nm (4-aminophenol). For this reason, the progress of the reaction is being plotted according to the concentration of 4-

nitrophenol at wavelength 317 nm (Figure 5.4) and according to the intensity of the peak at 400 nm, which regards the 4-nitrophenolate ion (Figure 5.5). The inset plots regard the first 5 minutes of the reaction.

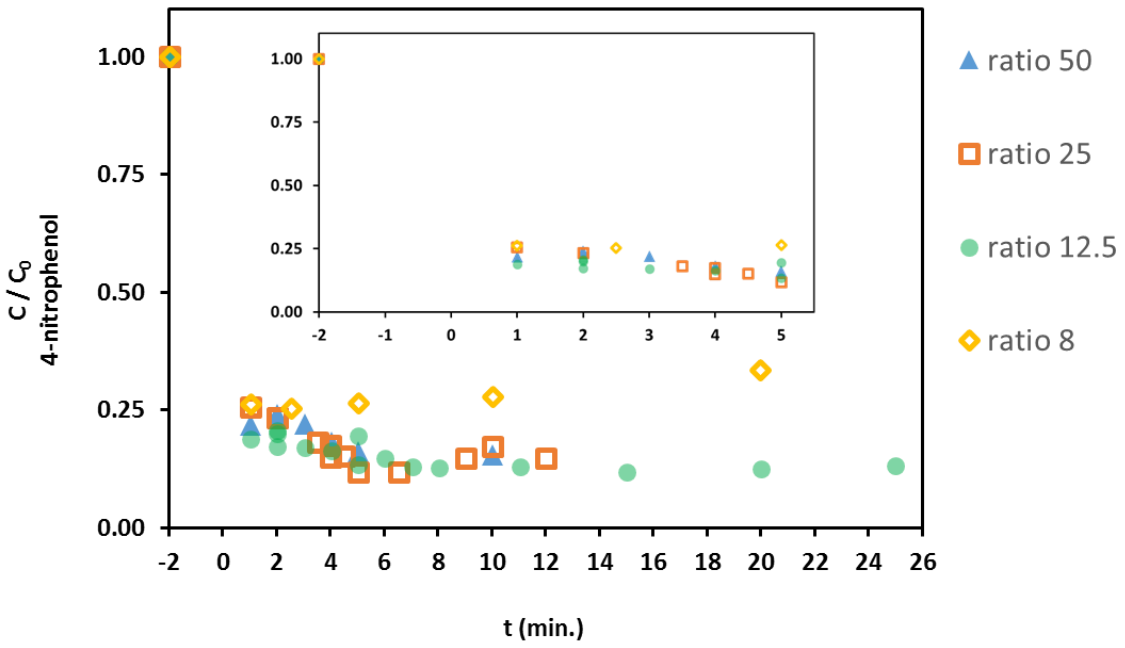

Figure 5.4 Decrease of concentration of 4-nitrophenol in the presence of ZIF-9 and $NaBH_4$ at molar ratios 50, 25, 12.5 and 8, in the dark.

The decrease of the concentration of 4-nitrophenol with time in the presence of ZIF-9 and $NaBH_4$ ranges at similar levels, regardless of the molar ratio of the reducing agent over the substrate. In fact, the inset plot of Figure 5.4 shows that the deepest decrease occurs during the first minute of reaction and further decrease observed is slight. However, the interest focusses on the next plot (Figure 5.5), because it shows the simultaneous behaviour of the intensity of the peak at 400 nm for the ion.

It should be noted that the intensity of the peak at 400 nm of the spectra varies and for this reason, the results are normalised. The vertical axis hosts the ratio of the intensity of the peak at 400 nm to the highest intensity of the same peak recorded during the reaction. This ensures the best comparison between the spectra of different ratios since all data are transformed from values of absolute intensity to relative values ranging from 0 to 1.

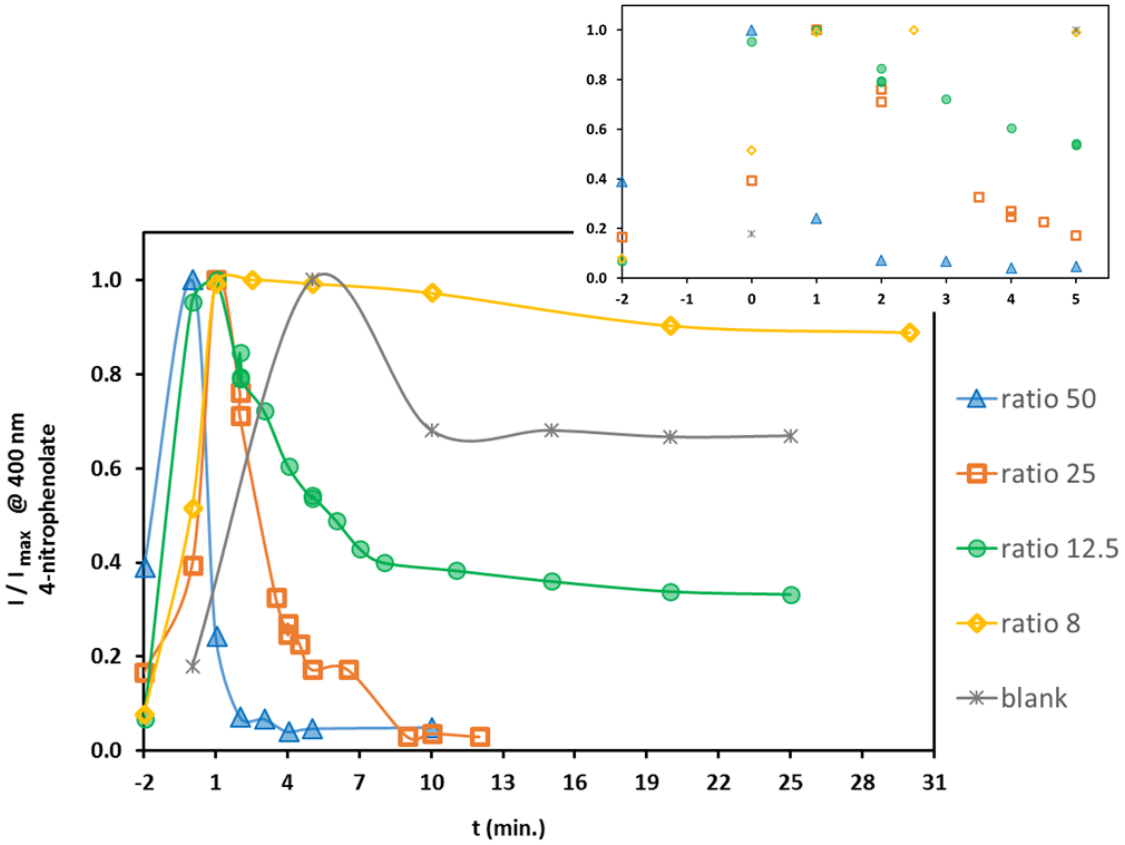

Figure 5.5 Ratio of intensity of peak at 400 nm (4-nitrophenolate ion) versus time of reaction between 4-nitrophenol and $NaBH_4$ at different molar ratios of reducing agent over substrate.

Observing the plots of Figure 5.5, the catalytic activity of ZIF-9 in the presence of $NaBH_4$ is obvious and dependent on the ratio of the reducing agent over the substrate. At molar ratio 50, the peak at 400 nm has been reduced by ca. 75% in the first minute of the reaction and after the second minute, the peak has dropped another 20%. Halving the molar ratio at 25, it takes longer time for the peak to start reducing, which could be interpreted as an induction time. Consequently, within the first minute, the peak is intensified by 60%. After this induction time, the achieved reduction is 30-35% in the next two minutes, an additional reduction of 40-45% is achieved in the next 2.5 minutes and reaches the level of 90% reduction after overall 10 minutes.

Halving the ratio further at 12.5, the peak at 400nm is initially enhanced and then starts reducing gradually at a lower rate. While it behaves similarly to the ratio 25 during the first 3-4 minutes, the rate of the reduction slows down and after overall 8 minutes, the reaction seems to have reached the lower levels achieving a total reduction no more than 65%. At ratio 8, the reducing agent is not enough to achieve reduction and the peak at 400 nm is levelled at high intensities. However,

comparing to the blank (absence of catalyst), the intensity of the peak at 400 nm is higher when the catalyst is present. Although this appears to be a paradox, one should consider that the molar ratio between the reducing agent and the substrate is 6.25 times higher when no catalyst is used.

At the same time, the behaviour of the precursors of ZIF-9 in the reaction exhibits another interesting piece of information. In detail, the precursors of ZIF-9 are the raw materials used for the cobalt nodes and the organic linkers of the hybrid scaffold. Cobalt nitrate and benzimidazole are, therefore, used separately and combinatorically in this reaction with a molar ratio of reducing agent over substrate equal to 50 and the spectra are shown in Figure 5.6.

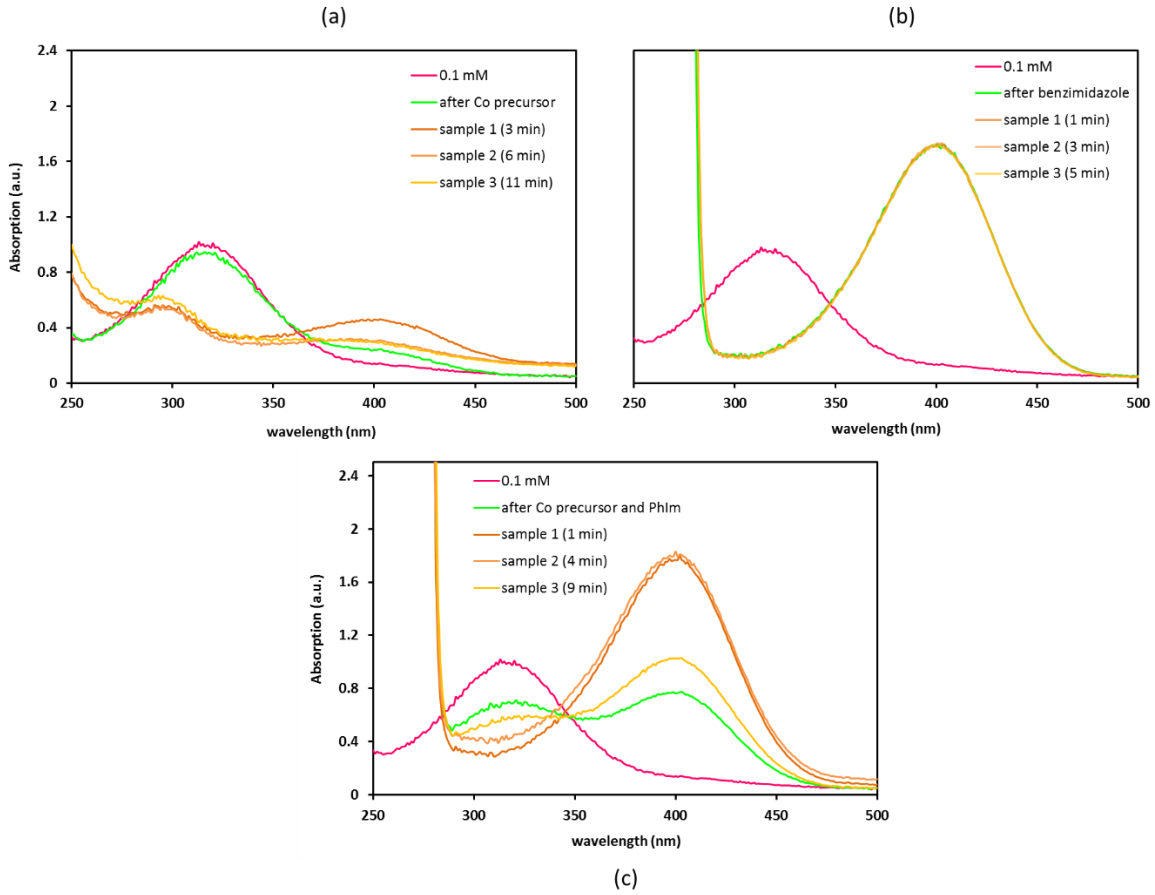

Figure 5.6 Spectra obtained during the reaction of 4-nitrophenol with $NaBH_4$ at molar ratio 50 in the dark, in the presence of cobalt nitrate (a), benzimidazole (b) and their combination (c).

Figure 5.6(a) shows that the introduction of the cobalt precursor is responsible for the reduction of 4-nitrophenol to 4-aminophenol. The peak at 400 nm reduces over time of reaction, while a peak at 300 nm is formed, indicating the formation of 4-aminophenol. The benzimidazole molecule is responsible for the hydrolysis of nitrophenol with the shift of the peak from 317 nm to 400 nm, which does not

reduce over time (Figure 5.6(b)). It should be mentioned that the quantities used for these reactions correspond to the concentration 0.5 mg/mL. When the combination of the two precursors is used, each precursor is weighed to 0.25 mg/mL and the spectra in Figure 5.6(c) show a mixed behaviour of the two previous two cases.

Comparing with the results acquired for ZIF-9 at ratio 50 qualitatively, ZIF-9 is more active and faster than the cobalt precursor. At this point, it is possible to explain the differences between the cobalt species in ZIF-9 and the cobalt nitrate hexahydrate, the metal precursor. In both cases, cobalt is found at oxidation state II. However, the geometry is dissimilar; the cobalt in the precursor is associated with the ligands in an octahedral coordination, while it is in a tetrahedral coordination in ZIF-9. The difference between octahedral and tetrahedral geometry reflects the different splitting between the d orbitals along with the energy between them. In tetrahedral geometries, the energy difference is smaller and the top orbitals belong at a lower energy level, according to crystal field theory. This explains the insistence on taking into consideration the geometry since in tetrahedral structures the excitement of an electron from a d orbital to another d orbital of higher energy requires smaller quantum of energy (Figure 5.7).

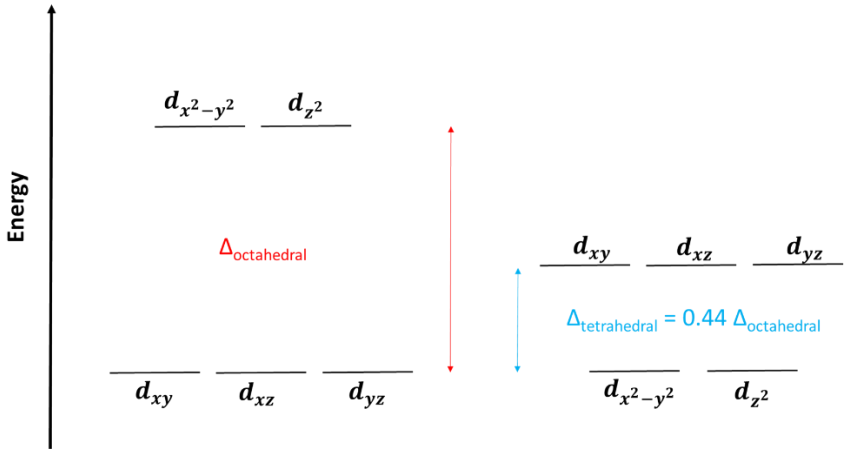

Figure 5.7 Representation of the splitting of the d-orbitals in an octahedral and a tetrahedral field.

Furthermore, cobalt nitrate and benzimidazole are diluted in the reaction mixture, while ZIF-9 is a recoverable solid, as it will be discussed later. A kinetic analysis in terms of the parameters that affect the rate of the reaction is also presented later in this chapter. It is interesting though to compare the overall reduction of the peak at 317 nm and 400 nm independently of the time needed.

In Figure 5.8, it is shown that the higher molar ratio can be linked to the higher overall conversion of 4-nitrophenol to 4-aminophenol.

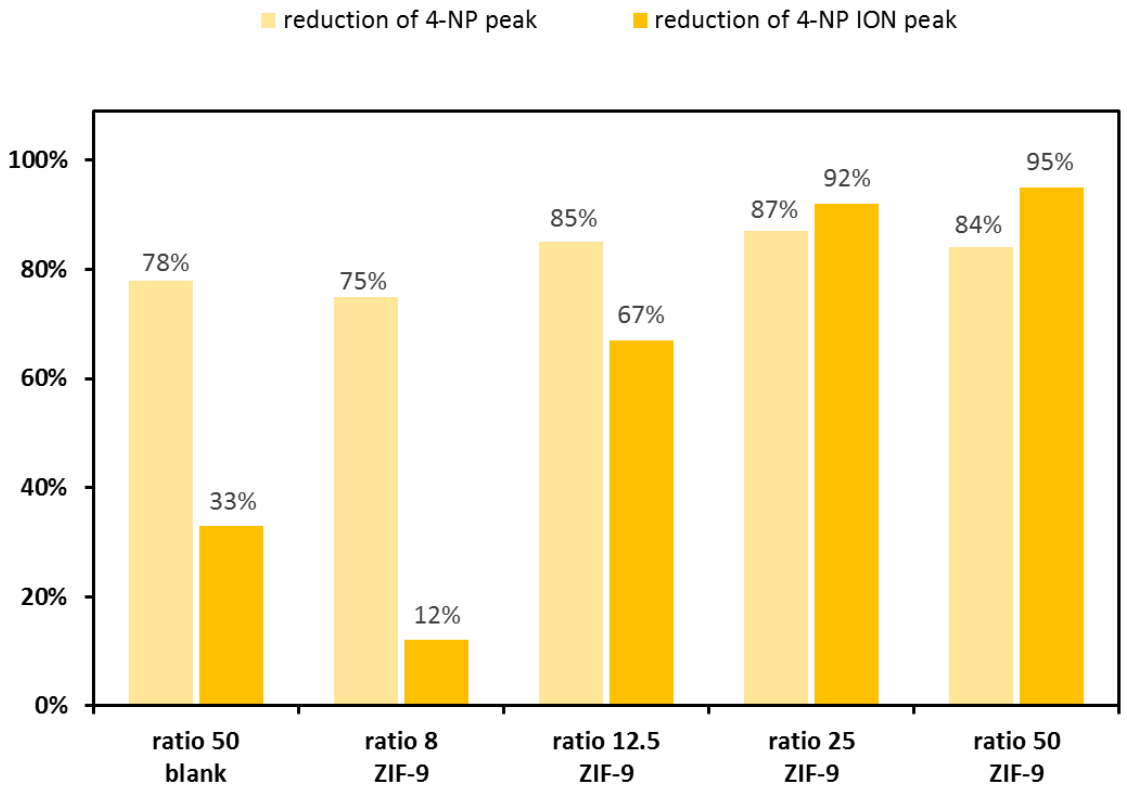

Figure 5.8 Overall reduction of the peak regarding the 4-nitrophenol and the 4-nitrophenolate ion, achieved in darkness with ZIF-9 at 0.5 mg/mL for different molar ratios between the reducing agent and the substrate.

Prior to any further study of the reaction with ZIF-9, it is useful to employ the rest of the catalysts in this reaction and compare their activity. From the plotted data in Figure 5.5 and Figure 5.8, the best ratio for comparative study is considered the molar ratio 25. The reaction at ratio 25 with ZIF-9 is fast but the rate is easier to measure than for ratio 50. Simultaneously, the ratio 25 gives a very high reduction percentage. Consequently, it is selected to probe the activity of the rest of the catalysts (CoAlPO-5, CoMOF-4, CuAlPO-5 and HKUST-1) in the darkness for the reduction of 4-nitrophenol to 4-aminophenol. The results are normalised accordingly and are plotted in Figure 5.9.

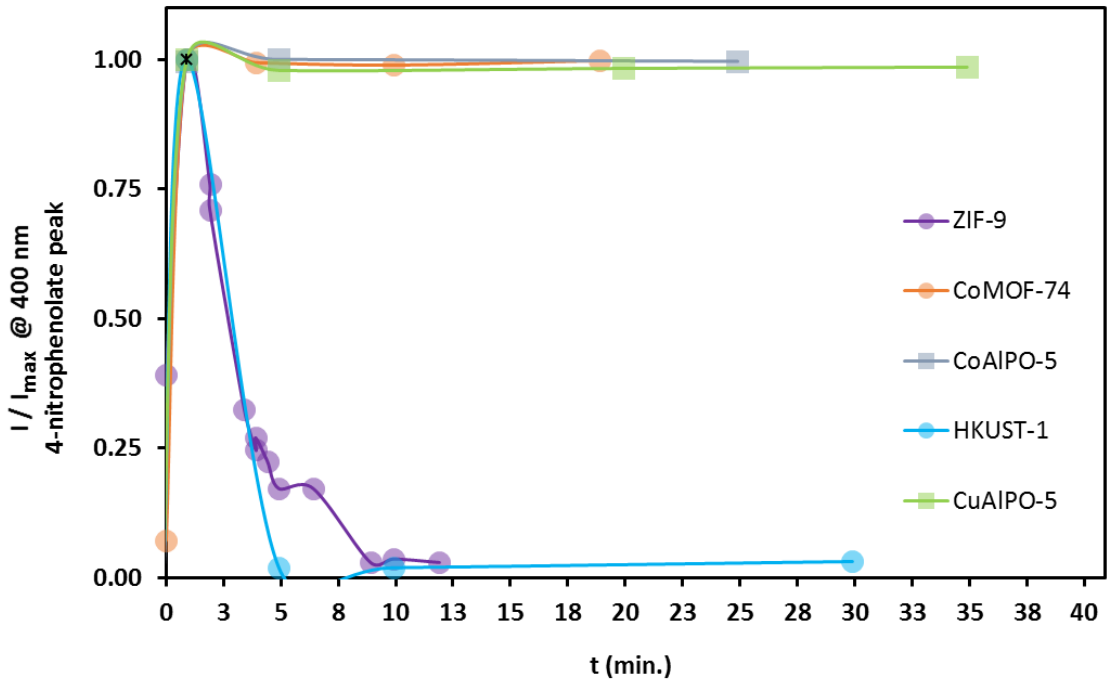

Figure 5.9 Comparative activity of catalytic materials for the reduction of the peak at 400 nm, corresponding to the 4-nitrophenolate ion, at molar ratio of reducing agent and substrate equal 25 and in the darkness.

The plot in Figure 5.9 demonstrates that the AlPO materials (CoAlPO-5 and CuAlPO-5) and CoMOF-74 are not suitable for this reaction, as unable to reduce the intensity of the peak over time. It is important to highlight here that all these materials have some features in common, as they exhibit 1-D channels and the biggest size particles among all the materials. On the other hand, HKUST-1 appears active. However, a closer look at the obtained spectra during the reaction and the disclosure of observational details reveal whether HKUST-1 is a functional catalyst for this reaction to study and deduce useful conclusions.

In more detail, the spectra depicted in Figure 5.10 show that, unlike ZIF-9, HKUST-1 does not promote the hydrolysis of the substrate to the ion. The green spectrum noted as “after catalyst” shows practically no difference from the pink line (starting solution – 0.1 mM) within the visible range. In the 1st minute, the spectrum absorbs intensively within the visible range. The elliptically shaped inset picture shows that the reaction acquires a dark brown colour while the rectangular inset picture shows how the reaction mixture is decolourized after the reaction has been completed. Between the 1st and 5th minute of the reaction, UV-VIS is not a suitable technique to monitor the progress of this reaction. One more interesting detail concerning the spectra pattern is the lack of evidence

around 300 nm, which would connect to the formation of 4-aminophenol. For these reasons, HKUST-1 is not shortlisted as a catalyst to study in this reaction, with the available techniques of analysing the data.

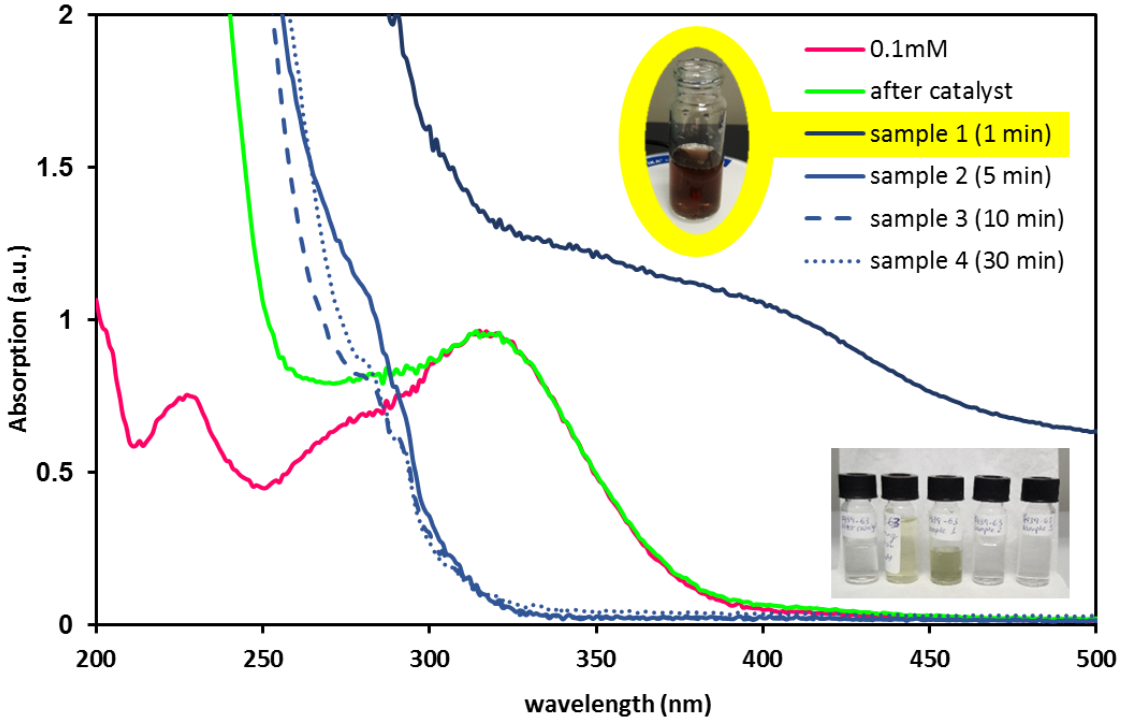

Figure 5.10 Spectra of samples obtained at 1st, 5th, 10th and 30th minute of reaction of 4-nitrophenol with $NaBH_4$ in the dark and in the presence of HKUST-1.

Reminding here the structural characteristics of HKUST-1, the material has a complex geometry of voids with copper(II) in dimeric configuration. Upon activation, HKUST-1 discloses open metal sites, which are known to coordinate fast with a water molecule. HKUST-1 is known as a material that interacts highly with hydrogen, while ZIF-9 has been reported in similar applications. However, ZIF-9 does not exhibit water sensitivity; on the contrary, the benzimidazole ligands give a hydrophobic nature to the material, which could possibly function protectively for the framework of ZIF-9 in aqueous reactions.

5.2.4 Catalysis and photocatalysis of the reduction of 4-nitrophenol to 4-aminophenol with ZIF-9: A kinetic approach

There are a few parameters that affect the rate of the reaction, as literature supports, such as pH and temperature.[39] The hydrogen evolution from $NaBH_4$ and nitrophenol are exothermic reactions, hence the rise of the temperature is

expected to facilitate the reaction. Similarly, the higher pH with the addition of NaOH is also expected to facilitate a reduction, since reductive reactions are hard to be realised in an oxidative environment. In most cases, the reaction is reported to occur with a high excess of reducing agent and only a few times the concentration of the catalyst is taken into consideration. For this reason and for the reason that ZIF-9 is a new catalyst, it is considered useful to vary these two parameters (molar ratio of reductant over substrate and catalyst's concentration) and analyse how the rate of the reaction is affected.

The molar ratio of $NaBH_4$ and 4-nitrophenol is the first parameter under study, as presented in the section 5.2.3. For the kinetic analysis and for a comparable basis, the data into account are based on the peak at 400 nm, are normalised as a ratio to the overall highest intensity and calculated logarithmically for more impactful differences. For an initial qualitative comparison, the points that regard the induction times of the reaction are omitted. Linear fitting is attempted and the results regarding the ratios 50, 25, 12.5 and 8 are plotted in Figure 5.11.

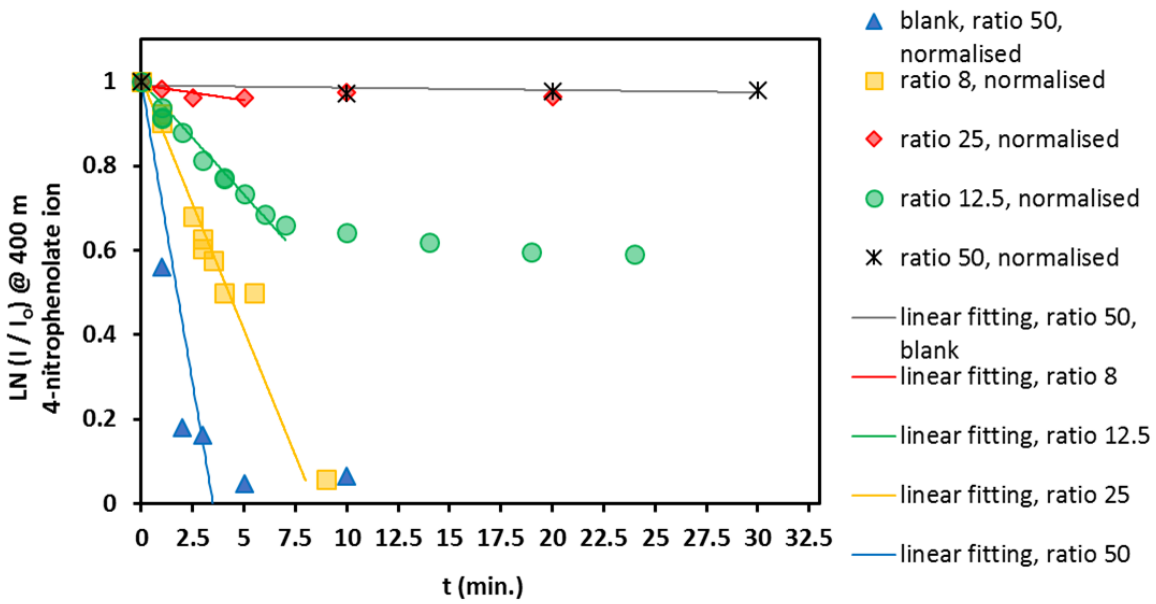

Figure 5.11 Qualitative comparison of the kinetic analysis obtained for the reduction of 4-nitrophenolate to 4-aminophenolate with $NaBH_4$ and ZIF-9 at 0.5 mg/mL for different ratios of reducing agent over substrate.

Figure 5.11 demonstrates clearly that the molar ratio of the reductant over the substrate influences directly the rate of the reaction. Increasing the ratio accelerates the reduction, which is apparent from the steeper fitted lines of the data. In the absence of catalyst, the reaction does not exhibit any progress, while

for a ratio as low as 8, the rate is slow and the achieved conversion is low. Only the data that showed a continuous change were taken into account for the linear fitting.

Detailed and quantitative kinetic analysis is presented hereafter for each of the ratios under study, with induction times included for further comparison. The data are normalised to the highest intensity recorded for the peak at 400 nm for the specific ratio. The points of induction time, of reaction in progress and of reaction being complete are marked with different colours and only the middle points are taken into account for the fitting, noted as “reaction progress”. Figure 5.12 to Figure 5.15 regard the kinetic study for molar ratio 50, 25, 12.5 and 8, progressively.

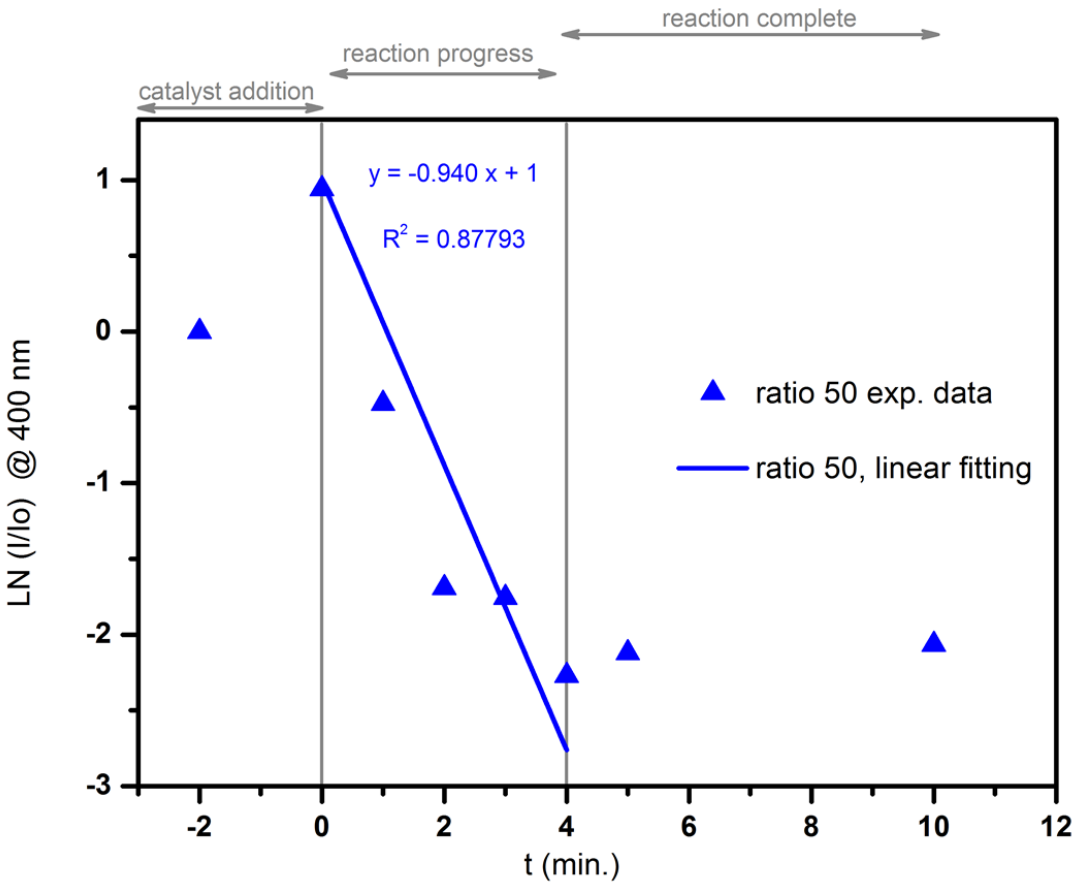

Figure 5.12 Experimental data for ratio 50 and linear fitting of data, regarding the reduction of 4-nitrophenol with $NaBH_4$ in the presence of ZIF-9 at 0.5 mg/mL in the dark.

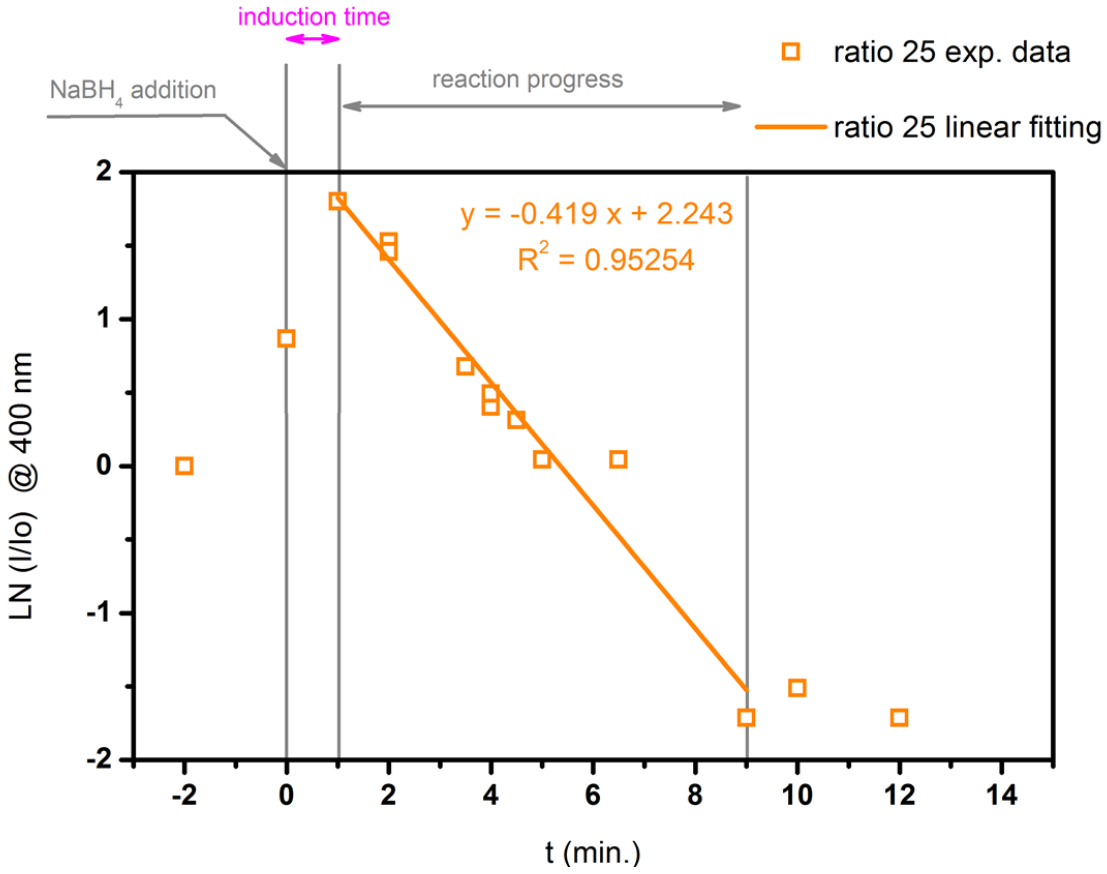

Figure 5.13 Experimental data for ratio 25 and linear fitting of data, regarding the reduction of 4-nitrophenol with $NaBH_4$ in the presence of ZIF-9 at 0.5 mg/mL in the dark.

The successful linear fitting is indicative of first-order reaction, according to the transformation of the mathematic equation that describes the rate for first-order reaction, as shown in Equation 5.1.

$$[rate] = -\frac{d[A]}{dt} = k \cdot [A] \Leftrightarrow \frac{d[A]}{[A]} = k \cdot dt \xLeftrightarrow{\int_o^t} \ln\left(\frac{[A]_t}{[A]_o}\right) = -k \cdot t \qquad \text{Equation 5.1}$$

However, the slope of the linear fitting changes with the change of the ratio of the reducing agent $NaBH_4$ over the substrate 4-nitrophenol. Subsequently, a pseudo-first order reaction describes better the kinetic analysis. For a given ratio, the reaction depends on the concentration of the substrate, but essentially the reaction is dependent on the concentration of both the substrate and the reductant.

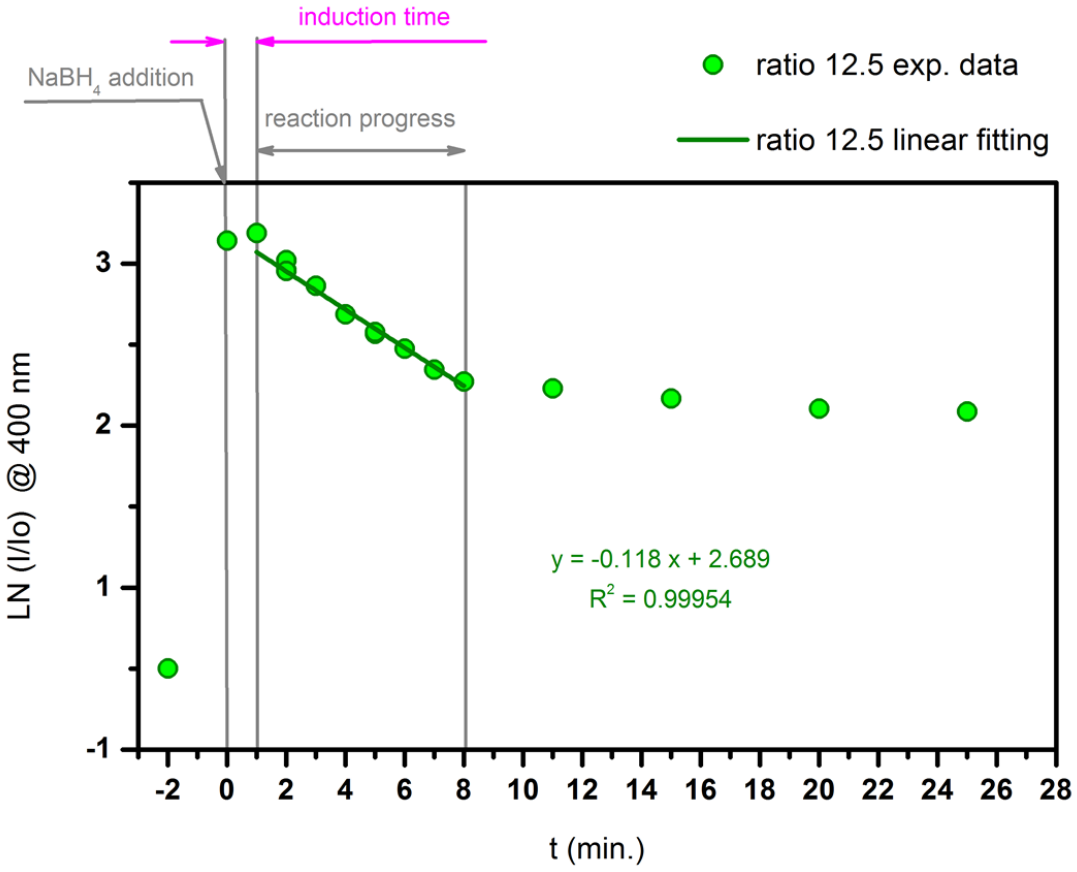

Figure 5.14 Experimental data for ratio 12.5 and linear fitting of data, regarding the reduction of 4-nitrophenol with $NaBH_4$ in the presence of ZIF-9 at 0.5 mg/mL in the dark.

The progressive change of the slope with the change of the molar ratio is obvious from the plots. The induction time is not significant since there seems to be one minute between the moment of the addition of the reducing agent and the reduction of the peak of 4-nitrophenolate only for the ratio 12.5. For the rest of the cases, the reduction seems to start directly after the addition of $NaBH_4$.

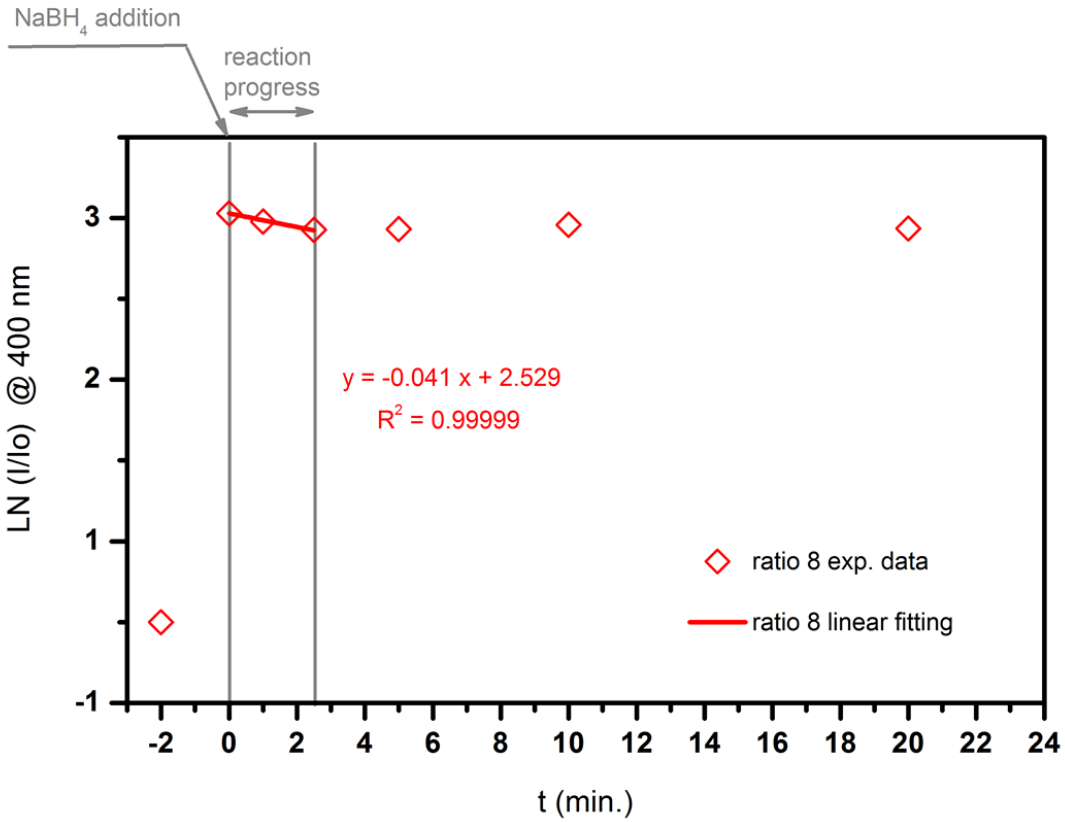

Figure 5.15 Experimental data for ratio 8 and linear fitting of data, regarding the reduction of 4-nitrophenol with $NaBH_4$ in the presence of ZIF-9 at 0.5 mg/mL in the dark.

Tabulating the rate constants (slopes) for all the ratios under study in Table 5.2 for comparative reasons, it is apparent that, as the ratio of the reductant over the substrate decreases, the reaction slows down significantly. In fact, for the lowest ratio under study, ratio 8, the rate constant is approximately 0.04 s^{-1}. Combining it with the data in Figure 5.8, the molar ratio affects both the totally achieved conversion and the rate of the reaction.

Table 5.2 Rate constants for the reduction of 4-nitrophenol in the presence of ZIF-9 at 0.5 mg/mL in the dark for different ratios of reducing agent over substrate.

Molar ratio ($NaBH_4$: 4-nitrophenol)	Rate constant (s^{-1})	Remarks
50	0.940	k_1
25	0.419	$k_2 \approx {}^{k_1}/_2$

Molar ratio ($NaBH_4$: 4-nitrophenol)	Rate constant (s^{-1})	Remarks
12.5	0.118	$k_3 \approx {}^{k_1}/_{8}$
8	0.041	$k_4 \approx {}^{k_1}/_{23}$

Another important observation that should be mentioned regards the intensity of the peak at 400 nm after the addition of the reducing agent. In Figure 5.11, the plots are normalised to the highest intensity remarked among all the intensities for reasons of qualitative comparison of the rate of the reaction. Figure 5.16 demonstrates the plotted data normalised to the highest intensity registered for each ratio. It is obvious that the higher the molar ratio is, the smaller the increase of the intensity of the peak of the ion is.

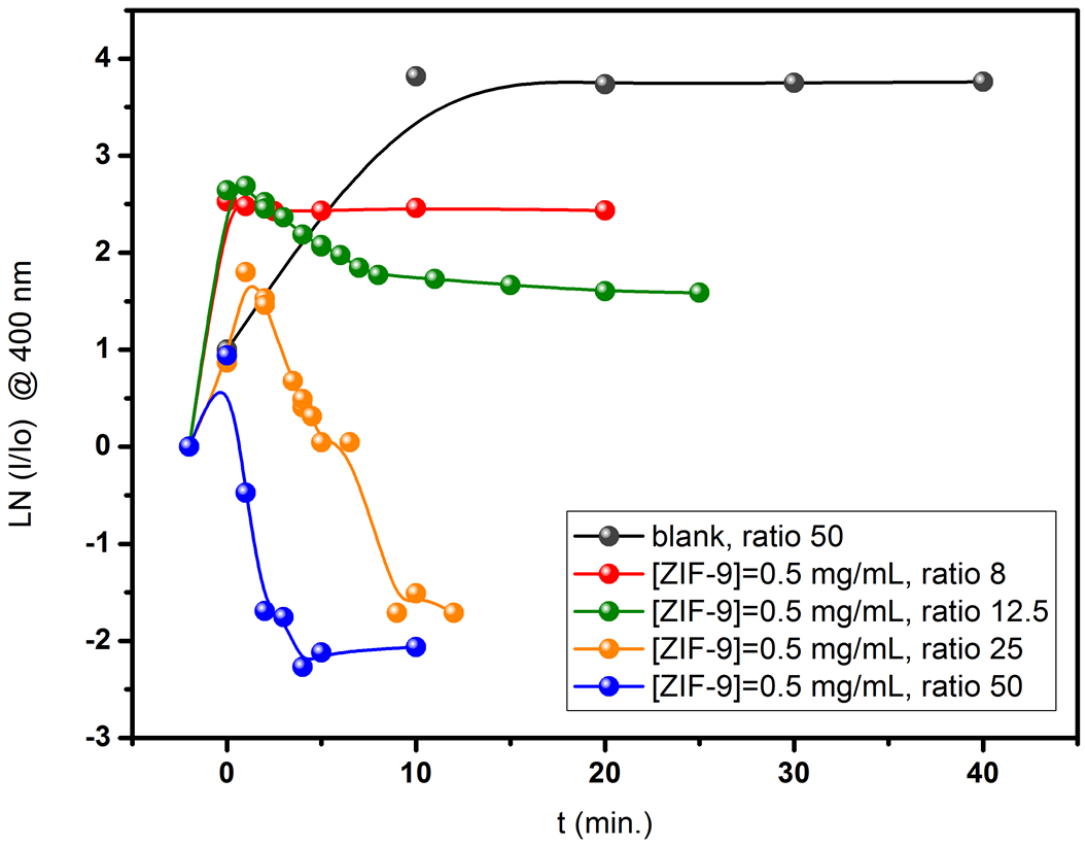

Figure 5.16 Qualitative comparison of the intensity of the peaks at 400 nm in the reaction of 4-nitrophenol with $NaBH_4$ at different ratios in the presence of ZIF-9 at 0.5 mg/mL.

In order to investigate the influence of the concentration of ZIF-9, a relevant set of experiments was carried out. A progressive reduction of the concentration starting from 0.5 mg/mL is performed at molar ratio 12.5. The high rate of the reaction at molar ratios 50 and 25 turns these ratios hard to control and monitor the reaction, while the slow rate of the reaction and the inability to obtain a moderate conversion at molar ratio 8 leads the choice of study at ratio 12.5.

Figure 5.17 refers to the experimental data acquired for ZIF-9 at a concentration of 0.3 mg/mL and at molar ratio 12.5. As demonstrated in the plot, the reaction did not proceed enough after ca. 6 minutes in terms of conversion, while the rate is slower compared to the rate for ZIF-9 at 0.5 mg/mL. For this reason, addition of reducing agent was performed in two more increments (phase 2 and 3). For the addition of $NaBH_4$, the deduction of the volume of the previous samples was taken into account so that the extra amount of $NaBH_4$ agrees with the molar ratio 12.5.

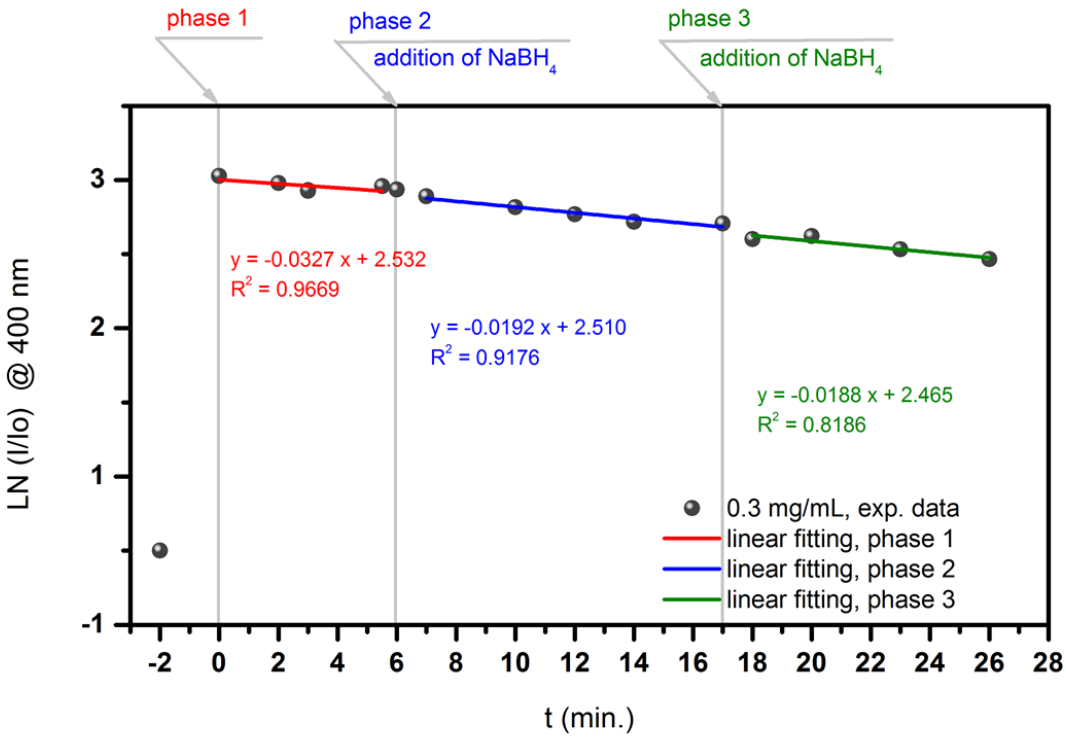

Figure 5.17 Experimental data for ratio 12.5 and linear fitting of data, regarding the reduction of 4-nitrophenol with $NaBH_4$ in the presence of ZIF-9 at 0.3 mg/mL in the dark.

The main observations for this set of data regard the high impact of the decrease of the concentration of the catalyst on the rate of the reaction, with the rate constant decreasing from 0.12 s^{-1} to 0.03 s^{-1}. The decrease is almost fourfold,

while the rate slows more, even after addition of extra reducing agent. However, addition of reducing agent keeps the reaction in progress. A similar experimental strategy was followed for ZIF-9 added at a concentration of 0.1 mg/mL as Figure 5.18 shows.

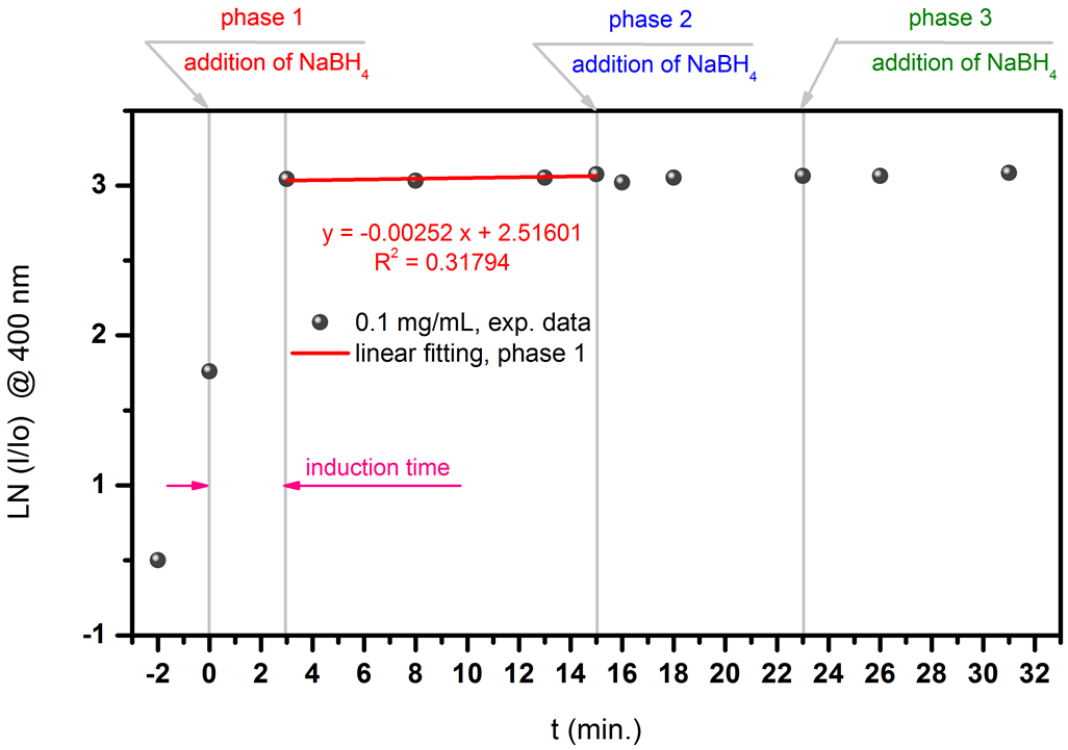

Figure 5.18 Experimental data for ratio 12.5 and linear fitting of data, regarding the reduction of 4-nitrophenol with $NaBH_4$ in the presence of ZIF-9 at 0.1 mg/mL in the dark.

However, the results for this concentration of ZIF-9 are not similar. On the contrary, the intensity of the peak at 400 nm only rises, as the sampling at 3 minutes after the addition of $NaBH_4$ proves. During the first 15 minutes of the reaction, no evidence of reduction appears. Further addition of reducing agent after the first 15 minutes and after another 8 minutes was not able to activate any reactants and the reaction seems unable to proceed. Consequently, one can conclude that a concentration of 0.1 mg/mL of ZIF-9 in the reaction mixture is not sufficient for reaction progress, independently of the presence of reducing agent.

In order to gain a better understanding of the impact of the molar ratios and the catalytic concentration on the kinetics of the reaction, a correlation of the rate constants versus the molar ratios is attempted. Figure 5.19 shows that there is a

linearity between the ratios and the rate constants. Hence and at least for a concentration of ZIF-9 at 0.5 mg/mL, the rate could be predictable. Moreover, the kinetic regime potentially remains unchangeable and follows the pseudo-first order. The inset plot is a zoom-in of the rate constants for ratio 12.5 at lower ZIF-9 concentrations.

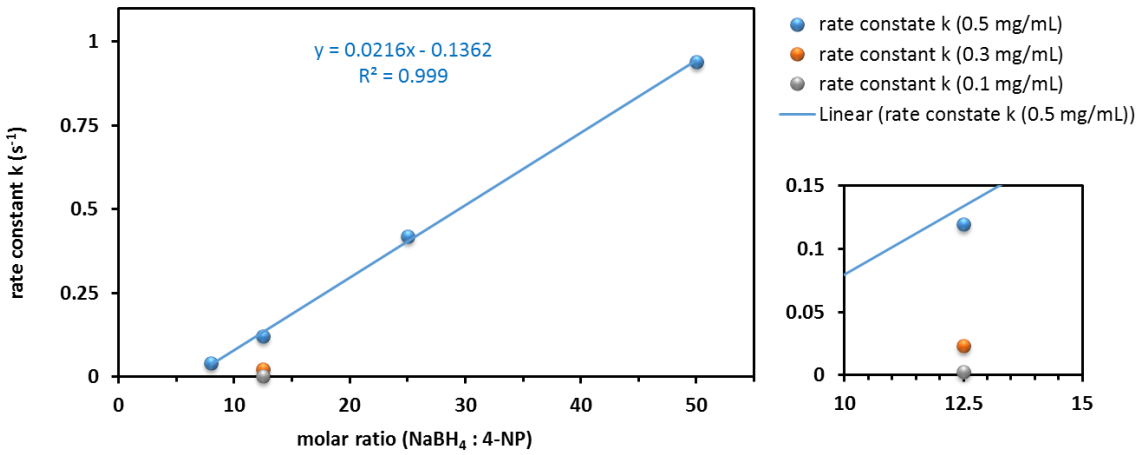

Figure 5.19 Plotted rate constants versus molar ratios of reducing agent over substrate for the reduction of 4-nitrophenol in the presence of ZIF-9 in the dark.

Calculating the effect of decreasing the catalytic concentration on the constant rate, a decrease of ZIF-9 content from 0.5 to 0.3 mg/mL slows down the reaction by 80% and a further decrease from 0.3 to 0.1 mg/mL annuls the reaction totally, for a molar ratio 12.5. Plotting the total reduction achieved regardless the time needed as shown in Figure 5.20a is good evidence that the reaction is strongly catalytic and that ZIF-9 at a concentration above 0.3 mg/mL for a ratio of reductant over 4-nitrophenol equal to 12.5 is able to advance the reaction by or over ca. 50%. Plot b in Figure 5.20 shows the effect of the $NaBH_4$ molar ratio variance for a concentration equal to 0.5 mg/mL.

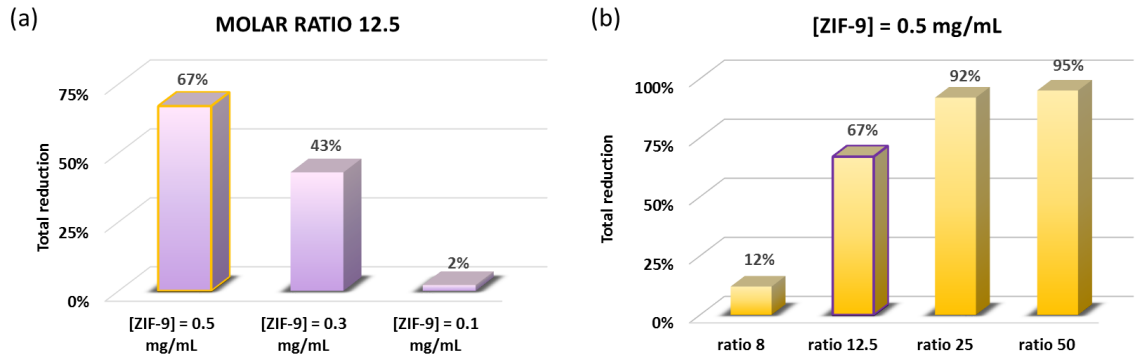

Figure 5.20 Overall reduction of 4-nitrophenolate ion achieved with ZIF-9 at different molar ratios of reductant over substrate and catalyst concentrations.

Plotting these results, as shown in Figure 5.21, it becomes evident that there is a linearity between the concentrations of ZIF-9 and the achieved reduction for a specific molar ratio. Although the concept of stoichiometry of the solid with the substrate does not exist in heterogeneous catalytic reactions, the results can be indicative of the number of active sites needed for the reaction.

The turnover number and frequency are usually a more acceptable, academically, magnitude for comparison of catalytic activity. However, in the case of the heterogeneous catalysts, its calculation requires specific methods, in order to measure the number of active sites applying chemisorption techniques. Similarly, the ICP values of fresh ZIF-9 can be used theoretically for the estimation of the active sites. For example, the case of 0.5 mg/mL catalyst concentration corresponds to a very high number of atoms of cobalt in the solution ($2.8 \cdot 10^{20}$). The assumption that all these atoms are equally dispersed in the bulk of the catalyst and function equally as active sites, results into unrealistically small TON ($1 - 10 \cdot 10^{-23}$) and TOF values ($\sim 8 \cdot 10^{-26}\ sec^{-1}$). For this reason, it is preferable to carry on the comparison using conversion and catalyst concentration.

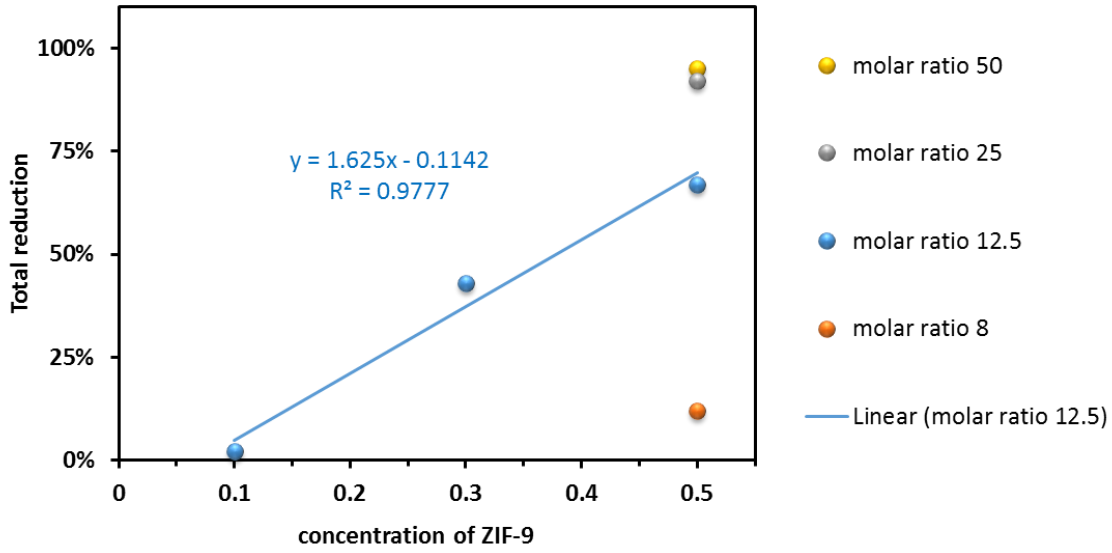

Figure 5.21 Plotted percentage conversion achieved versus concentration of ZIF-9 for the reduction of 4-nitrophenol with $NaBH_4$ at different ratios in the dark.

Further interpretation of the results includes the effect of the molar ratio to the total conversion. For the ratios 8, 12.5 and 25, it is apparent that higher ratio increases the achieved reduction. For catalytic concentration equal to 0.5 mg/mL, an increase of ratio from 8 to 12.5 improves the conversion achieved 4.6 times. Doubling up the concentration of ZIF-9 brings improvement by 37% and approximately completes the reaction. Judging from the behaviour of the constant rates at a lower ZIF-9 concentration, further increase of ZIF-9 in the reaction mixture would most probably accelerate the reduction achievement.

Having realized the influence of the molar ratio and the catalytic concentration or number of active sites to the rate and completion degree of the reaction, it is useful to evaluate one more parameter. With the example of the photocatalytic activity of ZIF-9 in the CDC application (Chapter 4), the influence of white (visible) light is under assessment. For this experiment, the case of molar ratio 12.5 is selected to be studied with concentration of ZIF-9 varying from 0 (blank) to 0.5 mg/mL, as previously. The reactions at this molar ratio in the dark demonstrated a controllable rate and conversion and thus, if light assists the reaction, its impact will be visible for this parameter. The volume of the reaction mixture is 25 mL and the white light shines directly the glass reactor via a filter which permits only visible wavelengths. Figure 5.22 hosts the spectra acquired for these reactions and the results are analysed further down.

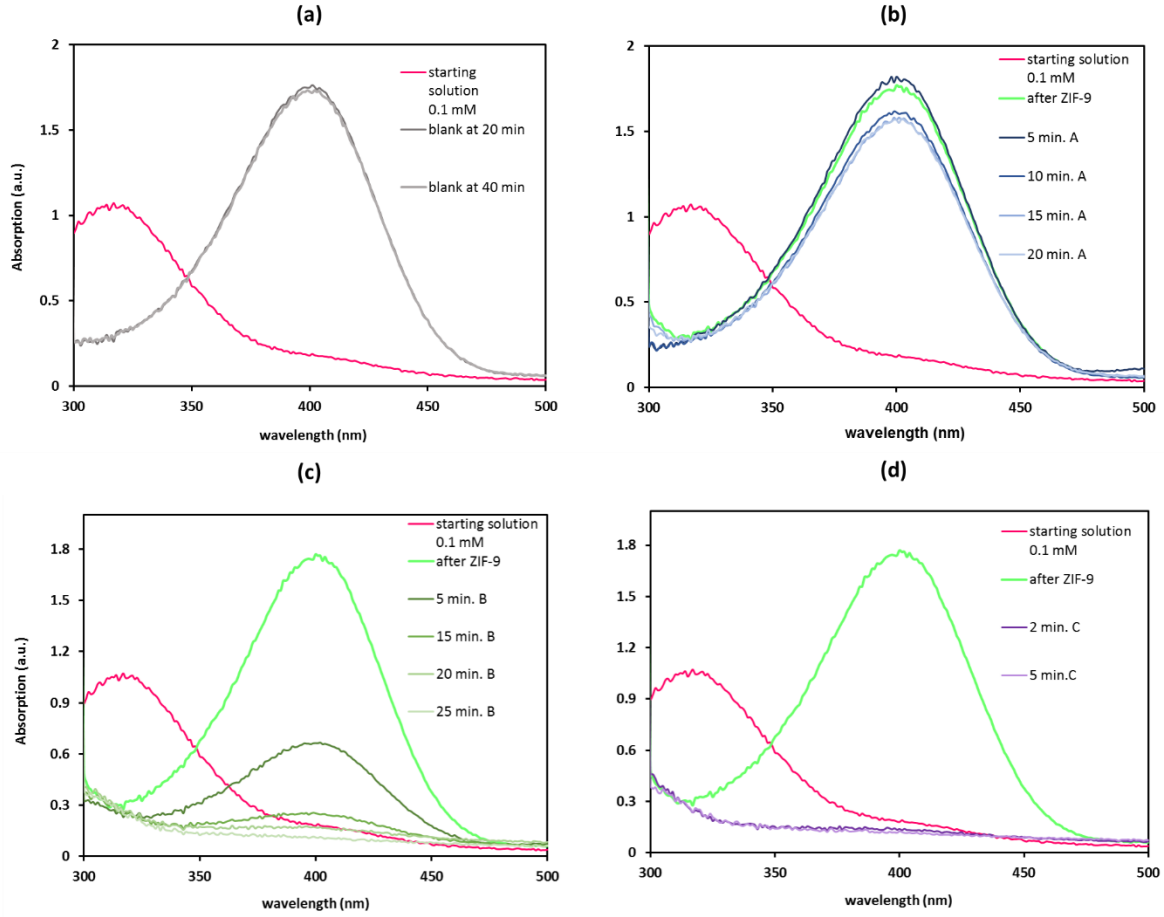

Figure 5.22 Spectra of 4-nitrophenol : $NaBH_4$ reaction mixture at molar ratio 1:12.5 under the irradiation of white light in the absence of ZIF-9 (mixture blank, plot a) and in the presence of ZIF-9 at concentration 0.1 mg/mL (mixture A, plot b), 0.3 mg/mL (mixture B, plot c) and 0.5 mg/mL (mixture C, plot d).

The corresponding spectra acquired from the reaction in the dark are found in Appendix C.1 for reasons of comparison. A qualitative evaluation of the spectra in Figure 5.22 convinces that the irradiation of light assists ZIF-9 significantly to catalyse the reduction of 4-nitrophenol. It should be noticed that the blank reaction (without ZIF-9) does not proceed under the irradiation of light, which indicates that there is practically no background reaction to take into account. Therefore, ZIF-9 is an efficient photocatalyst for the reduction of 4-nitrophenol. It is important to note that the material appeared as an efficient photocatalyst for the CDC reaction. Therefore, it is rational to consider that the same catalytic species are responsible for applications. A kinetic analysis of the results is worthwhile for comparison with the kinetic results obtained for the respective reaction in the dark. Figure 5.23 depicts the progress of the light-assisted reaction with time for various ZIF-9 concentrations.

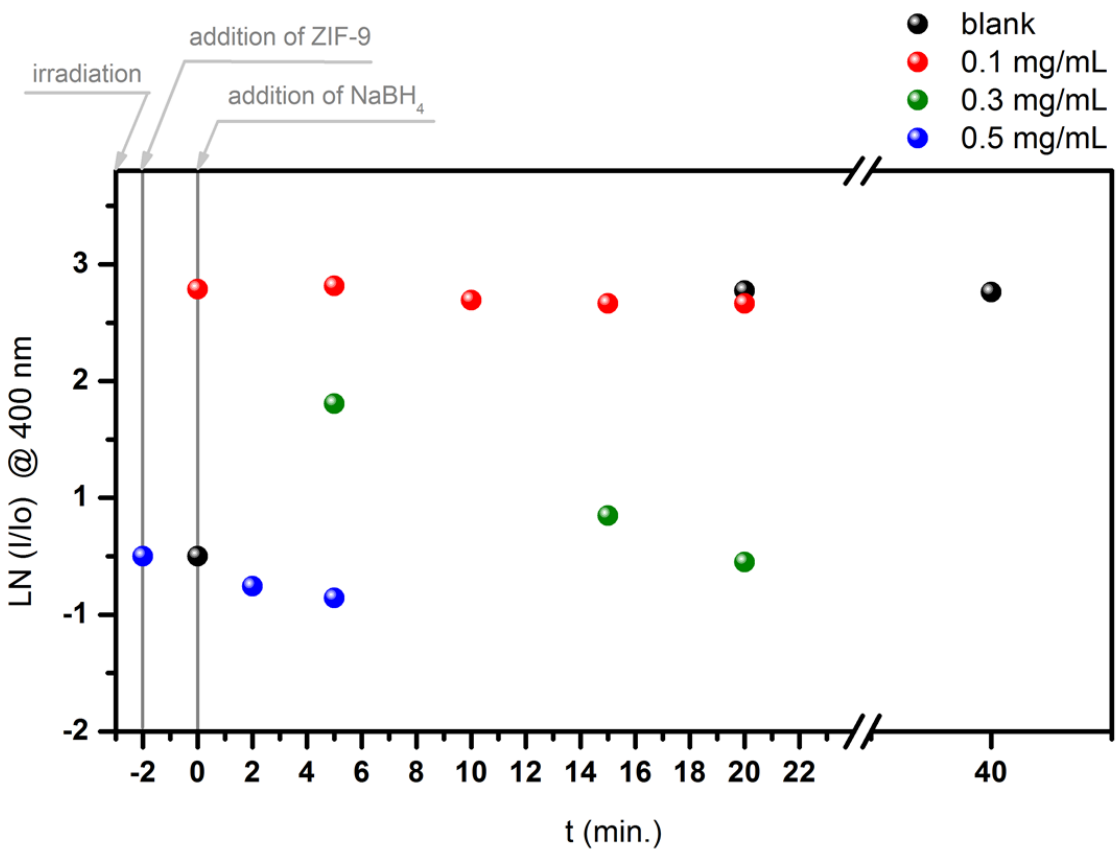

Figure 5.23 Experimental data for ratio 12.5, regarding the light-assisted reduction of 4-nitrophenol with $NaBH_4$ in the presence of various concentrations of ZIF-9.

Attempting linear fitting of the data, the rate constants that accrue from the calculations are tabulated in Table 5.3 and compared with the corresponding values for the reaction in dark. The increase of the rate is obvious in the previous cases, except for the case that the concentration of ZIF-9 is 0.5 mg/mL. In that particular case, the rate constant is not representative, as it has resulted from the linear regression of only three points, due to the high speed of the reaction. Comparing the data of Figure 5.23 with the data of Figure 5.14, the reaction was complete in 8 minutes in the dark, while it needed only 4 minutes when light was employed.

Table 5.3 Rate constants for the reduction of 4-nitrophenol in the dark and under white light, in the presence of various concentrations of ZIF-9 at molar ratio of reducing agent over substrate 12.5.

Concentration of ZIF-9 mg/mL	Rate constant (s^{-1}) Reaction in dark	Rate constant (s^{-1}) Light-assisted reaction
0.1	0.003	0.015
0.3	0.024	0.090
0.5	0.118	0.068

For this reason, it is also important to compare the total reduction achieved in each case of ZIF-9 concentration in the dark and under the white light. Figure 5.24 shows the total conversion achieved. Regarding the case of ZIF-9 at a concentration equal to 0.5 mg/mL, the reduction achieved in the dark was 67%, while it was 93% when the reaction was light-assisted. Overall, it is apparent that the irradiation of light enhances significantly the reaction progress both in terms of reaction rate and total conversion. It should also be remarked that, in both light and dark, the conversion achieved with content of ZIF-9 in the reaction mixture as low as 0.1 mg/mL is significantly lower than for higher content. Thus, ZIF-9 is capable to proceed the reaction at content higher than 0.1 mg/mL and can work both as a catalyst and a photocatalyst.

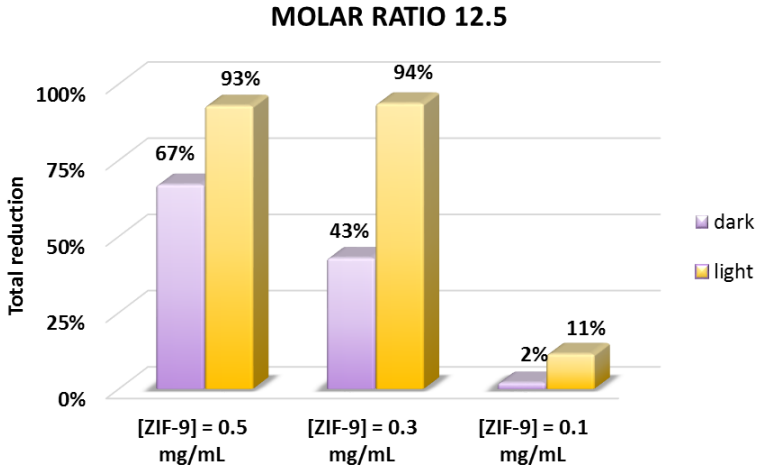

Figure 5.24 Comparative plot of total reduction achieved at molar ratio of $NaBH_4$ to 4-nitrophenol 12.5 in the presence of various concentrations of ZIF-9 in the dark and in the light.

5.2.5 Evaluation of heterogeneity and reusability of ZIF-9 for the reduction of 4-nitrophenol in the dark

As ZIF-9 was proved to be a very efficient catalyst and photocatalyst for the reduction of 4-nitrophenol with $NaBH_4$, it is important to assess its heterogeneity. ZIF-9 is a material with partially hydrophobic nature. When used in an aqueous reaction mixture, the solid particles disperse in the solution under vigorous stirring. At a lab scale, its recovery is not very easy. The method of centrifugation is used to collect the solid at the bottom. However, due to the material's hydrophobicity, it was observed that ZIF-9 prefers to stay on the surface of the aqueous solution when stirring is stopped. On the other hand, filtration of the solution is significantly slow and a significant part of the solid particles remained on the filtration paper, unable to be reused. Thus, although the recovery method of centrifugation is not the best, it is the clearest and fastest available.

The experiment of heterogeneity evaluation was designed as follows. A high molar ratio of reductant over substrate (50) and catalyst concentration (0.5 mg/mL) were selected, while the reaction mixture was scaled up (reaction mixture volume 50 mL) so that the starting weight of ZIF-9 was 25 mg. The reaction was let to run for 2 min. in the 1st cycle. After the 1st cycle, the mixture was centrifuged and the catalyst was collected and added into a new reaction mixture of 50 mL. The procedure was repeated for 15 cycles of 2 minutes each, but sampling of the mixture for measurement of the activity of the catalyst took place after the 5th, 10th and 15th cycle. The corresponding spectra are found in Figure 5.25.

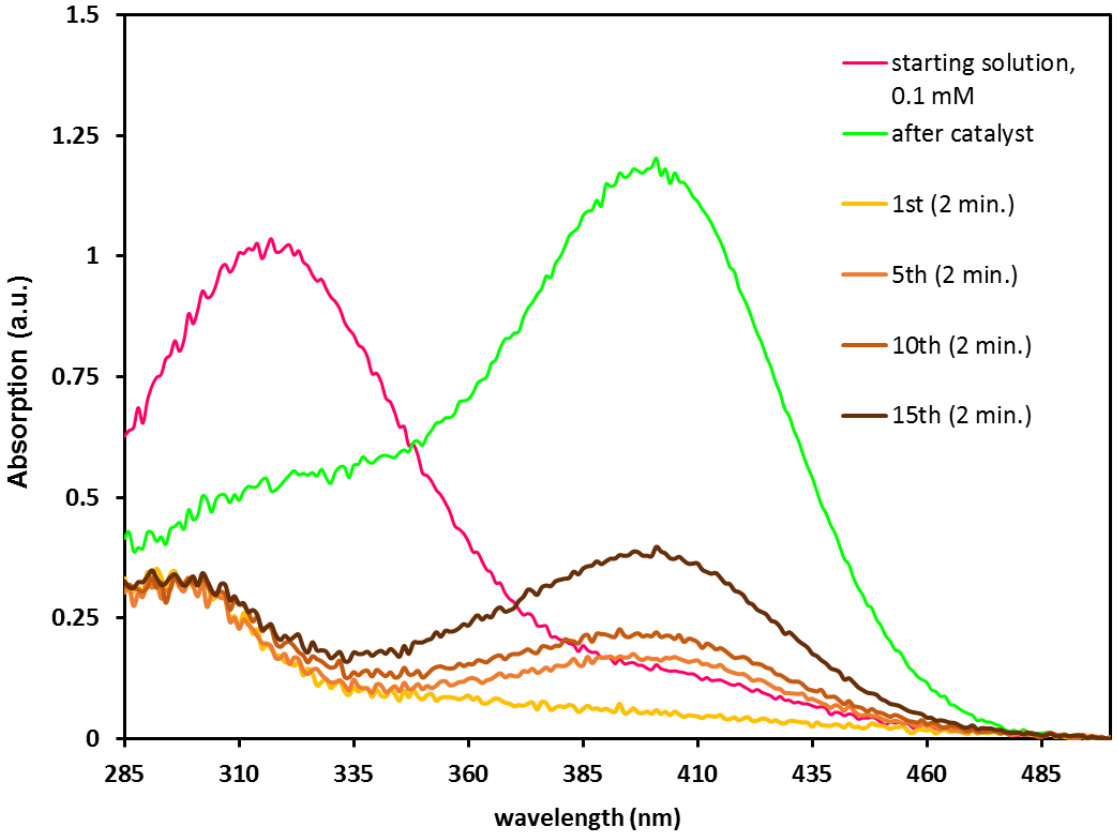

Figure 5.25 Spectra collected after the 1st, 5th, 10th and 15th cycle of reaction of 4-nitrophenol and $NaBH_4$ with a molar ratio 50 in the dark.

As expected, the reduction of the peak at 400 nm is significant after the 1st cycle of reaction. After the 5th and the 10th cycle of reaction, the peak at 400 nm is evident and much more intense after 15 cycles. The peak at 300 nm appears in each spectrum and regards the formation of 4-aminophenol. Calculating the reduction achieved after these cycles, the results are plotted in Figure 5.26.

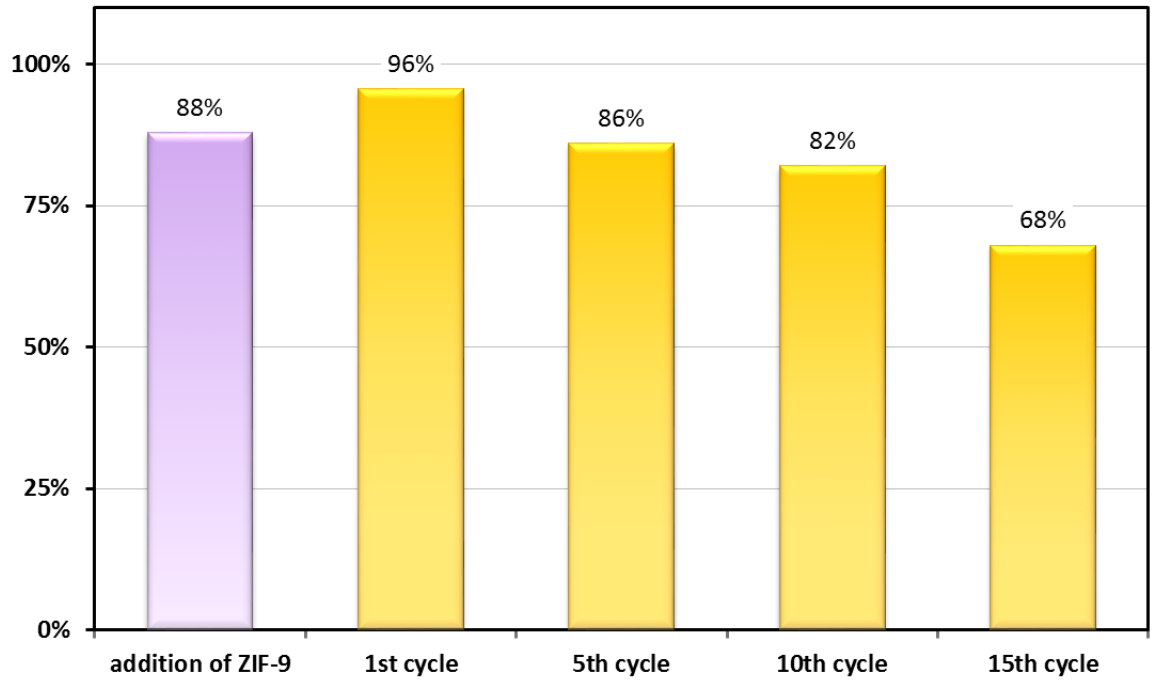

Figure 5.26 Reduction of 4-nitrophenol achieved after the 1st, 5th, 10th and 15th cycle of reaction in dark and rise of the intensity of peak at 400 nm after the addition of ZIF-9.

According to the findings, the loss of activity between the 1st and 15th cycle is approximately 30%. However, it is interesting to take also into account the loss of mass of catalyst between the 1st and 15th cycle. As mentioned before, the reaction mixture was scaled up so that the starting weight of ZIF-9 in the reaction is 25 mg and. After the 15th cycle, the catalyst was collected, left to dry and weighed at 6 mg. Thus, the loss of catalytic mass was 76% and this mass can be translated in concentration as low as 0.12 mg/mL. Although the value of the achieved reduction for ratio 50 and 0.1 mg/mL concentration of fresh ZIF-9 is not available, it is obvious that used catalyst at that low concentration for ratio 50 is active enough to achieve a conversion as high as 68%. This should be attributed to the mechanism of the reaction and the species formed on the surface of the catalyst. For this reason, post-catalysis characterisation takes place and presented further down, while the mechanistic process is discussed later.

5.2.6 Post-catalysis characterisation of used ZIF-9 in the reduction of 4-nitrophenol

ZIF-9 is a crystalline microporous material with distinct architectural features. Cobalt at the 2^+ oxidation state coordinates tetrahedrally with 4 benzimidazolate anions. All are linked together via a bond of ionic nature between nitrogen and

cobalt. Characterisation of fresh ZIF-9 proved the existence of this tetrahedral geometry and the oxidation state of cobalt, as presented in Chapter 3. The good catalytic and photocatalytic performance of ZIF-9 in the reduction of 4-nitrophenol with $NaBH_4$ and the heterogeneity of the catalyst were also successfully proven. However, it is important to realize the degree of the structural disturbance of the scaffold and its active sites. Initially, it should be noted that post-catalysis characterization was employed to the material spent for proof of concept of heterogeneity and thus, it has been submitted to 15 cycles of reaction. Next, PXRD is applied to compare the spent ZIF-9 with the simulated and the starting crystalline pattern, as shown in Figure 5.27.

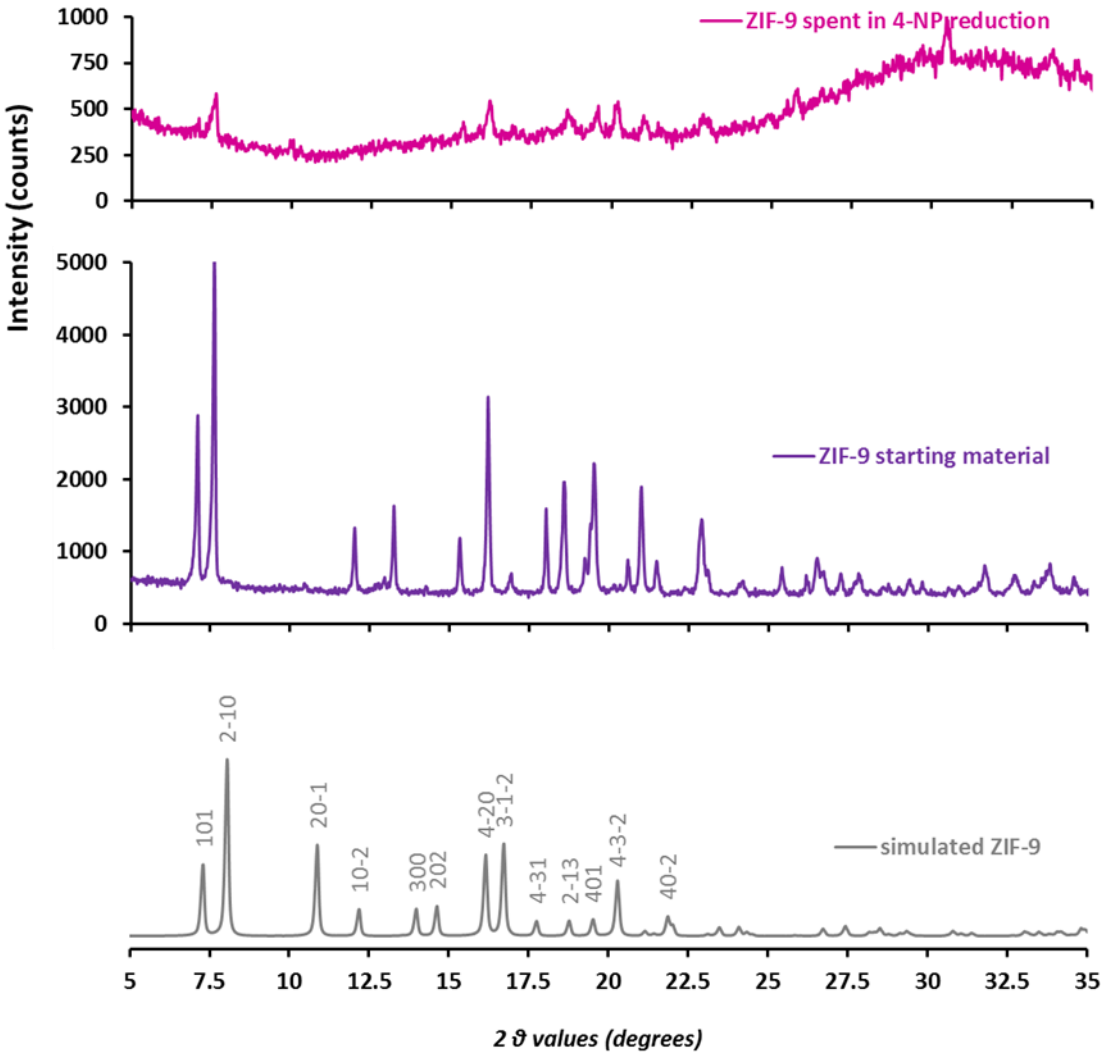

Figure 5.27 Comparative PXRD plot of simulated, synthesized and used ZIF-9 in the reduction of 4-nitrophenol to 4-aminophenol.

Considerable disturbance of the crystalline ZIF-9 can be observed from the PXRD patterns. The spent ZIF-9 pattern appears almost flat compared to the starting

material pattern. However, the few peaks that can be distinguished have not shifted angle position, which is more obvious from the inset plot, while these peaks belong in the low-angle region. Hence, it is possible that the elementary structure and crystallinity has not been lost, but the detailed microcrystalline arrangement has diminished. Another significant comment regards the elevation of the baseline for angles above 25 degrees. This is possibly due to the irradiation of the source which is stronger than the reflections of the material at the higher degrees and therefore, it is not safe to assume that amorphous phase has been formed. However, if crystalline disruption is agreed, it does not seem to affect the ability of ZIF-9 to catalyse the reaction, possibly a sign that it keeps its catalytic character and chemical integrity. However, SEM technique would reveal more information, especially regarding the surface and the morphology of the used ZIF-9.

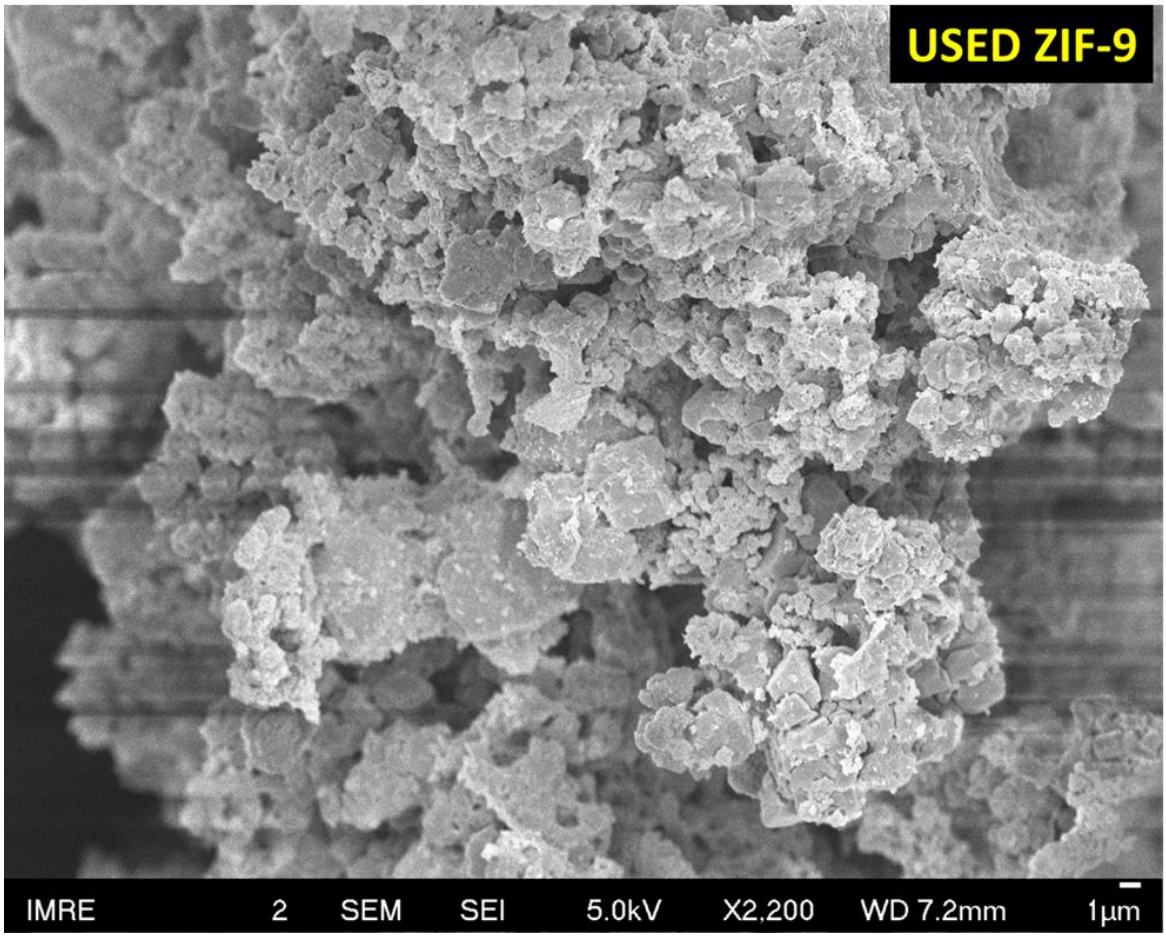

Figure 5.28 SEM image of the used ZIF-9 in the reduction of 4-nitrophenol to 4-aminophenol.

Severe particle agglomeration and disturbance of their surface can be observed from the SEM images in Figure 5.28. The well-distinguished rod-like shapes of the

fresh ZIF-9 particles which used to measure approximate length of 7 μm has been replaced by a coral or sponge-like aggregation. It is nearly impossible to discriminate flat surfaces and shapes, which strongly infers the stark alteration of the surface of the material caused after 15 cycles of reaction in aqueous solution in the presence of $NaBH_4$. However, the structure appears highly porous with a hierarchical composition, lacking though a repeated pattern.

Further analysis of the bulk surface of the used ZIF-9 has taken place applying the XPS technique. Constraints were implemented again in order to fit the raw data, as shown in Figure 5.29. The XPS pattern of the used ZIF-9 in the reduction of 4-nitrophenol demonstrates interesting similarities and significant differences from the XPS data obtained for the fresh ZIF-9 as shown in Chapter 4. The binding energies of the main cobalt peaks are located at 781.3 eV for Co $2p^3/_2$ and at 797.7 for Co $2p^1/_2$, opposed to the 781.7 eV and 797.7 eV respectively for the fresh material. Therefore, the energy gap is reduced from 16 eV to 15.7 eV, while the shift of the main peak (Co $2p^3/_2$) to lower binding energy could also infer reduction of cobalt. The raw data fitting requires more satellite peaks of the used ZIF-9, which the fitted peaks in the main regions are wider.

This is good indication of the existence of mixed oxidation states of cobalt (Co^{2+} and Co^{3+}) in the used ZIF-9. Overall, the XPS data of the used ZIF-9 exhibit slight shift of peaks to lower binding energies and minor decrease of the energy gap of the cobalt doublet split in respect with the data of the fresh ZIF-9, while the pattern of the satellites and the width of the peaks indicate more than one oxidation states of cobalt in the spent material. Combining with the PXRD findings and judging from the catalytic activity after recovery, it is possible that ZIF-9 framework does not break down. Its high crystallinity possibly reduces due to grinding, but it preserves its chemical accordance, while SEM images suggest that the particles assemble together into bigger entities.

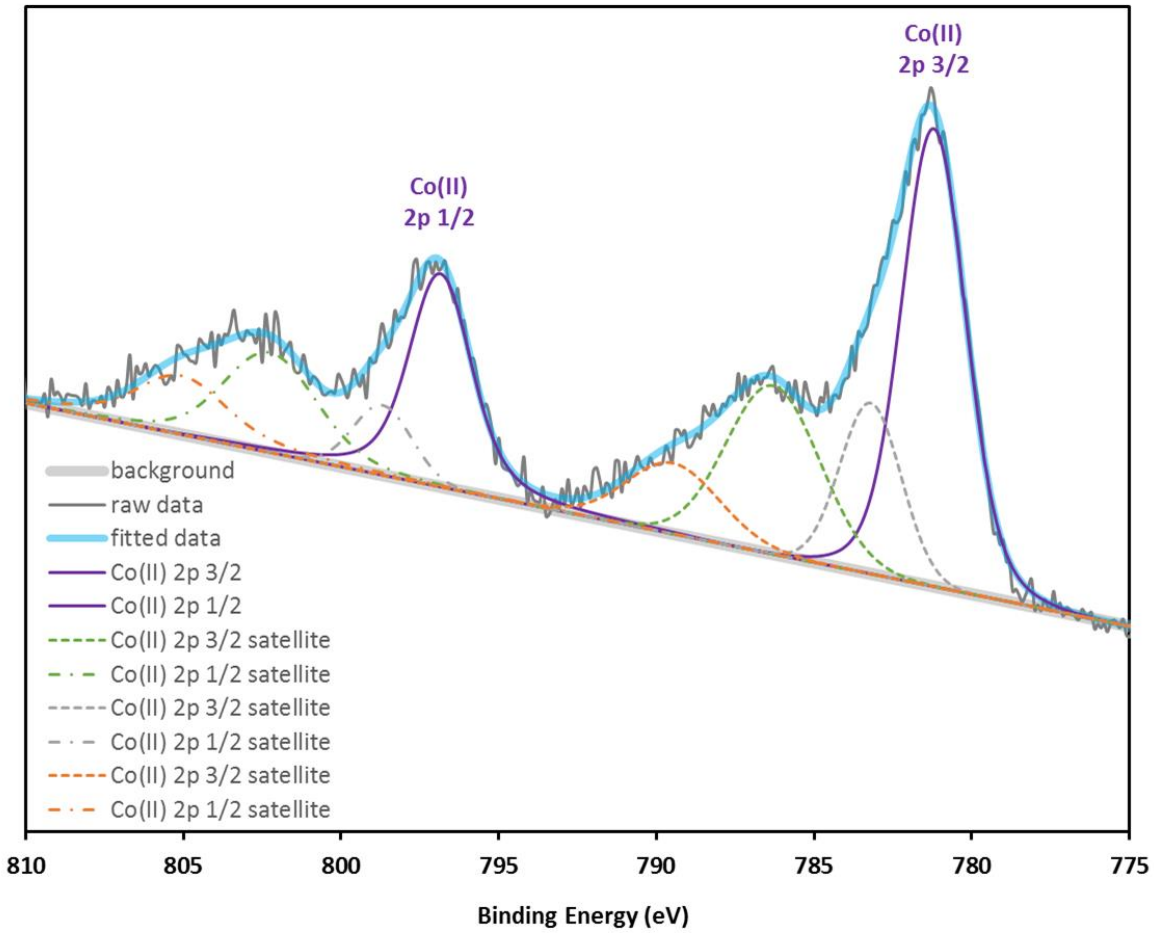

Figure 5.29 Experimental XPS spectra and fitting of the used ZIF-9 in the reduction of 4-nitrophenol to 4-aminophenol.

PXRD and SEM exhibited interesting structural and morphological information, while XPS gave an insight regarding the changes through which the cobalt active sites were submitted during the reduction of 4-nitrophenol. Further investigation concerning the active sites includes examination of the coordination of cobalt and for this reason, DR UV-VIS has been employed. Figure 5.30 shows some interesting features and also reveal interesting information regarding the photoresponse and the coordination of the cobalt sites, as explained further down.

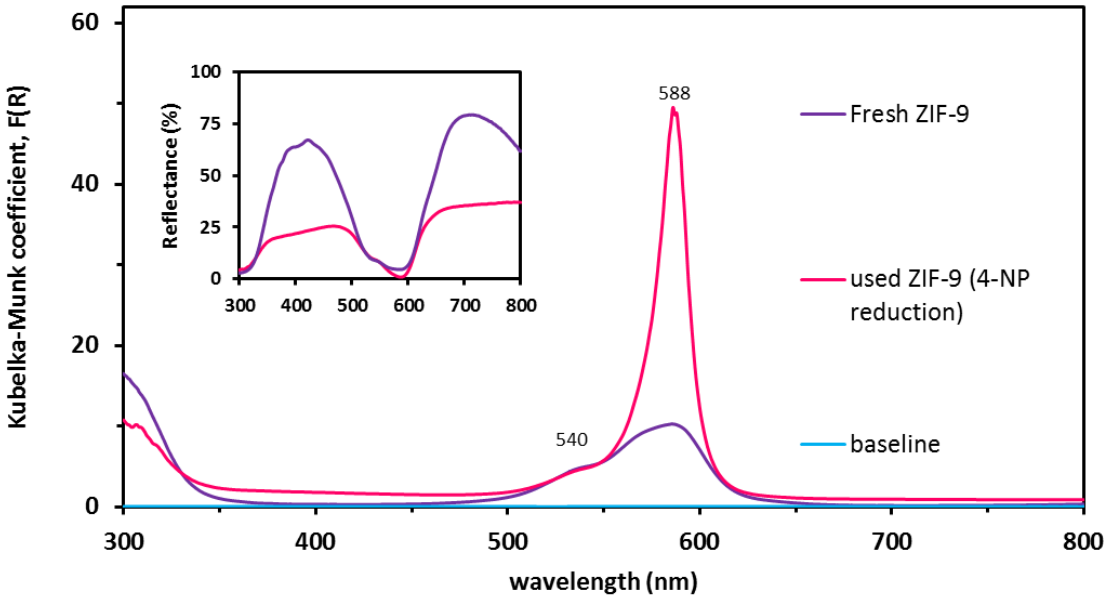

Figure 5.30 DR UV-VIS spectrum of fresh and used ZIF-9 in the reduction of 4-nitrophenol.

Initially, the wavelengths of absorption have remained the same before and after the submission of the catalyst to the reaction. However, the pattern of the used ZIF-9 has changed with the absorption peak of ZIF-9 becoming more dominant and sharper. Therefore, the coordination of cobalt in the material has not changed and fourfold coordination has been maintained. As no shift of the main peak is observed, the d-d transitions are still active and the electrons do not need a different energy quantum to jump to a d orbital of higher energy. The lack of new peaks in other regions of the spectrum indicates that charge transfer between ligands and metal ions (LMCT and MLCT) has not changed.

Moreover, the inset plot refers to the reflectance of ZIF-9, from which it is more obvious that fewer photons are reflected with the used ZIF-9. This finding along with the higher intensity of the main peak in the DR UV-VIS could associate with surface activation of the material during the reaction. In other words, more cobalt species might have become reactive and different bonds may have been formed but the technique is not suitable to support this opinion profoundly.

A more appropriate method is the FTIR analysis of the solid and the comparison of the spectra before and after the use of ZIF-9 in the reaction. It should be remarked that the FTIR spectrum of the fresh ZIF-9 is in agreement with the literature[40] and that the spectra in Figure 5.31 are also compared with the spectrum of 4-nitrophenol reported in databases.[41] Main purpose of this process

would be to comprehend the entities that may be formed during the reaction and elucidate the process mechanistically.

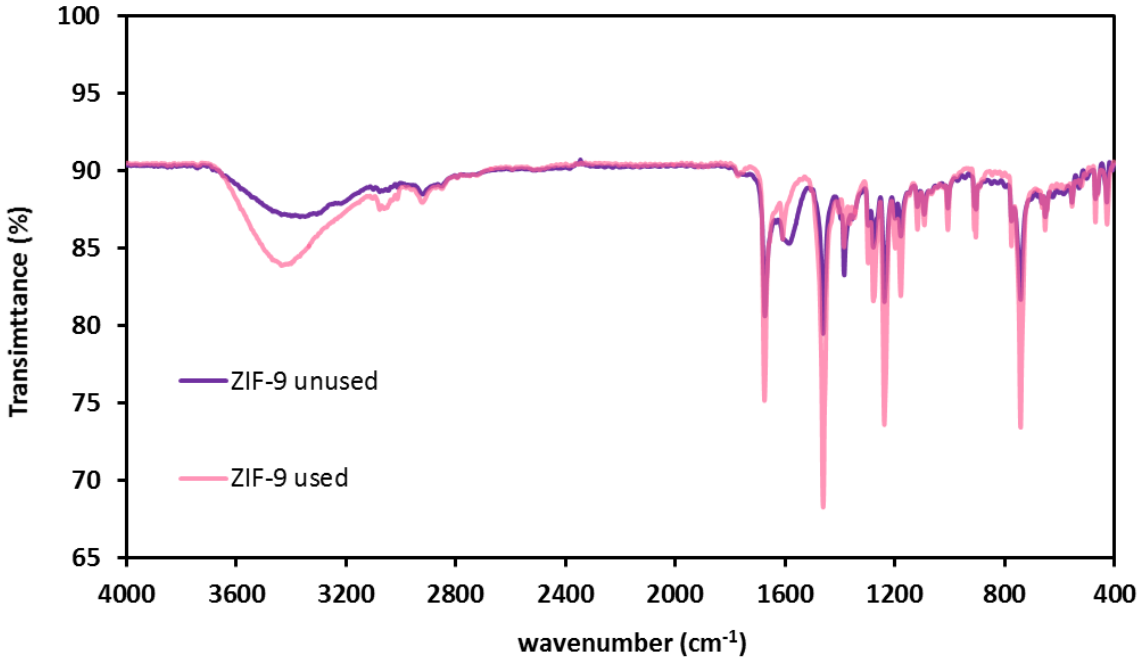

Figure 5.31 FTIR spectra of the fresh and used ZIF-9 in the reduction of 4-nitrophenol in the presence of $NaBH_4$.

The spectra presented for the ZIF-9 before and after use in the reduction of 4-nitrophenol differ mostly in the intensities of the peaks since the bands are practically not shifted, missing or added. Therefore, it is not easy to certify the formation of new bonds and new entities on the surface of ZIF-9 during the reaction. The band differences observed in the region centred around the wavenumber 3430 cm^{-1} are mostly attributed to the stretching of the O-H and N-H bonds of primary amines, which are probably due to the formation of 4-aminophenol. The same broad band along with the smaller peaks in the region 3080-3050 cm^{-1} and around 1608 cm^{-1} indicate the presence of 4-nitrophenol on the solid if compared with the fingerprint of 4-nitrophenol (Appendix C.2 and C.3).

5.3 Conclusions and Discussion

ZIF-9 was used among other catalysts based on cobalt and copper and outperformed the rest of the catalysts (CoMOF-74, CoAlPO-5, HKUST-1, CuAlPO-5) in the reduction of 4-nitrophenol to 4-aminophenol in the presence of $NaBH_4$. Its catalytic activity was measured with respect to the conversion of 4-nitrophenol to

4-aminophenol with varying molar ratio of $NaBH_4$ to 4-nitrophenol and with varying amount of solid in the reaction mixture.

A higher ratio of reductant to substrate leads to quicker conversion and for a concentration of ZIF-9 in the reaction mixture equal to 0.5 mg/mL the decrease of the constant rates is steeper than the decrease of the ratio of the reducing agent over 4-NP In terms of overall reduction ability independent of the time required, molar ratio of $NaBH_4$ to 4-NP equal to 25 achieves over 90% of reduction, a percentage close to that achieved with a molar ratio of 50. Thus, for a high ZIF-9 concentration, the molar ratio of the reductant to substrate has a greater impact on the rate of the reduction than the total conversion.

Studies of the influence of the concentration of ZIF-9 in the reaction mixture indicated that higher amounts of ZIF-9 (up to 0.5 mg/mL) drive the reaction both faster and more efficiently. A 40% decrease of the catalyst concentration lowers the degree of reduction by 20% and the rate of reaction by 4 times. An additional decrease of the catalyst gives results that are practically identical to the blank reaction. These findings show that the reduction of 4-nitrophenol with $NaBH_4$ is strongly catalytic. Overall, the kinetics resemble a pseudo-first order reaction, since it is highly dependent on the availability of the hydrogen, except for the concentration of the substrate and on the amount of the catalyst (for studies up to 0.5 mg of ZIF-9 per mL of reaction mixture).

Further investigation of the photocatalytic activity of ZIF-9 for this reaction involved the use of white light. In the irradiation of white light over the reaction mixture in the presence of ZIF-9 and $NaBH_4$, much higher rate and activity are observed. In detail, the irradiation of light activates ZIF-9 and the reaction can be completed reaching a conversion of almost 95% with both less solid and reductant requirements, turning the process greener. This finding shows that ZIF-9 functions as an efficient photocatalyst for the reduction of 4-nitrophenol with $NaBH_4$.

Probing the precursors of ZIF-9 in the reaction in the dark, it is possible to understand that Co^{2+} is the active ingredient able to reduce 4-nitrophenol in the presence of hydrogen, while the benzimidazole molecules are responsible for the hydrolysis of the hydroxyl group of the substrate. A mixture of the two conveys, as expected, a mixed behaviour. However, none of the precursors is recoverable, since cobalt nitrate and benzimidazole dissolve in the reaction mixture. On the contrary, cobalt(II) and benzimidazolate in the form of ZIF-9 prove to be

heterogeneous and able to catalyse faster and more actively the reduction of 4-nitrophenol. In fact, reusability tests of ZIF-9 showed loss of activity of approsimately 30% after 15 catalytic cycles, which could also be due to the simultaneous big loss of catalytic mass that the combination of the recovery method and the hydrophobicity of the particles may cause.

In terms of the mechanism of the reaction, there are possibly two factors that should be taken into account. One factor regards the effect of the catalyst on the hydrolysis of $NaBH_4$ and the other factor regards the adsorption of nitrophenol on the surface of the catalytic particles. The combination of these two processes results into the reduction of nitrophenol to aminophenol. It can be speculated that the adsorption of nitrophenol along with the hydrolysis of its hydroxyl group is not the rate determining step since the change of the colour of the 4-nitrophenol aqueous solution from a pale yellow to intense yellow with the addition of the catalyst is instant.

A lot of attention has been given recently to the catalytic hydrolysis of borohydrides and boranes, since they are considered a suitable energy carrier and a clean source of hydrogen, leading potentially a step closer to the era of hydrogen economy. Although the hydrolysis of complex hydrides, such as sodium borohydride (Scheme 5.1), is a spontaneous reaction, it is characterized by low rate, while the high decomposition temperatures of hydrides turn the hydrolysis method to a more sustainable process.[42,43] In addition, the reaction of one mole of sodium borohydride with two moles of water releases 4 moles of hydrogen in ideal conditions. In reality, the water requirement is bigger, due to low solubility of sodium borohydride, the precipitation of sodium metaborate and the rise of the pH during hydrolysis.

Scheme 5.1 Hydrolysis of sodium borohydride.

According to literature, acids are able to catalyse successfully this reaction.[44,45] The use of acids is not considered sustainable though, mostly due to parameters that regard the purity of the produced hydrogen. For this reason, metals, such as ruthenium,[46,47] nickel[48,49] and platinum,[50] have been reported as successful catalysts. However, cobalt-based catalysts[51–54], have shown a remarkable catalytic

activity in the hydrolysis of hydrides and are, of course, attractive due to their low cost, replacing noble metals.

In more detail, cobalt borides prepared with diverse methods[51–53] are popular for the effective hydrolysis of $NaBH_4$ and the efficient hydrogen production, while cobalt oxides and $CoCl_2$ are the most studied systems.[54] However, the exact mechanism and the active phase are still in question, notwithstanding the extensive *in situ* and *ex situ* characterisation of the studied systems, previously referred to. In general, the presumed mechanism consists of the *in situ* reduction of cobalt(II) and the formation of a reactive bond between cobalt and boron, while the cobalt-based catalysts appear highly distorted and the particles reduce in size. The transformation of the cobalt-based catalysts is accompanied by an induction period, which is the time needed for the reduction of cobalt and the change of the phase. With regards to the phase, reference has been made to cobalt borides (Co_xB),[52] Co-B alloys[53] and $Co_2B_2O_5$.[53]

ZIF-9 has also been tested by Li and Kim[55] for the hydrolysis of $NaBH_4$ and they report a relatively slow hydrogen production, in the beginning, justifying the prolonged time needed with the difficulty to form CoB active centres at ZIF-9's distinct structure. They also report linear increase after the formation of the catalytically active phase and values of hydrogen production close to the theoretically expected ones. Additionally, they report excellent reusability with ZIF-9 able to reach same levels of hydrogen production skipping the induction time after the 1st cycle of use, explaining that once the active centres are formed the catalyst remains active and heterogeneous.

In consistence with the aforementioned scientific findings, ZIF-9 effects hydrogen production, which is vital for the reduction of 4-NP. Thus, a possible clogging of the surface of ZIF-9 with $NaBO_2$ could deactivate the catalyst and slow down the reaction. In addition, ZIF-9 catalyst is a hybrid of Co^{2+} and benzimidazolate ions with unique photocatalytic activity. This information could hint that the distribution of charge on the surface is possible. If this is true, then positive areas (holes) might attract the phenolate part of the substrate, while the negatively charged ones (electrons) could attract the hydrogen atoms, forbidding their immediate escape to the atmosphere (Figure 5.32).

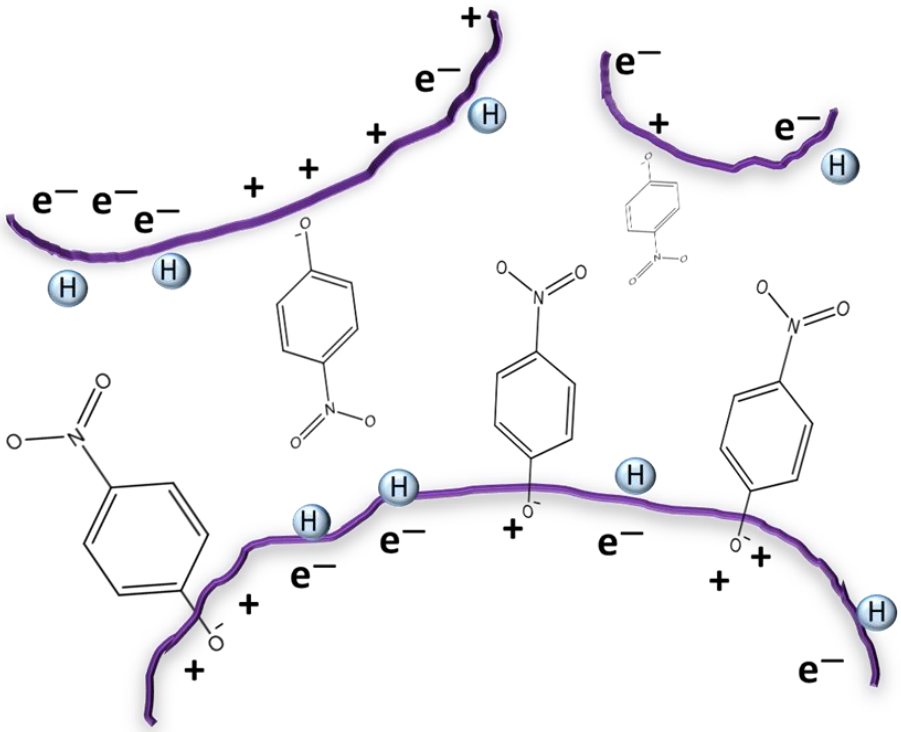

Figure 5.32 Distribution of charge on ZIF-9 particle and adsorption of hydrogen atoms and 4-nitrophenolate ions.

This could leave the nitro-groups exposed for the reduction to amino-groups, following a widely accepted mechanism for the reduction of the nitro groups with hydrogen (Scheme 5.2). In principle, this path would start from the transition of the nitro group to nitroso group, which can easily be reduced to hydroxylamine. The presence of a metal with H^+ can then protonate the oxygen with a single electron transfer and reduce hydroxylamine further to amine.

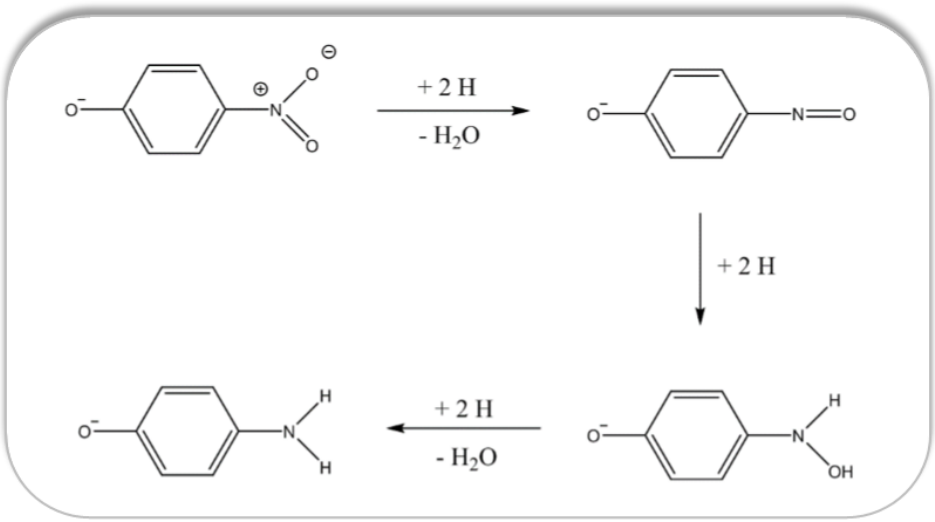

Scheme 5.2 Simplified mechanism of the reduction of 4-nitrophenol to 4-aminophenol.

As mentioned earlier, the CoB active sites are the most dominant theory and reported characterisation has not revealed specific findings to the used catalytic systems. In this project, post-catalysis characterisation with FTIR did not reveal significant alterations that would imply new bonds or entities. However, the FTIR patterns are more likely to reveal the presence of 4-nitrophenol and 4-aminophenol as adsorbed species. Moreover, XPS analysis of the spent ZIF-9 showed a mixture of oxidation states of cobalt, in contrast to the presence of cobalt(II) of the fresh ZIF-9, which indicates a subtle chemical alteration.

The peak of the DR UV-VIS spectrum became sharper, due to a more intense and narrower absorption, possibly because of the formation of reactive species on the surface of ZIF-9, as explained in section 5.2.6. PXRD spectrum did not reveal the formation of amorphous phase, but decrease of the intensity of the peaks was significant. The dominant peaks that could be discerned did not appear shifted. Overall, the microcrystallinity of the materials seems to have been degraded.

Last but not least, the SEM images of the used material showed vast change of the surface morphology. Instead of repeated particles, sponge-like masses were discerned. However, it should be remarked that the SEM image of the used ZIF-9 in the reduction of 4-nitrophenol in the presence of $NaBH_4$ depicted entities which were more alike to the catalytic entities reported in the literature, regarding the cobalt-based catalysts used in $NaBH_4$ hydrolysis for hydrogen production[51–54]. In most cases, the catalysts seem to obtain a rough surface with a large pore volume and flower/flake-like morphology, which is close to the appearance of the used ZIF-9.

Overall, ZIF-9, a topologically isomorphic to sodalite metal-organic framework based on cobalt II, has performed as an excellent catalyst and photocatalyst for the reduction of 4-nitrophenol to 4-aminophenol in the presence of $NaBH_4$. ZIF-9 has been mainly employed in carbon capture applications and has been reported for gas separation uses, while its catalytic properties have not been exploited extensively. These findings enhance its catalytic and photocatalytic character, while its hydrophobic nature makes this material applicable in catalysis in aqueous phases without decay or deactivation taking place.

5.4 References

1 P. Ray, M. A. Oubelli and C. Löser, *Appl Microbiol Biotechnol*, 1999, **51**, 284–290.

2 G. Rippen, E. Zietz, R. Frank, T. Knacker and W. Klöpffer, *Environ. Technol. Lett.*, 1987, **8**, 475–482.

3 U.S. Environmental Protection Agency, *Integrated Risk Information System (IRIS) on p-Nitrophenol*, Washington DC., 1999.

4 M. I. O. Ishag and P. G. N. Moseley, *Tetrahedron*, 1977, **33**, 3141–3144.

5 O. A. O'Connor and L. Y. Young, *Environ. Toxicol. Chem.*, 1989, **8**, 853–862.

6 X. Zhang, M. Lin, X. Lin, C. Zhang, H. Wei, H. Zhang and B. Yang, *ACS Appl. Mater. Interfaces*, 2014, **6**, 450–458.

7 M. Nasrollahzadeh, S. M. Sajadi and M. Maham, *RSC Adv.*, 2015, **5**, 40628–40635.

8 R. Patel and S. Suresh, *J. Hazard. Mater.*, 2006, **137**, 1729–1741.

9 L. G. Devi, S. G. Kumar, K. M. Reddy and C. Munikrishnappa, *J. Hazard. Mater.*, 2009, **164**, 459–467.

10 J. Staehelin, R. E. Buehler and J. Hoigne, *J. Phys. Chem.*, 1984, **88**, 5999–6004.

11 B. M. Güell, I. M. T. da Silva, K. Seshan and L. Lefferts, *Appl. Catal. B Environ.*, 2009, **88**, 59–65.

12 A. Acher, E. Fischer, R. Turnheim and Y. Manor, *Water Res.*, 1997, **31**, 1398–1404.

13 O. Legrini, E. Oliveros and A. M. Braun, *Chem. Rev.*, 1993, **93**, 671–698.

14 J. Prousek, *Chem. List.*, 1996, **90**, 229–237.

15 M. A. Oturan and J.-J. Aaron, *Crit. Rev. Environ. Sci. Technol.*, 2014, **44**, 2577–2641.

16 P.-T. Huong, B.-K. Lee, J. Kim and C.-H. Lee, *Mater. Des.*, 2016, **101**, 210–217.

17 M. Babaahamdi-Milani and A. Nezamzadeh-Ejhieh, *J. Hazard. Mater.*, 2016, **318**, 291–301.

18 A. Hatamifard, M. Nasrollahzadeh and S. M. Sajadi, *New J. Chem.*, 2016, **40**,

2501–2513.

19 A. Hatamifard, M. Nasrollahzadeh and J. Lipkowski, *RSC Adv.*, 2015, **5**, 91372–91381.

20 L. Tang, J. Tang, G. Zeng, G. Yang, X. Xie, Y. Zhou, Y. Pang, Y. Fang, J. Wang and W. Xiong, *Appl. Surf. Sci.*, 2015, **333**, 220–228.

21 F. Deng, Y. Liu, X. Luo, S. Wu, S. Luo, C. Au and R. Qi, *J. Hazard. Mater.*, 2014, **278**, 108–115.

22 N. Daneshvar, M. A. Behnajady and Y. Z. Asghar, *J. Hazard. Mater.*, 2007, **139**, 275–279.

23 A. M. Umabala, *Inter. J. Eng. Apli. Sci*, 2015, **2**, 122–125.

24 X. Li, C. Zeng, J. Jiang and L. Ai, *J. Mater. Chem. A*, 2016, **4**, 7476–7482.

25 C. Wang, H. Zhang, C. Feng, S. Gao, N. Shang and Z. Wang, *Catal. Commun.*, 2015, **72**, 29–32.

26 H. Jiang, Q. Yan, Y. Du and R. Chen, *React. Kinet. Mech. Catal.*, 2016, **117**, 307–317.

27 T. Bhowmik, M. K. Kundu and S. Barman, *RSC Adv.*, 2015, **5**, 38760–38773.

28 J. Shu, Z. Wang, G. Xia, Y. Zheng, L. Yang and W. Zhang, *Chem. Eng. J.*, 2014, **252**, 374–381.

29 C. Singh, A. Goyal and S. Singhal, *Nanoscale*, 2014, **6**, 7959–7970.

30 P. Zhao, X. Feng, D. Huang, G. Yang and D. Astruc, *Coord. Chem. Rev.*, 2015, **287**, 114–136.

31 W. Ye, J. Yu, Y. Zhou, D. Gao, D. Wang, C. Wang and D. Xue, *Appl. Catal. B Environ.*, 2016, **181**, 371–378.

32 Y. Wu, M. Wen, Q. Wu and H. Fang, *J. Phys. Chem. C*, 2014, **118**, 6307–6313.

33 F. Taghavi, C. Falamaki, A. Shabanov, L. Bayrami and A. Roumianfar, *Appl. Catal. A Gen.*, 2011, **407**, 173–180.

34 S. C. Mitchell, P. Carmichael and R. Waring, in *Kirk-Othmer Encyclopedia of Chemical Technology*, 2003.

35 R. A. Sheldon and H. van Bekkum, in *Fine Chemicals through Heterogeneous Catalysis*, WILEY-VCH, Weinheim, 2007, pp. 553–587.

36 Y. Du, R. Z. Chen and N. P. Xu, *Appl. Catal. A Gen.*, 2004, **277**, 259–264.

37 M. Goepel, M. Al-Naji, P. With, G. Wagner, O. Oeckler, D. Enke and R. Gläser, *Chem. Eng. Technol.*, 2014, **37**, 551–554.

38 Prof Research, *4-Aminophenol Market 2022 Analysis and In-depth Research on Market Size, Trends, Emerging Growth Factors and Forecasts*, 2017.

39 D. Tassios, in *Applied Chemical Engineering Thermodynamics*, Springer Berlin, Heidelberg, Springer-V., 1993, pp. 545–583.

40 Z. Öztürk, J. P. Hofmann, M. Lutz, M. Mazaj, N. Z. Logar and B. M. Weckhuysen, *Eur. J. Inorg. Chem.*, 2015, **2015**, 1625–1630.

41 *http://sdbs.db.aist.go.jp/sdbs/cgi-bin/direct_frame_top.cgi*, 2017.

42 B. Bogdanović , M. Felderhoff and G. Streukens, *J. Serbian Chem. Soc.*, 2009, **74**, 183–196.

43 I. P. Jain, P. Jain and A. Jain, *J. Alloys Compd.*, 2010, **503**, 303–339.

44 H. I. Schlesinger, H. C. Brown, A. E. Finholt, J. R. Gilbreath, H. R. Hoekstra and E. K. Hyde, *J. Am. Chem. Soc.*, 1953, **75**, 215–219.

45 E. Y. Marrero-Alfonso, A. M. Beaird, T. A. Davis and M. A. Matthews, *Ind. Eng. Chem. Res.*, 2009, **48**, 3703–3712.

46 S. C. Amendola, S. L. Sharp-Goldman, M. S. Janjua, N. C. Spencer, M. T. Kelly, P. J. Petillo and M. Binder, *Int. J. Hydrogen Energy*, 2000, **25**, 969–975.

47 S. C. Amendola, S. L. Sharp-Goldman, M. S. Janjua, M. T. Kelly, P. J. Petillo and M. Binder, *J. Power Sources*, 2000, **85**, 186–189.

48 D. Hua, Y. Hanxi, A. Xinping and C. Chuansin, *Int. J. Hydrogen Energy*, 2003, **28**, 1095–1100.

49 J. Peng, R. He, M. Tan, Y. Dou, Z. Wang, G. Z. Chen and X. Jin, *J. Electrochem. Soc.* , 2015, **162** , H271–H277.

50 Y. Kojima, K. Suzuki, K. Fukumoto, M. Sasaki, T. Yamamoto, Y. Kawai and H. Hayashi, *Int. J. Hydrogen Energy*, 2002, **27**, 1029–1034.

51 J. Manna, B. Roy, M. Vashistha and P. Sharma, *Int. J. Hydrogen Energy*, 2014, **39**, 406–413.

52 S. Cavaliere, J. Hannauer, U. B. Demirci, O. Akdim and P. Miele, *Catal. Today*, 2011, **170**, 3–12.

53 A. M. Ozerova, V. I. Simagina, O. V Komova, O. V Netskina, G. V Odegova, O. A. Bulavchenko and N. A. Rudina, *J. Alloys Compd.*, 2012, **513**, 266–272.

54 V. I. Simagina, O. V Komova, A. M. Ozerova, O. V Netskina, G. V Odegova, D. G. Kellerman, O. A. Bulavchenko and A. V Ishchenko, *Appl. Catal. A Gen.*, 2011, **394**, 86–92.

55 Q. Li and H. Kim, *Fuel Process. Technol.*, 2012, **100**, 43–48.

Chapter 6: Decolouration of aqueous and non-aqueous dye solutions

This chapter includes collaborated work with colleagues, whose contribution is appreciated and acknowledged.

Dr Zhang Zheng, a scientist II in IMRE, performed the XPS experiments of the used materials.

Part of this work included has been orally presented in the 5th International Conference in Engineering, Science, Technology and Waste Management, in August 2017, in Singapore.

6.1 Azo-dyes in water and solvents

The discovery of purple mauveine in 1856 was a serendipity that transformed the industry of dyes and pigments. Until then, the source of colours was natural, lacking stability and occurring in a costly manner from plants, insects, mucus or minerals. The English chemist Sir William Henry Perkin discovered accidentally the first aniline dye, while he was experimenting for a synthetic method of quinine, the antidote to malaria. The new substance was dissolved in ethanol and the solution painted silk purple deeply and extraordinarily stably in washing and light, introducing simultaneously a new branch in the chemical industry of the 19th century.[1,2] Since then, knowledge around dyes has expanded significantly and hundreds of synthetic dyes have been discovered. Today, over 100,000 different dyes and pigments are registered and over 1-1.5 megatons are produced.[3] Over 700,000 tons are used globally in industry only, making the business of dyes obviously huge and profitable, with first the textile and second the printing ink business being the largest consumers.[4]

The colouring behind dyes and colours relies on basic principles. The distinction of a visible colour is due to the existence of specific bonds that can absorb selectively wavelengths of light. The light promotes the electrons in the molecule and excites it to a higher energy level. The involved electrons usually belong to double and triple bonds and the involved molecules contain conjugated systems that increase the electron delocalisation. The chemistry of dyeing depends on the compatibility of the dye and the substrate, but in general terms, the process involves the modification of the substrate which will increase the affinity between the dye and the surface. Then, the dye can adhere onto the surface by several methods, such as solution, covalent bonding, adsorption, complex formation etc.

The classification of the dyes may depend on different parameters, such as the type of medium in which the dye is soluble, chemical structure and main application, resulting in numerous ways to organize them. The azo-dyes constitute probably 60-70% of the available synthetic dyes[3] and they are named after the presence of one or more azo-groups in their molecular structure, which must involve at least a pair of conjugated systems between which an azo-group is found.

The presence of other groups, such as amino/nitro-groups, carboxyls, hydroxyls, sulfonates, methines, anthraquinones, etc., affects the degree of conjugation, which successively results in the wide variation of colours. This has led to more than 800 colours and 600 colour auxiliaries and agents. These groups are generally categorised as auxochromes (electron donors) and antiauxochromes (electron acceptors), while the rule of thumb is that groups that are electron rich or poor give respectively a bathochromic or hypsochromic effect to the dye.

Additionally, the presence of such groups varies the electron transfer and, according to contradictory studies that have been published,[5,6] this can either accelerate or delay the out fading of the dyes. Behind this contradiction lies the tautomeric equilibrium between the azo and the hydrazone form (Scheme 6.1). The hydrazone formation is totally dependent on the presence of a hydroxyl group next to the azo-group and the dominance of any form depends on parameters, such as alkalinity of the solution, temperature, light irradiation.[7] Then, the dominance of any form in the molecule may affect other processes, too. For example, when a specific tautomeric form prevails, oxidation or reduction may favour the degradation,[5,6] demanding specific antioxidant capacity for the longevity of the dye or, alternatively, specific reagents for its decomposition for environmental reasons. Prevalence of tautomeric forms may also influence

photostability, colour shade and tone, surface fixation, antibacterial appliance etc.,[7-10] and can enhance applications, such as dye-sensitised solar cells, sensors, optical devices.[11-13]

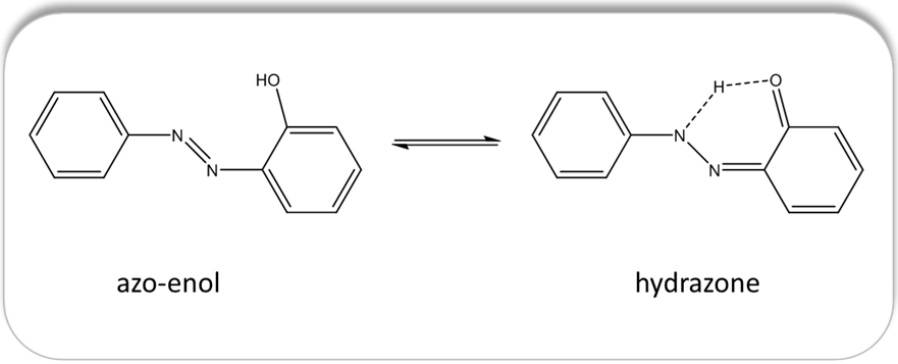

Scheme 6.1 Effect of a hydroxyl group at ortho-position relative to an azo-group in a conjugated system, leading to tautomerism between the azo-enol and the hydrazone form.

Although degradation, decolouration and colour alteration are applied extensively nowadays, the exact mechanisms are still under study. By degradation, the decomposition of the molecule is usually meant, so that the azo-group stops existing between aromatic rings. Scheme 6.2 is adapted by literature[14] and illustrates one mechanistic pathway proposed for the cleavage of the N-C bond of a hydrazone-type molecule, based on the concept that hydroxyl groups can attack positively charged carbon atoms. Another way is based on the sensitivity of azo-groups to nucleophilic additions, while pH variation renders the azo-groups sensitive.[14]

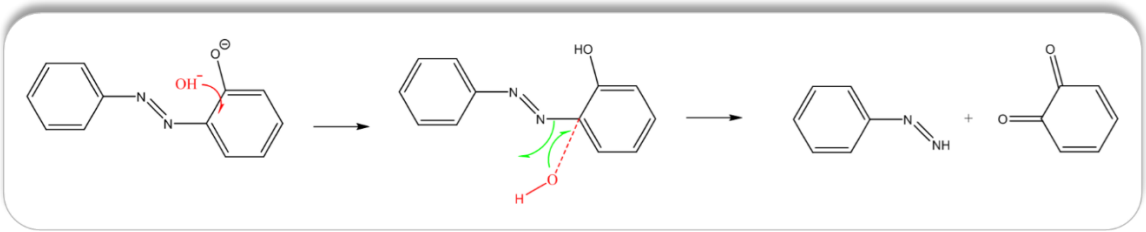

Scheme 6.2 Schematic illustration of the proposed decomposition of an azo-containing molecule via hydroxyls (adapted from literature[14]).

Decolouration and dye degradation can be important processes for the environmental remediation caused by the dye industry. Estimations from 1995 regard a percentage of 2% of dyes being directly discharged in water bodies and a percentage as high as 10% leaking from the dyeing process.[15] With all these percentages being by weight and for a basis of 1 kt of dye production, the

absolute numbers are scary: 20,000 tons of dyes are disposed in rivers, lakes or sea and 100,000 tons are lost from the industrial mass balance. Other data regard 200,000 tons of dyes escaping from the textile industry in effluents.[16]

Consequently, large quantities of dyes end up in water effluents and constitute a significant fraction of the industrial wastewaters. Unfortunately, there is no technical and practical information that the situation is improving. The imposing of stricter rules and narrower restrictions concern the USA, Canada, Australia and the European Union countries, pushing the dye manufacturers to other sides of the world.[17] Turkey, Morocco and Thailand mostly follow strict directives, but the limits in Pakistan and Malaysia are just recommended.[17,18] India and China are, as expected, the leading countries in dye production and consumption[19] and in dirty production, since the regulations there are non-specific and relatively loose.[18]

According to the numbers, the environmental problem of the dyes is big and becomes more serious, given the fact that azo-dyes do not occur naturally, threaten the health of humans and ecosystems[20,21] and are resilient in aerobic biological degradation, increasing the necessity for chemical processes and active materials.[22] Generally, the research community makes diverse efforts to tackle the problem and there is a considerable number of studies, where the application of mainly semiconductors, noble metals, bacteria and, even, plants is addressed as a solution. Some of these examples are tabulated in Table 6.1.

Table 6.1 Dye degradation achieved with a range of inorganic or organic systems.

Application [REFERENCE]	Catalyst system	Performance	Comments
Degradation of Direct Black 38[23]	TiO_2 (P-25)	50% in ca. 3 h.	Use of UV light, production of hydroxyl radicals
Degradation of Methyl Orange and Methyl Blue[24]	MnO_2 on Diatomite	30 min.	Use of UV light, production of hydroxyl radicals over $Mn^{4+} \rightarrow Mn^{2+}$

Application REFERENCE	Catalyst system	Performance	Comments
Degradation of Acid Orange 7[25]	TiO_2 (P-25) / Al_2O_3	n.a.	Use of visible light to excite the dye
Degradation of Methylene Blue (a) and Eosin Y (b)[26]	ZnO	(a): 76% in 2 h. (b): 74% in 2 h.	Use of UV-light
Degradation of Yellow / Blue / Black neutracyl or dispercatyl dyes[27]	Ag / Nb_2O_5	90 – 99.5 % in 24 h.	Use of UV-light
Degradation of textile Azo dye Acid Orange (100 mg/L)[28]	Staphylococcus hominis RMLRT03	92.32 % in 60 h.	Bacterial process conditioned over pH=7 and 35 °C
Degradation of Remazol Red (70 mg/L)[29]	Atternathera pliloxeriodes	100 % in 72 h.	Phytoremediation process
Degradation of Methylene Blue (10 mg/L)[30]	Lemma minor	98 % in 144 h.	

However, bacterial degradation is uncertain. Anaerobic bacteria have been employed for the dyes' reduction to aromatic amines and the intermediates are accused of carcinogenicity.[31,32] By the same token, the enzymatic decomposition of dyes highly depends on the degree of substitution of the aromatic rings. Hydroxyl groups, for instance, at the ortho position relative to the azo linkage forbid any bacterial access. Even more, bacterial or enzymatic degradation or transformation of the dyes is not at all possible if the complex molecules of dyes are not even miscible in aqueous media.

The use of non-aqueous solvents for dyeing is applied when the substrates are synthetic textiles, polymeric materials, plastics and hydrophobic fibres.[33,34] The

necessity for non-aqueous solvents emerged from the development of new methods of colourisation and decolourisation. These methodologies responded to a range of needs, such as substrates, friendlier dyeing processes, new dye designs, better fixation on the material etc. In any case, the processes in non-aqueous phases are challenging requiring usually the addition of liposomes,[35] the implementation of ultrasonic energy[36] or other techniques.

Overall, the chemistry of dyes and specifically azo-dyes is a huge topic which entails many different subjects. It is important to understand that the solution might be not only one material or process, but a combination of them. For example, industrial dye effluents require a direct treatment with inorganic materials. Industry needs to tackle the degradation of dyes on a large scale and reduce the level of their concentration enough so that bacterial degradation can take over and decompose the intermediates. Phytoremediation can be applied around industrial premises and polluted water lagoons to ensure a long-term environmental remediation. Thus, from a chemistry point of view, it is interesting to realise the effect of catalytic materials on the dyes, since, from an engineering point of view they may not be the entire solution, but only an effective part of it.

6.2 Experimental approach

6.2.1 ZIF-9 performance of Oil Red O decolouration in 1-octanol

6.2.1.1 Objective and experimental methodology

The previous project (reduction of 4-nitrophenol) proved that ZIF-9 is an efficient catalyst and photocatalyst, that can effectively hydrolyse $NaBH_4$ and accelerate the reduction of the substrate dissolved in water. With ZIF-9 having a hydrophobic affinity itself, it is useful to test whether it can hydrolyse the borohydride in an oily medium. As the hydrophobic character of ZIF-9 is one of the interesting features of the material for this application, it is also interesting to compare the efficiency of the cobalt(II) sites in the hydrogen production and dye degradation from the hydride in the non-aqueous medium.

The effect of this hydrolysis can be measured by the presence of an oily dye. The availability of hydrogen is expected to reduce the azo-groups of the dye and possibly alter or break down its molecular structure. This process could result to complete or partial decolouration and can be monitored via UV-VIS spectroscopy. To the author's knowledge, oily dye degradation and non-aqueous hydrogen

extraction from sodium borohydride have not been reported before with inorganic/organic materials.

The oily dye chosen for this experiment is a diazo dye called Oil Red O (Scheme 6.3). It is a dye soluble in fat and typically used in biology to stain the fat cells in frozen tissues. Attempt to dissolve the Oil Red O in two chosen candidate media resulted in the rejection of silicon oil and the prevalence of 1-octanol. The rationale behind the 1-octanol option stemmed from the octanol/water partition coefficient (K_{ow} or usually applied as $logK_{ow}$) where the octanol phase represents the lipid cells of a living organism and the water phase represents aqueous fluids low in protein, such as blood serum and plasma. (The coefficient itself is an index of distribution of a chemical, such as a drug or a pollutant, in the different parts of a living body, such as human body or a fish, used for a series of applications, such as drug permeability in target organs or bioaccumulation). As highlighted in Scheme 6.3, Oil Red O can have both azo (green highlight) and hydrazone (yellow highlight) form present in the molecule.

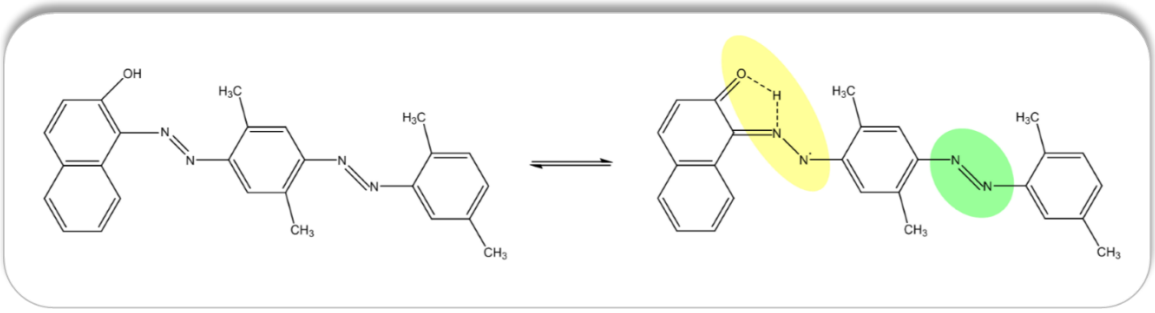

Scheme 6.3 Illustration of the Oil Red O molecule in azo-enol and hydrazone tautomers.

The addition of the dye in 1-octanol resulted in a red homogeneous phase, where no particles of the solid dye were apparent for a range of dye concentrations. The solutions of different concentrations were spectroscopically probed with UV-VIS against 1-octanol as reference solvent, from where the concentration of 0.025 mM was selected as ideal for starting solution. The pairs of the UV-VIS absorption intensities with the corresponding concentrations were used for the calculation of the calibration curve. Two calibration curves were formed due to the two peaks (one at 359 nm and one at 518 nm with an intensity ratio ca. 1:1.5) that are present in the spectrum of Oil Red O (inset plot in Figure 6.1). Syringe filters for hydrophobic solvents were also used and showed no significant difference before and after their application. The calibration curves are plotted in Figure 6.1.

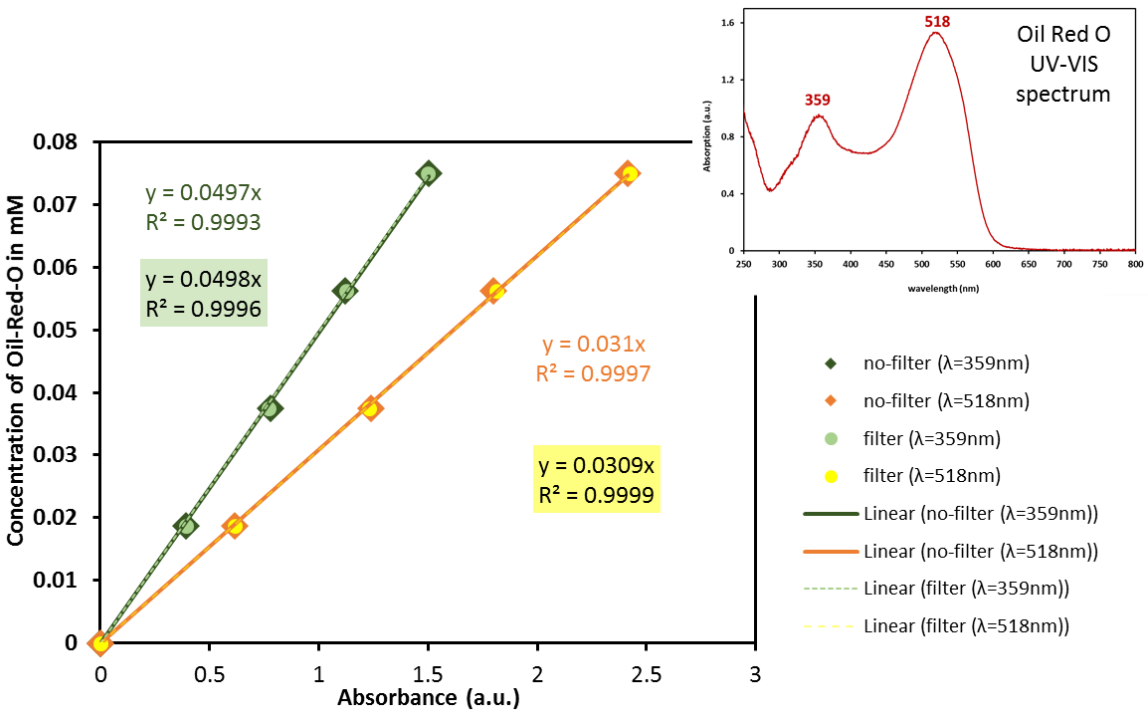

Figure 6.1 Calibration curves between the concentration and the intensity of the absorption peaks measured with UV-VIS for Oil Red O.

The reaction is taking place in glass vials in the darkness and the reaction mixture is 20 mL, unless stated otherwise, while the sampling volume is 1mL occurring every 30 minutes. Different concentrations of ZIF-9 are tested (0.1 mg/mL, 0.3 mg/mL and 0.5 mg/mL) and the results are also analysed kinetically. The reducing agent is $NaBH_4$ and is kept in excess, with a mass concentration equal to 0.4 mg of $NaBH_4$ per mL of starting reaction mixture (translated into a molar ratio of $NaBH_4$ over Oil Red O equal to 560).

Preliminary experiments showed that borohydride at this concentration can be completely dissolved in the solvent and is active. In detail, reactions of Oil Red O with borohydride at 0.2 mg/mL showed a small catalytic effect after 5 hours, while reactions progress at 0.75 and 1 mg/mL showed similar effect with reactions at 0.4 mg/mL, which was attributed to the observations that $NaBH_4$ crystals were found intact in the solution when the concentration was higher. Subsequently, the 1-octanol/dye mixture has a low capacity to dissolve excessive amount of borohydride, while data for the solubility of the borohydride are found mainly for water.

Hydrogen peroxide is considered a friendly oxidant for dye degradation, as it decomposes towards water and oxygen and published examples have shown good efficiencies (Table 6.2). For this reason, it is attempted to decolourise Oil

Red O solution in 1-octanol with the use of oxidant. For this reason, H_2O_2 is employed and used in relative excess with the quantity of Oil Red O. The peroxide is 30% w/w in water and for this reason, vigorous stirring is applied, to maximise the contact between the two phases. The hydrogen peroxide is used in fresh Oil Red O solution in combination with ZIF-9 to compare the degree of decolouration achieved with sodium borohydride. Then, the hydrogen peroxide is also used in the Oil Red O solution which has been processed with the borohydride.

Table 6.2 Degradation of azo and non-azo dyes accomplished with H_2O_2 and heterogeneous catalytic systems.

Application REFERENCE	Catalyst system	Performance	Comments
Degradation of Acid Orange 12[37]	Mn IV porphyrins	93% in 15 min.	Azo-dye, pH=10
Degradation of Brilliant Green[38]	Mn IV porphyrins	(a): 70% in 2h. (b): 99% in 2 h.	Non-azo dye Molar ratio of Mn:Oxidant:Dye (a): 1:5000:100 (b): 1:5000:10
Degradation of Congo Red (100 mg/L)[39]	$Cu_xCo_{1-x}O$	(a): 50% in 5 h. (b): 95% in 5 h.	Azo-dye (a): 20 °C (b): 50 °C 100 mg of catalyst/L
Degradation of Acid Orange 7 (0.2 mM)[40]	Metal-free Carbonate activated peroxide	80% in 6 h.	Azo-dye Conditions: 25 °C, pH=12 $[H_2O_2]$ = 5 mM
Degradation of Crystal Violet (20 ppm)[41]	Iron Oxide	90% in 2.8 h.	Non-azo dye $[H_2O_2]$ = 0.39 mM

Application [REFERENCE]	Catalyst system	Performance	Comments
Degradation of Acid Blue 29[42]	Cu^{2+} complex	(a): 90% in 20-40 min. (b): 90% in 4.8 h.	Azo-dye (a): $[H_2O_2]$ = 0.4 mM (b): $[H_2O_2]$ = 0.01 mM
Degradation of carmoisine	Co^{2+}/NaY	99% in 2 h.	Azo-dye, pH=6
	Fe^{3+}/HY	97.5 % in 1 h.	

6.2.1.2 ZIF-9 activity in the oily phase: catalytic results and kinetic regime

In the previous project (reduction of 4-nitrophenol) in Chapter 5, the addition of ZIF-9 in the solution altered significantly the starting solution spectrum. However, the addition of ZIF-9 in the1-octanol based solution of Red Oil O does not have the same effect and the spectrum remains practically unchanged. However, when $NaBH_4$ is employed in the reaction mixture in the presence and absence of ZIF-9, the spectral patterns of the solutions change significantly, indicating different mechanistic pathways of the dye reduction.

In more details, the spectra in Figure 6.2 regard the catalyst-free mixture (left) and the reaction mixture with ZIF-9 at 0.5 mg/mL (right). The peak at 518 nm is reducing in both spectra with the reduction being faster and more effective when the catalyst is present. Hence, the background reaction exists and it cannot be negligible, as a reduction of 20% is achieved over 3.5 hours. However, ZIF-9 at 0.5 mg/mL achieves 80% reduction of the intensity of the specified peak over the same amount of time.

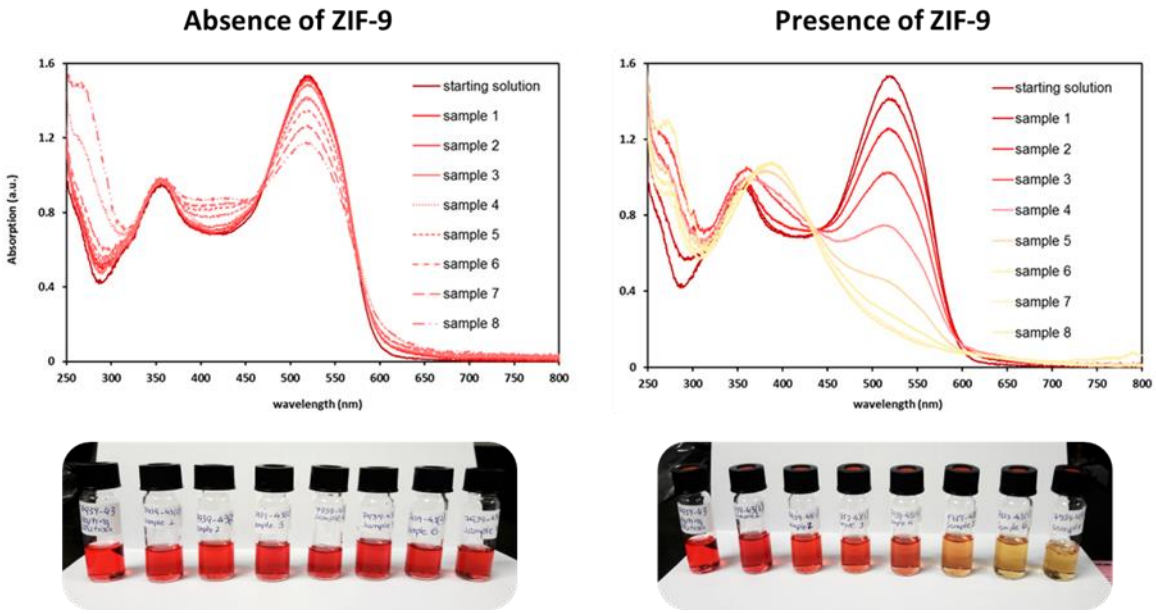

Figure 6.2 Interaction of Oil Red O with $NaBH_4$ in the absence and presence of ZIF-9 at 0.5 mg/mL over time.

Regarding the peak at 359 nm, not only does it shift towards longer wavelengths when ZIF-9 is present, but it also becomes broader. The specified peak for the blank reaction mixture (absence of ZIF-9) remains at the same intensity and wavelength position. However, the valley between the two peaks raises progressively over time for the catalyst-free mixture, whereas shift and broadening of the peak regarding the ZIF-9 containing reaction mixture takes place, practically disappearing the valley.

Given this observation, the reduction of the peak at 518 nm is selected for the kinetic analysis of the results later on as the most dominant and clearest effect of the availability of hydrogen. Furthermore, despite the change of the shape of the curves, one can observe in both spectra the formation of isosbestic points (isoabsorption). Yet, the isosbestic points appear at different wavelengths in the case of blank and catalytic reaction. All the catalyst-free regarding spectra cross at a wavelength much higher than 450 nm, while the catalyst regarding spectral curves exhibit this intersection both at lower wavelength than 450 nm and lower intensity than in the previous case.

The appearance of isosbestic points at non-monotonous spectral curve patterns is not accidental and is connected with another parameter of the system different from the concentration of the dye in the solution. Isosbestic points occurrence is typical in UV-VIS or Raman spectra of molecules bearing chromophore groups and

usually reflects the different forms that these groups take. For azo-dyes, the dominance of each form depends most frequently on the pH of the solution[43,44] as Scheme 6.4 shows.

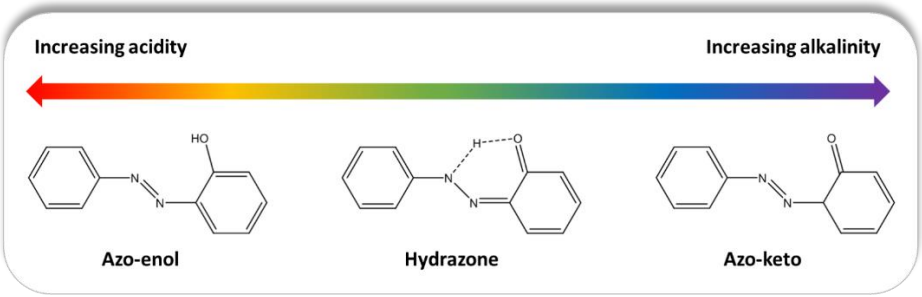

Scheme 6.4 Schematic illustration of the dependence of the various azo forms on the pH.

In particular, the azo-keto form is expected at high pH values, because it is more stable in alkaline conditions, but as the conditions turn more acidic, the hydrazone form predominates as the hydrogen bonds contribute towards this transition. The spectral peak dominance is important in this case, as tautomeric forms prevalent in basic/acidic environment or polar/apolar solvents will appear at different wavelength bands.[43] Generally, azo forms are expected to appear at shorter wavelengths of the visible spectrum in relation to hydrazone, due to the charge transfer interaction within the groups.[7,45–47] Provided this information, the peak at 359 nm is assigned to the azo groups of Oil Red O dye and the peak at 518 nm is assigned to the formed hydrazone groups.

The pattern of the spectra obtained from solutions with lower ZIF-9 concentrations did not change. The intensity of the dominant peak decreased, although less than for ZIF-9 concentration at 0.5 mg/mL, while the other peak demonstrated a red shift, disappearing the valley between the two peaks. Isosbestic points were again apparent. The achieved total reduction of the intensity of the main peak has been calculated and plotted in Figure 6.3 and regards the same reaction time. The reduction achieved with 0.5 mg of ZIF-9 per mL of reaction mixture is over 80%, while the reduction achieved for 0.3 and 0.1 mg/mL is around 75%. $NaBH_4$ in the absence of ZIF-9 achieved less than 25% of reduction.

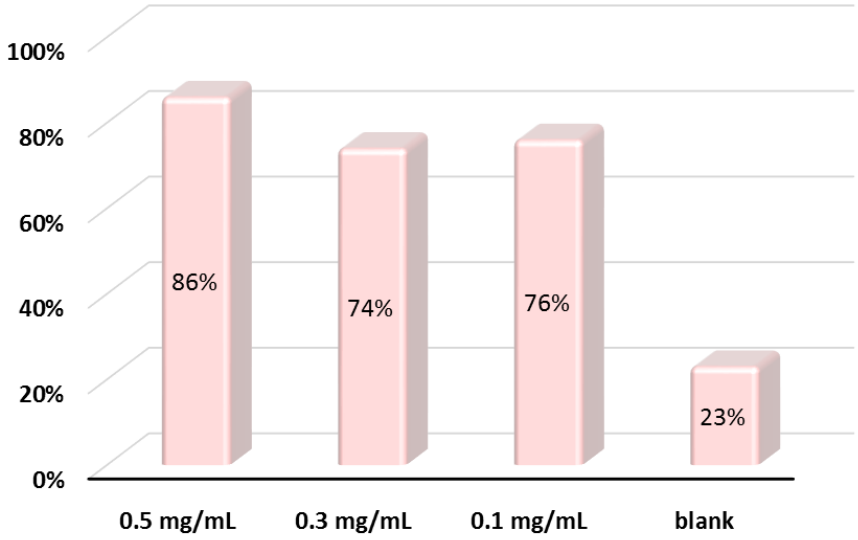

Figure 6.3 Total reduction of the peak at 518 nm after 3.5 hours of reaction of Oil Red O with $NaBH_4$, in the presence ZIF-9 at various concentrations.

This difference between the blank and the catalyst-containing reaction mixture is most probably due to the contact of ZIF-9 with the borohydride. Lately, MOFs have been studied as effective platforms for hydrogen generation from hydrides.[48] Mg-MOF-74, Zn-MOF-74 and Fe-MIL-53 have been used successfully for dehydrogenation of ammonium borane at temperatures lower than 80 °C.[49–51] ZIF-9 has been employed in the dehydrogenation of $NaBH_4$ in room temperature[52] and ZIF-8 has been proven efficient for hydrogen production from ammonium borane at 85 °C.[53] The general concept behind these applications is the interaction of the open frameworks with hydrogen atoms and the relatively small molecules of the hydrides which fit into the pores of the MOFs and access the active sites, while the hydrogen molecule can very easily diffuse out of the solid structure.

The total reduction achieved with different ZIF-9 concentrations does not vary significantly and the spectra mostly follow the same pattern. The pattern of the reduction overtime draws the attention since induction times are observed when ZIF-9 is present and the curves follow a sigmoidal shape (Figure 6.4). Unlike the catalytic reactions, the blank reaction kinetics regime shows a good fitting with linear regression. Generally, sigmoidal decay is considered a good indication of heterogeneous catalysis with metals under reducing conditions,[54] while it is very frequently applied to describe enzymatic reaction is biochemistry, where biomolecules may hinder the enzymatic activity. In heterogeneous catalysis, the

sigmoidal decrease is usually explained by Langmuir adsorption on the surface of the catalyst and in situ formation of reactive species.[54]

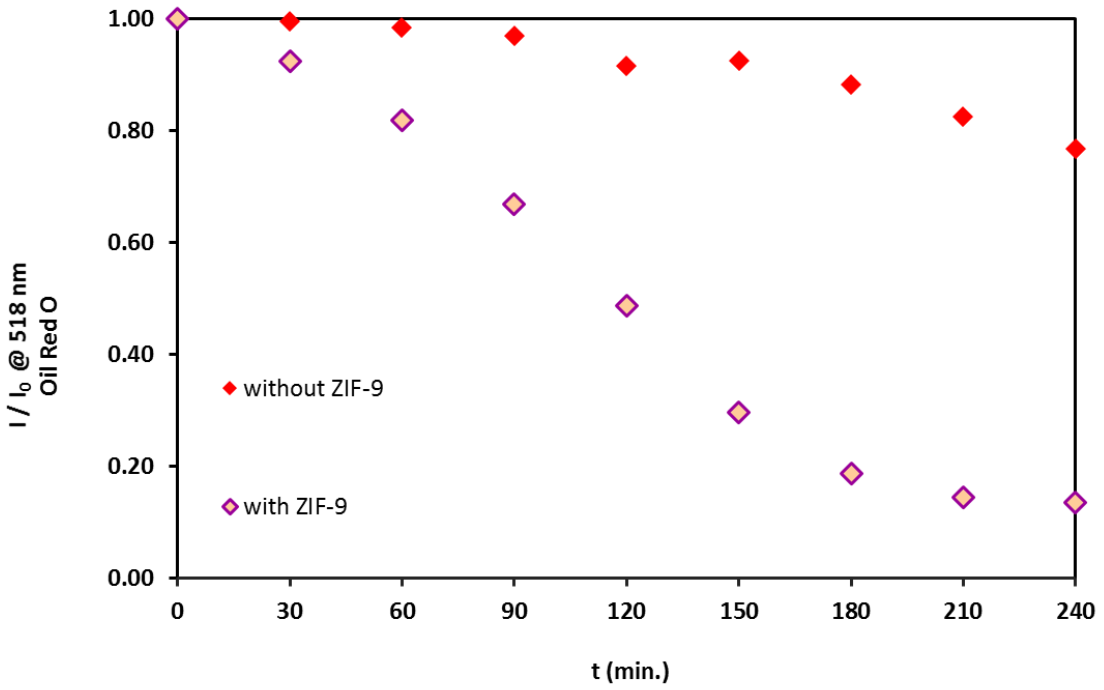

Figure 6.4 Reduction of the intensity of the peak at 518 nm overtime, in the reaction of Oil Red O with $NaBH_4$ in the presence of ZIF-9 at 0.5 mg/mL.

Due to the linear regression that can be applied to the blank solution, the analysis is based on the logarithm of the ratios of the concentration (intensity of dominant peak) of the sample over the corresponding value of the starting solution. However, either absolute ratios or ratio logarithms will lead to the same conclusions, since the kinetic analysis is comparative. The model that is applied to the sigmoidal curves is the Hill decay model and is well-described with Equation 6.1. Convergence is considered achieved if the calculated tolerance is below $1 \cdot 10^{-9}$, while the R-square metric is also used as an indicator of good fitting of data.

$$f(x) = \frac{x^n}{k^n + x^n} \qquad \text{Equation 6.1}$$

The Hill model is purely mathematical and thus, the order of the formula and the k constant are not of physical interpretation. However, the Hill model describes sigmoidal curves, which consist of an upper and initial plateau, followed by a

"linear" part and ending with a lower plateau. The sigmoidal curves are technically the sum of different phases which correspond to non-concurrent phases during which the catalyst binds to the substrates, the sites get saturated and the products desorb. The sigmoid trend is also connected to affinity of the catalyst (usually enzymes) with more than one sites, which means that the catalytic system undergoes a change and can bind to more than one site.[54] The upper plateau indicates an induction time. The "linear" part reflects the reaction process. The lower plateau appears obviously when the reaction system does not demonstrate any further progress.

Therefore, the important parts are the upper plateau and the linear part. The induction time will show how long the catalyst takes to become active in order to start catalysing the reaction. The "linear" section will reveal information relative to the reaction rate and mathematically, it regards the steepness of the curve at the point of its inflection (Figure 6.5). Practically, it is a line with slope equal to the 1st derivative at the inflection point, the midpoint of the turnings of the curvatures. Mathematically, it is the point where the direction of the concavity change, and can be found from the calculation of the 2nd order derivative. The change of the concavity is accompanied by a value of the 2nd derivative equal to zero along with change of the sign on either side of the critical point.

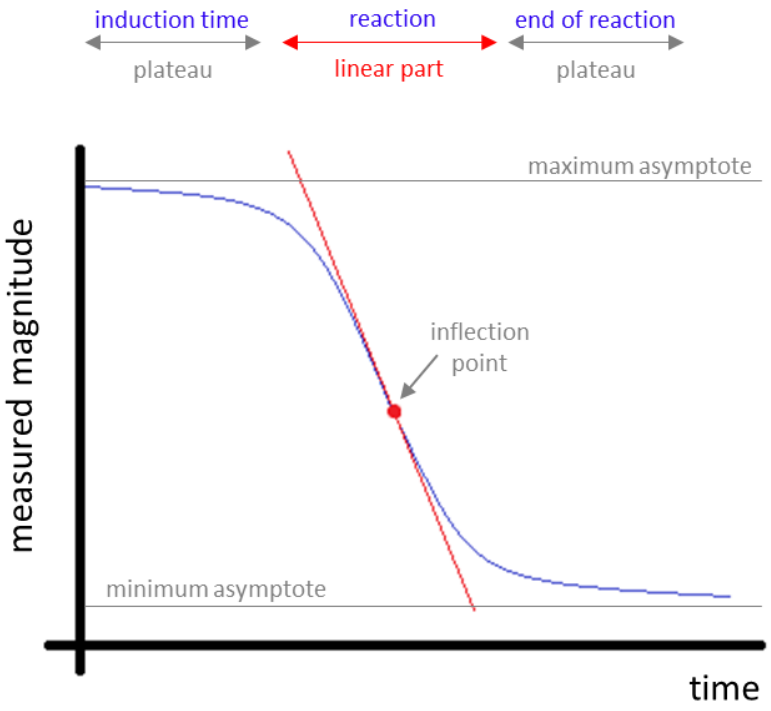

Figure 6.5 Demonstration of the important parameters of a sigmoidal decay.

Having described the mathematical approach for the kinetic analysis, the experimental and fitted data are shown in Figure 6.6. All the results are tabulated for comparison of the different ZIF-9 concentrations in Table 6.3. Induction times are calculated qualitatively and slopes of the lines at the inflection points have been calculated after the Hill model application. All results refer to the same molar ratio of $NaBH_4$ over Oil Red O (560) and different ZIF-9 concentrations, while the total reduction achieved for each case has been added for reasons of comparison. The functions that accrued from the non-linear regression of the experimental data are found in the Appendix D.1.

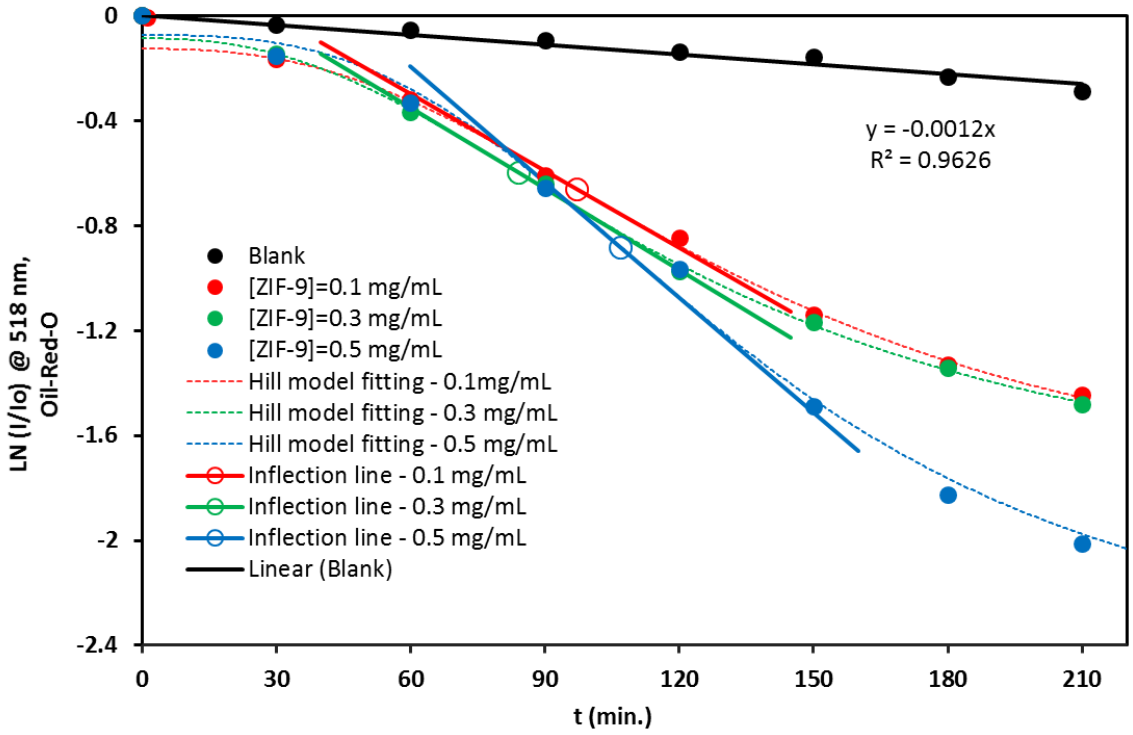

Figure 6.6 Experimental data and Hill model fitting of the decrease of the 18 nm peak intensity monitored overtime for the reaction mixture of Oil Red O with $NaBH_4$ and different ZIF-9 concentrations.

Table 6.3 Collected results for the Oil Red O reaction with $NaBH_4$ in the darkness.

[ZIF-9] in mixture	Induction time	Absolute slope of line at inflection point	Total reduction of peak intensity
$0\ ^{mg}/_{mL}$ (blank)	N.A.	$\lvert slope \rvert = 0.001$	23%
$0.1\ ^{mg}/_{mL}$	$t \cong 60\ min.$	$\lvert slope \rvert = 0.010$	76%
$0.3\ ^{mg}/_{mL}$	$t \cong 45\ min.$	$\lvert slope \rvert = 0.010$	74%
$0.5\ ^{mg}/_{mL}$	$t \cong 30\ min.$	$\lvert slope \rvert = 0.015$	86%

Overall, a slow background reaction between the Oil Red O and the $NaBH_4$ is observed, which is enhanced via the addition of ZIF-9. Addition of 0.1 and 0.3 mg/mL resulted in 10 times faster reaction than the blank and ca. 50% increase in

reduction. Addition of 0.5 mg/mL improved slightly the results, by reducing the induction time, accelerating the progress of reaction and increasing the achieved reduction.

Finally, H_2O_2 experiments were performed with and without ZIF-9. Initially, a volume of 20 mL of fresh Oil Red O solution 0.025 mM was combined with 1 mL of H_2O_2 (30% w/w/ in water), which results into a molar ratio of peroxide over dye equal to 19.5 and the mixture was vigorously stirred without ZIF-9. The same experiment was performed with ZIF-9 at concentration 0.5 mg/mL. The registered spectra (Appendix D.2) showed a reduction of the peak at 518 nm and no significant alteration of the spectral pattern.

In particular, the peak at 359 nm did not shift wavelength or width, while the catalyst-free mixture also showed 10% reduction of the 359 nm peak. The same peak did not change for the ZIF-9 containing mixture. For the ZIF-9 free mixture, the intensity of the peak at 518 nm was reduced by 13% in the first 30 minutes, against the 24% reduction, which was achieved when ZIF-9 was used over the same amount of time. However, the first sample of the catalytic reaction was taken at 10 minutes, which showed 22% of reduction. The reactions were left for another hour and no significant change was monitored, which was practically interpreted as the end of the reaction.

A similar experiment was designed with peroxide, where 1 mL of H_2O_2 is added to the mixture of Oil Red O with ZIF-9 at 0.5 mg/mL processed in prior to 3.5 hours with $NaBH_4$. Thus, the starting solution lacks the peak at 518 nm and this would help understand better the ability of H_2O_2 to decrease the peak at 359 nm, which was shifted at 410 nm. The spectrum showed reduction in the region centred around 518 nm by ca. 25%. The peak at 410 nm showed no significant reduction in terms of intensity (less than 5% over 45 minutes), but it moved towards the blue area by 10 nm.

Subsequently, the hydrogen peroxide effect is not significant in this system in the presence or absence of ZIF-9. Unlike the examples gathered in Table 6.2, this system is not aqueous. Moreover, ZIF-9 contains organic ligands in its framework. The interaction of the peroxide with the organic parts can deactivate the catalyst, by oxidizing violently the organic parts and the active Co(II) sites to Co(III). No further experiments have been conducted with H_2O_2.

6.2.2 Dye wastewater decolouration with ZIF-9

6.2.2.1 Objective and experimental methodology

Having established that ZIF-9 decolourises oily solutions of the Oil Red O dye, use of ZIF-9 for the decolouration of real wastewater is probed with $NaBH_4$. The wastewater is subjected to decolouration with $NaBH_4$ in the darkness and in the presence of ZIF-9 and the parameters probed in this experiment regard the concentration of ZIF-9, the concentration of $NaBH_4$ and the stirring speed.

A green piece of fabric (a common headscarf of blue-green colour) is soaked in warm water for 12 hours and the wastewater takes a vivid blue-green colour (Figure 6.7b). The dye wastewater was submitted to FTIR analysis and the spectrum was compared to the FTIR spectrum of the solution of Oil Red O in 1-octanol. It is noted that the collection of each spectrum followed the collection of the spectrum of the corresponding solvent (tap water for the wastewater and 1-octanol for the Oil Red O dye) in order to perform correction of the baseline. The spectra are found in Appendix E.1 and it can be deduced from the comparison that the dye wastewater has similar functional groups as the Oil Red O dye.

Additional analysis of the wastewater is performed via UV-VIS. Initially, a UV-VIS calibration curve (Figure 6.7c) is produced for 1:3 and 2:3 dilution of the sample with deionized water, in order to ensure that the pattern of the UV-VIS curves does not change with dilution and that Beer-Lambert law is valid (Figure 6.7a). Interestingly, the pattern does not change dramatically. The main peaks do not shift, while a double split can be discerned for the highest wavelength peak. However, the split is small and therefore, one band (centred around 659 nm) is taken into consideration. Moreover, the ratio of intensities between the two main peaks changes with water content. The two peaks represent the two forms, with the azo group at 610 nm and hydrazone group or azo-keto group at 659 nm.

Next, brief preliminary tests are performed and the control experiment is designed as follows: 10 mL of wastewater is combined with 4 mg of $NaBH_4$ (thus, concentration of borohydride set at 0.4 mg/mL) and ZIF-9 at concentration of 0.5 mg/mL. Monitoring of the progress of the reaction took place via UV-VIS spectroscopy. Variation of the control experimental regarded variation of the ZIF-9 concentration (0.1, 0.3 and 0.5 mg/mL), variation of the $NaBH_4$ concentration (0.4 and 0.8 mg/mL) and variation of the stirring speed (at 250 and 700 rpm). Total reduction and kinetic regime were studied and are presented hereafter.

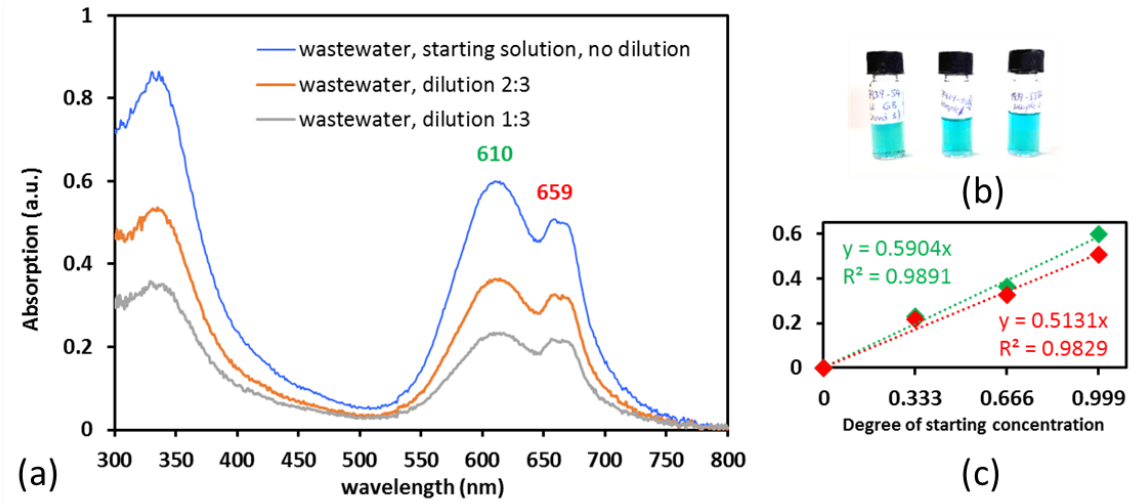

Figure 6.7 (a) UV-VIS spectra of dye wastewater at different dilution degrees, (b) picture of the dilution samples and (c) calibration curve for the two maximum absorption peaks.

Next, brief preliminary tests are performed and a set of control experiments is designed in order to gain an initial insight of the reaction in terms of the effect of the catalyst and $NaBH_4$ presence and of the reaction time. Table 6.4 gathers the parameters checked for the control experiments, while monitoring of the progress of the reaction took place via UV-VIS spectroscopy. Having established the catalytic effect of ZIF-9 in this reactive system with $NaBH_4$, the next two sets of experiments focuses on the catalyst concentration (0.1, 0.3 and 0.5 mg/mL) and on the stirring speed (at 250 and 700 rpm). Total reduction of the intensity of the dominant peak and kinetic regime were studied and are presented hereinafter.

Table 6.4 Design of set of control experiments to study the decolouration of real dye wastewater.

Exper.	[ZIF-9] mg/mL	[$NaBH_4$] mg/mL	Purpose of experiment
a	—	0.4	Blank reaction
b	0.5	0.4	Study of ZIF-9 presence, by comparison between *a* and *b*
c	0.5	0.8	Study of $NaBH_4$ concentration, by comparison between *b* and *c*

Exper.	[ZIF-9] mg/mL	[$NaBH_4$] mg/mL	Purpose of experiment
d	1	0.4	Study of ZIF-9 concentration, by comparison between *b* and *d*

6.2.2.2 Catalytic results and kinetic study of the dye wastewater decolouration

The spectroscopic results regarding the set of control experiments, as described in Table 6.4, are found in Figure 6.8. The corresponding images depicting the colours of the samples are found in the Appendix E.2. Experiments a and b showed strong catalytic dependency on ZIF-9 for the decolouration of the dye wastewater. Doubling the concentration of borohydride in experiment c results in a much faster reaction, without significant improvements in the achieved total reduction. Doubling the concentration of the catalyst in experiment d though leads into a regime similar to inhibition of reaction reflected both on the total reduction of the peaks and the reaction rate. It is observed that the pattern of the spectra does not change, except for the high concentration of reducing agent, where the spectra acquired from the first reaction samples stop resembling with the initial double band curve.

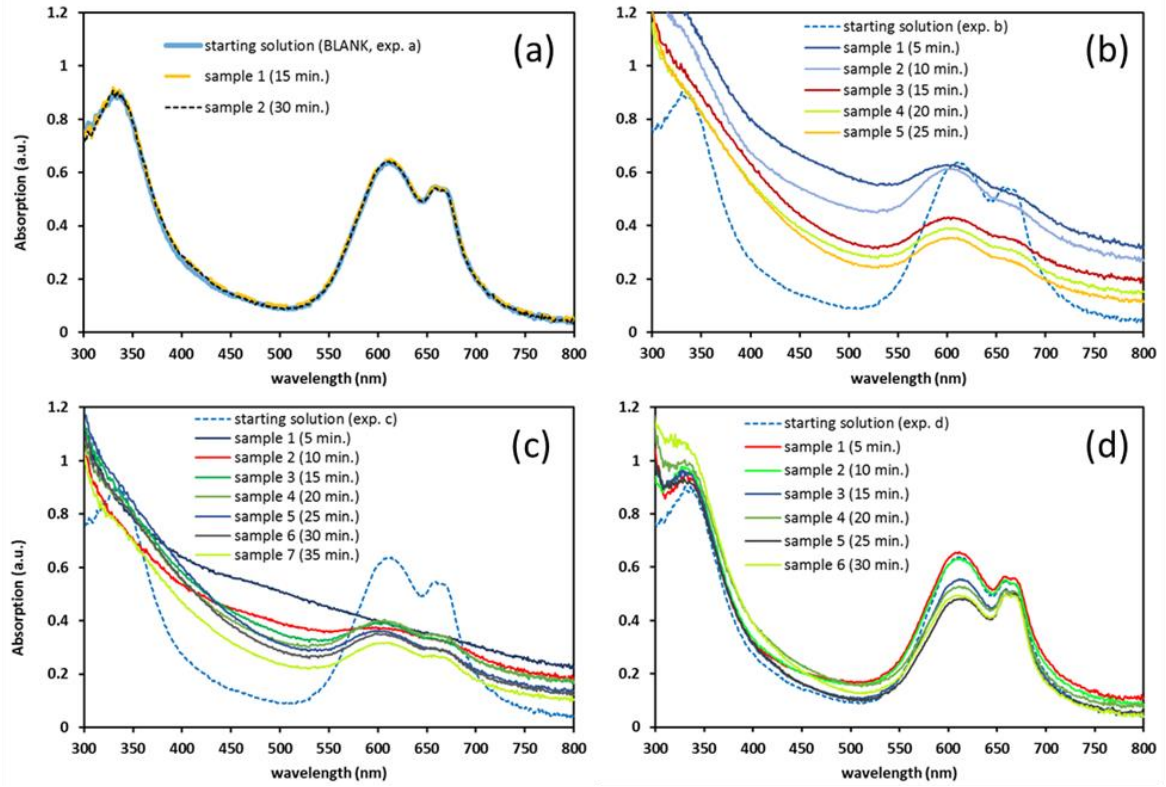

Figure 6.8 Overtime obtained spectra, regarding the set of control experiments a, b, c and d, as described in Table 6.4, for the decolouration of dye wastewater.

Translating the spectra into ratio of the main peak intensity versus time in Figure 6.9 the abovementioned observations are evident. The inset bar chart refers to the total reduction achieved over time. It should also be remarked that the experimental data follow again an almost sigmoid sequence of decay. Experiment c seems to be the exception. However, following the rationale of the experiment with Oil Red O, the data seem to lack an induction time. Simultaneously, an anomaly of the trend observed around the value at 20 minutes is accompanied by a spectral anomaly too. A closer look at Figure 6.8c shows that, towards the end of the sampling period, the spectra regain the shape of two distinguished and broad peaks, with the concavity between 350 and 550 nm becoming deeper.

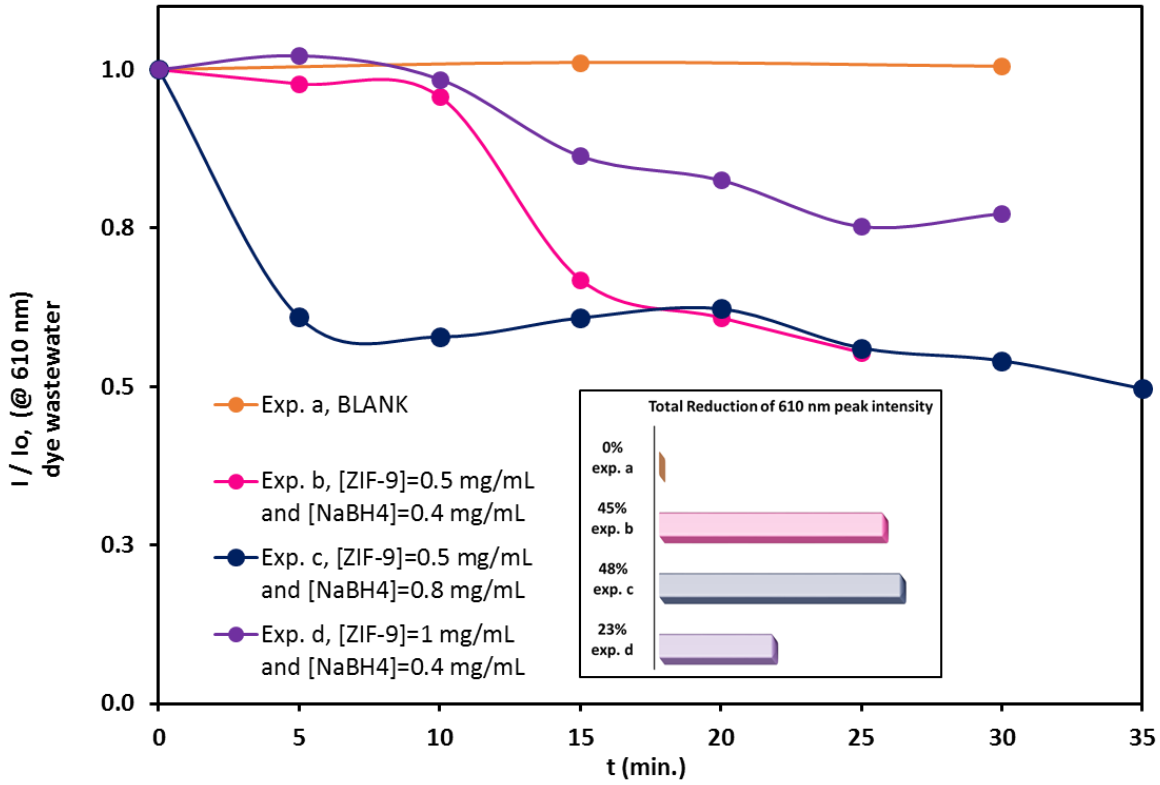

Figure 6.9 Decrease of intensity of peak at 610 nm versus time regarding the control experiments of dye wastewater and total reduction achieved (inset plot).

The smaller concentration of ZIF-9 in the reaction mixture is studied next with the concentration of $NaBH_4$ was kept at 0.8 mg/mL. The blank reaction showed that the reductant has no effect alone in the mixture. On the contrary, the presence of ZIF-9 turns reactive in the presence of the reducing agent, thus a high content of reductant will immediately show the effect of various concentrations of ZIF-9. Finally, since the reaction can be monitored over half an hour, the impact of the stirring speed is interesting due to the hydrophobic nature of the catalytic particles. With the concentration of $NaBH_4$ kept at 0.8 mg/mL, stirring speed is lowered at 250 rpm to assess preliminarily the diffusion effects.

The evaluation of the variation of these parameters is initially studied in terms of total reduction, achieved over 30 minutes of reaction (Figure 6.10). The case of the pair ZIF-9 at 0.1 mg/mL and $NaBH_4$ at 0.8 mg/mL regards the reduction over 20 minutes because the reaction did not show significant progress. It is obvious that the concentration of ZIF-9 affects the reaction significantly since 0.1 mg/mL achieve almost 30% smaller decrease of that achieved with 0.3 mg/mL and 0.5 mg/mL achieve ca. 15-20% higher reduction. Figure 6.10 also shows that the

stirring speed has an important role since the low stirring speed achieves smaller reduction of the peak than using less ZIF-9 in the mixture.

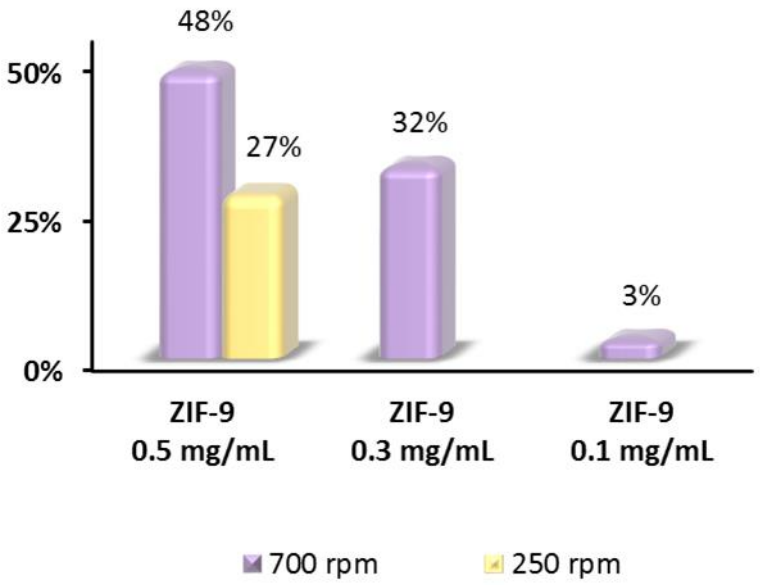

Figure 6.10 Total reduction of the 610 nm peak intensity after 30 minutes of reaction for the dye wastewater decolouration with $NaBH_4$ at 0.8 mg/mL in the darkness.

The total reduction results follow an expected order for the studied parameters. Focusing on the kinetic behaviour, analysis of the results over time takes place using the Hill model and linear regression wherever possible. Because of the linear fitting attempted in certain cases, it is preferable to keep the same basis of analysis, calculating the logarithm of the ratios, in order to have a common ground for comparison. The kinetic analysis of the control experiments is found in Figure 6.11 and the important results (induction time and slope as metric of reaction rate) are tabulated in Table 6.5.

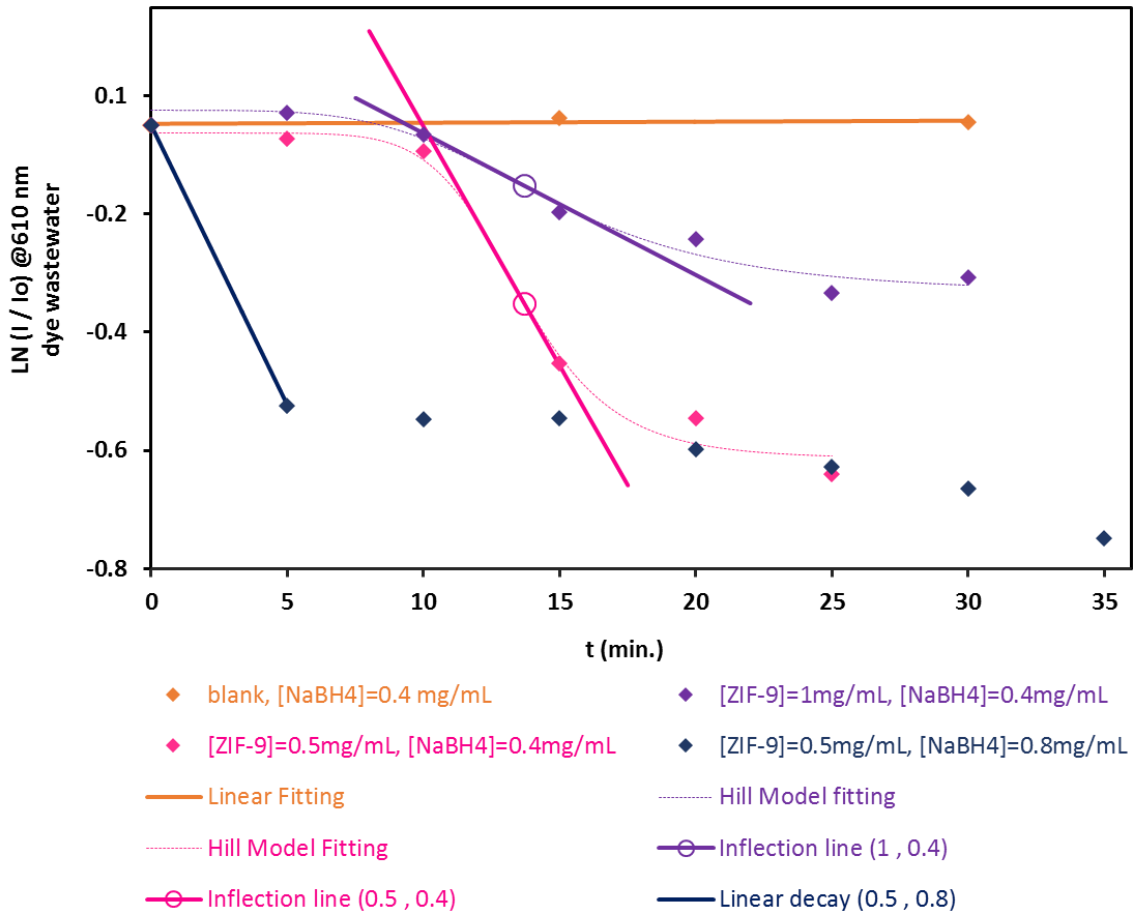

Figure 6.11 Kinetic regime of the control experiments for the decolouration of dye wastewater in the darkness using ZIF-9 and $NaBH_4$ in various concentrations.

It is obvious that the reaction is immediately occurring for the highest concentration of $NaBH_4$, while the case of increasing the catalyst does not have the same effect. Interestingly, when the reducing agent is 0.8 mg/mL in the mixture, the reaction seems to follow a decreasing sigmoidal trend after the initial decay observed. The equations that describe mathematically the trends are found in the Appendix E.3.

Table 6.5 Results of kinetic analysis of the control experiments of decolouration of dye wastewater.

[ZIF-9] in mixture mg/mL	[$NaBH_4$] in mixture mg/mL	Induction time $min.$	Absolute slope sec^{-1}
0	0.4	N.A.	$\cong 0$

[ZIF-9] in mixture mg/mL	[$NaBH_4$] in mixture mg/mL	Induction time $min.$	Absolute slope sec^{-1}
0.5	0.4	$\cong 10$	0.082
0.5	0.8	$\cong 0$	0.095
1	0.4	$\cong 8$	0.024

Similarly, the kinetic study of the reaction with various concentrations of ZIF-9 in the mixture is plotted in Figure 6.12. The best fitting for the case of ZIF-9 at 0.1 mg/mL seems to be linear and hence, linear regression was applied. The induction times and slopes are tabulated in Table 6.6.

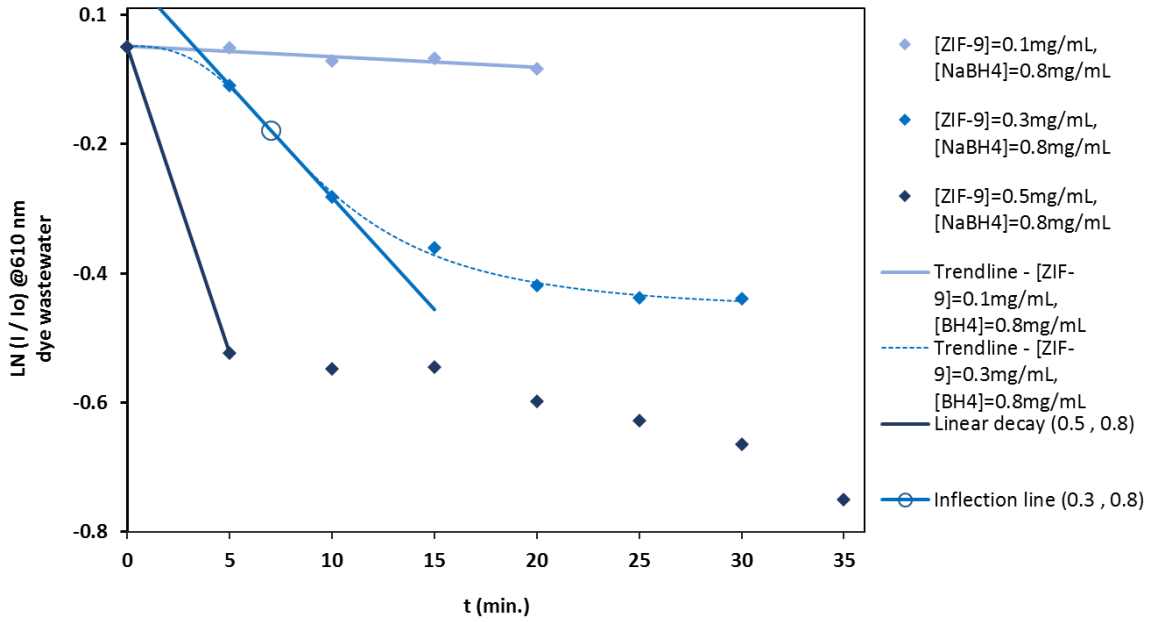

Figure 6.12 Kinetic regime of decolouration of dye wastewater in the darkness using ZIF-9 at 0.1, 0.3 and 0.5 mg/mL and $NaBH_4$ at 0.8 mg/mL.

Table 6.6 Results of kinetic analysis of the decolouration of dye wastewater carrying the ZIF-9 concentration and keeping $NaBH_4$ at 0.8 mg/mL.

[ZIF-9] in mixture mg/mL	Induction time $min.$	Absolute slope sec^{-1}	Total reduction %
0.1	N.A.	$\cong 0$	3
0.3	$\cong 5$	0.035	32

[ZIF-9] in mixture mg/mL	Induction time $min.$	Absolute slope sec^{-1}	Total reduction %
0.5	$\cong 0$	0.095	48

Finally, the kinetic approach in Figure 6.13 regards the impact of the stirring speed in the reaction system. The slopes are evident from the equations in the plot. The linear regression for the high-speed case is applied improperly as the R-square value shows. However, it serves the purpose of comparison between the rates of the reaction at different speeds.

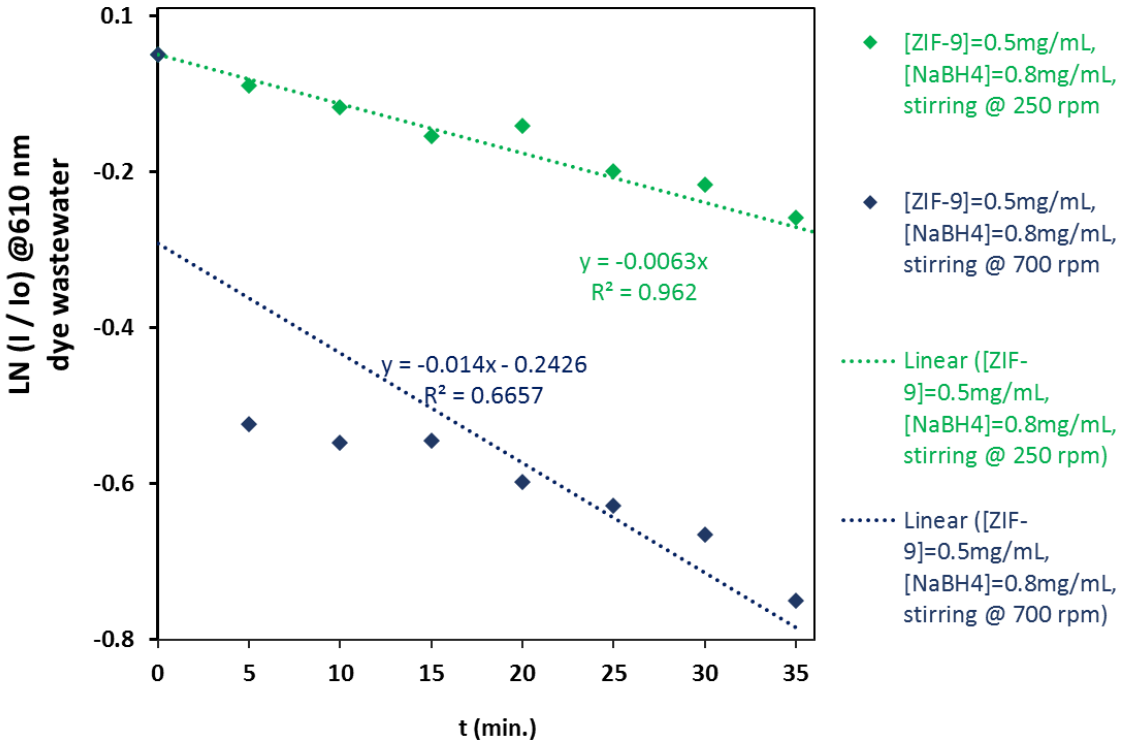

Figure 6.13 Kinetic regime of decolouration of dye wastewater in the darkness in the presence of ZIF-9 at 0.5 mg/mL and $NaBH_4$ at 0.8 mg/mL, at low and high stirring speed.

Generally, the approach that has been followed in this work shows a clear interaction between ZIF-9 and $NaBH_4$ in an oily and in an aqueous medium. ZIF-9 has been tested within the framework of dye degradation and performs catalytic activity for the decolourisation of the dyed solutions and catalytic activity for the dehydrogenation of the borohydride. It behaves as a realistic heterogeneous catalyst, since it underperforms in the lack of vigorous stirring, inferring demand for efficient contact of its solid phase, the liquid reaction mixture and the gas

production of hydrogen. Above all, it shows good catalytic activity and promotes the progress of the reactions, ensuring its catalytic nature.

6.2.3 Post-catalysis characterisation of used ZIF-9 in the decolouration of Oil Red O solution and dye wastewater

ZIF-9 is a material of crystalline microporosity as former characterisation with PXRD revealed. It has cobalt nodes linked via benzimidazolate ions, with cobalt at 2^+ oxidation state, as XPS characterisation revealed previously. Distinct particles approximately 5 nm long were observed via SEM imaging. Its catalytic activity for decolouration of Oil Red O solution and dye wastewater was measured both kinetically and in terms of final performance. However, it is interesting to also measure the degree of surface and bulk distortion of the material after having employed it for the decolouration of Oil Red O solution and dye wastewater.

The PXRD spectra of the spent ZIF-9 in the Oil Red O is compared in Figure 6.14 with the spectrum of the starting material and the theoretical pattern. Unfortunately, the quantity of ZIF-9 spent in the dye wastewater experiment proved inadequate to perform the analysis technique. However, the results for ZIF-9 used in the Oil Red O decolouration experiment indicate some interesting features.

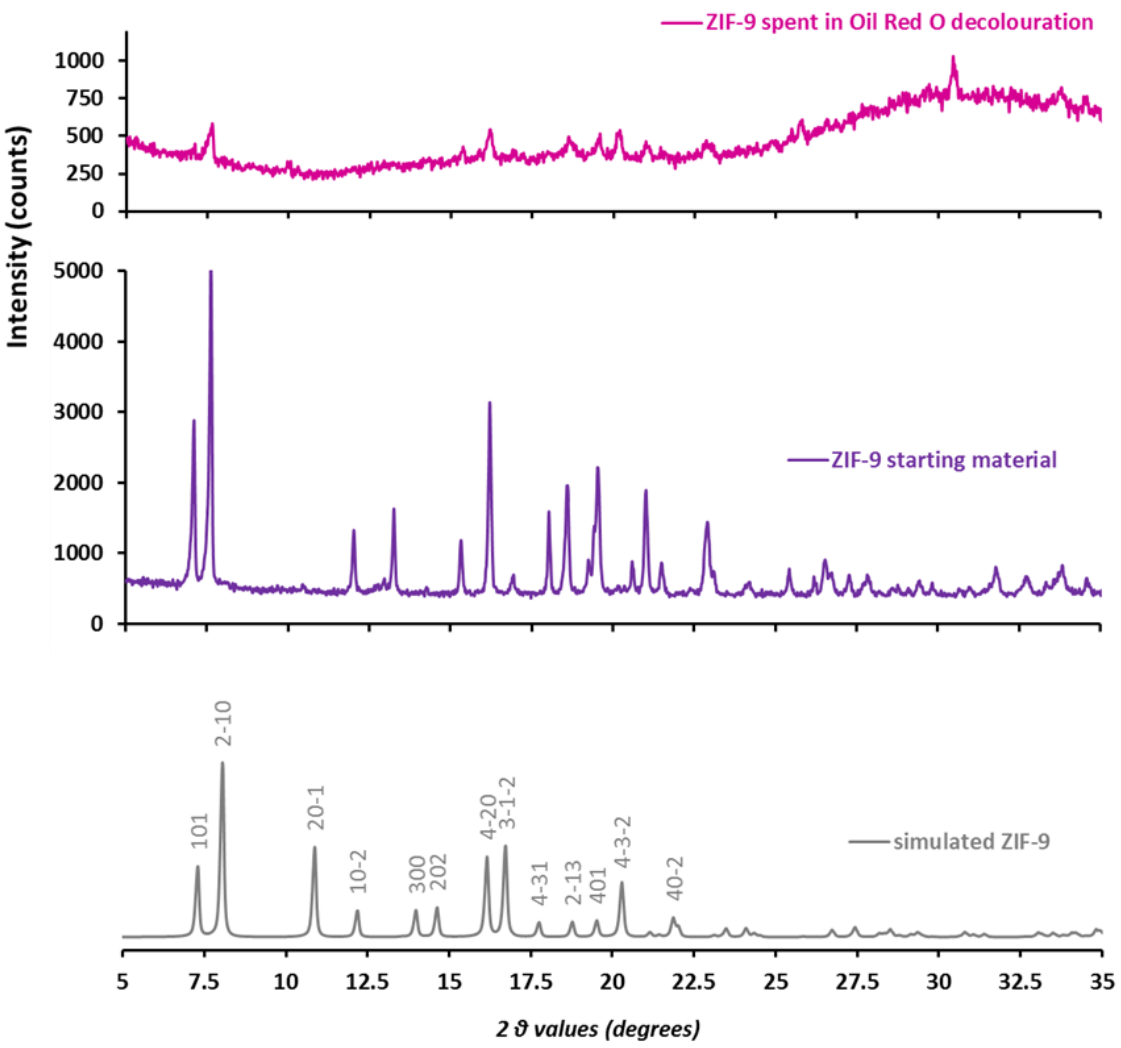

Figure 6.14 Comparative PXRD plot of simulated, as synthesized and used ZIF-9 in the decolouration of Oil Red O solution.

A considerable decrease of intensity of the main peaks is observed, with the spectrum appearing almost flat, compared on the same scale of intensity. Taking into account the inset plot, the distinguished peaks did not shift from the starting material, while rise of the background has taken place in the region of 10-25 degrees and more considerably, around the angle of 30 degrees. While the second rise is possibly connected with the instrument, the rise of the baseline in the middle area is possibly a result of amorphous phase.

Shift of the peaks is not observed but the detailed microcrystalline arrangement has diminished as the intensity of the peaks has decreased considerably (Figure 6.14). In the absence of second catalytic run, there is no specific indication that the chemical integrity has remained and that the catalyst is stable. At the same time, some extra peaks in the area above 25 degrees show the formation of a

new phase. A relatively stronger peak around the angle of 30 degrees is discerned, which could potentially be indicative of Co_3O_4.

Moving on with the XPS analysis (Figure 6.15), the spectrum acquired can be fitted when three pairs of satellite peaks are added. The main peaks are wider than the ones that belong to the Co II 2p orbit, but the positions are found at binding energy 780.9 and 796.7 eV. Therefore, the difference of the split is equal to 15.8 eV, reduced by 0.2 eV compared with the fresh material, with each peak shifting lower by 1-1.2 eV. These findings are indicative of mixed cobalt states in the used ZIF-9 and the used ZIF-9 hosts both Co^{2+} and Co^{3+} sites.

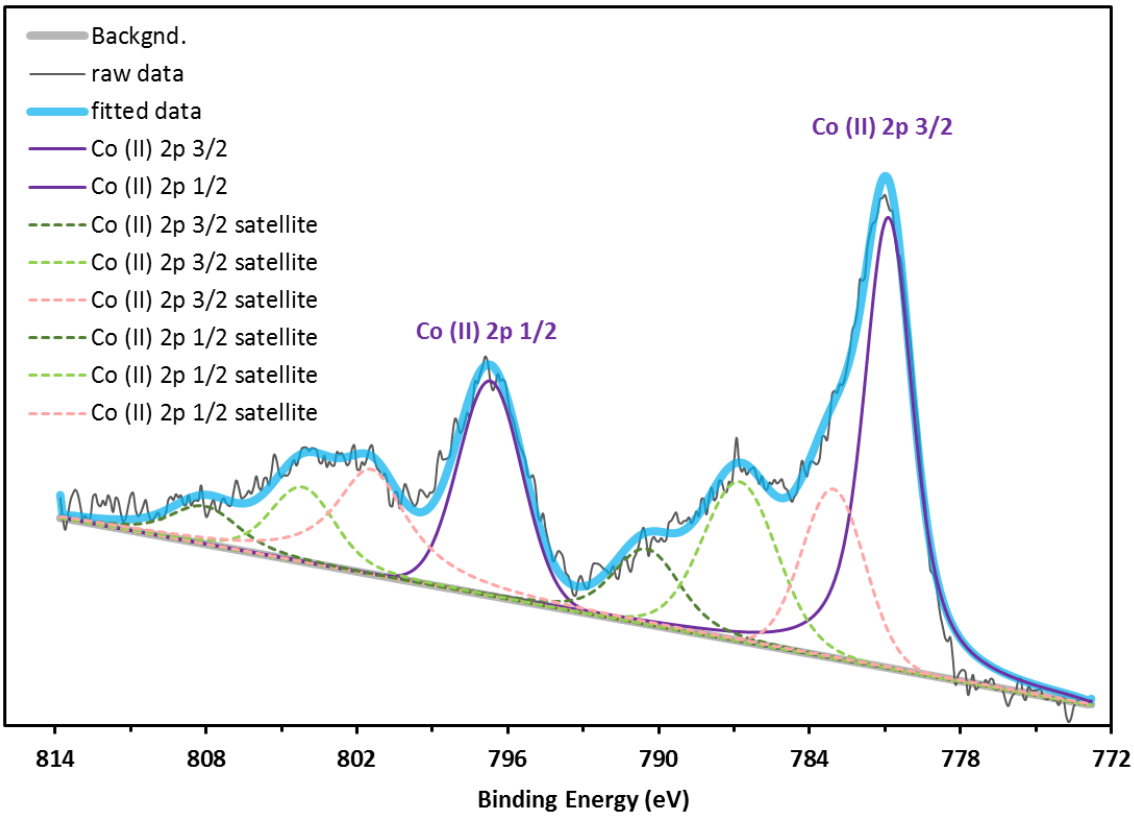

Figure 6.15 Experimental XPS spectra and fitting for the used ZIF-9 in the decolouration of Oil Red O solution.

Similar findings have been observed for the XPS analysis of the used ZIF-9 in the dyed wastewater, as Figure 6.16 shows. The fitting of the experimental data required 3 pairs of satellite peaks for the double split of Co II 2p orbit. The shift of the main peaks in relation to the fresh material is -0.7 eV with the difference of the split remaining practically the same. The main peaks appear broader and again mixture of Co^{2+} and Co^{3+} is possible on the bulk surface of the used ZIF-9.

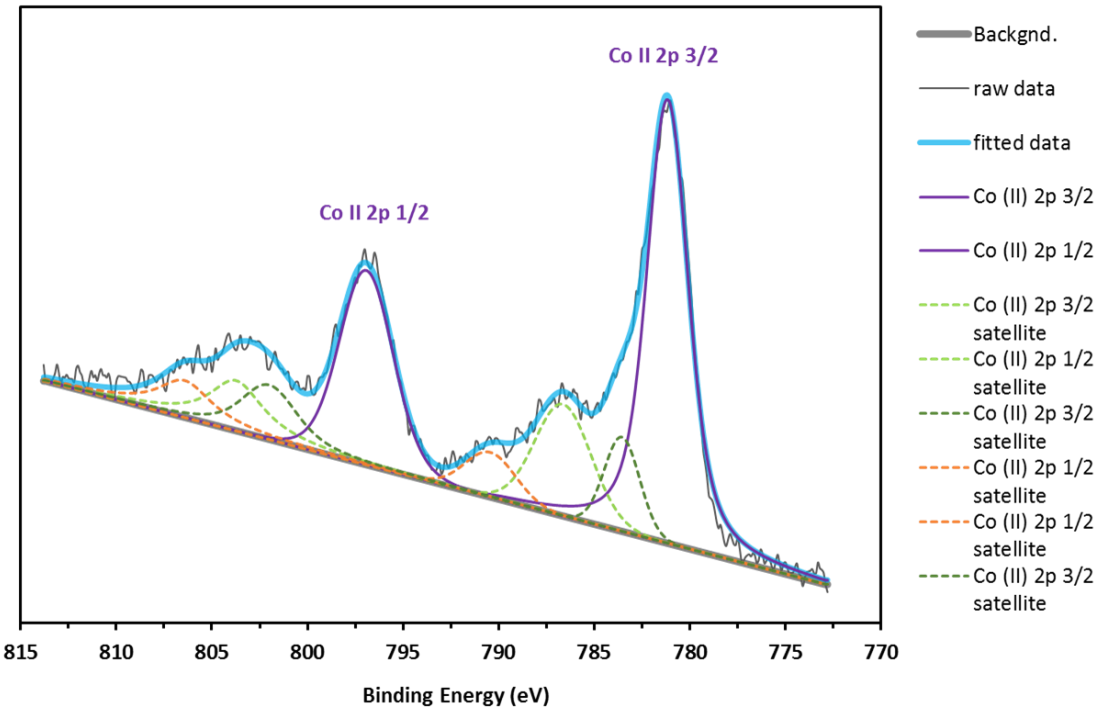

Figure 6.16 Experimental XPS spectra and fitting for the used ZIF-9 in the decolouration of dye wastewater.

After these findings, it is interesting to observe the SEM images of the material (Figure 6.17). The SEM image regards the used material in the decolouration of Oil Red O solution. However, the characterised ZIF-9 has not gone under a full catalytic cycle but regards material which was recovered after 1 hour of reaction with Oil Red O and $NaBH_4$. At this point, it should be remarked that the SEM instrument that was used for this powder gives a much higher resolution than the instrument which was employed in the characterisation of the fresh material. The SEM specifications are described in section 2.3 and the used of different instruments is due to the change of premises and instrument availability. The rod-like particles seem to have remained at good shape, with some aggregations being distinguished. However, due to the higher resolution achieved, the rod-like particles would be better characterized as brick-like particles, as it is discerned from the image. The length of the particle is ca. 5nm as it was estimated from the image of the fresh material.

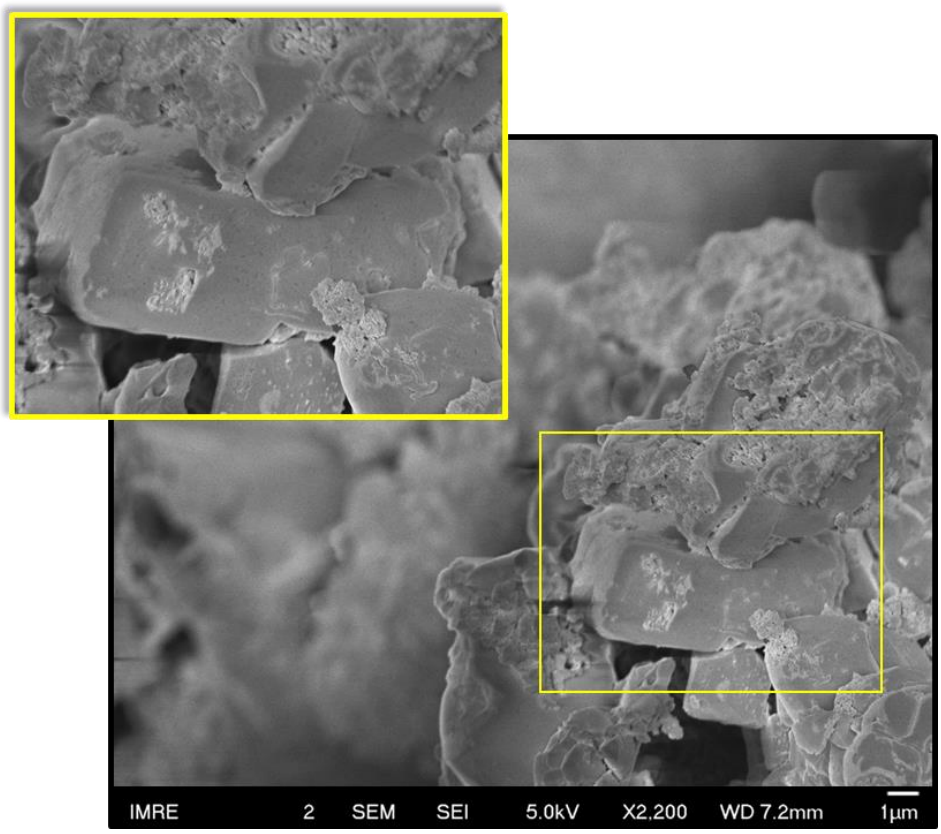

Figure 6.17 SEM image of the used ZIF-9 in the decolouration of Oil Red O solution.

Unfortunately, the amount of recovered ZIF-9 used in the decolouration of either of Oil Red O solution or dye wastewater was not sufficient for a straightforward DR UV-VIS characterisation. For this reason, fresh ZIF-9 was treated separately with the dye and the hydride and accordingly analysed. DR UV-VIS spectra in Figure 6.18 were obtained after ZIF-9 was stirred in Oil Red O solution and after treatment with borohydride. In detail, a quantity of ZIF-9 (about 0.5 mg) was stirred in 5 mL of Oil Red O solution and a quantity of ZIF-9 (about 0.5 mg) was added in water (10 mL) in the presence of $NaBH_4$ (0.8 mg/mL). The catalyst which came in contact with the Oil Red O showed an enhanced absorption, with the main peak of ZIF-9 considerably more intense and broader towards the band of 518 nm, which is the main peak of the dye. Simultaneously, the curve between 350 nm and 500 nm is elevated, but no peak can be discerned around 359 nm to be attributed to the Oil Red O second peak. On the other hand, the catalyst which was treated with borohydride has a UV-VIS pattern very similar to the fresh ZIF-9 with the intensity of the peak decreasing by approximately 20-25%.

Analysing further the DR UV-VIS spectra, the broader peak of the spectrum of the catalyst treated with the dye indicated stronger d-d transitions. In detail, as dye must have absorbed on the surface of the catalyst, the spectrum practically

reflects the behaviour of dye molecules which absorb light. The shape of the peak of the spectrum of the catalyst treated with the hydride is a good indication that the coordination geometry of the cobalt sites has not changed. Combining these findings with the XPS findings, it is possible that the amount of Co^{3+} sites is not very big and thus, chemical integrity is not largely affected.

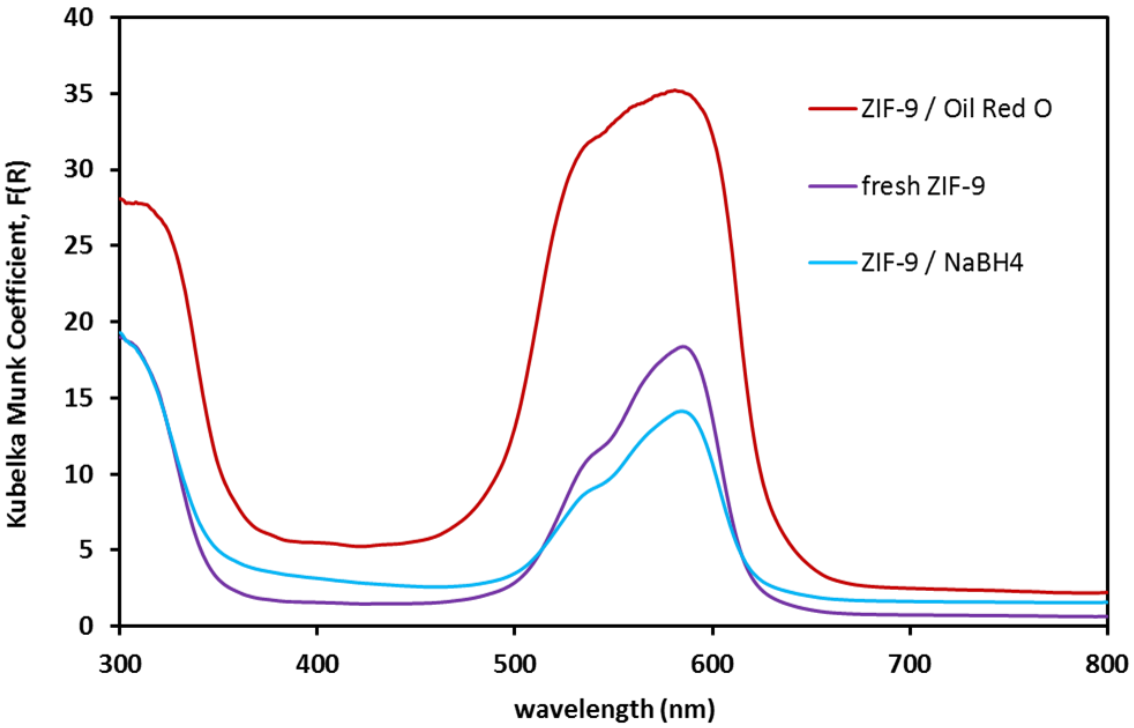

Figure 6.18 UV-VIS spectrum of Fresh ZIF-9 compared with the spectra of ZIF-9 used in solution of Oil Red O and in solution of $NaBH_4$.

Last but not least, some observations regarding the appearance of the catalyst should be noted. Recovery procedure was incredibly slow due to the 1-octanol / Oil Red O filtering. The recovered catalyst had a characteristically intense smell of 1-octanol and for the purpose of characterisation, no washing-off was performed with any solvent. Similarly, the catalyst treated with sodium borohydride was characterised as it is and attempt to perform XPS on this catalyst did not give any interesting peaks for cobalt. However, intense peaks for sodium and small peaks for borium appeared. Moreover, the experiments with H_2O_2 turned the catalyst totally black and the particles aggregated on a macroscale, evidence of total deactivation and clustering of the catalyst.

6.3 Conclusions and Discussion

ZIF-9 was used for decolouration experiments in water and 1-octanol In detail, the material was used for the reduction of Oil Red O, dissolved in 1-octanol and showed an interesting behaviour. Simultaneously, dye wastewater was used for decolouration experiments with ZIF-9. The material's good performance was added to the applications list of ZIF-9.

The catalytic results regarding the Oil Red O experiments demonstrated that the presence of ZIF-9 enhances the rate of the reaction. $NaBH_4$ on its own is able to decolourise the solution, but ZIF-9 accelerates the reaction considerably (almost 1-1.5 times faster in the presence of ZIF-9), achieving 50-60% higher total reduction upon adequate concentration of reducing agent. The decolouration reaction with and without ZIF-9 follows different paths according to the obtained spectra and the red shift of the smaller peak of Oil Red O. Interestingly, the addition of an oxidation agent (H_2O_2) does not seem to change to have any effect on this particular peak nor perform better with ZIF-9. On the contrary, strong oxidation seems to deactivate ZIF-9, possibly by oxidizing the organic parts.

Except for the speculation in the difference of reaction pathways, the decolouration reaction with ZIF-9 occurs with the formation of isosbestic points. The latter can be assigned to the achievement of an equilibrium between different forms of the dye. Generally, isosbestic points exist when two state processes occur, which do not have an intermediate in-between. In this case, if the two states respond to the two forms of the dye, then the change is elementary and immediate, while any molecular change should not regard the chromophore.

Dye wastewater decolouration experiments with ZIF-9 and $NaBH_4$ showed that the reaction was strongly dependent on the presence of ZIF-9. However, excess of ZIF-9 did not improve the reaction, while high excess of reductant changes considerably the kinetic regime reducing induction times and quickly achieving best reduction percentages. Decreasing considerably the stirring speed impacts both the kinetic regime and the performance, as a part of the catalytic particles do not come in contact with the reaction mixture, which gives the same results as working at high speed with lower ZIF-9 content. ZIF-9 concentration of 0.1 mg/mL underperformed in the wastewater experiment, while 0.3 and 0.5 mg/mL followed an increasing trend of activity. Dissimilarly, ZIF-9 at 0.1 mg/mL in the Oil Red O solution did not perform much lower than ZIF-9 at 0.3 mg/mL or 0.5

mg/mL. Variation of the ZIF-9 content in the Oil Red O solution had a bigger effect on the induction times rather than the total reduction.

Post-catalysis characterisation revealed that the initial crystallinity of ZIF-9 is maintained at a low degree, while XPS analysis exhibited the presence of a mixture of cobalt oxidation states accompanied by a consistent decrease in the binding energy level. Interesting results were also retrieved via SEM images, as at the start of the decolouration of wastewater, aggregation and rough surfaces are already being formed.

Focusing on the kinetic regime, the induction times and the tales of the catalytic reactions over time point towards true heterogeneous catalysis under reducing conditions. According to Widegren and Finke,[54] the above description of sigmoid kinetics are characteristic for reductive heterogeneous catalysis and predominantly hydrogenation catalysis, but under no circumstance, are they sigmoid kinetics prerequisites. In fact, they focus on the *in situ* formation of metal nanoparticles in the excess of hydrogen and reducing conditions and the colouration of the solutions in dark colours in the beginning of the reactions. Although there is a partial agreement with their findings, the performed post-catalysis characterisation was insufficient to conclude that cobalt metal nanoparticles were formed. However, the sigmoid patterns that were observed could enhance the high heterogeneity of ZIF-9, which has been demonstrated in the previous chapters.

Overall, ZIF-9 is a catalyst that interacts with $NaBH_4$ in the oily or aqueous phase and is able to evolve hydrogen efficiently from the hydride in water of 1-octanol. At the same time, it performs catalytically for the decolouration of dyes with high activity, which is dependent on major parameters that principle heterogeneous catalytic reactions, such as content of reducing agent, concentration of catalyst and diffusion regime. While it is not mechanistically clear whether ZIF-9 is able to decolourise efficiently dye solutions under reducing conditions, it shows good potential for catalytic transformation of the dyes, which can be used for a variety of different applications. Dye-oriented chemistry, characterisation and engineering could reveal that ZIF-9 is able to alter the production methodology of dye molecules.

6.4 References

1 T. F. G. G. Cova, A. A. C. C. Pais and J. S. Seixas de Melo, *Sci. Rep.*, 2017, **7**,

6806.

2 R. Brightman, *Nature*, 1956, **177**, 815–821.

3 H. A. Boyter, in *Environmental aspects of textile dyeing*, ed. R. M. C. Christie, Woodhead Publishing Limited, Cambridge, England, 2007, pp. 30–42.

4 Y. Anjaneyulu, N. Sreedhara Chary and D. Samuel Suman Raj, *Rev. Environ. Sci. Bio/Technology*, 2005, **4**, 245–273.

5 R. H. Kienle, E. I. Stearns and P. A. Van Der Meulen, *J. Phys. Chem.*, 1946, **50**, 363–373.

6 E. Atherton and I. Setzer, *J. Soc. Dye. Colour.*, 1949, **65**, 629–638.

7 N. M. Rageh, *Spectrochim. Acta, Part A*, 2004, **60**, 1917–1924.

8 M. H. Habibi, A. Hassanzadeh and A. Zeini-Isfahani, *Dye. Pigment.*, 2006, **69**, 111–117.

9 H. R. Maradiya, *J. Saudi Chem. Soc.*, 2010, **14**, 77–81.

10 A. Mohammadi, H. Ghafoori, B. Ghalami-Choobar and R. Rohinejad, *J. Mol. Liq.*, 2014, **198**, 44–50.

11 V. Chigrinov, H. S. Kwok, H. Takada, H. Takatsu and H. Hasebe, *SID Symp. Dig. Tech. Pap.*, 2007, **38**, 1474–1477.

12 L. Zhang, J. M. Cole, P. G. Waddell, K. S. Low and X. Liu, *ACS Sustain. Chem. Eng.*, 2013, **1**, 1440–1452.

13 E. Ortyl, J. Jaworowska, P. T. Seifi, R. Barille and S. Kucharski, *Soft Mater.*, 2011, **9**, 335–346.

14 J. J. F. Coen, A. T. Smith, L. P. Candeias and J. Oakes, *J. Chem. Soc.{,} Perkin Trans. 2*, 2001, 2125–2129.

15 J. R. Easton, in *Color in dye house effluent*, eds. P. Cooper and S. of D. AndColourists, Society of Dyers and Colourists, Bradford, England, 1995, pp. 9–21.

16 C. J. Ogugbue and T. Sawidis, *Biotechnol. Res. Int.*, 2011, **2011**, 1–11.

17 C. Hessel, C. Allegre, M. Maisseu, F. Charbit and P. Moulin, *J. Environ.*

Manage., 2007, **83**, 171–180.

18 T. Rajaram and A. Das, *Futures*, 2008, **40**, 56–69.

19 *China & India: Two immense powers of textile chemicals and dyestuff manufacturing*, 2012.

20 G. de Aragão Umbuzeiro, H. S. Freeman, S. H. Warren, D. P. de Oliveira, Y. Terao, T. Watanabe and L. D. Claxton, *Chemosphere*, 2005, **60**, 55–64.

21 K. L. Hatch and H. I. Maibach, *Contact Dermatitis*, 1995, **32**, 319–326.

22 P. I. M. Firmino, M. E. R. da Silva, F. J. Cervantes and A. B. dos Santos, *Bioresour. Technol.*, 2010, **101**, 7773–7779.

23 R. de F. P. M. Moreira, T. P. Sauer, L. Casaril and E. Humeres, *J. Appl. Electrochem.*, 2005, **35**, 821–829.

24 T.-D. Dang, A. N. Banerjee, Q.-T. Tran and S. Roy, *J. Phys. Chem. Solids*, 2016, **98**, 50–58.

25 K. Vinodgopal, D. E. Wynkoop and P. V Kamat, *Environ. Sci. Technol.*, 1996, **30**, 1660–1666.

26 S. Chakrabarti and B. K. Dutta, *J. Hazard. Mater.*, 2004, **112**, 269–278.

27 M. K. Silva, R. G. Marques, N. R. C. F. Machado and O. A. A. Santos, *Brazilian J. Chem. Eng.*, 2002, **19**, 359–363.

28 R. P. Singh, P. K. Singh and R. L. Singh, *Toxicol. Int.*, 2014, **21**, 160–166.

29 N. R. Rane, V. V Chandanshive, A. D. Watharkar, R. V Khandare, T. S. Patil, P. K. Pawar and S. P. Govindwar, *Water Res.*, 2015, **83**, 271–281.

30 R. M. Reema, P. Saravanan, M. D. Kumar and S. Renganathan, *Sep. Sci. Technol.*, 2011, **46**, 1052–1058.

31 C. I. Pearce, J. R. Lloyd and J. T. Guthrie, *Dye. Pigment.*, 2003, **58**, 179–196.

32 H. M. Pinheiro, E. Touraud and O. Thomas, *Dye. Pigment.*, 2004, **61**, 121–139.

33 S. M. Burkinshaw, in *Physico-chemical Aspects of Textile Coloration*, John Wiley & Sons, Ltd, Chichester, UK, 2016, pp. 571–599.

34 R. B. Love, *J. Soc. Dye. Colour.*, 1978, **94**, 440–447.

35 L. Lesoin, C. Crampon, O. Boutin and E. Badens, *J. Supercrit. Fluids*, 2011, **57**, 162–174.

36 Z. Khatri, M. H. Memon, A. Khatri and A. Tanwari, *Ultrason. Sonochem.*, 2011, **18**, 1301–1307.

37 A. C. Serra, C. Docal and A. M. d'A. R. Gonsalves, *J. Mol. Catal. A Chem.*, 2005, **238**, 192–198.

38 G. M. Ucoski, G. S. Machado, G. de Freitas Silva, F. S. Nunes, F. Wypych and S. Nakagaki, *J. Mol. Catal. A Chem.*, 2015, **408**, 123–131.

39 Y. Shen, Z. Zhang and K. Xiao, *RSC Adv.*, 2015, **5**, 91846–91854.

40 Y. Li, L. Li, Z.-X. Chen, J. Zhang, L. Gong, Y.-X. Wang, H.-Q. Zhao and Y. Mu, *Chemosphere*, 2018, **192**, 372–378.

41 Y. Benjelloun, A. Lahrichi, S. Boumchita, M. Idrissi, Y. Miyah, K. Anis, V. Nenov and F. Zerrouq, *J. Mater. Environ. Sci.*, 2017, **8**, 2259–2269.

42 I. A. Salem, H. A. El-Ghamry and M. A. El-Ghobashy, *Beni-Suef Univ. J. Basic Appl. Sci.*, 2014, **3**, 186–192.

43 J. Geng, D. Xu, F.-F. Chang, T. Tao and W. Huang, *Dye. Pigment.*, 2017, **137**, 101–110.

44 X.-C. Chen, T. Tao, Y.-G. Wang, Y.-X. Peng, W. Huang and H.-F. Qian, *Dalton Trans.*, 2012, **41**, 11107–11115.

45 A. Ünal, B. Eren and E. Eren, *J. Mol. Struct.*, 2013, **1049**, 303–309.

46 Y. H. Ebead, M. A. Selim and S. A. Ibrahim, *Spectrochim. Acta, Part A*, 2010, **75**, 760–768.

47 A. Hassanzadeh, A. Zeini-Isfahani, M. H. Habibi, M. R. A. P. Heravi and M. Abdollahi-Alibeik, *Spectrochim. Acta, Part A*, 2006, **63**, 247–254.

48 A. Rossin, G. Tuci, L. Luconi and G. Giambastiani, *ACS Catal.*, 2017, **7**, 5035–5045.

49 G. Srinivas, W. Travis, J. Ford, H. Wu, Z.-X. Guo and T. Yildirim, *J. Mater. Chem. A*, 2013, **1**, 4167–4172.

50 G. Srinivas, J. Ford, W. Zhou and T. Yildirim, *Int. J. Hydrogen Energy*, 2012, **37**, 3633–3638.

51 S. R. Caskey, A. G. Wong-Foy and A. J. Matzger, *J. Am. Chem. Soc.*, 2008, **130**, 10870–10871.

52 Q. Li and H. Kim, *Fuel Process. Technol.*, 2012, **100**, 43–48.

53 R.-Q. Zhong, R.-Q. Zou, T. Nakagawa, M. Janicke, T. A. Semelsberger, A. K. Burrell and R. E. Del Sesto, *Inorg. Chem.*, 2012, **51**, 2728–2730.

54 J. A. Widegren and R. G. Finke, *J. Mol. Catal. A Chem.*, 2003, **198**, 317–341.

Chapter 7: Future work and epilogue

This chapter includes collaborated work with colleagues, whose contribution is appreciated and acknowledged.

Miloš Petrović, a final year PhD student in NUS and a SINGA scholar in IMRE, helped with the performance of the time-resolved absorption experiment of the pristine ZIF-9 and provided fruitful discussion upon the technique and analysis. Dr Zhang Zheng, a scientist II in IMRE, performed the XPS experiment of the modified ZIF-9.

7.1 White-light mediated decolouration of Oil Red O solution with ZIF-9: A kinetic approach

7.1.1 Objective and experimental methodology

In Chapter 6, ZIF-9 was tested for the decolouration activity of Oil Red O dissolved in 1-octanol. The material proved reactive in the presence of $NaBH_4$ and achieved partial decolouration, changing the colour from red to yellow within 3.5 hours. The kinetic patterns followed a sigmoid shape and were characterized by induction times, during which ZIF-9 became reactive. Usually, these induction times lasted 30-60 minutes, after which the reaction was accelerated 1-1.5 times in relation to the blank one.

In this project part, the experiment with Oil Red O solution and ZIF-9 at concentration 0.5 mg/mL was repeated under irradiation of white light. The experimental conditions, such as reaction volume, Oil Red O starting concentration and ratio between $NaBH_4$ and substrate, along with sampling volumes and sampling times, were kept the same as in Chapter 6. In detail, the concentration of Oil Red O in the starting solution is 0.025 mM and the concentration of $NaBH_4$ is 0.4 mg/mL (molar ratio of $NaBH_4$ over Oil Red O is 560).

The light-mediated experiment took place within the same setup consisting of glass vials as reactors, placed on a stirring plate exposed to the optical bias through a cut-off filter which allows visible light, as discussed in Chapter 2 in detail.

7.1.2 Kinetic study of the photocatalytic results and comparison with the catalytic results

The spectra obtained during the light-assisted reaction of decolouration of Oil Red O solution with ZIF-9 show that light has affected the rate of the reaction and, most probably, not the mechanism. In detail, Figure 7.1 shows the progress of the photocatalytic reaction with and without ZIF-9. The presence of ZIF-9 shifts the absorption peak from 359 nm to ca. 400 nm. In the absence of ZIF-9, the peak is unmoved and the valley between the peaks rises quickly, almost creating a new peak. At the same time, the intensity of the peak at 518 nm decreases overtime and isosbestic points form again. Thus, comparing with the results in Chapter 6, the pattern behaviour of the reaction mixture with and without ZIF-9 does not change with the white light, but the rate of the expressed behaviour has increased.

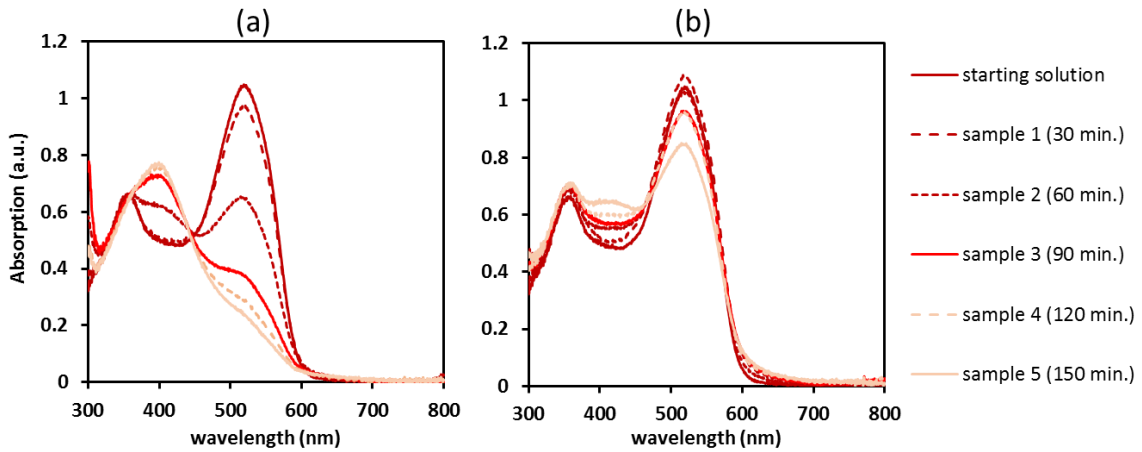

Figure 7.1 Spectra of Oil Red O solution with $NaBH_4$ in the presence (a) and absence (b) of ZIF-9 in the irradiation of white light.

Translating the above spectra into kinetics, the decrease of the intensity of the main peak is plotted versus time in Figure 7.2. The pattern of the kinetics remains sigmoid and thus, application of the Hill decay model is suitable for the analysis. The parameters under study are the induction time, the slopes of the lines at the inflection points and of course, the total achieved reduction after 2.5 hours of reaction.

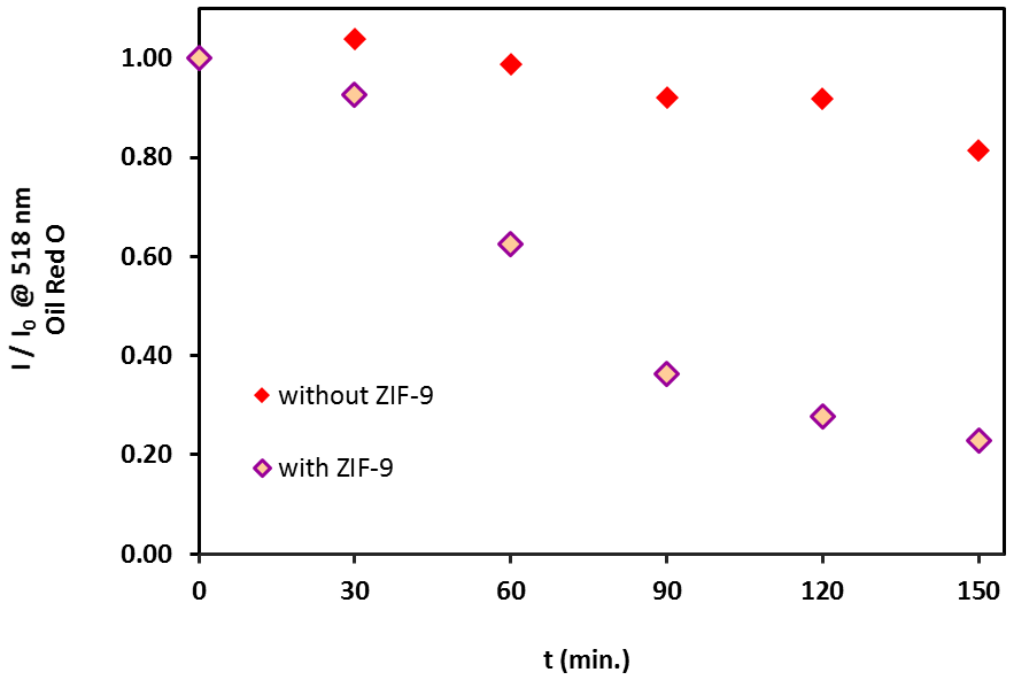

Figure 7.2 Light-assisted reduction of the intensity of the main of Oil Red O solution in the presence and absence of ZIF-9 overtime.

The mentioned factors are tabulated in Table 7.1, along with the corresponding values in the absence of the illumination of white light (values have been calculated in Chapter 6). For the comparison to be on the same basis, the Hill model fitting and the calculation of the lines at inflection points were conducted after the values on the Y axis of Figure 7.2 were transformed to the corresponding logarithms. The respective plots and equations that describe the fitting line are found in the Appendix D.3 and the plotted fittings are depicted in Figure 7.3.

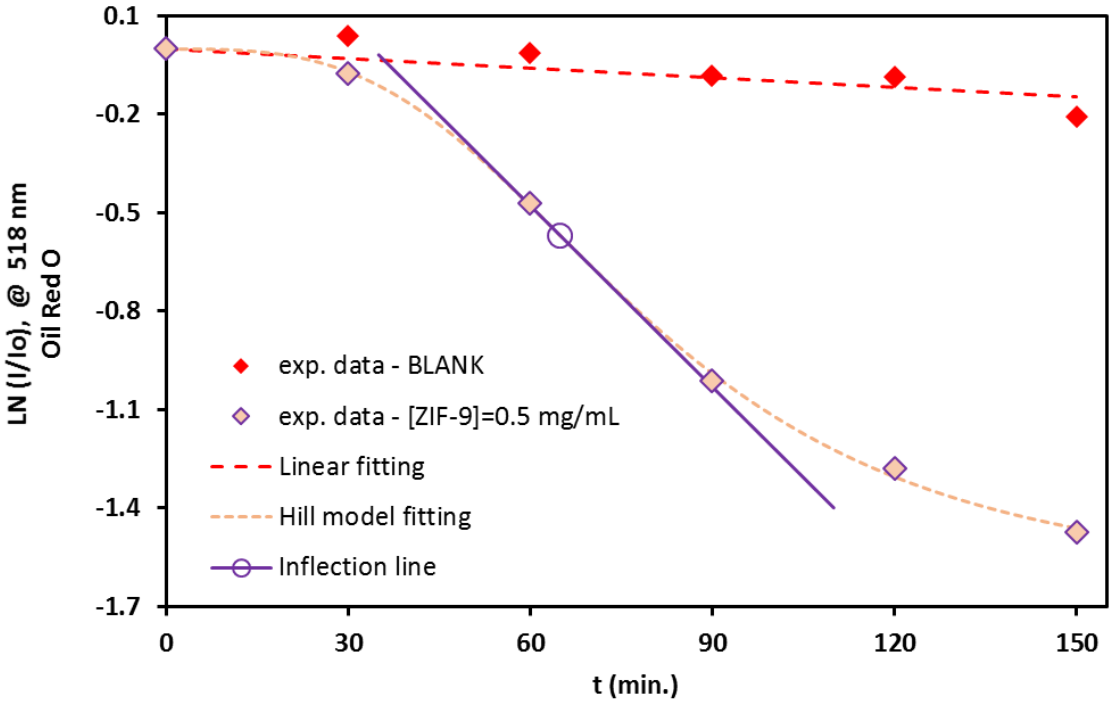

Figure 7.3 Experimental data and fitting of data for the decolouration of Oil Red O with $NaBH_4$ under white light irradiation.

Table 7.1 Comparative results for the Oil Red O reaction with $NaBH_4$ in the darkness and in the irradiation of white light.

[ZIF-9] in mixture	Dark		White light	
	Induction time	Absolute slope of line	Induction time	Absolute slope of line
0 $^{mg}/_{mL}$ - (blank)	N.A.	$\|slope\| = 0.001$	N.A.	$\|slope\| = 0.001$
0.5 $^{mg}/_{mL}$	$t \cong 30\ min.$	$\|slope\| = 0.015$	$t \cong 30\ min.$	$\|slope\| = 0.018$

Finally, the ongoing reaction was kept under stirring and light-irradiation for another 3 hours, before it was sampled. The obtained spectra for the catalyst-free and catalyst-containing reaction are depicted in Figure 7.4. The reduction of the intensity of the peak at 518 nm is comparable for both cases. However, the curve at the lower wavelength bands shows some interesting features. While the peak at 359 nm has not shifted in the case of the catalyst-free reaction, the rising valley has resulted in a new and intense peak. In the case of the reaction involving ZIF-9,

the peak at 359 nm has not shifted further than before, while the intensity has slightly increased.

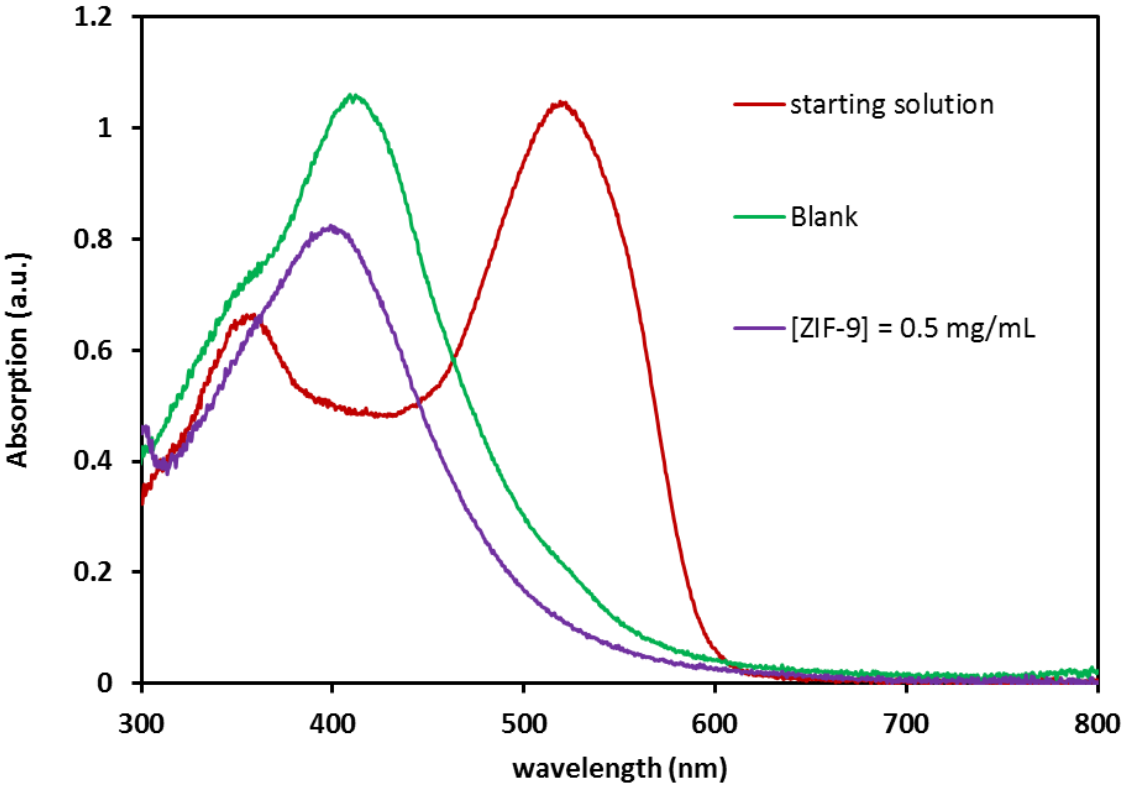

Figure 7.4 Long-term decolouration of Oil Red O solution in the presence of $NaBH_4$ and white light irradiation.

In particular, the decrease of the main peak intensity is ca. 79% for the blank and 89% when ZIF-9 is employed. The blank reaction demonstrates the formation of a new peak in the area of the valley between the peaks, which is centred at 409 nm, while a shoulder at 359 nm is apparent. The catalytic reaction exhibits a shift of the peak of 359 nm to 399 nm and its intensity is 22% lower than the intensity of the peak of the blank reaction.

7.1.3 Conclusions and discussion for future work

ZIF-9 was used for the decolouration of Oil Red O in 1-octanol under white light irradiation and exhibited photocatalytic behaviour. The decolouration of the blank solution is a slow reaction which proceeds in the absence of ZIF-9 or light similarly. However, upon the addition of ZIF-9, the reaction proceeds faster and is further accelerated with light. ZIF-9 is able to evolve hydrogen from the reducing agent $NaBH_4$ in an oily solvent, such as 1-octanol, and is also capable of utilising white light rendering the overall process more efficient.

Judging from the long-term reaction spectra, ZIF-9 leads the reaction through a different reaction path. The reduction of the main peak, responsible for the intense red colour of the solution, is comparable for the blank and the catalytic reaction, with the catalytic results being lower by 10%. New peaks occur in both cases, with the catalytic reaction causing a red shift of the lower peak and the blank reaction exhibiting the formation of a new and intense peak.

The potential of ZIF-9 as a photocatalyst in oily phase has been demonstrated. ZIF-9 performs well as catalyst and photocatalyst for the decolouration of dyes in the darkness and in the white light, in the presence of $NaBH_4$. Further study of the reaction with light should include a variation of ZIF-9 and $NaBH_4$ concentration, while it would be interesting to observe the effect of different light wavelengths in the reaction. Dye oriented characterisation might also help to elucidate the mechanism of the reaction.

7.2 Transient Absorption: A preliminary characterisation of ZIF-9 as photocatalyst

7.2.1 Time-resolved absorption technique

Steady-state spectroscopy has been applied for many years in science, in order to characterise matter, tracking its response to continuous electromagnetic radiation. The steady-state spectroscopic techniques are based on the continuous irradiation of the samples, which results in a constant formation of excited states which relax to their ground states. This dynamic process reaches quickly an equilibrium and the response is registered with the steady-state spectra, which do not reveal any information relevant to the kinetics of the excitation and relaxation procedures, but only the wavelengths at which the transitions occur.

While static information is important for basic and initial characterisation, the kinetics information is crucial in understanding deeper the properties of the materials, molecules or proteins, along with the photophysical, photochemical and photobiological mechanisms.[1] It is rather more important in fields that require harnessing of light, such as solar cells or photocatalysts, bestowing useful information to design photoresponsive material more efficiently. The reason behind this statement lies in the principles of the time-resolved spectroscopic techniques and the information they reveal.

In transient spectroscopy, the light fluctuates with time illuminating the matter with pulses. A pulse induces the excitement of a part of the matter, permitting the monitoring of the progress of the concentration of the excited states over time.[2] The usual spectroscopic techniques are reflectance or absorption, emission and transmittance and, as transient methods, they are all used to detect metastable electronic properties. Transient absorption spectroscopy records the rate of the decay of the excited states and of the formation of photoresponsive species, giving information about their lifetime.[2] Transient emission, on the other hand, supplements with lifetime data, but, most importantly, provides information about the type of the relaxation (phosphorescence or fluorescence) and intersystem crossing.

A typical setup for transient spectroscopy includes the usual broadband (UV-VIS-NIR) light beam and an extra light source, usually a laser or diode, set to irradiate the sample with high time resolution (Figure 7.5) at (or near) the wavelength of maximum absorption for steady-state conditions. A mono- or polychromatic detector can register part or full spectrum changes from femtoseconds to kiloseconds.[2] The obtained spectra trade off sensitivity for kinetics, which is reflected with intense background noise, making their analysis more complex. The transient absorption curves represent the difference of the absorption before and after the pulse as a function of the wavelength. Data obtained in such a way confirm the occurrence of excitation, while the processing of collected spectra overtime conveys the evolution of the excited states and new photoresponsive species at specific wavelengths, namely the rate of the decay or creation and the lifetime of the products.[2,3]

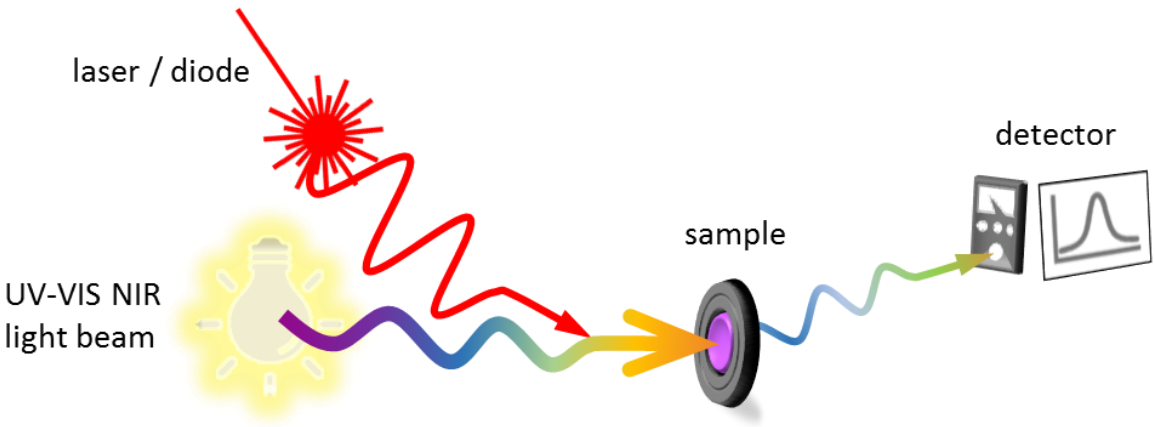

Figure 7.5 Simplified instrumental layout for transient absorption spectroscopy.

Further interpretation of the transient absorption spectra regards the mathematic sign of the signals difference. A positive sign means that the delayed pulse was able to promote the electrons to higher excited states, while a negative sign is an indication of emissions occurrence and ground state bleaching.[2] Ground state bleaching is the phenomenon where no more ground state species were left to be promoted to the excited state. The time-resolved data can be used in combination with other techniques to prove presence or absence of electron traps, stability of ground and excited states etc.[2,4]

Transient spectroscopy may also be referred to as flash or fast or time-resolved spectroscopy and the time records of the events can indicate the type of event (Figure 7.6). The combination of individual transient spectroscopic techniques can be beneficial for the discovery of additional information. For instance, the coupling of transient absorption and emission spectra can disclose how fast the electrons (or more generally the charge carriers) transfer and between which energy levels.[2] More importantly, the characterisation of matter with transient spectroscopy can promote the use and design of materials for specific scientific causes (such as photocatalysts, photosynthesis mimes etc.) or everyday appliances (such as photo-grade car windows etc.).

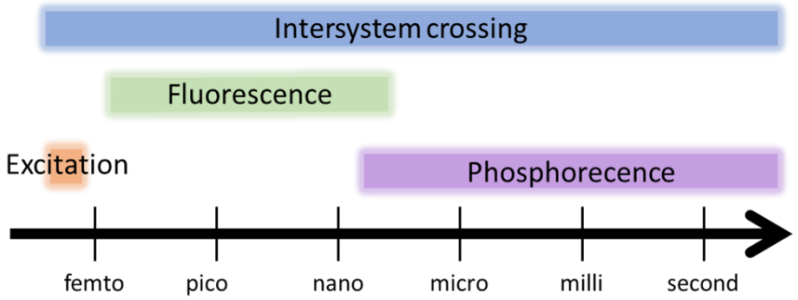

Figure 7.6 Time duration of states transition and energy transfer.

7.2.2 Objective and experimental methodology

ZIF-9 has performed well as visible-light photocatalyst for a number of applications within this work. Starting from the CDC reaction through the 4-NP reduction and finishing with the decolouration of Oil Red O in 1-octanol, ZIF-9 has been established as a photocatalyst. Therefore, further characterisation of its electronic properties is required to comprehend how it works and which applications it can benefit. For this reason, ZIF-9 was submitted to transient absorption technique.

The material was ground finely and placed into the sample holder. Time-resolved spectroscopy experiments were conducted on a setup with 10 ns resolution consisting of an Edinburgh Instruments flash-photolysis spectrometer LP920 equipped with an LP920-K PMT detector (Edinburgh Instruments) and time-gated ICCD camera (Andor DH-720), while the probe light was provided by a xenon lamp (Hamamatsu C7535). Samples were excited at 515 nm using Nd-YAG laser with 4 ns pulse duration (Expla-NT341A OPO). In order to avoid possible damage of the material, initial laser fluence ($0.98\ mJ\ cm^{-2}$) was attenuated with the help of 0.6 neutral density filter and beam area was reduced to 2 mm^2 using the iris diaphragm. Resulting transients were averaged 512 times and obtained data are plotted as the change in optical density (ΔOD) of the measured sample, which is a function of change in the absorbance ΔA, as defined by $\Delta OD \times ln10 = -\frac{\Delta A}{A}$.

The aim of this experiment is the extraction of information regarding the lifetime, the decay rate and the quality of the excited states of ZIF-9 when the material is radiated with light of 515 nm. Forty-one spectra were collected starting from 0.01 to 200.01 μs. The experimental data were analysed and processed and are presented alongside appropriate comments in the following section.

7.2.3 Characterisation of fresh ZIF-9

According to the aforementioned parameters, 41 spectra were collected representing the transient absorption progress. The se spectra are plotted in Figure 7.7 in a 3D view, with axes ΔOD versus wavelength versus time. From this plot, a maximum absorption around the wavelength of 550 nm can be observed, while high absorptions at shorter than the visible range wavelengths are not induced by the laser and, accordingly, show no intensity fluctuation in response to the applied time steps. The compression of these plots on one plane with axes ΔOD versus wavelength (Figure 7.8) shows clearly that the maxima ΔOD appear within the range 550-600 nm, while photobleaching is also obvious, as some spectra appear below the zero axis.

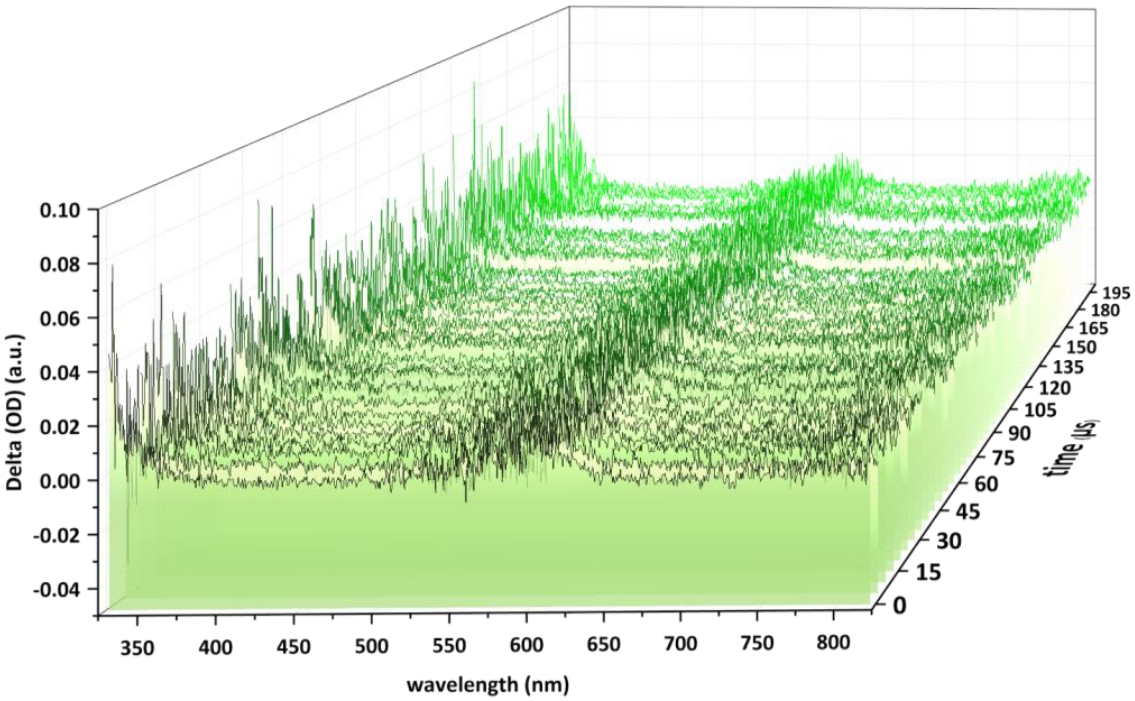

Figure 7.7 Time-respective acquisition of transient absorption spectra regarding pristine ZIF-9 radiated with a laser at 515 nm, plotted in 3D view.

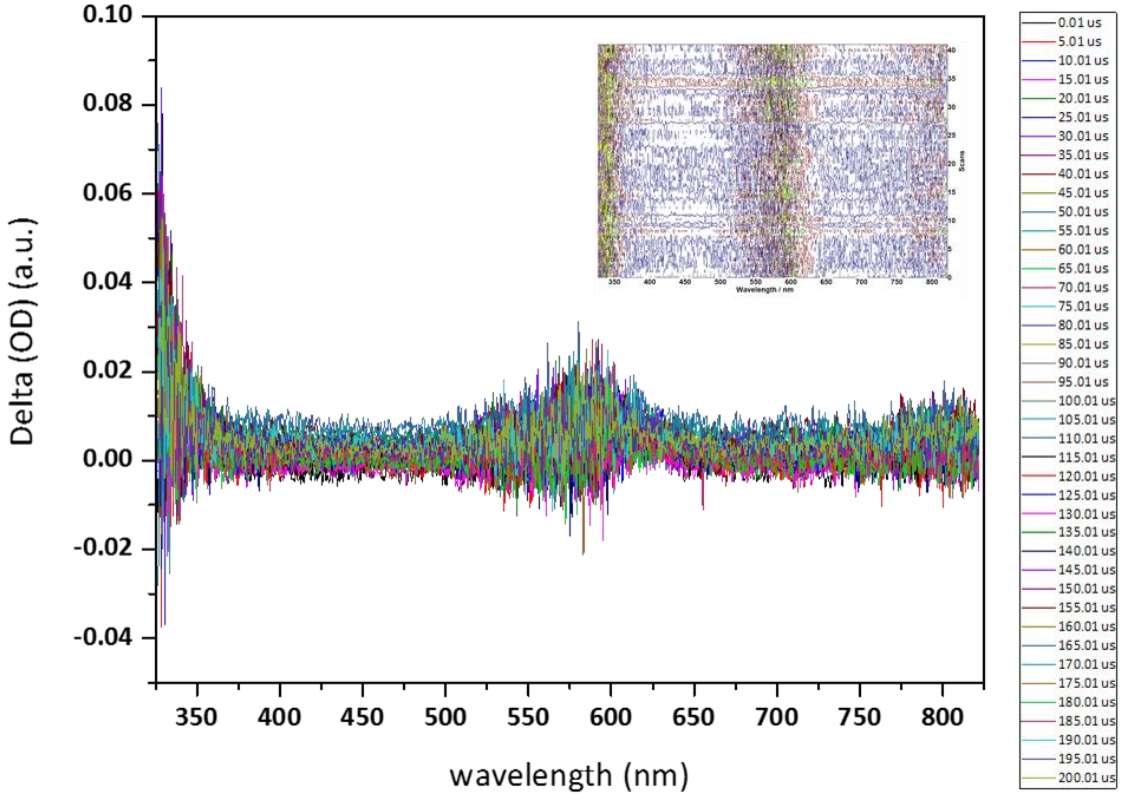

Figure 7.8 Transient absorption spectra regarding pristine ZIF-9 radiated with a laser at 515 nm, compressed on ΔOD vs. wavelength plane.

Collected data were processed using the L900 acquisition and analysis software package, resulting in sliced data for the transient time window up to 1 μs. This means that the maxima points can be plotted with time, as the 3D plot is compressed on a plane with axes ΔOD versus time (Figure 7.9). However, the value of lifetime along with the process of its calculation is a significant point of reference for future work.

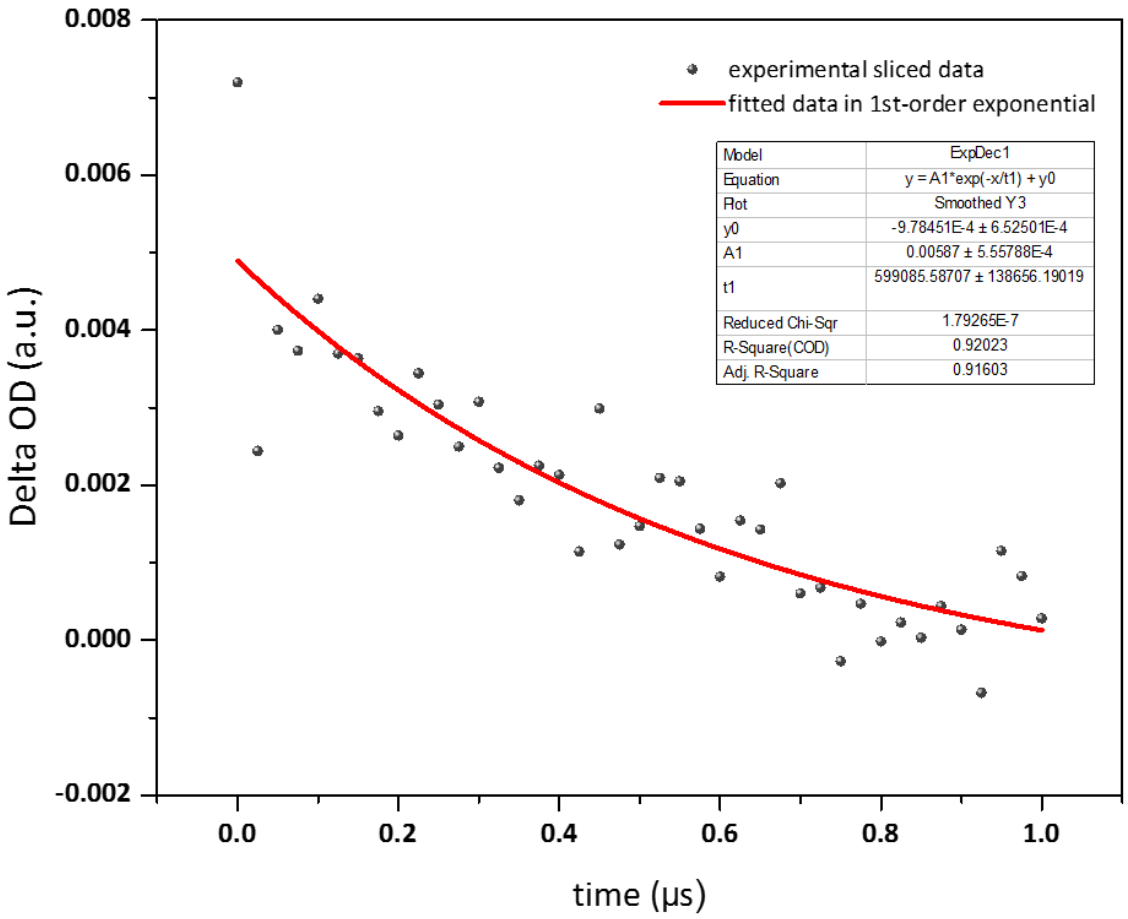

Figure 7.9 Decay curve of the transient absorption of pristine ZIF-9 during the 1st μs.

Smoothing of the signal was performed and data were fitted according to the 1st order exponential decay model.[2,5] The fitting matched the experimental data with high R^2 (0.91603), indicating successful fitting of data to the model. The first order exponential decay was chosen as the simplest and mostly common and reveals first-order kinetics. This is often associated with a one-step transition of species, such as $X \rightarrow Y$. Multiple step transitions of the excited states to photo-intermediates are also possible.

The decay trend was fitted in accordance with the mono-exponential decay model, as Equation 7.1 shows. Coefficient A represents the relative amplitude and denominator τ is the lifetime associated with the recombination process. The mathematical software used for the fitting of data calculated the lifetime close to 600 ns.

$$y = y_o + A \cdot \exp\left(t/\tau\right) \qquad \text{Equation 7.1}$$

Finally, it is interesting to observe the fluctuation of the wavelength of the maximum change of absorption with each scan. In Figure 7.10, the maximum absorption change wavelength is plotted against the scan number, which is proportional to the time of the scan. The wavelengths range from 565 nm to 601 nm and, performing basic statistics to these data, the median value is 587 nm, the mean value is 586 nm and the standard deviation is calculated at 9.5 nm. This means that 90% of data are found within the range of standard variation (586 ± 9.5 nm). Hence, the wavelengths are considered within normal limits and the values do not fluctuate intensely. This evaluation is essential as the transient spectroscopic techniques have a lower sensitivity along with background noise and it is important to assess whether the data can be trusted.

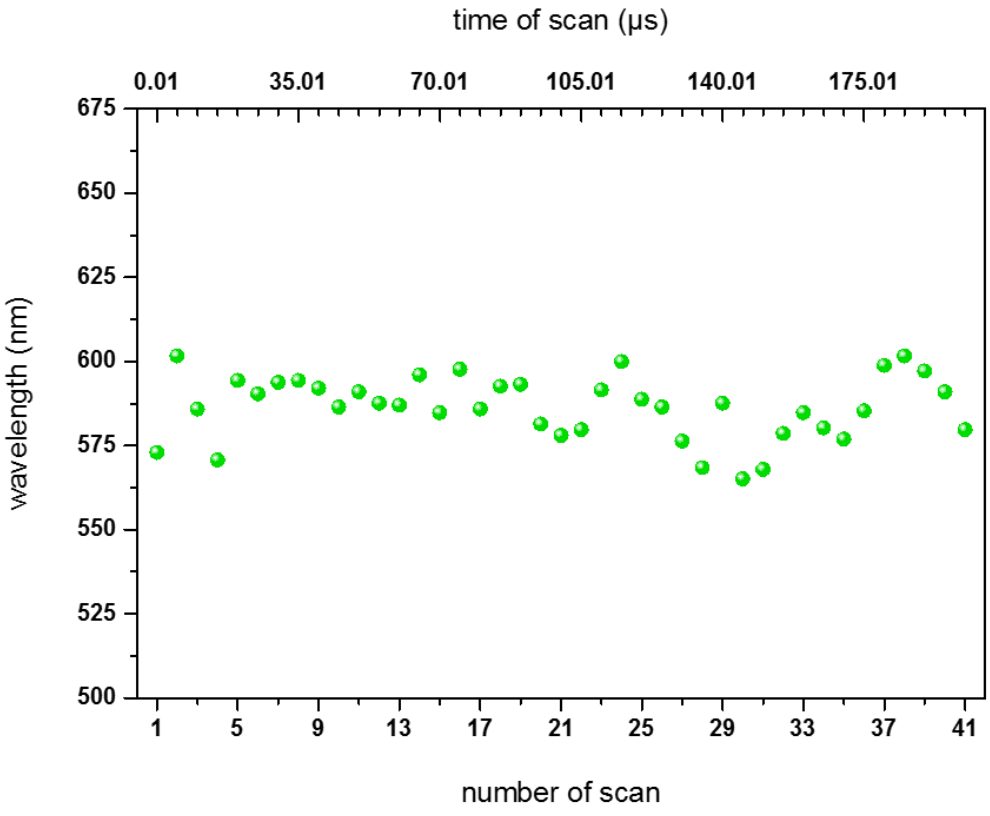

Figure 7.10 Fluctuation of the wavelength of maximum absorption change against the scan or time of scan.

7.2.4 Conclusions and Discussion

The transient absorption technique applied for the characterisation of the pristine ZIF-9 has been enlightening for the study of the photoactivity of this material. Initially, the material responded to excitation within the 556-601 nm absorption window, caused by a laser pulse excitation at 515 nm. This range encompasses wavelengths longer than the absorption wavelength observed in the steady-state technique. Both the excited states and the excitation wavelength of the laser beam at 515 nm fall approximately in the middle of the visible spectrum, which explains the photoresponse of ZIF-9 to the white light exposure.

The lifetime of the triplet excited states was calculated to be nearly 600 ns or 0.6 μs. This value was calculated by data respective to the response of the 1st μs. However, this corresponds to sliced data of 20% of the first scan, implying that the actual lifetime is much longer and which indicates, in turn, phosphorescence events taking place.[6,7] This means that once ZIF-9 is excited, the triplet excited species possibly undergo long intersystem crossing. Simultaneously, the possible elimination of fluorescence can be interpreted in terms of avoidance of energy loss as heat. In general, ZIF-9 has the possibility to maintain the separated charge for an extended amount of time, enough to commence chain photochemistry to the substrates.

The obtained data are evaluated valid for the extracted information and more transient spectroscopic techniques could be applied in the future to fully characterise the electronic properties of ZIF-9. Transient emission spectroscopy could show in detail the energy levels of the excited states. This information is useful for the prediction of the photochemical transformations that can be possibly realised by the material, according to the electrochemical potential of the reactions. Further studies employing ultrafast laser spectroscopy techniques with a femtosecond resolution could reveal more information that could shed light on the design and engineering of the material, modifying it accordingly for a range of photochemical applications.

7.3 Modification of ZIF-9 with graphene oxide for light-aided 4-NP reduction

7.3.1 The idea behind modification of ZIF-9 with graphene

The imagination and the anticipation for further progress, along with the confidence in the development, the inherited optimism of the previous achievements and the easiness of familiarisation with new concepts and devices, has sometimes made the line between fiction and science audaciously fine, yet expected. The technological advancement underlines almost all newer changes and a tendency to make everything smaller monopolises the current era of nanotechnology. As such, there is no wonder how the 21st century is already, at its rise, baptised as the century of graphene, way before its set.

Graphene was the result of "scientific playfulness", as Andre Geim and Konstantin Novoselov preferred to call it, when they were awarded in 2010 with a Nobel Prize in Physics for their discovery.[8,9] The carbon atoms in graphene are arranged in hexagonal planar cells, resembling a honeycomb geometry. Unlike the carbon allotropes graphite and diamond, graphene is a two dimensional material with unique properties. It is a non-metal sheet of highly-ordered carbon atoms that behaves better than a metal, with profound stability, elasticity, thinness, toughness, electric and heat conductivity, impermeability and transparency, due to which it concentrates vast potential to be applied to small electronic devices, solar cells, fuel cells, rubber applications, sensors and detectors.[10–12]

Although graphene sounds like an exceptional nanomaterial on its own, functionalized graphene-based nanocomposites and graphene derived nanoproducts can play a more important role in technology and industry.[13] As the practical work done with graphene is at a lower level than anticipation and theory, there is uncertainty around the chemical methods applied on graphene hybrids regarding the level of disturbance that these methods could cause on the lattice converting it to a common material, such as graphite. However, this is a good reason for more experimentation in the laboratory, before large commercialisation starts.

The use of common or supercritical solvents to effectively disperse the metal particles, decrease their size and prevent aggregation, has become a common practice in the formation of nanoparticles, while, most frequently, the deposition of metal nanoparticles on graphene involves noble and precious metals, such as

Ag, Au, Pd and Pt.[14,15] The need for low-cost materials shifts the research focus towards non-precious metals, with cobalt being a good alternative for platinum. By the same token, different approaches and methods have been tested to anchor the metal nanoparticles, such as impregnation, pyrolysis, chemical vapour deposition etc.[16–19]

With most proposed systems being high-tech or requiring non-benign conditions of preparation, recently published work of several research groups prompted the idea of "planting" metal nanoparticles on graphene sheets starting from metal-organic frameworks. Based on their carbon content, metal dispersion and their self-assembly ability, it is speculated that MOFs can blend with the carbon nanomaterial implanting their metal nodes in the graphene grid.[20–24] In fact, zeolitic imidazolate frameworks seem to be a viable option, due to the high carbon and low oxygen and nitrogen content of the imidazolate-based linkages.

The bonds between the carbon atoms of a graphene sheet are covalent, while the Van der Waals forces between the graphene sheets are extremely loose, which forces the sheets to remain flat. This yields carbon atoms with sp^2 hybridisation and a hexagonal pattern network of tightly packed carbon atoms, each one of them bonding strictly with another three carbon atoms, whereas carbon has the ability to bond with four atoms. For this reason, functionalisation of the sheets is possible and theoretically easy, since a carbon atom can bond with other groups and well-designed molecules can attach to both sides of the sheet, due to the degrees of freedom that such an assembly provides, along with the high surface area.

Substitution of carbon atoms with nitrogen or oxygen can enhance the variation of attachments or create useful defects, giving new electronic properties to graphene. The honeycomb configuration of the carbon atoms practically constitutes a huge platform of delocalised electrons, as if it were a sheet of aromatic rings. This is why graphene behaves electrically as a superconductor at room temperatures, as the electrons can move along the sheet without disruption. Apart from that, the electrons can move incredibly fast, which explains its rare electronic features. Thus, doping a graphene sheet with nitrogen, oxygen or other elements, such as boron, silicon or transition metals, the resulting nanomaterial can be assigned with new properties, such as semiconducting, electromagnetic, redox, catalytic and other.

The offered possibilities with graphene seem multiple and the applications where it can be used may transform the materials industry. It may replace usual materials, such as metal and plastics and provide amazing solutions in situations that still trouble the technologists' community. Graphene may also be just the beginning of a new direction towards 2-D materials. Nevertheless, the research around it is still in its infancy and nobody knows if the future can actually be written in graphene. Meanwhile, further experimentation is only beneficial.

7.3.2 Preparation and basic characterisation of modified ZIF-9 with graphene

The modified ZIF-9 with graphene will be referred to as ZIF-9@Graphene. For its synthesis, the selected graphene precursor selected was graphene oxide dispersed in ethanol solution and was used without further purification or alteration. The method was inspired by the experimental approach proposed by Yang et al.,[21] with some modifications. In particular, cobalt hexahydrate (0.5 g) and benzimidazole (0.15 g) were added in dimethyl formamide (45 mL) and, while stirring, graphene oxide dispersion in ethanol (0.3 mg) was added. The solution was left stirring at room temperature for 30 minutes and 2 NaOH tablets (5-10 g.) were added before the solution was sealed in the glass bottle of 100 mL. The bottle was left for crystallization in an oven at 130 °C for 48 hours and then, it was left to cool to ambient temperature.

The formed purple-grey solid was separated via centrifugation performed three times, followed by methanol washing-in and rotary evaporation. The crystals were left to dry at 80 °C for 24 hours and the material was then ground and annealed under nitrogen flow at 650 °C for 8 hours. The collected product had taken a black-yellowish colour and had a non-sticky and non-fluffy texture. The material was named ZIF-9@Graphene and was submitted to basic structural and spectroscopic characterisation.

The XRD analysis of ZIF-9@Graphene in Figure 7.11 shows that the new material does not afford a crystalline order, since there is a lack of peaks. The modification of pristine ZIF-9 caused disappearance of microcrystalline structure. Analysis at higher angle degrees might have revealed the presence of cobalt.[21] However, XPS analysis confirms its presence and is used to characterise the chemical state of the element. In regard to the pattern of the XPS spectrum in Figure 7.12, the presence of satellite peaks and the breadth of the main peaks leads towards the concept of mixed oxidation states of cobalt.

Generally, the Co 2p emission spectrum is fitted into the characteristic two spin-orbit doublets, with the in-between difference equal to 15.7 eV. The Co $2p^3/_2$ peak appears at 777.9 eV and the Co $2p^1/_2$ at 793.6 eV. These values are lower by approximately 3-4 eV than the respective ones for fresh and used ZIF-9 and this shift to lower binding energies could also infer the presence of metallic cobalt. However, it should be noted that the most acceptable feature for metallic cobalt is a shoulder of the Co $2p^3/_2$ peak on the side of lower binding energy, but this phenomenon is most prominent when the ratio of metallic cobalt over the rest elements is relatively high.

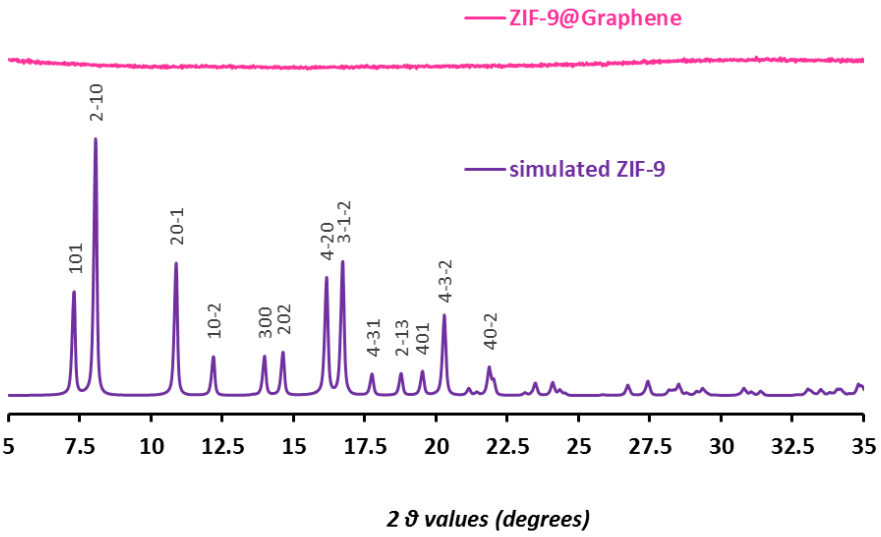

Figure 7.11 PXRD of ZIF-9@Graphene.

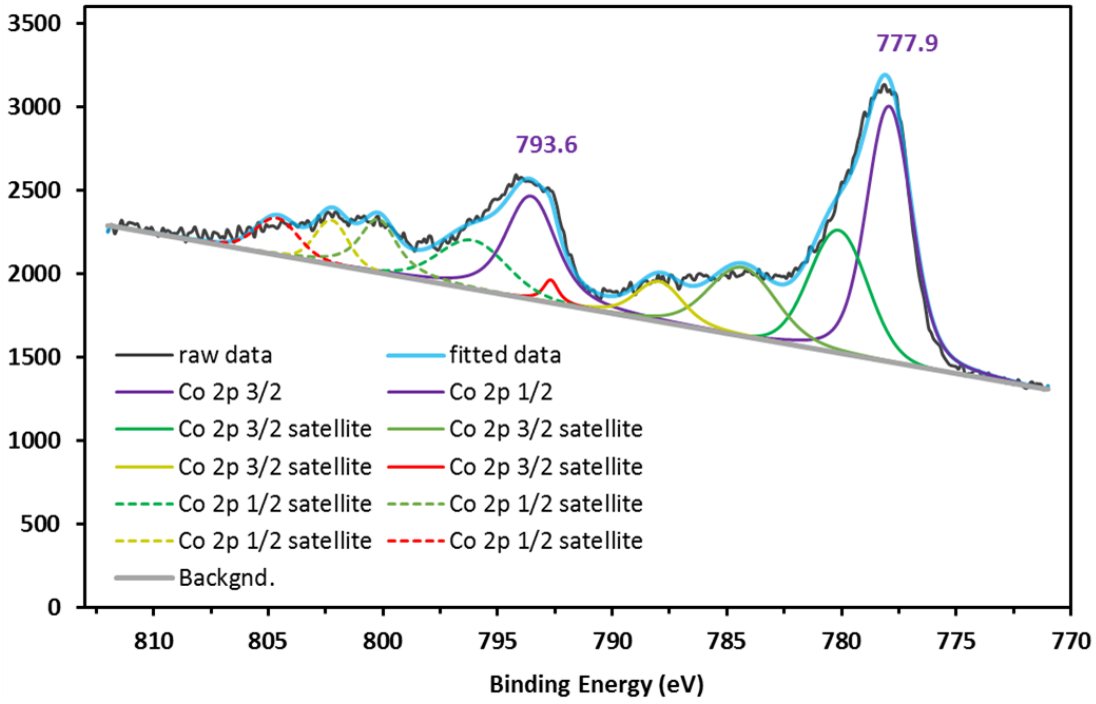

Figure 7.12 Experimental and fitted XPS spectrum of ZIF-9@Graphene.

Interestingly, the shape of the satellite peaks is differentiated from the previous spectra, which regarded the fresh and the used ZIF-9 in previous chapters. According to Cohran et al., the parting of the satellite peaks from the main peaks serves as an indicator of the nature of the bonds formed between cobalt and its neighbouring atoms.[25] More particularly, Matienzo et al. reported that the well-separated satellite peaks are connected with (more) covalent bonding.[26] Therefore, the XPS analysis of ZIF-9@Graphene mainly shows that the chemical state of cobalt is mixed and that part of cobalt is possibly metallic, while it exhibits loss of its ionic character.

SEM technique was employed to depict and analyse the morphology of the surface of ZIF-9@Graphene. The texture of ZIF-9@Graphene resembles that of a sponge and the size of the voids is small as the SEM images in Figure 7.13 depict. Transmission Electron Microscopy (TEM) technique could reveal whether a sheet-like effect has been achieved, along with the dispersion of cobalt. Here, the SEM images in Figure 7.13 reveal the absence of regular and repeated particles, which were present in the case of pristine ZIF-9, but a consistency in the pattern of the surface of the material. A two-dimensional result and the formation of cobalt nanoparticles, along with their size, would be possible to distinguish over application of TEM.

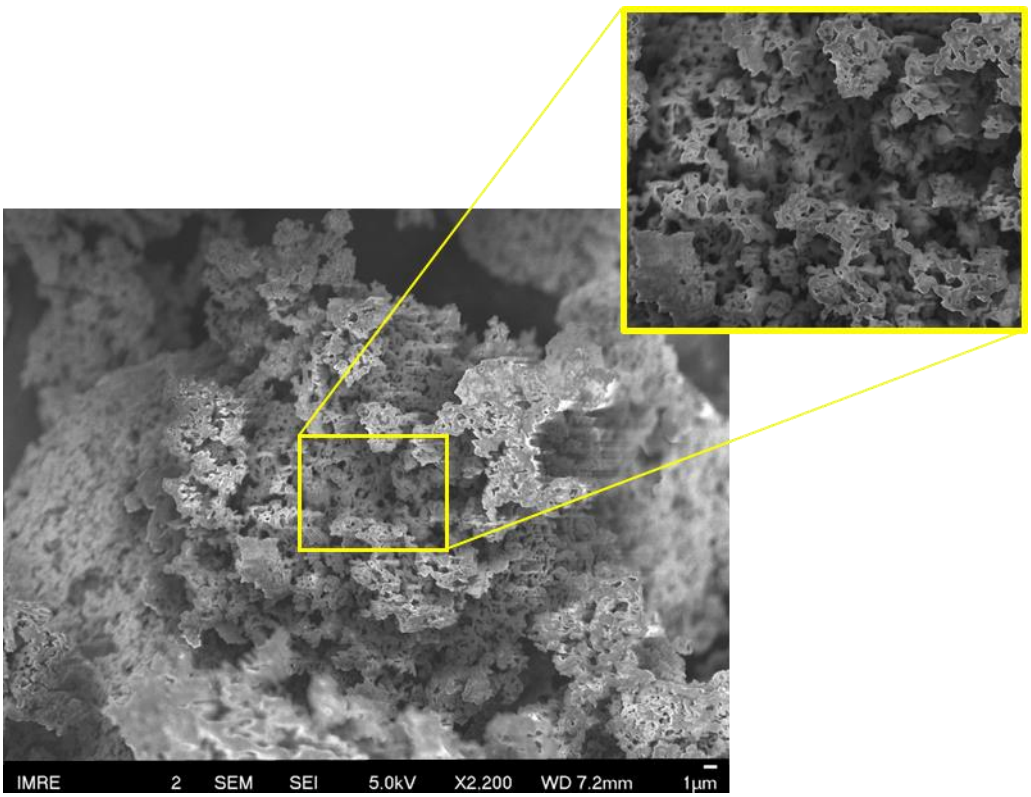

Figure 7.13 SEM image of ZIF-9@Graphene.

With graphene being a well-known material for its remarkable charge mobility, it is highly possible that it can perform in photocatalytic applications. For this reason, DR UV-VIS is a useful technique to characterise the material's photoresponse. The plot in Figure 7.14 demonstrates the Kubelka-Munk coefficient versus the wavelength of ZIF-9@Graphene. For reasons of comparison, the corresponding plot of pristine ZIF-9 is also presented. The difference between the curves is significant, with the ZIF-9@Graphene pattern resembling more to the shape of a semiconductor and losing the peak dominance that the pristine ZIF-9 gave.

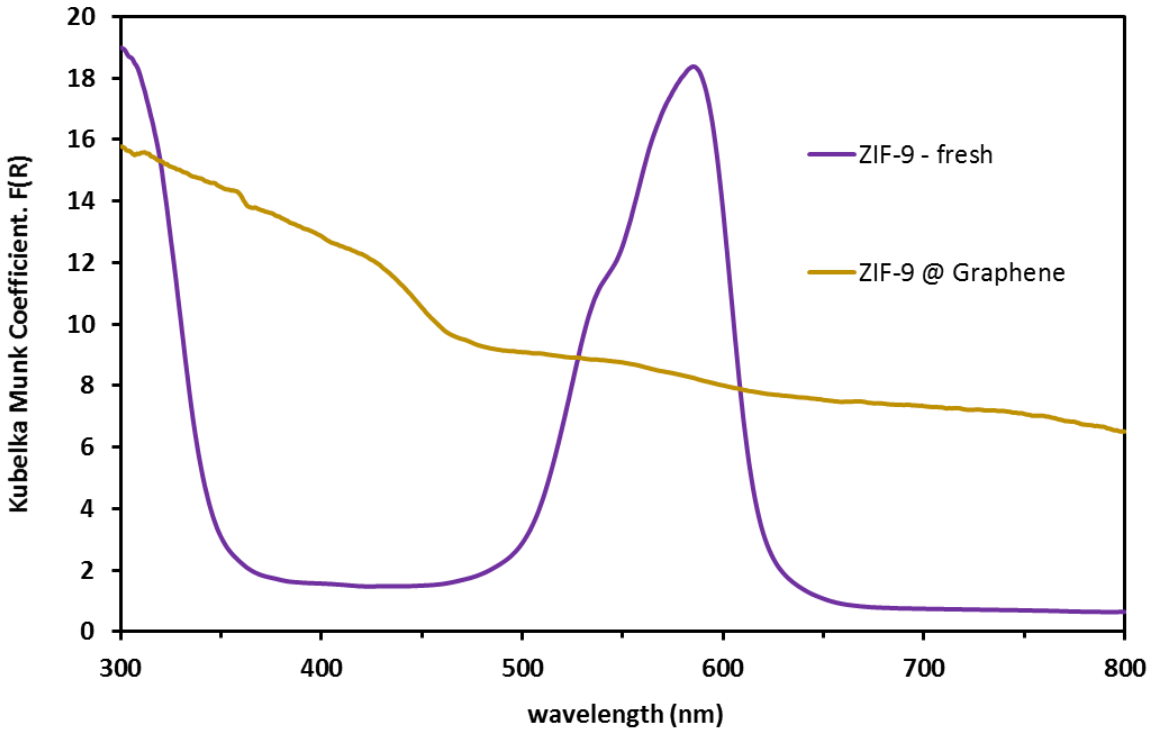

Figure 7.14 DR UV-VIS of pristine ZIF-9 and ZIF-9@Graphene.

For further characterisation as a semiconductor, it is useful to employ the TAUC model to estimate the energy bandgap. The mostly reported TAUC plots reported for semiconductor characterisation regard the allowed transitions between the energy levels. The quantity $(F(R) \cdot hv)$ to the power of ½ is related to direct semiconductors, while the aforementioned quantity to the power of 2 is related to indirect semiconductors. The difference between the two stems from the pathway of the transition between allowed energy levels. In a direct semiconductor, the conduction band is located above the valence band and the electron jump and drop is vertical and represented by a direct photon transition.

In an indirect semiconductor, the two bands are not located one above the other. In the latter case, the electron transfer from the valence band to the conduction band requires energy and momentum, which is gained by the interaction of the electron with the light and, mechanically, by the oscillation of the atoms of the crystal grid at its resonance frequency. Consequently, the movement of the electron can be analysed as a vertical and a horizontal transfer or, simpler, a photon and phonon. The photon is a particle/wave that carries certain energy, able to produce the electron-hole pair (exciton), while the phonon occurs by the lattice vibration at quantized steps, able to add energy to the moving electron or hole (Figure 7.15).

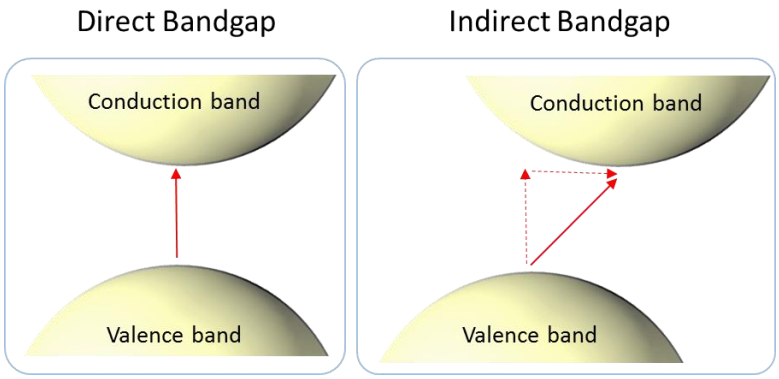

Figure 7.15 Illustration of the direct and indirect bandgap in a semiconductor.

Practically, the main impact is observed on the rate of the processes, with the e^- /h^+ creation and recombination process being slower in the indirect semiconductors. However, solid materials usually have both types of bandgaps, but they cannot be expressed at the same time. In principle, the bandgap is direct if the material is crystalline and indirect if the material is non-crystalline, while partial crystallinity may attribute both direct and indirect bandgaps.

The mathematic approach to recognise the type of the bandgap and calculate the energy difference is usually the two corresponding TAUC plots ($\sqrt{F(R) \cdot hv}$ vs. hv and $(F(R) \cdot hv)^2$ vs. hv). The TAUC plots are formed and analysed for the formation of straight lines and inflection of curves. The TAUC plots that accrue from the DR UV-VIS data of ZIF-9@Graphene are found in Figure 7.16, from which it is obvious that the second type of bandgap (indirect) is most probable, since the corresponding TAUC plot demonstrates a better fitting to the materials' photoresponse.

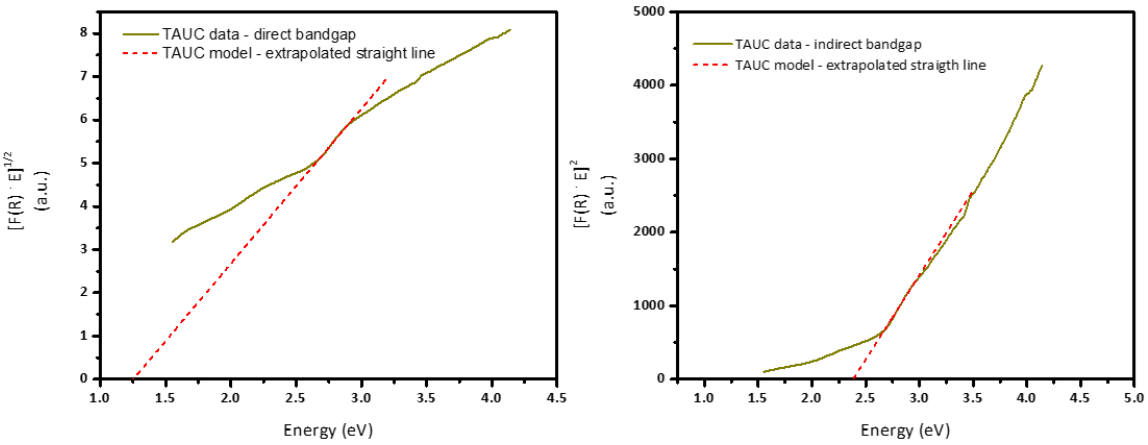

Figure 7.16 TAUC plots of ZIF-9@Graphene.

The extrapolation of the straight lines is used for the calculation of the direct and the indirect bandgaps, which are the values of the energy at the intercept of the straight line with the horizontal axis. The smaller bandgap is equal to 1.25 eV, which corresponds to 992 nm and, hence, is out of the range of visible light. The indirect bandgap is calculated at 2.38 eV and corresponds to 521 nm, which is within the visible spectrum.

The performed basic characterisation reveals that ZIF-9@Graphene has a different set of properties from the pristine ZIF-9. Having established the interesting photocatalytic behaviour of ZIF-9, it is considered prudent to probe the modified material's performance in a mainstream catalysis reaction. For this reason, the reduction of 4-NP is employed with ZIF-9@Graphene in the presence of visible light for comparison with the results obtained with pristine ZIF-9. The characterisation of ZIF-9@Graphene is followed by the details of the experiment and the observed photocatalytic behaviour.

7.3.3 Photocatalytic results of ZIF-9@Graphene and kinetic analysis

The experiment of the reduction of 4-NP with ZIF-9@Graphene was performed in the same setup as with the pristine ZIF-9, with white light irradiating a glass vial containing 25 mL reaction mixture and ZIF-9@Graphene at concentration equal to 0.1 mg/mL. Stirring was kept constant at 750 rpm and the starting concentration of 4-NP aqueous solution was set to 0.1 mM. In this experiment, the behaviour of the material was first tested in the absence of reducing agent, named as molar ratio 0. The reducing agent was added later (after 20 minutes of reaction at ratio 0) and the selected molar ratio of $NaBH_4$ over substrate was 12.5.

For the measurement, the former methodology as described in Chapter 5 was followed, with UV-VIS spectroscopy of the aqueous solution of 4-NP being the main method of analysis and the samples being passed through 40 μm pore hydrophilic filters for syringes. The reduction of the peaks at 317 nm and 400 nm and the formation of a new peak at 300 nm were being monitored over time. The spectra obtained over the reaction progress reaction in the absence and in the presence of $NaBH_4$ are plotted in Figure 7.17.

The peak at 400 nm increases over time in the absence of the reducing agent, while the peak at 317 nm remains practically unchanged. No peak at 300 nm corresponding to 4-AP is being registered. However, as soon as the reductant is added, the performance of the material improves, compared with the

corresponding spectra in Figure 5.21b, which demonstrates the progress of the reaction with pristine ZIF-9 at a molar ratio 12.5 and catalyst concentration of 0.1 mg/mL. According to the plotted spectra, ZIF-9@Graphene immediately reduces the 4-NP to 4-AP. Within the first 5 minutes after the addition of the reducing agent, $NaBH_4$, the peak at 400 nm shows over 50% reduction, continuously dropping to nearly 85% after an additional 5 minutes of reaction time.

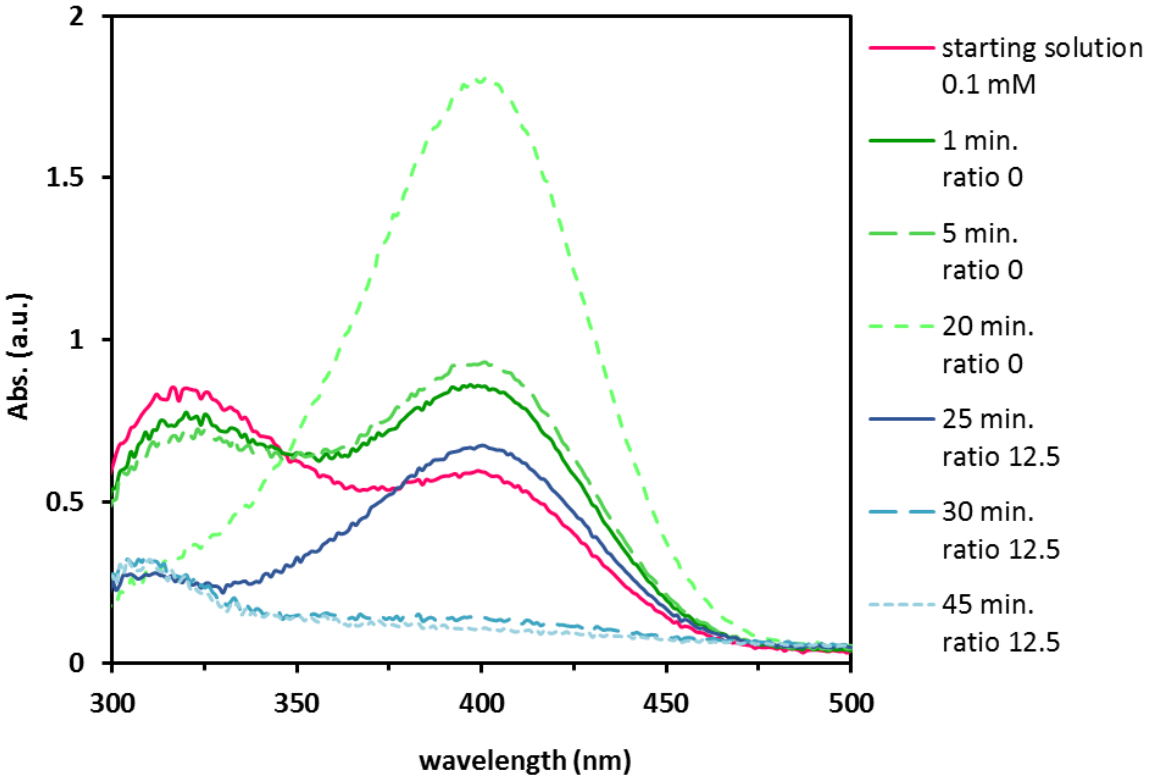

Figure 7.17 Spectra of the reaction mixture of 4-nitrophenol over time, in the absence and in the presence of $NaBH_4$ at a molar ratio 12.5, with ZIF-9@Graphene in the irradiation of white light.

Reflecting the spectra in plots of logarithms of ratios of absorption versus time in Figure 7.18 and comparing the results obtained with pristine ZIF-9 and with ZIF-9@Graphene under the same conditions, the rate of reduction of the peak at 400 nm is much faster when the modified ZIF-9 is used. In fact, the rate is calculated as ca. 10 times faster, with the two rate constants being 0.12 s^{-1} and 0.015 s^{-1}.

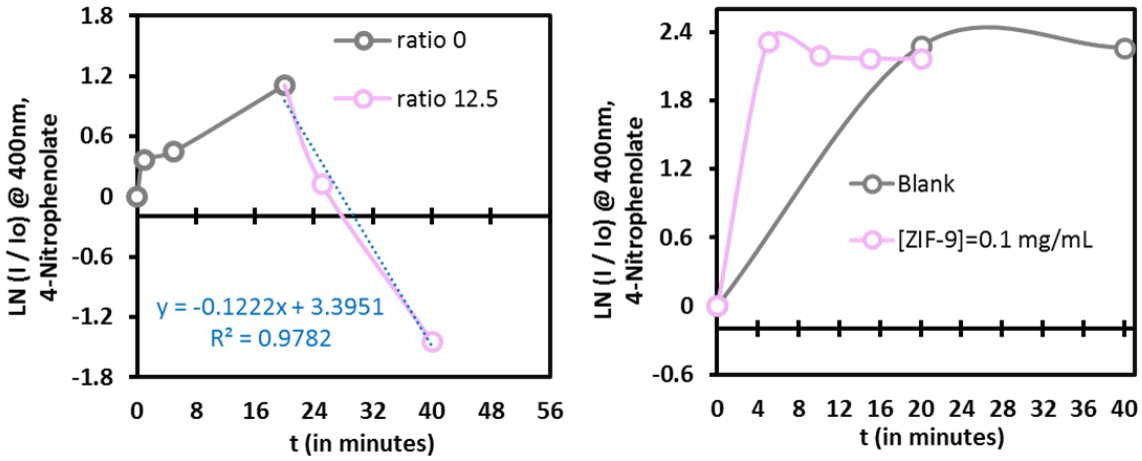

Figure 7.18 Experimental data for ratio 12.5 regarding the reduction of 4-NP with $NaBH_4$ in the presence of ZIF-9@Graphene and ZIF-9 pristine at 0.1 mg/mL in the irradiation of white light.

It should be mentioned that the comparison is not straightforward because the increase of the peak at 400 nm over time after 20 minutes with ZIF-9 @Graphene does not reach the level of intensity achieved with pristine ZIF-9 upon the addition of the catalyst. For this reason, the total reduction achieved with ZIF-9@Graphene is calculated on the basis of the starting intensity at 400 nm rather than the intensity level after 20 minutes of stirring with the modified ZIF-9. The reduction of the intensity registered in the case of pristine ZIF-9 is 11%, while ZIF-9@Graphene achieves 82% reduction (Figure 7.19).

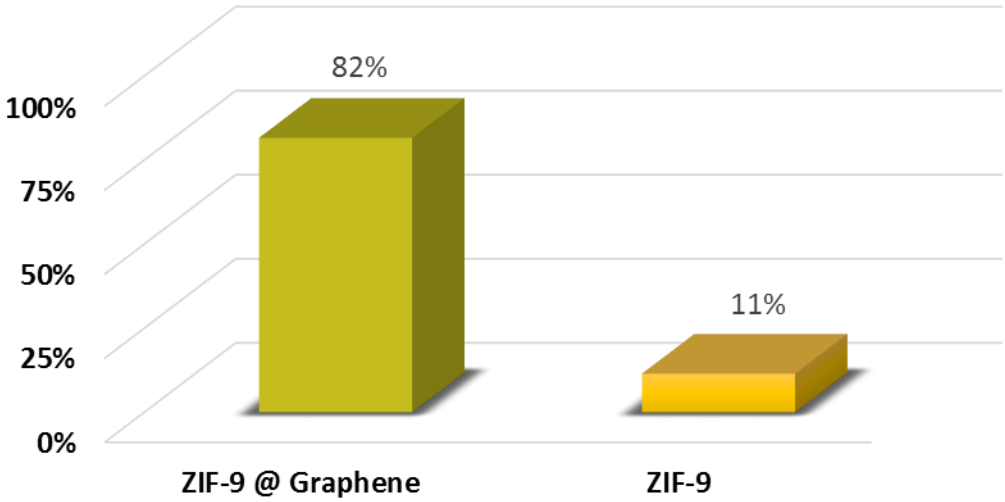

Figure 7.19 Total reduction of intensity of peak at 400 nm achieved with ZIF-9@Graphene and ZIF-9 pristine at a concentration of 0.1 mg/mL and the molar ratio of $NaBH_4$ over 4-nitrophenol at 12.5, in the irradiation of white light.

7.3.4 Conclusions and discussion for future work

The modification of ZIF-9 with graphene was proven to provide remarkable photocatalytic activity in the model reaction of the 4-NP to 4-AP reduction. The reduction achieved with ZIF-9@Graphene is almost 8 times higher and 10 times faster, while the hydrolysis of 4-NP to the corresponding ion is slower and less intense than with pristine ZIF-9. The experiment was performed under white light and ZIF-9@Graphene proves excellent photocatalytic performance.

Among the results, the most important and interesting one regards the concentration of the catalytic material. When pristine ZIF-9 was used at concentration of 0.1 mg/mL, the reaction could not proceed and the content of the catalyst in the mixture was not enough for the effective hydrogen production from the reducing agent. As a consequence, the reaction rate is extremely slow, resulting in incomplete conversion. After modification of ZIF-9 with graphene, which is an efficient charge carrier, the photocatalytic reaction is significantly improved.

The potential of the modified ZIF-9 with graphene is high for photocatalytic applications. ZIF-9@Graphene is an efficient photocatalyst in the application of 4-NP to 4-AP reduction and thus, could be probed for a number of photoreactions that require the evolution and utilisation of hydrogen. Apart from a number of reactions, further characterisation should be performed. For instance, PXRD performed at the range of bigger angles and TEM and BET surface area analysis could reveal more information about this material, especially in terms of structure. The optimisation of the material could also include experiments regarding the change of the synthetic route, such as different ratios, various annealing times, different precursors, pH values etc. Overall ZIF-9@Graphene can be considered as a promising material with numerous research possibilities.

7.4 Epilogue and future perspectives

In the synopsis of this thesis, from a range of porous crystalline materials that have been employed for a CDC reaction, the reduction of 4-nitrophenol and or dye degradation with the simultaneous dehydrogenation of $NaBH_4$ in the oily phase, ZIF-9 has performed best among CuAlPO-5, CoAlPO-5, HKUST-1 and CoMOF-74. The ZIF-9 structural architecture combines the zeolitic SOD topology and the Co(II) tetrahedral sites with the high content of metal and hydrophobic nature of ligand. The interaction of ZIF-9 with the substrates of each application

has been determining not only the catalytic but also for the photocatalytic properties of the material.

Unlike ZIF-9, copper and cobalt substituted AlPO-5 lack the high metal capacity which decreases their photoresponse due to eliminated LMCT and MLCT and d-d transitions. Similarly, the CoAlPO-5 and CuAlPO-5 are inorganic frameworks, while ZIF-9, HKUST-1 and CoMOF-74, as hybrid materials which contain aromatic ligands and demonstrate a level of conjugation with the metal, are able to use energy from light and induce LMCT. Unlike HKUST-1 and CoMOF-74, ZIF-9 contains the electron-rich nitrogen in its framework, which contributes to enhanced electron donation, raising the energy level of the HOMO, thus interacting better with the visible photons. These reasons can explain the improved photocatalytic performance of ZIF-9 in applications mediated with visible light.

Furthermore, the extraction of hydrogen from $NaBH_4$ in the aqueous and in the oily phase has been successful with ZIF-9, along with 4-NP reduction and decolouration of dye solutions. The material affords a complex structure and multidimensional pore access, along with metal sites. Similar structural characterisation has been attributed to HKUST-1, which also performed interestingly in the 4-NP reduction along with $NaBH_4$ dehydrogenation. Therefore, the complex topology may play a fundamental role when gas phase is involved, since CoMOF-74, CuAlPO-5 and CoAlPO-5 with their bigger pores and monodimensional channels system interacted poorly with the hydride.

The cobalt sites in ZIF-9 and in CoMOF-74 are, respectively, tetrahedral and square pyramidal but open and at high content. On the other hand, given that CoAlPO-5 also contains tetrahedral sites of cobalt but performed poorly, the role of the coordination geometry is questioned and it seems that it may eventually have an indirect role in the applications. Although in all cases the access to the metal sites is easy, the tetrahedral coordination can enhance the photoresponse in the region of the light spectrum that is needed. Furthermore, the control of the oxidation state of cobalt is limited in CoAlPO-5, which does not help with the required photoresponsive behaviour.

Judging ZIF-9 from its catalytic performance and characterisation after at least one catalytic run, the material preserves its activity, although its structure appears degraded. In terms of morphology, the small size of the particles of ZIF-9 affords a bigger external surface area. Overall, the material is promising and

opens a new window of applications to be tested, while the preliminary transient photoresponse measurements showed that the material has big potential as a photocatalyst for the long lifetime excited states. Modification of ZIF-9 with graphene enhances its photoactivity and promotes its applicability in photocatalysis.

The applications tested in these projects of the current thesis cover a range of problems that chemistry and engineering need to tackle together in a green manner. The cross-dehydrogenative couplings respond to a fundamental problem of organic synthesis. However, the dominance of mild conditions and less waste are urgent requirements that need to be met and green chemistry and engineering principles point it out strongly. Moreover, the application of visible light photocatalysis enhances the possibilities of harnessing the light and transforming this energy into useful and clean products. The reduction of nitro-aromatics and the dye degradation are only parts of bigger environmental solutions that need to be implemented. This applies from industrial wastewaters to marine quality upgrade. In engineering, the solution is never single. On the contrary, it is the combination of solutions that is required and only the synergy between different fields can make it appear more sustainable, since the problems are similar among the industrial sectors, while the solutions have a positive impact to all of them.

7.5 References

1 R. Berera, R. van Grondelle and J. T. M. Kennis, *Photosynth. Res.*, 2009, **101**, 105–118.

2 S. Monti and C. Chiorboli, in *The Exploration of Supramolecular Systems and Nanostructures by Photochemical Techniques*, ed. P. Ceroni, Springer Netherlands, Dordrecht, 2012, pp. 185–207.

3 X. Wang, A. Kafizas, X. Li, S. J. A. Moniz, P. J. T. Reardon, J. Tang, I. P. Parkin and J. R. Durrant, *J. Phys. Chem. C*, 2015, **119**, 10439–10447.

4 A. Furube, T. Shiozawa, A. Ishikawa, A. Wada, K. Domen and C. Hirose, *J. Phys. Chem. B*, 2002, **106**, 3065–3072.

5 Y. Kajii, T. Nakagawa, S. Suzuki, Y. Achiba, K. Obi and K. Shibuya, *Chem. Phys. Lett.*, 1991, **181**, 100–104.

6 P. Irmler and R. F. Winter, *Dalton Trans.*, 2016, **45**, 10420–10434.

7 X. Cui, J. Zhao, Z. Mohmood and C. Zhang, *Chem. Rec.*, **16**, 173–188.

8 E. Gerstner, *Nat. Phys.*, 2010, **6**, 836.

9 J. Colapinto, *New Yorker*, 2014.

10 A. H. C. Neto, F. Guinea, N. M. R. Peres, K. S. Novoselov and A. K. Geim, *Rev. Mod. Phys.*, 2009, **81**, 109–162.

11 Y. Liu, B. Xie, Z. Zhang, Q. Zheng and Z. Xu, *J. Mech. Phys. Solids*, 2012, **60**, 591–605.

12 X. Chen, R. Meng, J. Jiang, Q. Liang, Q. Yang, C. Tan, X. Sun, S. Zhang and T. Ren, *Phys. Chem. Chem. Phys.*, 2016, **18**, 16302–16309.

13 X. Huang, F. Boey and H. Zhang, *Cosmos*, 2010, **6**, 159–166.

14 K. S. Subrahmanyam, A. K. Manna, S. K. Pati and C. N. R. Rao, *Chem. Phys. Lett.*, 2010, **497**, 70–75.

15 Y. Ioni, E. Buslaeva and S. Gubin, *Mater. Today Proc.*, 2016, **3**, S209 – S213.

16 R. Torres-Mendieta, D. Ventura-Espinosa, S. Sabater, J. Lancis, G. Mínguez-Vega and J. A. Mata, *Sci. Rep.*, 2016, **6**.

17 S. M. Choi, M. H. Seo, H. J. Kim and W. B. Kim, *Synth. Met.*, 2011, **161**, 2405–2411.

18 P. T. Yin, S. Shah, M. Chhowalla and K.-B. Lee, *Chem. Rev.*, 2015, **115**, 2483–2531.

19 M. Zeng, Y. Liu, F. Zhao, K. Nie, N. Han, X. Wang, W. Huang, X. Song, J. Zhong and Y. Li, *Adv. Funct. Mater.*, 2016, **26**, 4397–4404.

20 Y.-X. Zhou, Y.-Z. Chen, L. Cao, J. Lu and H.-L. Jiang, *Chem. Commun.*, 2015, **51**, 8292–8295.

21 X. Yang, S. Wu, J. Hu, X. Fu, L. Peng, Q. Kan, Q. Huo and J. Guan, *Catal. Commun.*, 2016, **87**, 90–93.

22 M. Thomas, R. Illathvalappil, S. Kurungot, B. N. Nair, A. A. P. Mohamed, G. M. Anilkumar, T. Yamaguchi and U. S. Hareesh, *ACS Appl. Mater. Interfaces*, 2016, **8**, 29373–29382.

23 D. Kim, D. W. Kim, W. G. Hong and A. Coskun, *J. Mater. Chem. A*, 2016, **4**, 7710–7717.

24 S. Gupta, S. B. Carrizosa, B. McDonald, J. Jasinski and N. Dimakis, *J. Mater. Res.*, 2017, **32**, 301–322.

25 S. J. Cochran and F. P. Larkins, *J. Chem. Soc.{,} Faraday Trans. 1*, 1985, **81**, 2179–2190.

26 J. Matienzo, L. I. Yin, S. O. Grim and W. E. Swartz, *Inorg. Chem.*, 1973, **12**, 2762–2769.

Appendix A Supplementary results from solids characterisation

A.1 Table of statistical coefficients calculated via the Rietveld Refinement procedure

The Rietveld Refinement numerical process was applied to the observed data against the simulated XRD data with the help of the EVA software.

Material	R_{wp} (%)	R_p (%)	R_{exp} (%)	x^2	max $^{shift}/_{e.s.d.}$
AlPO-5	17.10	12.47	3.97	18.4974	0.001
CuAlPO-5	14.14	10.31	3.06	21.2485	0.963
CoAlPO-5	16.55	11.90	3.70	20.0391	0.001
SAPO-5	21.50	15.43	3.64	34.8114	0.074
SAPO-34	33.17	26.79	3.93	71.0980	0.004
CoMOF-74	7.22	4.95	3.23	4.9795	0.083
HKUST-1	19.00	13.85	2.18	75.5247	0.029
CoZIF-9	6.39	4.15	2.98	4.6099	0.174

A.2 Collection of SEM images of various magnification scale

A.2.1 SEM images of CoAlPO-5

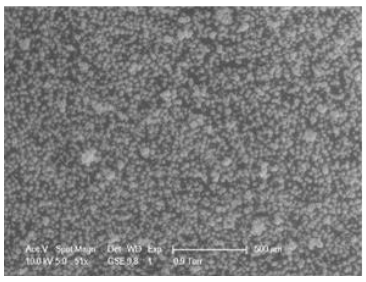
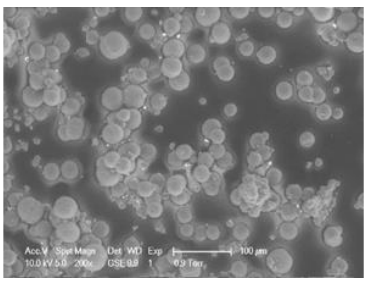
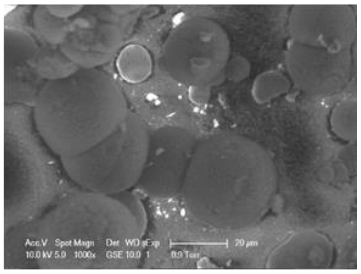

A.2.2 SEM images of CuAlPO-5

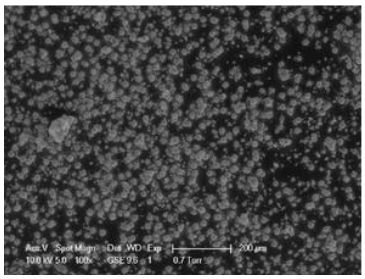
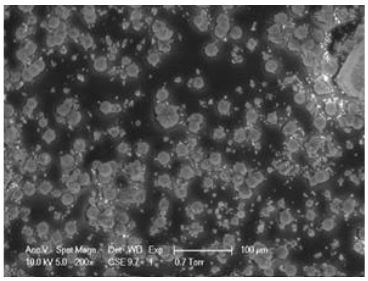
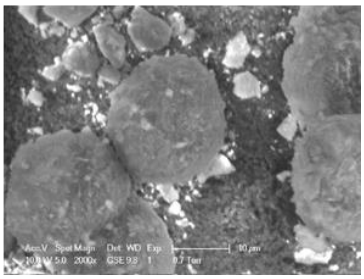

A.2.3 SEM images of HKUST-1

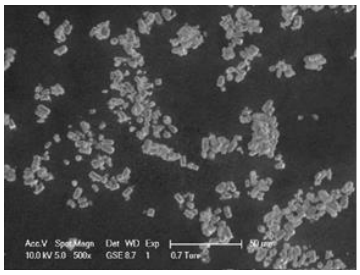
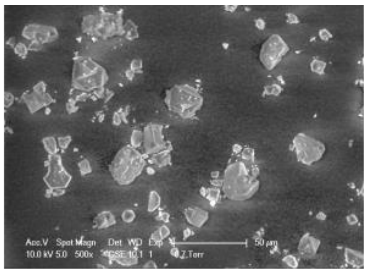
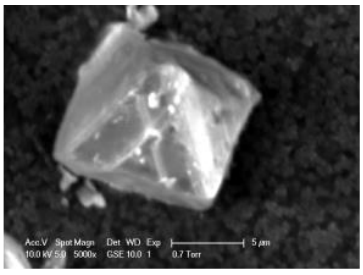

A.2.4 SEM images of ZIF-9

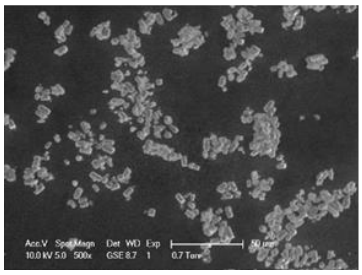
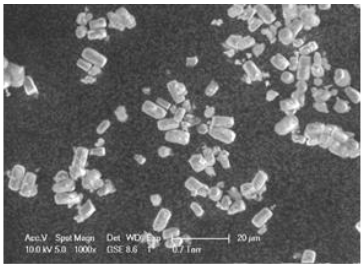
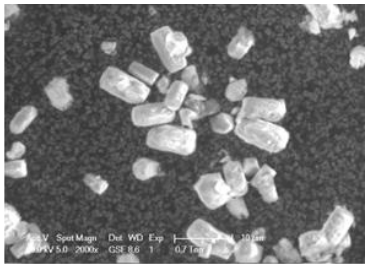

A.2.5 SEM images of CoMOF-74

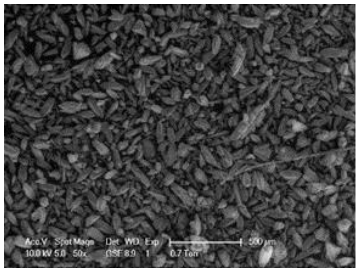
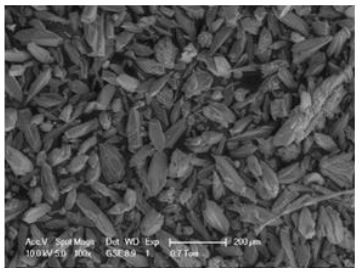
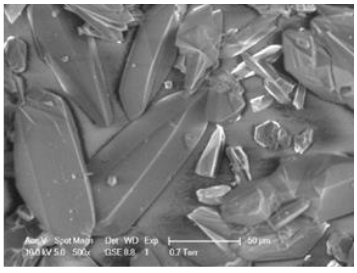

A.2.6 SEM images of used CuAlPO-5

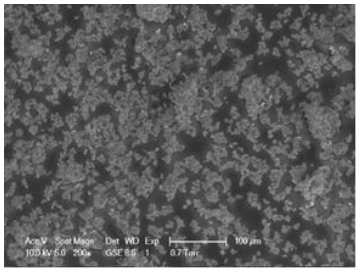
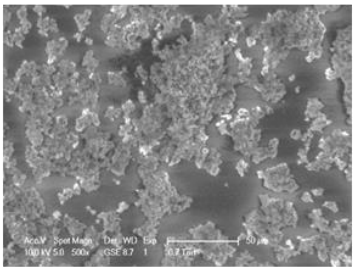
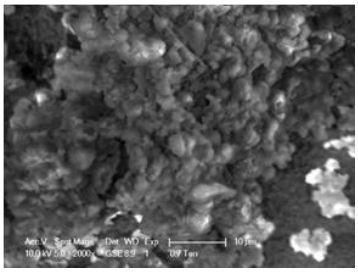

A.2.7 SEM images of used HKUST-1

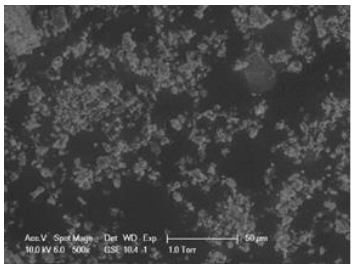
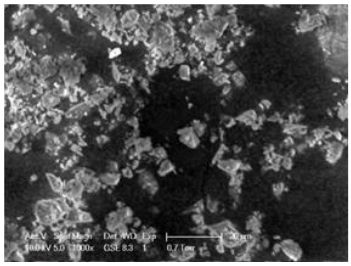
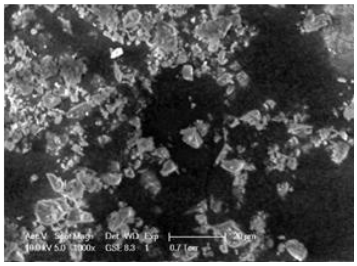

A.2.8 SEM images of used ZIF-9

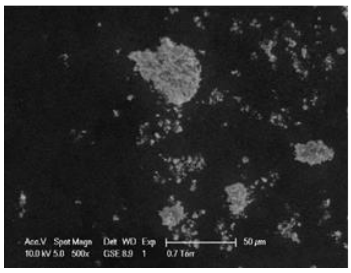
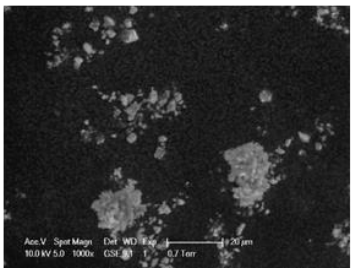
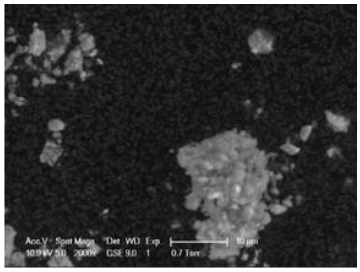

A.3 Values and errors of EDX measurements

Material	Weight % ± Error				Atom % ± Error			
ZIF-9	O (K)	N (K)	C (K)	Co (L)	O (K)		C (K)	Co (L)
	6.6 ± 0.8	20.4 ± 0.8	52.5 ± 0.3	14.4 ± 0.2	6.3 ± 0.2	22.1 ± 0.8	66.3 ± 0.9	5.3 ± 0.1
HKUST-1	O (K)		C (K)	Cu (L)	O (K)		C (K)	Cu (L)
	23.3 ± 0.1		50.2 ± 0.2	26.6 ± 0.2	24.0 ± 0.3		69.0 ± 0.1	6.9 ± 0.0
CuAlPO-5	O (K)	Al (K)	P (K)	Cu (L)	O (K)	Al (K)	P (K)	Cu (L)
	51.7 ± 0.9	26.7 ± 0.6	15.8 ± 0.6	5.8 ± 0.8	66.9 ± 1.1	20.5 ± 0.5	10.6 ± 0.4	1.9 ± 0.2
CoAlPO-5	O (K)	Al (K)	P (K)	Co (L)	O (K)	Al (K)	P (K)	Co (L)
	54.8 ± 0.6	20.4 ± 0.4	23.8 ± 0.5	1.0 ± 0.5	69.0 ± 0.8	15.3 ± 0.3	15.4 ± 0.4	0.3 ± 0.2

A.4 ICP-AES values

Material	Measured Concentration (wt. %)
Cu(4%)AlPO-5	20.14 (Al), 22.73 (P), 2.77 (Cu)
HKUST-1	27.60 (Cu), 28.64 (C), 3.20 (H), <0.10 (N)
ZIF-9	18.56 (Co), 55.31 (C), 3.70 (H), 18.92 (N)

A.5 PXRD plots of AlPO-5, SAPO-5, CoAlPO-5, CoSAPO-5 and SAPO-34

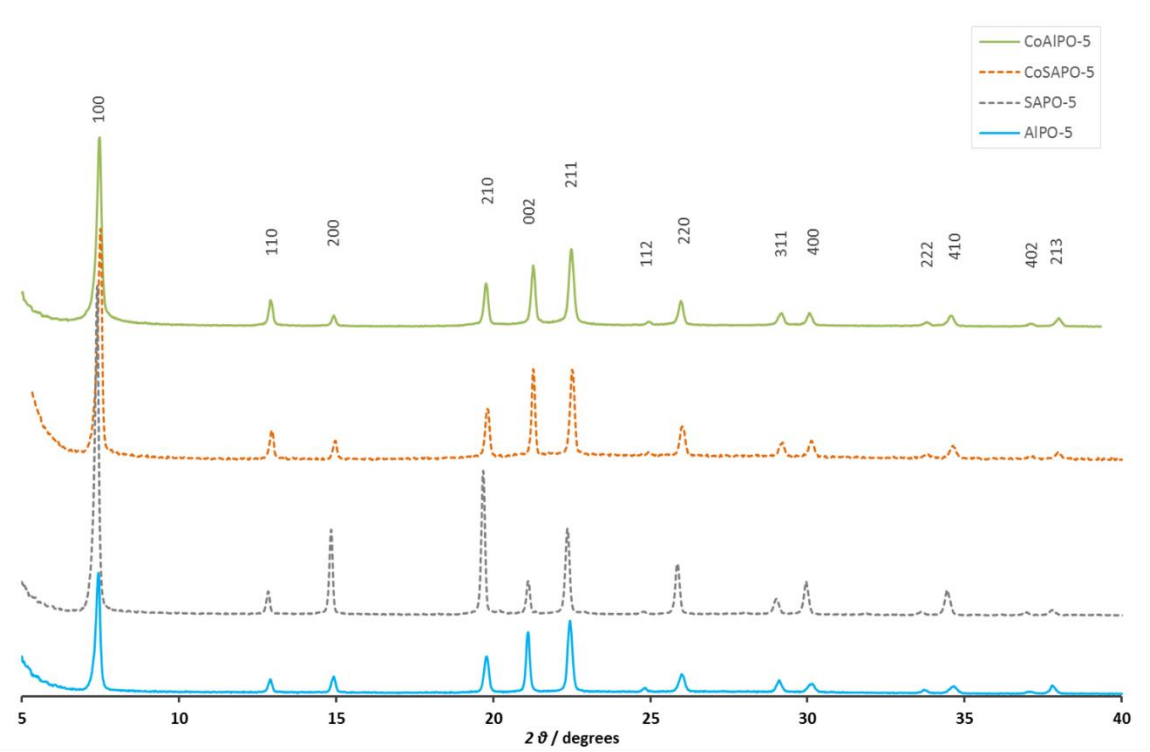

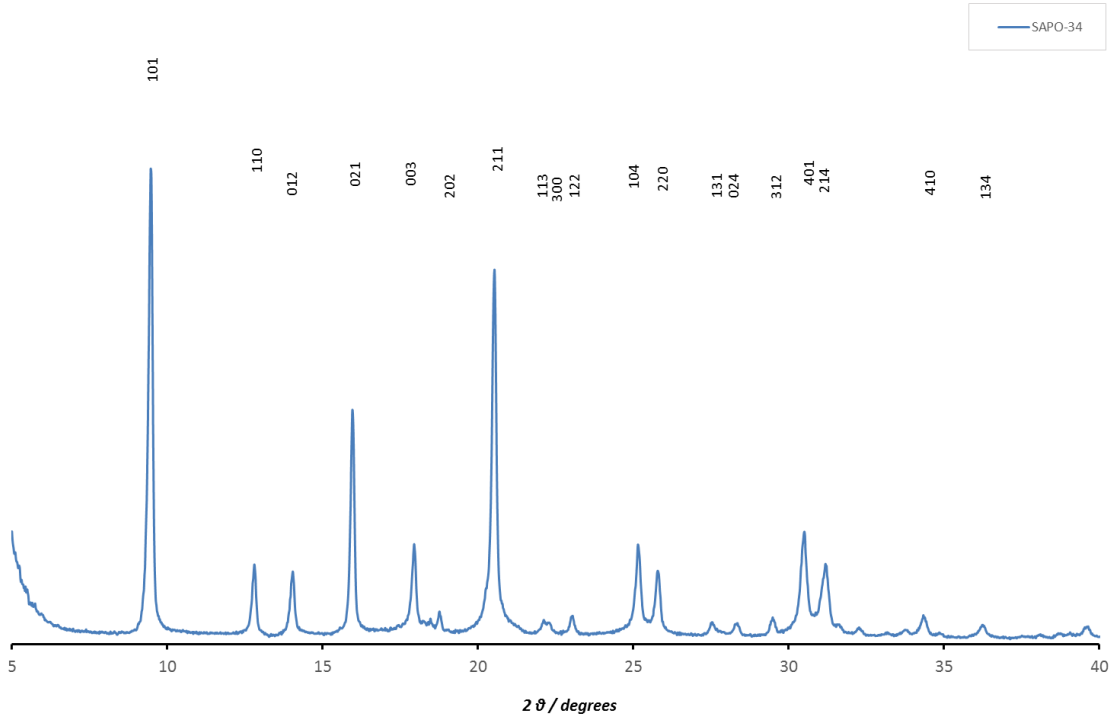

A.6 Cu LMM XPS plots CuAlPO-5 and HKUST-1

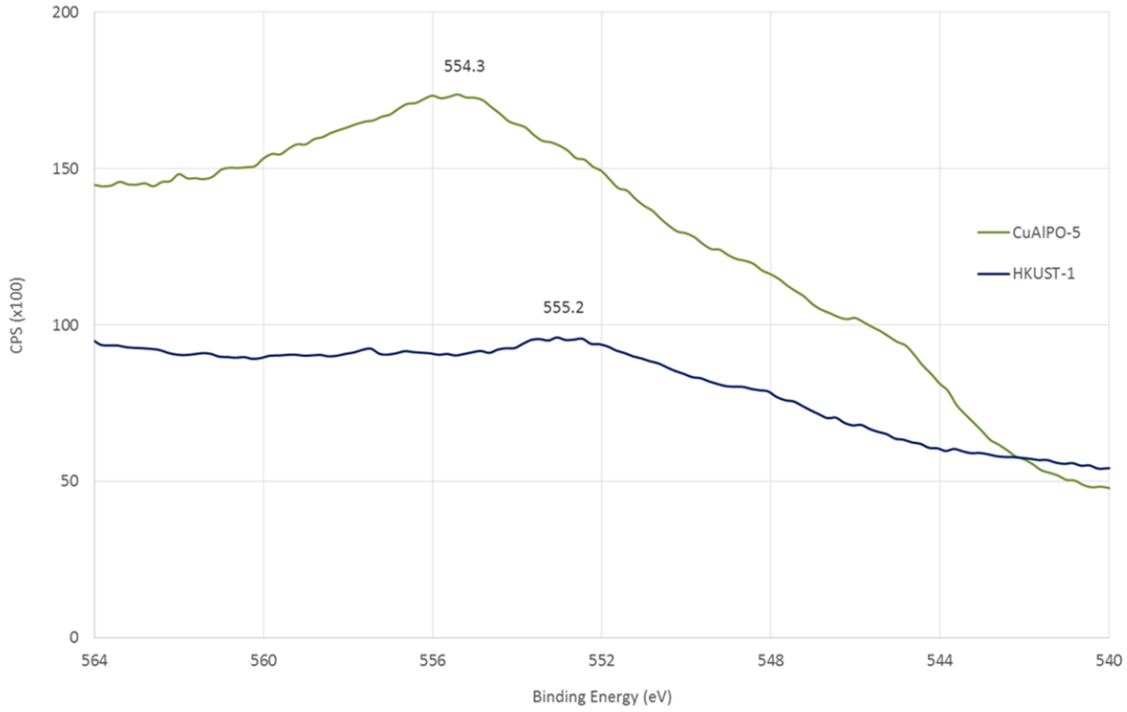

The XPS response of the copper-based materials due to the LMM electron transitions shows a difference of approximately 2 eV between the peaks for CuAlPO-5 and HKUST-1. Given the detection of Cu^{1+} in CuAlPO-5, this difference could be misinterpreted as existence of metal copper in HKUST-1. The low intensity of the LMM peak of HKUST-1 in combination with the higher intensity of the Cu^{2+} 2p peaks than the Cu^{1+} 2p peaks of CuAlPO-5 (as shown in Chapter 3) turn the Cu LMM spectra of the materials inadequate for accurate characterization. Moreover, the low intensity of the LMM peak of HKUST-1 may also be indicative of the stability of the copper coordination, which could prohibit the excitation of secondary electrons.

Appendix B Supplementary information for the preparation of materials

B.1 Preparation of the N-phenyl-tetrahydroisoquinoline

Copper (I) iodide, (476 mg, 2.50 mmol) and potassium phosphate (10.119 g, 47.7 mmol) were placed under inert atmosphere. Next, 2-propanol (23.8 mL), ethylene glycol (2.6 mL, 47.6 mmol), 1,2,3,4-tetrahydroisoquinoline (4.8 mL, 35.7 mmol) and iodobenzene (2.7 mL, 23.8 mmol) were added and the reaction mixture was then heated to 90 °C and left under stirring for 24 hours. Subsequently, it was allowed to cool down to room temperature in order to continue with adding diethyl ether (50 mL) and water (50 mL). Phase separation took place afterwards and the organic layer was then extracted with diethyl ether (2 x 50 mL). The combined organic phases were washed with brine (50 mL) and dried over magnesium sulphate. After careful collection of the liquid phase, the solvent was removed by rotary evaporation and the crude mass weighed approximately 7.5 g. The purification of the crude was achieved by column chromatography on silica gel and hexane/ethyl acetate 19:1 eluent. The yield was recorded at 3.238 g, 65 %. A peach coloured solid was collected with Rf of 0.25 in the eluent mentioned.

1H NMR (400 MHz, CDCl3): δ 7.31 (2H, td), 7.22-7.15 (4H, m), 7.00 (2H, d), 6.85 (1H, t), 4.43 (2H, s), 3.58 (2H, t), 3.01 (2H, t)

13C NMR (400 MHz, CDCl3): δ 150.58, 134.90, 134.50, 129.22, 128.53, 126.55, 126.34, 126.04, 118.68, 115.16, 50.76, 46.54, 29.14

B.2 Preparation of Cu_xAlPO-5

CuO is stirred with deionized water and phosphoric acid under heating (80 °C) until the solution is homogeneous and blue-turquoise. The solution is transferred into a Teflon beaker and stirred vigorously with alumina until a homogeneous result is obtained. The SDA is added dropwise and a gel is forming. Stirring is kept vigorous until complete homogenisation and then it is transferred into Teflon liners and stainless steel autoclaves. The autoclaves are transferred into a preheated oven and crystallisation takes place at 150 °C for 24 hours. Then, they are brought into an ice bath to cool down. Filtration under vacuum and washing with deionized water is taking place to recover the material, which is left to dry

overnight at 80 °C. The powder is then ground and calcined at 550 °C for 16 hours.

Cu_xAlPO-5 chemical sources and quantities

Elements	Molar ratio	Source	Mass or Volume
Al	0.5	Al_2O_3	3.1 g
P	0.41	H_3PO_4	3.4 mL
Cu	x=0.2, 0.4, 0.6, 0.8	CuO	0.2 g, 0.4 g, 0.6 g, 0.8 g
SDA	0.3	TEAOH	9 mL
solvent	7.1	H_2O	9.1 mL
Crystallisation time / T: 24 h / 150 ˚C			
Recovery method: filtration			
Calcination time / T: 16 h /550 ˚C			

B.3 Preparation of AlPO-5, SAPO-5, SAPO-34, CoAlPO-5 and CoSAPO-5

The general synthesis method of the non-metal containing (silico)aluminophosphates AFI (framework code 5) starts with the addition of phosphoric acid into water. During vigorous stirring, the Al source is added slowly and then the Si source. The SDA is then added dropwise and the mixture is left under vigorous stirring until a homogeneous hydrogel is formed. The mixture is transferred into Teflon liners of stainless steel autoclaves. The autoclaves are then moved into preheated oven and left for crystallisation at the end of which they are moved into ice bath to cool down. The materials are filtrated under vacuum and washed multiple times with water, before they are left to dry overnight at 80 °C. The crystals are then ground into powder and calcined.

If metals are involved, the procedure requires the metal precursors to be diluted into half of the needed water. Upon completion, the metal solutions are added dropwise before the addition of the silica. Stirring is kept vigorous at all times.

The SDA used here are mentioned as MDCHA for N,N-methyldicyclohexylamine and TEA for tetraethylammonium.

	AlPO-5		SAPO-5		CoAlPO-5		CoSAPO-5	
Elements	*Molar ratio*	*Source*		*Molar ratio*	*Molar ratio*	*Source*		*Molar ratio*
Al	*1*	*$Al(OH)_3$*		*2*	*0.96*	*$Al(OH)_3$*		*1.8*
P	*1*	*H_3PO_4*		*1.5*	*1.47*	*H_3PO_4*		*1.47*
Co					*0.15*	*$(CH_3COO)_2Co$*		*0.15*
Si			*SiO_2*				*SiO_2*	*0.25*
SDA	*0.75*	*TEA*	*MDCHA*	*0.8*	*0.15*	*MDCHA*		*1.05*
solvent	25		H_2O	100	26	H_2O		26
Crystal. t/T	20 h / 200 ˚C		23 h / 200 ˚C		2 h / 200 ˚C			
Recovery	Filtration, washing with water							
Calcin. t/T	16 h /550 ˚C							

The general synthesis of SAPO-34 starts with the mixing of the aluminium source in the solution of the phosphoric acid with the water. Under vigorous stirring, the SDA is added followed by the Si source. The hydrogel is left under stirring until complete homogenisation and then transferred into the Teflon liners of stainless steel autoclaves. The autoclaves are transferred into preheated oven and left for crystallisation. They are then moved into ice bath to cool down. The content is distributed into centrifugal tubes and separated multiple times using water. The crystals are left for drying overnight at 80 °C and then ground into fine powder to be calcined. The Al source is aluminium isopropoxide, referred here as $Al(O\text{-}i\text{-}Pr)_3$ and the SDA is tetraethylammonium hydroxide.

Elements	Molar ratio	Source
Al	0.5	$Al(O\text{-}i\text{-}Pr)_3$
P	0.85	H_3PO_4
Si	0.15	SiO_2
SDA	1	TEAOH

Appendix B

Elements	Molar ratio	Source
solvent	25	H_2O
Crystallisation time / T: 42 h / 200 ˚C		
Recovery method: centrifugation		
Calcination time / T: 16 h /550 ˚C		

Appendix C Supplementary information for the reduction of 4-nitrophenol to 4-aminophenol

C.1 Spectra of 4-nitrophenol : $NaBH_4$ reaction mixture ta molar ratio 1:12.5 in the dark in the presence of ZIF-9 at concentration 0.5 mg/mL

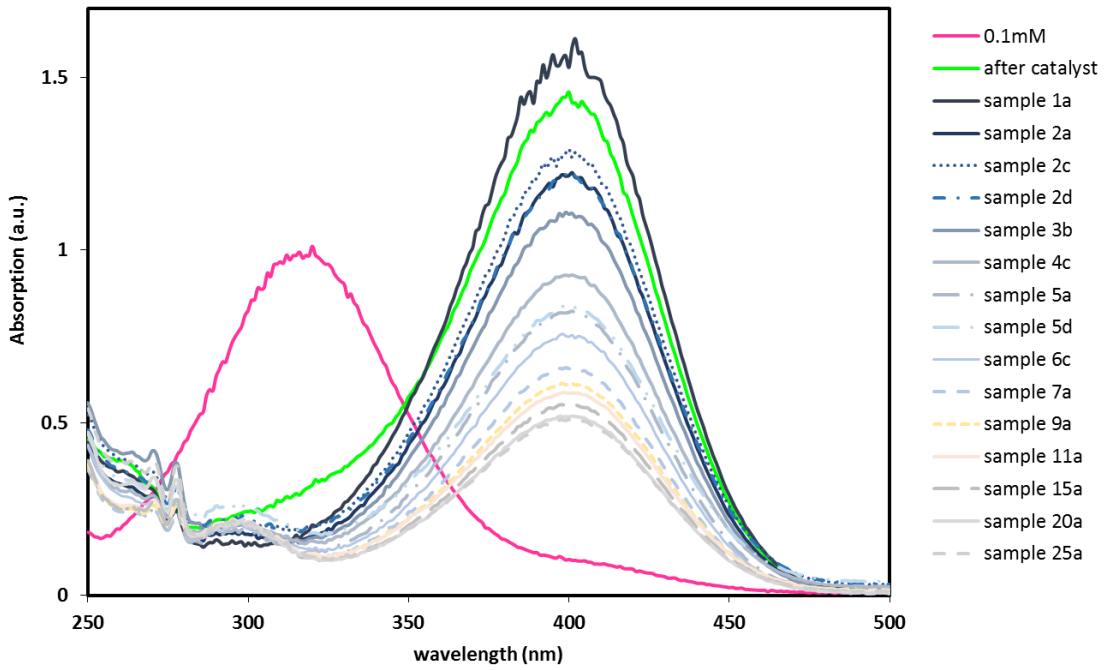

The nomenclature of spectra is based on the minute of sampling and the solution. Solutions a, b, c and d were identical and reactions ran simultaneously.

C.2 IR spectrum of 4-nitrophenol

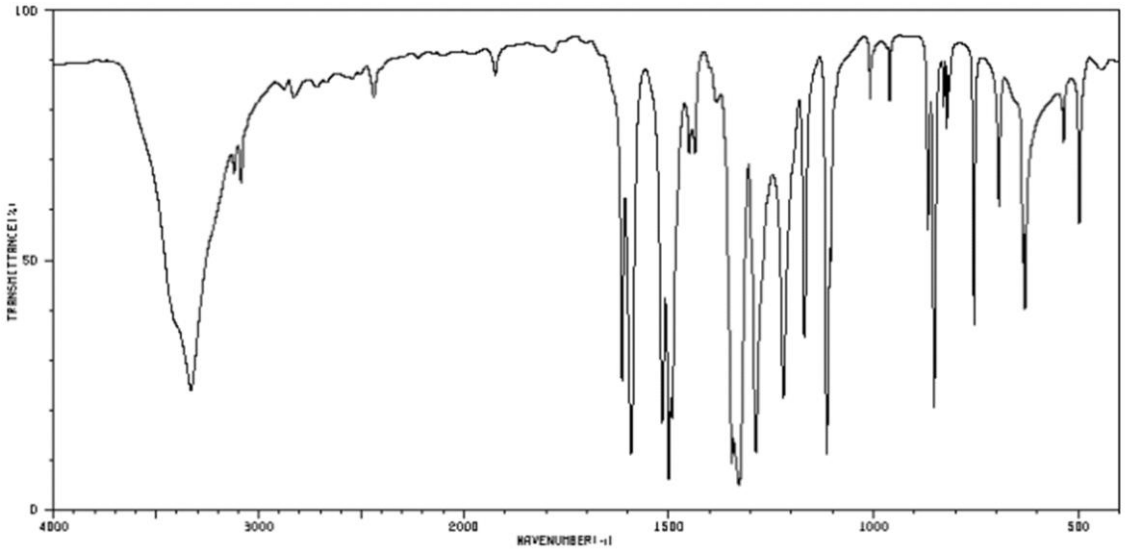

Spectrum obtained from AIST: Spectral database for organic compounds

C.3 IR spectrum of 4-aminophenol

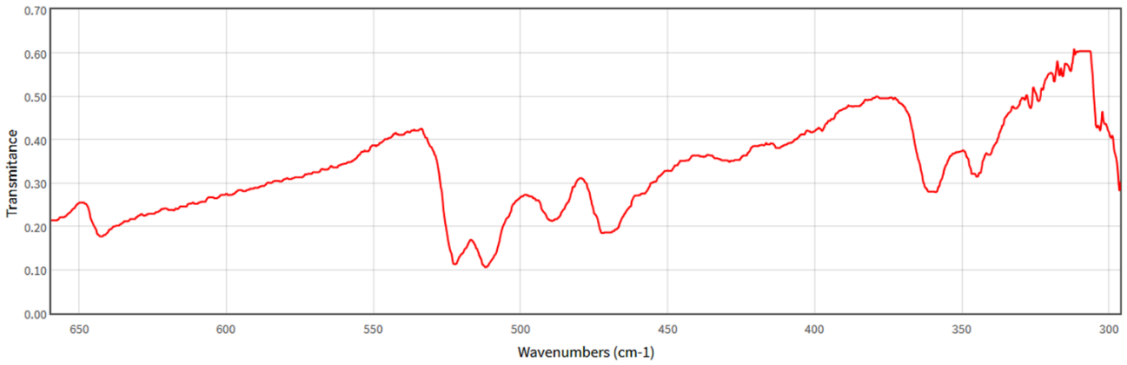

Spectrum obtained from NIST chemistry webbook

Appendix D Supplementary information for the degradation of Oil Red O

D.1 Hill decay functions for fitted data and R^2 values regarding the Oil Red O degradation in the dark

[ZIF-9]=0.1 mg/mL	$y = -0.1 - 2 \cdot \frac{x^{2.5}}{134.6^{2.5} + x^{2.5}}$	$R^2 = 0.991$
[ZIF-9]=0.3 mg/mL	$y = -0.1 - 2 \cdot \frac{x^{2.4}}{122.8^{2.4} + x^{2.4}}$	$R^2 = 0.996$
[ZIF-9]=0.5 mg/mL	$y = -0.1 - 2.6 \cdot \frac{x^{2.9}}{136.6^{2.9} + x^{2.9}}$	$R^2 = 0.994$

D.2 Spectra obtained in the experiment of Oil Red O degradation with H_2O_2

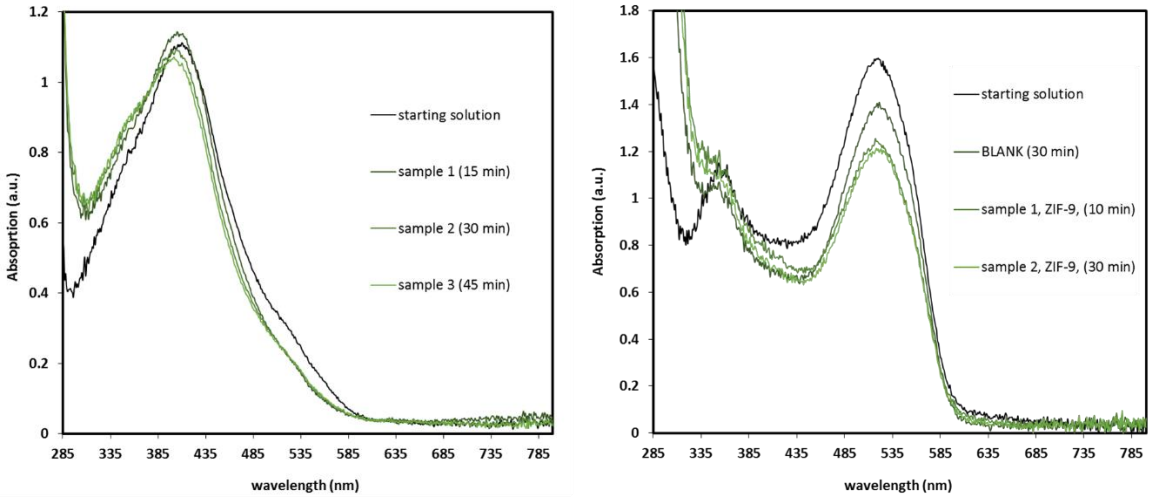

The spectrum on the left refers to the solution without ZIF-9 but with H_2O_2, after reduction with NaBH4 has been performed. The spectrum on the right refers to the solution with ZIF-9 and H_2O_2. The observation is that the peaks (new peak formed between 385 nm and 435 nm after $NaBH_4$ is used and non-main peak near 335 nm from the initial Oil Red O spectrum) are not reduced with the use of H_2O_2. Thus, the hydrogen peroxide interacts only with the main peak.

Appendix E Supplementary information for the decolourisation of dye wastewater

E.1 FTIR spectrum of dye wastewater, compared to Oil Red O FTIR spectrum

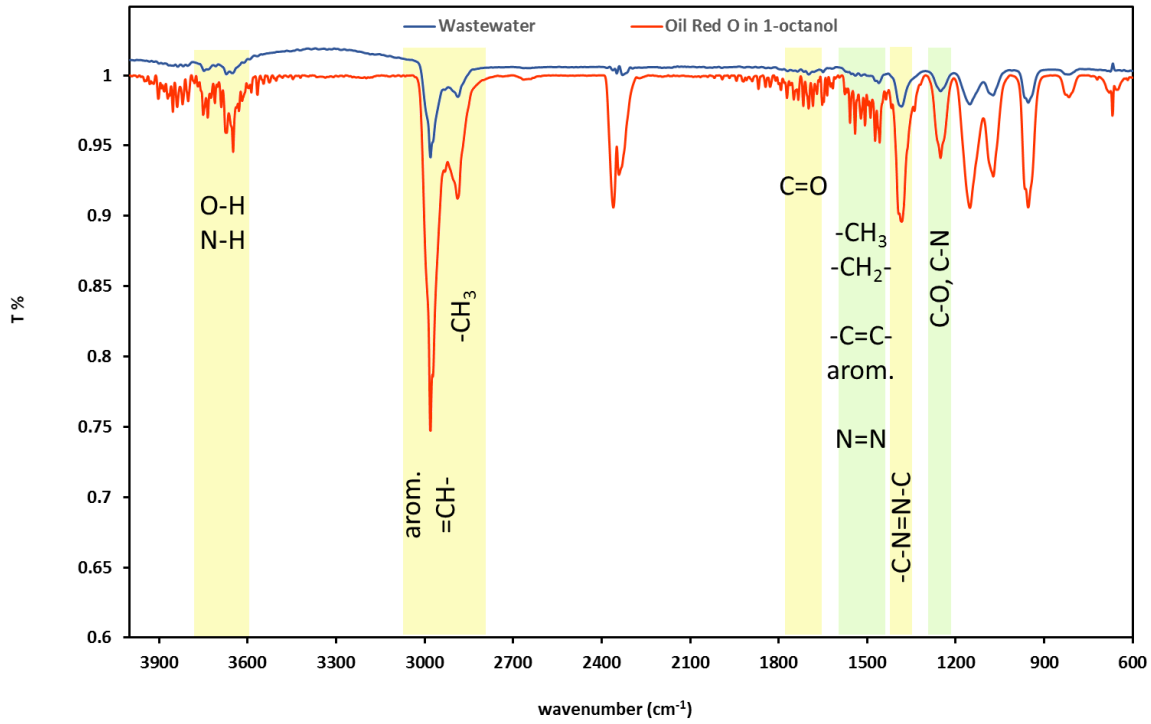

The spectrum of dye wastewater has been obtained after tap water spectrum was set as baseline. Similarly, the spectrum of Oil Red O in 1-octanol has been collected after collecting the spectrum of 1-octanol and setting it as baseline. The assignment of peaks and bands according to literature[1,2] regards the Oil Red O dye and it can be deduced that the dye wastewater has similar functional groups.

E.2 Pictures of solutions of dyed wastewater in a series of experiments

experiment (a)

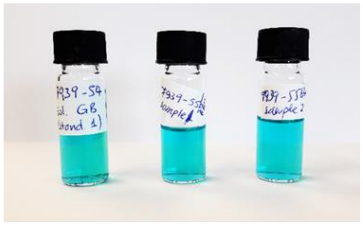

experiment (b)

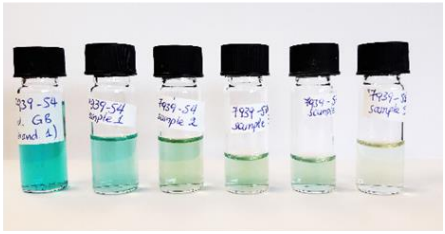

experiment (c)

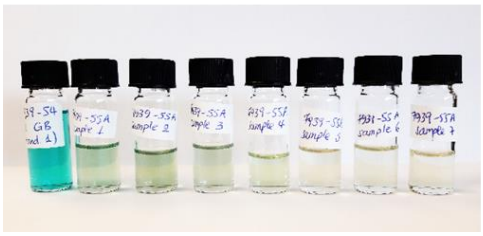

experiment (d)

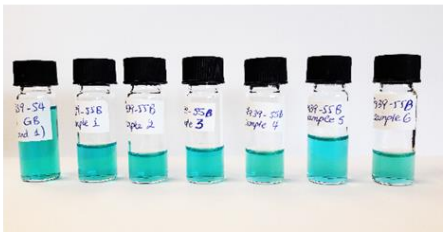

Experiment (a): Blank reaction

Experiment (b): [ZIF-9]=0.5 mg/mL and [$NaBH_4$]=0.4 mg/mL

Experiment (c): [ZIF-9]=0.5 mg/mL and [$NaBH_4$]=0.8 mg/mL

Experiment (d): [ZIF-9]=1 mg/mL and [$NaBH_4$]=0.4 mg/mL

E.3 Hill decay functions for fitted data and R^2 values regarding the decolourisation of the dyed wastewater

Experiment (b): $y = -0.01 - 0.57 \cdot \frac{x^{7.8}}{13.6^{7.8} + x^{7.8}}$ $R^2 = 0.991$

Experiment (d): $y = 0.03 - 0.25 \cdot \frac{x^{4.3}}{14.8^{4.3} + x^{4.3}}$ $R^2 = 0.973$

[ZIF-9]=0.3 mg/mL
[NaBH4]=0.8 mg/mL $y = -0.4 \cdot \frac{x^{2.7}}{9.2^{2.7} + x^{2.7}}$ $R^2 = 0.998$

[ZIF-9]=0.1 mg/mL
[NaBH4]=0.8 mg/mL $y = -0.002 \cdot x$ $R^2 = 0.862$

1 F. Ahmed, R. Dewani, M. K. Pervez, S. J. Mahboob and S. A. Soomro, *Bulg. Chem. Commun.*, 2016, **48**, 71–77.

2 C. W. M. Yuen, S. K. A. Ku, P. S. R. Choi, C. W. Kan and S. Y. Tsang, *Res. J. Text. Appar.*, 2005, **9**, 26–38.